Free-to-Roll Oscillations of Low Aspect Ratio Wings

Gresham, Nicholas

Award date:
2010

Awarding institution:
University of Bath

Free-to-Roll Oscillations of Low Aspect Ratio Wings

Nicholas Thomas Gresham

A Thesis submitted for the degree of Doctor of Philosophy

University of Bath
Department of Mechanical Engineering

October 2010

Copyright

Abstract

This Thesis aims to enhance the aerodynamic knowledge of the free-to-roll behaviour of low aspect-ratio wings by investigating newly found free-to-roll oscillations. Efforts were initially made on free-to-roll non-slender delta wings and roll oscillations were found with a low Strouhal number, which will affect wings with this planform in flight manoeuvres. It has also been shown that the non-zero roll trim angles are not due to the round leading-edge of the wing being tested as previously thought. Phase-averaged velocity measurements revealed the hysteresis effects during the self-induced roll oscillations.

Oscillations were observed for a non-slender delta wing of sweep angle of 50^o with fixed separation points and this phenomenon was seen for delta wings up to 60^o sweep (i.e. slender) with less reattached flow. Similar experiments done on cropped delta wings showed that the cropped portion reduces the non-zero roll trim angles, therefore the wing was stable. Different oscillations were found and investigated in a second region at higher angles of attack for delta wings of 57.5^o and 60^o sweep angle. Work was then performed on pitching free-to-roll delta wings, which were pitched up or down at a constant rate.

Low aspect-ratio ($AR \leq 4$) rectangular wings showed that oscillations and even autorotation existed at high angles of attack. It is suggested that the tip vortices are responsible for the oscillations. At low angles of attack, the separation bubble was asymmetric for the round leading-edge, which explains the non-zero roll trim angle for the free-to-roll wing. This separation bubble spread across the extent of the wingspan with increasing angle of attack and the oscillations were seen to begin once the separation bubble had left the trailing-edge and the side-edge vortices had increased in strength sufficiently. The vortices are seen to be well separated, and thus the effect of the side-edge vortices on one another is expected to be negligible, unlike for delta wing rock. Finally, other planforms were tested including a Zimmerman and an elliptical wing. Oscillations were found too, though smaller in magnitude.

Table of Contents

List of Figures and Tables

Acknowledgements

This work is sponsored by the US Air Force Office of Scientific Research, Air Force Material Command, USAF, under grant number FA8655-06-1-3058. I would like to acknowledge the continual support, advice and input of my supervisors Ismet Gursul and Zhijin Wang. My family have always supported me, which was necessary for the final year of this project, for which I am eternally grateful. I would also like to acknowledge the support of the Mechanical Engineering Instrumentation Department in the University of Bath, who have done some sterling work on very difficult projects that were necessary for my work. Finally, I should acknowledge the technicians who, besides being nice people and making good tea, have also kept me above board, happy retirement H!

Nomenclature

a = Acceleration, ms^{-2}

A = Wing surface area, m^2

AR = Aspect ratio

b = Wing span, m

c = Wing chord, m

C_D = Drag force coefficient

C_L = Lift force coefficient

$C_{L\varphi}$ = Lift force coefficient dependant on roll angle

f = Frequency, Hz

F = Force, N

I_{xx} = Moment of inertia about the x-axis, kgm^2

k = Reduced frequency, $\omega c / U_\infty$

L = Length, m

M = Mass, kg

n = Number of dimensionless groups

q = Free stream dynamic pressure, $\frac{1}{2} \rho U_\infty^2$

Re = Reynolds number, $U_\infty c / \nu$

s = Semi-span, m

St = Strouhal number, fc / U_∞

S = Time, s

Δt = Time interval, s

t = Thickness, m

T = Torque, Nm

U = Velocity perpendicular to wing surface, ms^{-1}

U_∞ = Wind tunnel free-stream velocity, ms^{-1}

V = Velocity normal to wing surface, ms^{-1}

x = Chordwise distance, m

x_{bd} = Chordwise distance for vortex breakdown, m

y = Spanwise distance, m

z = Distance from the wing surface in a plane normal to free-stream, m

α = Angle of attack, ^{o}

α_{eff} = Effective angle of attack, ^{o}

β = Sideslip angle, ^{o}

μ = Dynamic viscosity, 1.69 x 10^{-6} $kgm^{-1}s^{-1}$ (air at sea level)

ν = Kinematic viscosity, 1.51 x 10^{-5} m^2s^{-1} (air at sea level)

Λ = Wing sweep angle, ^{o}

Λ_{eff} = Wing effective sweep angle, ^{o}

Γ = Circulation, m^2s^{-1}

Φ = Wing roll angle, ^{o}

Φ_{min} = Minimum roll angle, ^{o}

Φ_{mean} = Mean roll angle, ^{o}

Φ_{max} = Maximum roll angle, ^{o}

ξ_B = Distance down wing for vortex breakdown

ω = Vorticity, dU / dt, s^{-1}

ρ = Air density, kgm^{-3}

Chapter 1 Introduction and Literature Review

Interest in Unmanned Air Vehicles (UAVs) and Micro Air Vehicles (MAVs) has increased in recent years. A review of the aerodynamics of small vehicles flying at low speeds is given by Mueller and DeLaurier[1]. For fixed-wing aircraft, the effects of transition, separation bubble and aspect ratio (AR) have been discussed in detail[2,3,4]. However, for delta, elliptical, Zimmerman, cropped and even rectangular wings (with low aspect ratio below 2.0) an unusual phenomenon occurs at certain combinations of Reynolds number (Re), angle of attack (α) and wing geometry, where the wings perform self-induced roll oscillations, including some not completely understood[5,6]. These roll oscillations may be encountered during a manoeuvre or by a sudden gust of wind, hence it is important to understand what causes them and how to control them, otherwise limitations are placed upon the flight envelope of small aircraft. This is the first time these oscillations have been seen.

Journal articles and conference papers have been published from the work to be presented and are referenced and attached in Appendices A and B.

1.1 Aerodynamics of slender delta wings

Delta wings were developed for their ability to fly supersonically and subsonically and because of their resilience to high angles of attack. This is due to the mechanism of lift generation, which incorporates two counter rotating vortices with low pressure centres over the suction surface due to the shear-layers rolling up. Figure 1.1 shows a slender delta wing with a typical flow field[7]. This incorporates two large primary vortices[8], where the flow separates and two smaller vortices, where the flow between the primary vortex and wing surface separates itself due to an adverse pressure gradient in a cross-flow plane. This secondary vortex pulls the primary vortex back towards the wing surface. Any air which is not sucked into the vortices, particularly for less slender versions, forms an inboard chordwise flow as shown in the diagram. This flows over the vortices and reattaches to the wing surface and has corresponding reattachment lines. Continuous feeding of the vorticity from the shear layer separating along the leading-edge preserves the vortical structures on the wing, which is caused by the wing's leading-edge.

Figure 1.2 presents the lift coefficients for various sweep angled delta wings[9]. It can be observed that with increased sweep angle there is a later stalling point (the angle of attack with maximum lift). This is due to larger vortices being formed and the subsequent lower pressures on the wing surface. It is also visible that lower sweep angled delta wings exhibit lower maximum values of C_L due to these planform shapes not relying on the vortices to generate the lift to such a degree (the vortices generate about 50 % of the lift for a 50^o sweep delta wing).

Vortex breakdown can be classed as either of bubble or spiral type for slender delta wings and can change between the two randomly[10]. It plays a damping role for wings in roll motion. Figure 1.3 shows how the position of vortex breakdown varies in relation to the angle of attack for different sweep angled delta wings[11]. This shows that the breakdown location of leading-edge vortices moves towards the apex as sweep angle is decreased for a given angle of attack. With increased sweep angle, a larger angle of attack is required to see vortex breakdown on the wing surface, whereas for a sweep angle of 55^o or below it is always present. Less sweep is effectively making the wing more rectangular in planform shape, so the vortices play less of a role. For this reason, a sweep angle of 55^o is normally taken as the difference between slender and non-slender delta wings, and whether reattached flow is present at the centre of the wing surface. Previous work[12] has shown that the normal and parallel velocity components are significantly higher for a slender delta wing of 70^o sweep angle than for non-slender delta wings. At very high angles of attack, slender wings undergo vortex shedding, but this is outside the envelope at which wing rock has been observed to occur.

1.2 Aerodynamics of non-slender delta wings

This investigation was inspired by the behaviour of low sweep delta wings, such as the a) Boeing X-45C[13] and b) AeroVironment Wasp[14] shown in Fig. 1.4, the Avro Vulcan, a cold war bomber and more modern fighter aircraft such as the Sukhoi Su-32 and the McDonnell Douglas F-4 Phantom (which incorporates a delta section). In these cases, non-slender delta wings operating at low/transitional Reynolds numbers are of importance. These and similar other planforms have been developed for UAVs and MAVs, and are used for their practical shape and good flight responses at high angle of attack. Whereas a rectangular wing of this size would stall at a low angle of attack, such

as that exhibited by a gust of wind, a delta wing is much more resilient to a large range of angles of attack.

The actual flow physics over a non-slender (50^o sweep) delta wing with a sharp leading-edge at an angle of attack of only 2.5^{o15} is shown in Fig. 1.5. This is a flow visualisation and the reattachment line of the vortex can clearly be seen. The wing has a sharp leading-edge thus fixed separation point, so a vortex of some magnitude would be expected. If the angle of attack is increased further, such as 17.5^{o15} as shown in Fig. 1.6, the vortices can be seen to become larger. This Figure shows the difference between a a) sharp and b) round leading-edge. With round leading-edge reattachment can be seen to be further inboard.

The effects of leading-edge shape and hence separation, have been previously investigated at the University of Bath[15] (Fig. 1.7). It was found that a delta wing with sharp leading edges stalled at lower α than round, 2:1 elliptical or 4:1 elliptical versions and that the difference was about 5^o. This is more significant than expected due to all the wings being exactly the same, bar the leading-edges. The reattachment line was also seen to be further inboard for the sharp leading-edged delta wing, and furthest outboard for the 2:1 elliptical version of the leading-edges. Because the flow over a delta wing incorporates separation, leading-edges are important for the flow physics, though this does depend on the size of the leading-edge in relation to the span. For furthest outboard reattachment, a compromise must be struck between a sharp leading-edge (fixed separation points) and a very gradual curvature incorporating a sharper version of the round leading-edge (4:1 elliptical). This is why the 2:1 elliptical leading-edge causes the separation point to be furthest outboard, and the reattachment furthest inboard.

Figure 1.8 shows a characteristic dual vortex flow structure over a non-slender (50^o sweep) delta wing. This is shown in experimental format[16] in Fig. 1.8a), a computation of which[17] is in Fig. 1.8b) and is present up to $\alpha \sim 15^o$ for a wing with $\Lambda = 50^o$. Where the secondary flow separates from the surface, the primary vortex is split into two same sign vortices. In Fig. 1.8a), at a relatively low angle of attack ($\alpha = 5^o$), the primary vortex is formed very close to the wing surface. This means there is interaction between the vortex formed by the leading-edge and the shear layer close to the wing surface, formed by attached flow. This creates the structure, which is shown in Fig.

1.8b) in a computational form at a slightly higher angle of attack of 7.5°. Reynolds number effect is large at low angles of attack because of the presence of this vortical structure. Flow structures over a 50° sweep delta wing have been investigated and it has been seen that even at a high angle of attack, $\alpha = 20^{o}$, even though vortex breakdown is at the apex of the wing there is still attached flow. Figure 1.9a) shows that vortex breakdown is at the apex of the wing[16] and that reattached flow is visible from the streamlines in Fig. 1.9b). This is another non-slender delta wing characteristic, as for slender delta wings breakdown at the apex means wing stall[18]. In this case, because the vortices do not generate all the lift, breakdown does not mean stall. For slender delta wings, vortex breakdown means no reattachment, thus any instability associated with reattaching flow is non-existent.

A unique feature of non-slender delta wings[19] is that primary attachment occurs outboard of the symmetry plane, even when vortex breakdown is near the apex. Vortex breakdown for non-slender wings is much less abrupt than for slender wings and it was noted[8] that vortex breakdown of non-slender delta wings differs from that of slender wings. This attachment moves inboard in a spanwise view with increasing angle of attack until there is no more reattachment and the wing is stalled. It has been shown that Reynolds number has a large influence on the stall angle of non-slender delta wings[12], not observed with slender delta wings. Work done on a wing with $\Lambda = 55^{o}$ and sharp leading-edges showed that stall occurred earlier as the Reynolds number was increased[20].

1.3 Slender delta wing rock

Most of the knowledge on unsteady aerodynamics of wings in roll motion is on slender delta wings[1,21]. This phenomenon is well understood and has been observed for sweep angles $\Lambda \geq 75^{o}$. Moment of inertia does have an effect on the frequency of oscillation. One suggestion to the commencement of wing rock is that it is initiated by vortex interaction, which results in asymmetries in vortex strength[22].

Arena and Nelson[23] suggest that to sustain the wing rock motion a time-lag in the position of the vortices normal to the wing surface is necessary[23]. Figure 1.10 shows that during wing rock, the vortices occupy the same position horizontally, but differ in

vertical positions (which alters lift on the corresponding wing half). The proposed mechanism for slender wing rock is that of an aerodynamic spring. Static and dynamic vortex trajectories over the wing differ and a time lag is present, which accounts for the hysteresis seen with this phenomenon. As Λ is increased, the onset angle of attack for wing rock decreases and this highlights the possible relation between the onset of wing rock and the proximity of leading-edge vortices. It was found that vortex lift-off, vortex breakdown and static hysteresis play no part in wing rock. Critical states exist and vortex breakdown location is important[24,25,26,27]. A delay in the response of the wing to the vortex movement is to blame for this. At high angles of attack, an 85^o sweep delta has been seen to move randomly between full stall and having one compact vortex and one stalled wing half[28]. Wing rock starts at the angle of attack at which roll damping of the wing is lost and it has been proven that the location of vortex breakdown moves aft with increasing sweep angle. Work done on a 76^o sweep angle delta wing[29] showed how the turbulent kinetic energy changed and how velocity fluctuations led to certain dominant frequencies for oscillations of the breakdown location. Some characteristics of wing rock are[27]:

- It oscillates about zero mean roll angle;
- Once initiated, it exhibits a constant amplitude;
- Strouhal number increases with increasing angle of attack;
- A highly swept wing is necessary, oscillations were not observed for a 76^o sweep wing, but were for an 80^o wing;
- Wing rock occurs over a large number of angles of attack. For an 80^o sweep wing, oscillations occur for $20 < \alpha < 50^o$;
- Increasing the Reynolds number leads to a larger amplitude of wing rock, but at the same frequency;
- Vortex breakdown has a damping effect;
- An oscillating wing still generates lift.

It is worth noting that for a 60^o wing with a forebody, limit-cycle oscillations have been seen[30] at $\alpha = 30^o$ and were initially explained by the presence of the forebody vortices passing over the wing (the 60^o planform itself did not exhibit the oscillations). Work has also been performed on investigating the effect of the fuselage on delta wing

vortex breakdown[31]. Subsequently a different explanation was offered[32] for this aforementioned 60° sweep wing suggesting the cause was undamping generated by the leeward wing half. In a separate paper[33], it was suggested that the sharp leading-edged wing does not undergo oscillations because the leeward surface generates a dead-air flow that has little effect on roll damping, whilst the windward side generates sufficient roll damping to prevent wing rock from developing. Non-zero roll attractors have been found for a 60° wing and a 65° wing both with sharp leading-edge and at $\alpha = 2.5^{o}$[34].

It was shown[24] that a delta wing configuration with 65° sweep angle had multiple stable trim points in roll. The phase plane (roll rate versus roll angle) trajectories, corresponding to two free-to-roll time histories for the 65° wing at $\alpha = 30°$, showed very different behaviour. For the initial roll angle $\phi = -58.3°$, the trajectory found a stable equilibrium point at zero roll angle, while for $\phi = 53.1°$, the final equilibrium position was around $\phi = 21°$. The existence of equilibrium positions at non-zero roll angles was also confirmed at other angles of attack. The measured static rolling moment was around zero at non-zero roll trim angles and asymmetric vortex breakdown is behind this behaviour. On the same note, work performed on a 65° sweep flat plate delta wing[35] at a fixed angle of attack of 30° showed that vortex breakdown was always present on the wing surface. There is movement of the vortices at sideslip angles, which is relevant to this work because as the delta wing rolls it undergoes sideslip. Small amplitude oscillations were also seen at $\alpha = 35^{o}$ for the 60° planform itself, but the oscillations at the lower angle of attack were not present. To explain the non-zero trim angles, it was postulated[36] that they were due to changing effective angles as the wing rolled according to equations (1), (2) and (3) and subsequent effects on wing damping:

$$\alpha_{eff} = \tan^{-1}(\tan\alpha \cos\Phi) \quad (1)$$

$$\Lambda_{eff} = \tan\Lambda \pm \tan^{-1}(\tan\alpha \sin\Phi) \quad (2)$$

$$\beta_{eff} = \sin^{-1}(\sin\alpha \sin\Phi) \quad (3)$$

A reason for the oscillations of the 60° wing with forebody was put forward[24]. At roll angles above around 15° it was found that the strength of both vortices dropped until after the wing rolling motion had finished because of a reduction in effective angle of attack. This played a larger part than the changing effective sweep at these high roll

angles. The changing effective angles are caused when the delta wing rolls about a fixed roll axis. The static rolling moment coefficient had a larger restoring rolling moment than the dynamic moment coefficient because of the lag in position and strength of the upper leading-edge vortex.

Asymmetry in the strength of the vortices due to a time lag appears to drive the rolling motion. Looking at the pitching of a 70^o sweep delta wing[37] at similar Reynolds numbers to be tested, 90,000 to 350,000 and reduced frequencies of between k = 0.05 to 0.30, delays in vortex breakdown were obtained. The pitching was in a sinusoidal motion, and the motion was seen to be more dependent on pitching frequency rather than reduced frequency. Reduced frequency was seen, however, to cause a hysteresis in breakdown location, becoming greater as the reduced frequency was increased. Larger delays were seen on the downstroke of the pitching motion to vortex breakdown, where the angle of attack was decreasing. Shifts were also seen in the breakdown location to be greatest at lower angles of attack. For another pitching slender delta wing, it has been found[38] that there is a time lag between the increase or decrease in α and vortex breakdown, and that this is not dependant on Re. It was also found that the time lag was longer for lower sweep angles. These create a hysteresis loop, which is larger for higher frequencies of pitching oscillation, seen in both the publications referenced.

Experimental and numerical work has been carried out investigating the wing rock phenomenon[39]. Differing Reynolds numbers were presented and experimental comparisons performed, after which a single degree-of-freedom mode was offered. To clarify the wing rock phenomenon, low Reynolds number computational simulations were performed[40] on an 80^o sweep delta wing undergoing a constant roll rate manoeuvre. This showed that as the wing rolled, the vortex created by the downward leading-edge moved inboard and towards the surface, while the vortex created by the upward leading-edge did the opposite. A lag in the body-normal position of the upper leading–edge vortex was observed, even though the cycle took around 6 s.

The use of actuators of some variety on the leading-edges of the wings may provide a means of controlling the oscillating wing. Work done on introducing turbulence into the shear layer of a flow over a backward-facing step[41] using piezoelectric actuators made the laminar or turbulent shear layer reattach earlier, though

not as effectively during transition. This may be relevant as it is suspected that reattachment may play a part in the oscillations, hence promoting reattachment may stabilise the wing. Other efforts were made using piezoelectric actuators in a slot along sharp leading-edges[42], which was found to increase the normal force, most effectively when the reduced frequency of oscillation of the actuators was around 1. The work was performed on a 60^o sweep angle half delta wing. It was also found that utilising the actuators downstream of vortex breakdown generated a streamwise vortex.

1.4 Self-induced roll oscillations of non-slender delta wings

The specifics of each type of delta wing roll oscillation, slender and non-slender, differ significantly. There are several reasons for the use of non-slender delta wings:

- Having a long root chord means that for general delta wings, wing thickness can be large. Thus, even with small thickness ratio (good from the point of view of structural efficiency), a large internal volume is available for the stowage of fuel, undercarriage, ancillaries and possibly the main engines;
- Delta wings have superior manoeuvrability and stability characteristics, operating safely at much larger angles of attack than could possibly be achieved by a conventional wing due to the different mechanism of generating lift at high angles of attack;
- Supersonic drag reduction applies to all delta wings due to their swept nature, though this is not relevant in this case as the project is concerned with low Reynolds numbers for UAVs and MAVs;
- Non-slender delta wings have more practical planforms than slender delta wings.

Certain aspects of slender wing rock will probably affect non-slender wing rock too. Modelling work[43,44] suggests that the angular acceleration (and subsequent parameters) depends on the:

- Density of air;
- Free-stream velocity;
- Surface area of the wing;

- Span of the wing;
- Wing chord;
- Moment of inertia of the wing about the roll axis;
- Bearing friction (very important in experimental studies);
- Angle of attack.

Limited amount of work on free-to-roll non-slender delta wings[19,45,46] showed that self-induced roll oscillations are possible but about a non-zero mean roll angle. Similarities to and differences from slender wing rock have been speculated[47]. If one looks at the position of vortex breakdown against roll angle for a non-slender delta wing, it shows some interesting traits. For non-slender delta wings the vortex breakdown is simply defined as a severe disruption of the core of the vortex and reversed mean axial flow is not always observed as it is for slender delta wings. In Fig. 1.11 it can be seen that at roll angles of +/- 30^{o}[18], the reattachment of the vortices is as expected as if the wing is stationary during the roll oscillations at an angle of attack of 20^{o}. However, upon increasing or reducing the roll angle a delay can be seen near a roll angle of 0^{o}, which shows an interesting delay of some sort upon forced movement of the wing in this case. It is thought that the flow structures as the wing rolls in either direction may differ because of two different roll rates being possible at the same roll angle. Both clockwise and anti-clockwise vortices do not meet at the roll angle of 0^{o}, thus there is a rolling force of some variety there due to this delay. This causes roll oscillations, which were found for a 45^{o} sweep wing with round leading-edge[48,49] but no oscillations were observed for a sharp leading-edged wing of the same sweep angle. A typical roll angle versus time plot of a round leading-edged wing undergoing self-excited roll oscillations[50] is shown in Fig. 1.12, which also shows an interesting non-zero mean roll angle. It was thought that the reason for these oscillations was asymmetry of the leading-edge vortices and changing effective angles[47].

Figure 1.13 shows the impact of leading-edge sweep angle and subsequent roll damping on slender delta wings[33]. They exhibit a positive value of C_L, which is in essence a force trying to make the wing rotate about its axis in a rolling motion. This comes into play when considering the effective angles of an oscillating non-slender delta wing. Here, the left-hand side vortex is seen to be compact at the larger roll angle, while

vortex breakdown is expected to be at the apex for the right-hand wing half; these factors are known to provide a stable trim point[36]. However, for the unstable case, two separated shear layers are evident. There seems to be reattached flow between the two vortical structures, which normally has a damping effect, hence it is thought that[19,45] the reattaching shear layers must be inherently unstable. The rolling moment coefficient has been investigated experimentally too (from static tests) and interestingly shows some stable point attractors, or not, depending on the angle of attack. It is suggested that the wing should settle at a particular point, depending on initial conditions and the effective angle relative to the roll angle of the wing.

It has been suggested[48] that the changing of amplitude in the free-to-roll oscillations is due to unsteady effects caused by the breakdown of the leeward vortex that forms as the wing rolls. If the roll oscillations are plotted as roll rate against roll angle, as in Fig. 1.14, an oval[6] is formed; with the differing amplitude of the roll oscillations visible from the fact the radius is not constant. It was suggested[51] that sharp edged wings do not exhibit roll oscillations. In the round leading-edge case, one wing half behaves like a stalled wing (due to the low effective sweep angle caused by rolling wing on one half) and hence creates dynamic undamping, whereas in the sharp leading-edged case this does not occur. It states that rounded leading-edged wings will exhibit roll oscillation if a) the angle of attack is high enough and b) the wing trims at a large roll angle that is non-zero.

Figure 1.15 offers a possible explanation[33] of the observed oscillations, showing that during the upstroke of the windward wing half, the flow attaches further around the leading-edge, producing a positive normal force. The undamping-in-plunge of the round leading-edge described[33,51] seems to accentuate the oscillations of the wing, but there appears to be a different reason for the root cause of the oscillations. The oscillations are observed around the stall angle where the reattachment of asymmetric flows is the most important factor; this is thought to have an effect[6]. On the down stroke however, the moving wall effect (flow moving into or away from wing surface) promotes flow separation, generating undamping-in-plunge. However, the aforementioned sharp-edged 50^{o} sweep wing[45] using a free-to-roll device does not have a round leading-edge nor do the effective angles suggest the wing should oscillate (the wing is expected to be damped at the angle of attack).

Ericsson[33] postulated that the non-zero trim angles found for a 45° sweep delta wing[50] were due to changing effective angles as the wing rolled, according to equations (1), (2) and (3) and subsequent effects on wing damping. Slight increases of Strouhal number were seen with increasing angle of attack, as has previously been observed for slender wing rock[34]. The mean roll angles of the 60° and 65° sweep wings at $\alpha = 30^o$ in this case were both 18°, while other work[24,30] has found slightly larger trim angles at the same angle of attack, with $\Phi_{mean} = 21^o$ for both sweep angles.

Flow visualisation at a Reynolds number an order of magnitude less than that at which roll oscillations were observed and only on a static wing with square leading-edges has been performed[50]. It showed that at a certain roll angle, the leading-edge vortex on the leeward half of the wing breaks down above the wing surface[48]. Phase lags were also observed for the oscillating wing, which show that hysteresis plays a part in the oscillations. As the roll angle is increased, the breakdown bubble moves towards the trailing-edge of the wing. The breakdown bubble is unsteady and moves back and forth, even when the roll angle is fixed. This will cause differing amounts of lift on the leeward wing half, while the windward wing half remains in a state of global flow separation, which could explain the differing amplitude of roll angle during the oscillations. At low Reynolds number, laser fluorescence flow visualisation has been done on the trim roll angles achieved during the free-to-roll motion (wing fixed in this case) at various angles of attack. This is shown[45] in Fig. 1.16. From these images it can be seen that the windward vortex (right-hand side in this case) is of a constant size at these changing angles of attack, thus of similar strength. The leeward vortex is of vastly different size, thus at an angle of attack of 20° the reattachment points of both vortices are very close to one another and may possibly interact. With a slight increase in angle of attack, oscillations would be expected at a higher Reynolds number, maybe caused by interactions between shear layers.

Videos were taken of a rolling, tufted thick wing with frames captured around the maximum and minimum roll angle and also around the average at $\alpha = 28^{o15}$, as shown in Fig. 1.17. These show that during the motion, the lower wing half is always stalled (reversed flow is visible); but that a coherent, leading-edge vortex together with attached flow is present on the upper wing half. It is difficult to discern the whereabouts

of the separation point on the wing from the tuft data, as they lack sufficient resolution. It also appears that near the minimum roll angle (right-hand picture) the upper leading-edge vortex is larger, though this is difficult to quantify. Free-to-roll oscillations were found for both a thick wing with a round leading-edge, and also a thin wing with a sharp leading-edge, although at lower amplitude and higher frequency; both wings had $\Lambda = 50^{o}$[46]. The roll oscillations that were found at the University of Bath for a 50^{o} sweep wing with sharp leading-edges demonstrate that a different mechanism to what has been proposed before is causing the motion. According to the effective angles and because of the sharp leading-edge, the motion for the 50^{o} wing with sharp leading-edge would be expected to always be damped.

Figure 1.18 shows that at $\alpha = 20^{o}$, small amplitude forced roll movements ($\Delta\phi = 5^{o}$) leads to the leading-edge vortices reattaching[18]. The movement of vortex breakdown location for a wing rolling with reduced frequency of 0.015 can be seen, which corresponds to the dominant frequencies of the shear layer[52]. Some hysteresis is visible from this plot, and this was found to increase with increasing frequency. It was found that for increasing roll angles, the vortex associated with the upward-moving leading-edge was stronger than for decreasing roll angles, which results in vortex breakdown being closer to the apex for increasing roll angles, as seen in this Figure. A rolling, rigid delta wing[53,54,55] at high angles of attack has been looked at with the wing oscillating and found that for an optimum range of frequencies, leading-edge vortices could be re-formed. This is contrary to what is expected because with an oscillating wing, the vortices become stronger due to the leading-edge motion. This usually causes premature rather than delayed breakdown, thus it is thought that the streamwise pressure gradient may be modified favourably due to the wing motion. A small lag was also noticed for this oscillating wing, though this reduced frequency is significantly higher than those previously seen and to be discussed for free-to-roll oscillations of non-slender delta wings. Re-formation of leading-edge vortices were observed for increasing periodic pitching oscillations of 1^{o} amplitude at angles of attack where the wing would usually be stalled.

Work has been performed on flow control of leading-edge vortices[20]. Re-formation of the leading-edge vortices was achieved with sufficient amplitude of forcing at the optimum frequency. This forcing has been seen to greatly increase the potential of

the wing to generate lift after stall[56], and has been found to be more effective for non-slender delta wings, where the reattachment of the leading-edge vortices plays a large part in their lift. Leading-edge blowing has been used as a tool to control non-slender delta wings, and the flow of debris over a wing surface has been investigated in a 3D mode[57], with the movement of the centre of pressure investigated. Oscillatory blowing at the leading-edge of a non-slender delta wing with a 50^o sweep angle was looked at and it was found that with an optimum momentum coefficient, the flow could be re-attained for a stalled wing surface. This is despite angles of attack above the stall angle. Tangential leading-edge blowing has been used in an attempt to control slender wing rock[58]. A particular problem encountered with this however, is the sensitivity of rocking wings to any disturbance torque. It was found that symmetric blowing alone damped wing rock[59], and that a control algorithm employing asymmetric blowing damped the wing rock even more effectively.

Efforts have been made to alter the flow physics. Work has been done on flexible delta wings[53,54,55,60,61] and oscillating rigid delta wings. This caused reattachment of the shear layer in the post-stall region due to the excitation of the shear layer, which energises the vortices shed and promotes reattachment. It is recalled that reattachment on the wing surface is typical for non-slender delta wings[62]. It was also found that there was an optimum range of forcing frequency corresponding to the natural frequency of the shear layer, which caused a maximum delay in vortex breakdown.

To summarise, the unsteady aerodynamics of delta wings in roll motion is important for various applications including high speed civil transportation, spacecraft and fighter aircraft. Whilst the lift/drag and stall characteristics may not be as good for non-slender delta wings as for slender delta wings as shown in Fig. 1.2, they still exhibit desirable manoeuvrability compared to conventional wing planforms (such as rectangular). However, it is also known for non-slender delta wings to undergo self-excited roll oscillations, with a non-zero mean roll angle. Although this is similar to the observations for a slender delta wing[28] with sweep angle $\Lambda = 65^o$, the flow physics appear to be different. Previous work[19,27] also confirmed that, even when there are no roll oscillations, free-to-roll non-slender delta wings may have trim positions at non-zero roll angles. In other words, zero roll angle is not free from roll disturbances.

1.5 Other planform shapes and flow characteristics

Free-to-roll oscillations are not necessarily limited to delta wings. Work done on low-aspect ratio rectangular wings found that the side edge vortices were sufficient to produce wing rock with similar characteristics to slender delta wing rock, provided that the aspect ratio was less than 0.5[2,4,63]. Rectangular wings of relatively low aspect ratio have a very three-dimensional flow structure due to the effect of the tip vortices, and significant variations in the bubbles due to the tip vortices have been noted previously[64]. These oscillations were seen to develop into autorotation for aspect ratio AR = 0.25 in the work of Levin and Katz[63], believed to be caused by lateral instabilities and driven by dynamic vortex interaction and associated lag effects caused by the motion of both the wing and leading-edge vortices. For low aspect ratio rectangular wings, the Strouhal number was seen to either go up or stay the same with increased angle of attack.

Figure 1.19 demonstrates the flow over a low aspect ratio rectangular wing, showing the three-dimensionality and the three vortices which drive the motion[63]. Other authors[65] noticed that the movement of the leading-edge vortex seemed to play a large part in the causes of how low aspect-ratio rectangular wings (AR < 0.55), but did not find anything for higher aspect rations. The movement of the vortices, as shown in Fig. 1.20, was thought to cause the oscillations[65]. No free-to-roll experiments on wings with larger aspect ratios have been reported in the literature. Tuft visualisation was used as a first tool to determine the role of the side-edge vortices and the location of the leading-edge separation bubble. This type of separation bubble is usually referred to as a long bubble because of it increases in length with angle of attack.

From a computational point of view, a model has been created for the flow structure of a low aspect-ratio wing[66] by solving the unsteady Navier-Stokes equation. The tip (or side edge) vortices were found to drive the motion and asymmetry was found for the formation of vortices on a normal aerofoil. Though the proposed basic mechanism of oscillations was the same, Williams and Nelson[67] suggested that the loss of the leading-edge vortex caused a shift from negative to positive damping, thus creating a dynamically unstable roll system, and also suggested that the leading-edge vortex played a significant role in the motion of the side-edge vortices perpendicular to

the wing surface. It was suggested that these limit-cycle roll oscillations are unique to slender delta wings and rectangular wings for which the vortices are relatively close to one another and generate a significant portion of the lift. For a different planform, work was performed on a simulation of the free-to-roll oscillations of a cropped slender delta wing[68], and it was found that the reason for the oscillations was the primary bending mode, due to the supersonic velocities being used. Unfortunately, work on cropped non-slender delta wings appears limited. Tests were performed on the characteristics of Zimmerman[69] (a common MAV planform), though not from a free-to-roll perspective.

Flow separation has been looked at in detail[70] and flow patterns in terms of streamlines have been investigated. Researchers agree that the existence of a particular skin-friction line on where the lines converge is a necessary condition for flow separation. It is also stated that local flow does not affect potential flow, whereas global flow does. Whether one can ignore delays, an aircraft is susceptible to wing rock because of the proportionality between chord length and the rolling moment or whether vortex breakdown is a necessity are all debatable. Looking at the flow structures themselves, descriptions of the three-dimensional versions including water tunnel visualisation has been performed[71]. It was found that Reynolds number was less important for fixed separation and that saddle points, foci and flow separation play central roles in the structure of 3D flows. Separation lines form a separation surface in 3D, which leads to vortices formed by them rolling up. The saddle points can relate to either separation or reattachment lines, or foci involving swirling flow structures. Work was also done on the formation of a leading-edge vortex and these vortices are thought to be the driving mechanism behind roll oscillations. In near-surface streamlines, foci are an outcome of three-dimensional separation caused by the interaction between the side-edge vortices and stalled flow within the separation bubble. Initial work was performed on testing other wing planforms including rectangular, elliptical, Zimmerman and lambda planform shapes[72].

An idea that has been tested successfully for roll control[73] is the use of Single Dielectric Barrier Discharge (plasma) actuators placed below the leading-edge of a $\Lambda = 47^{o}$ 1303 UAV model. The actuators were only effective at $\alpha > 10^{o}$, where it was found that they augmented lift, and that the effectiveness reduced as the frequency of pulsing was reduced from 3.3 Hz to 1 Hz. This model has a centrebody, which means the flow

over the wing is highly 3D, but the tests were performed at a similar Re to those achievable in the University of Bath wind tunnel. The actuator ionises the air around the leading-edge between two copper plates, and thus creates a force attracting the air to the wing and delaying separation, which could attenuate the roll oscillations due to charge on the wing itself.

1.6 Gaps identified

Slender wing rock is well understood and the primary research objectives remaining are in ways of counteracting it. Non-slender delta wings, however, have not been fully investigated. Other non-delta wing planforms could also exhibit oscillations, and it is worth investigating. Finally, it is worth investigating further other forms of movement that a wing may undergo such as pitching, as these everyday manoeuvres warrant further knowledge.

1.7 Objectives

In summary, the major contributions relating to this study are to:

i. investigate further the effect on delta wings of sweep angle in terms of self-excited roll oscillations at high angles of attack by examining the corresponding vortex topology and to endeavour to provide a suitable explanation for why the oscillations occur (Chapter 4);
ii. investigate the non-zero mean roll trim angles as a function of sweep angle, which will affect aircraft in flight (Chapter 5);
iii. investigate the pitching of delta wings in a free-to-roll motion related to actual flight manoeuvres (Chapter 6) and to
iv. further investigate other wing planforms used for aircraft and associated free-to-roll instabilities (Chapter 7).

Free-to-roll oscillations, especially of non-slender delta wings, are not yet fully understood, so it is hoped that utilising PIV will allow further interpretation.

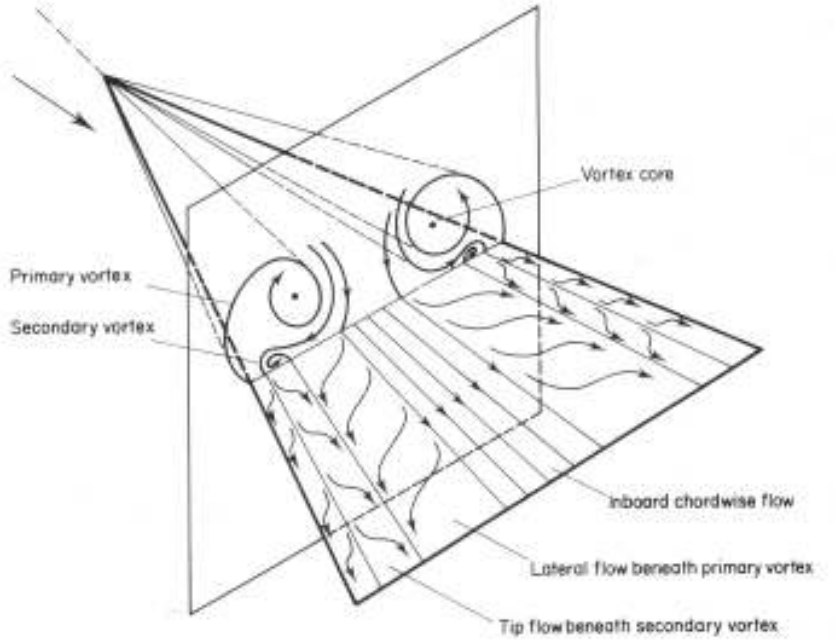

Figure 1.1 Schematic of the subsonic flow-field over a delta wing[7].

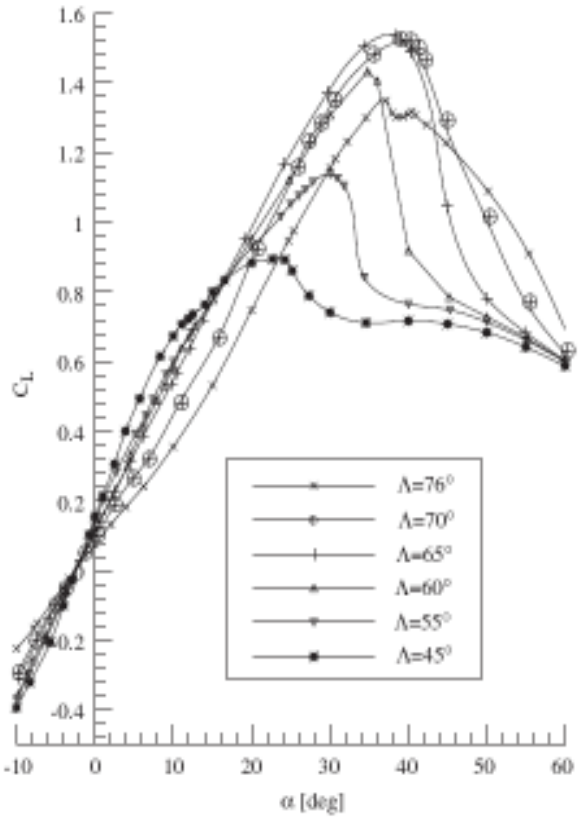

Figure 1.2 Variation of lift coefficient with angle of attack[9].

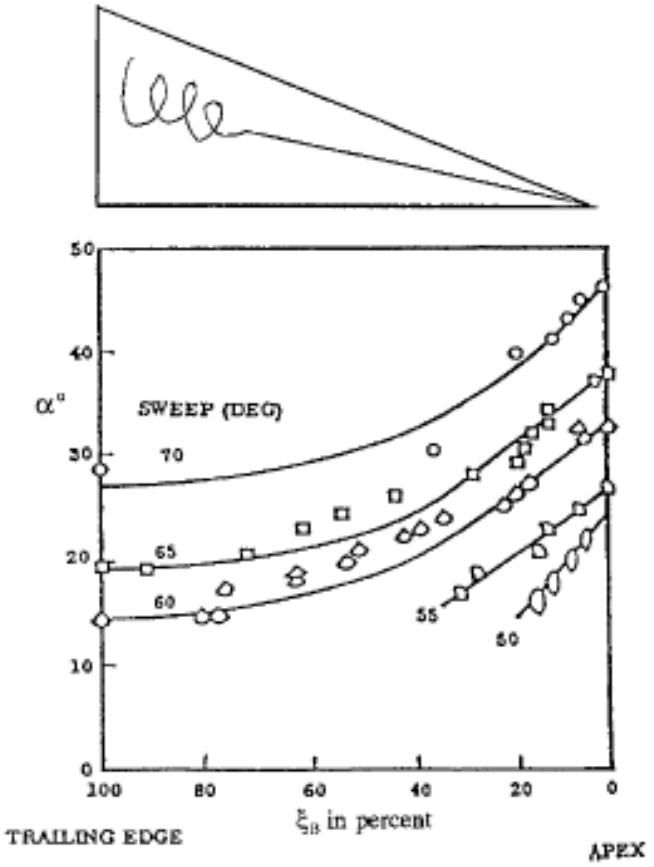

Figure 1.3 Effect of leading-edge sweep on vortex breakdown location for sharp-edged delta wings[11].

a) b)

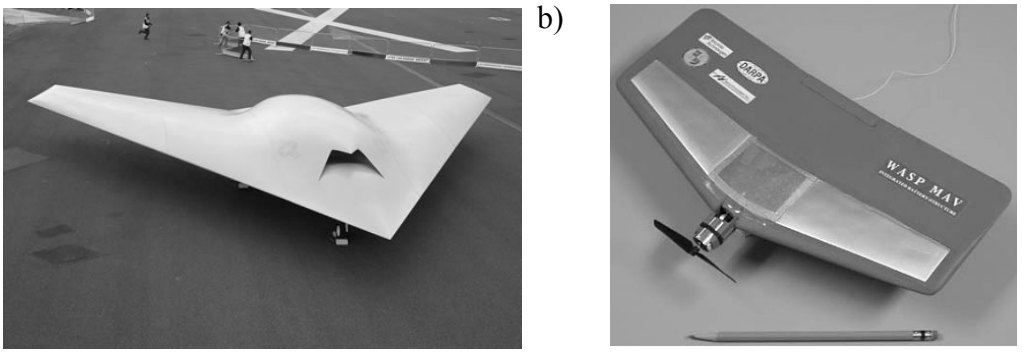

Figure 1.4 Example of a UAV (left, Boeing X-45C[13]) and an MAV (right, AeroVironment Wasp[14]).

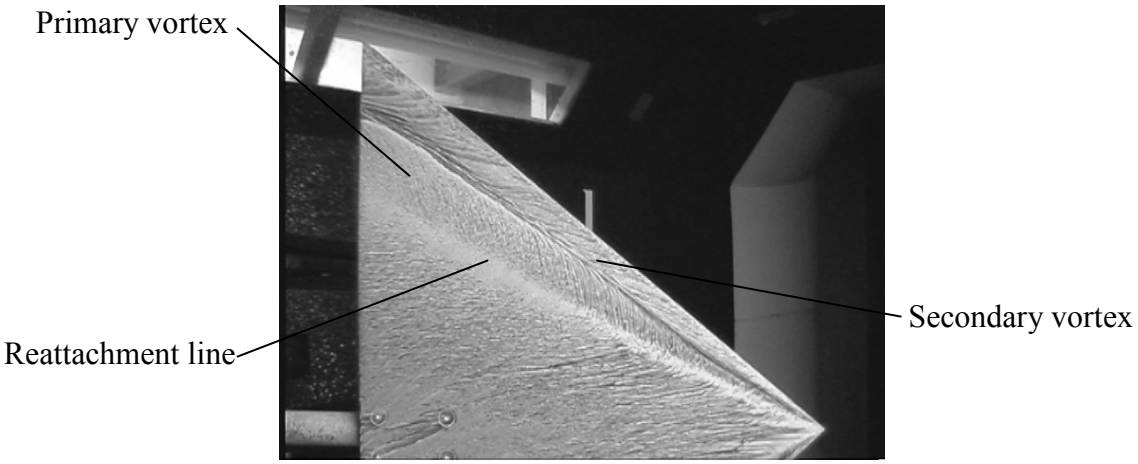

Figure 1.5 Surface flow visualisation at $\alpha = 2.5^{o}$ for a delta wing with 50^{o} sweep and sharp leading-edge[15].

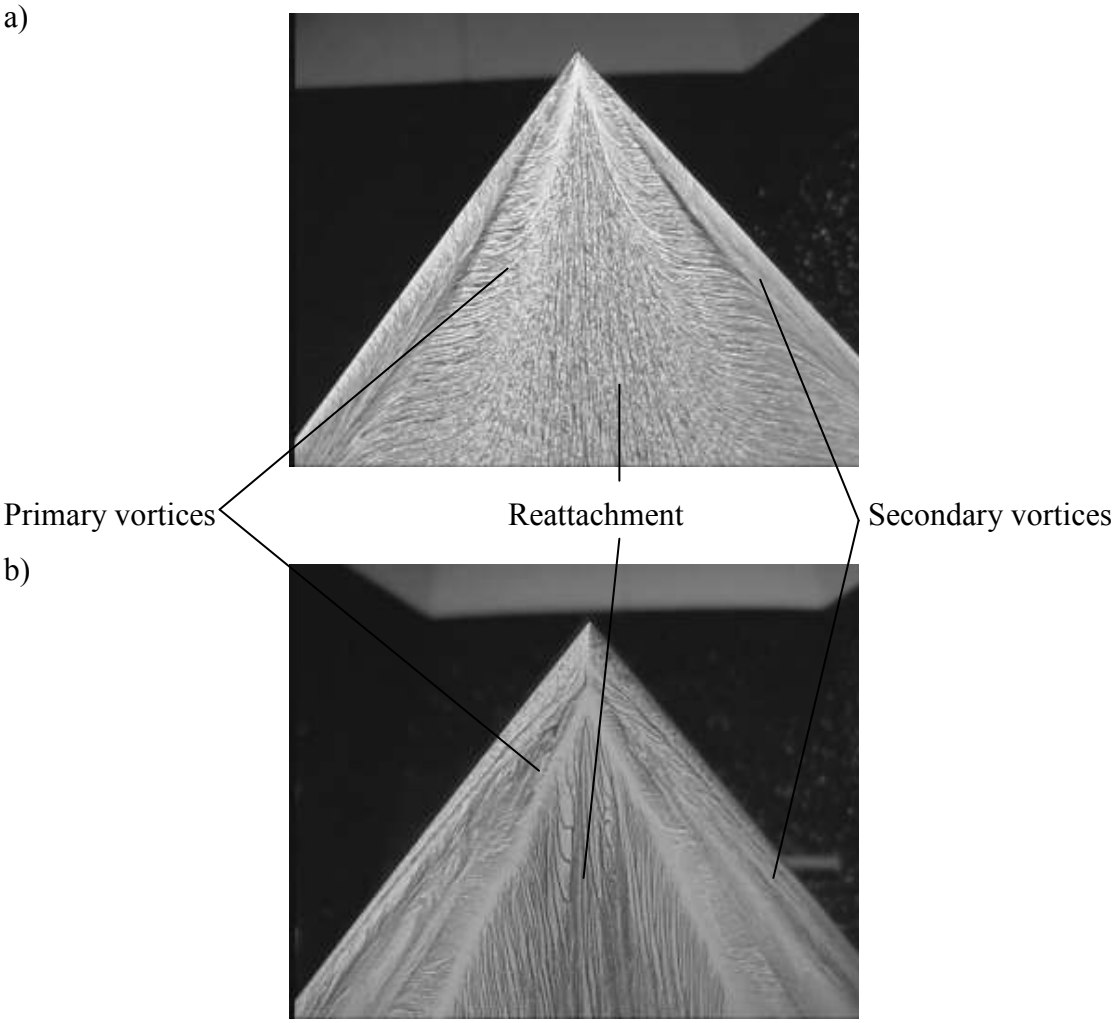

Figure 1.6 Flow visualisation of the apex of wings with $\Lambda = 50^{o}$ and a) sharp leading-edge and b) round leading-edge at $\alpha = 17.5^{o}$[15].

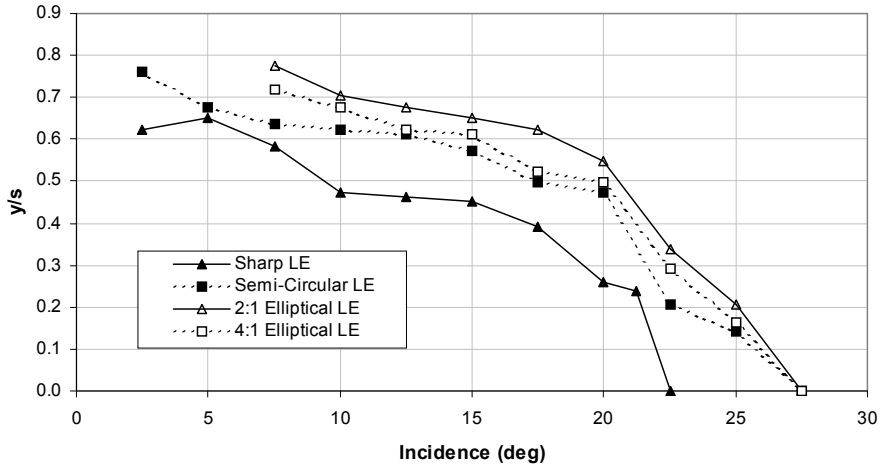

Figure 1.7 Effect of leading-edge shape on the location of the reattachment line as a function of angle of attack[15].

a) b)

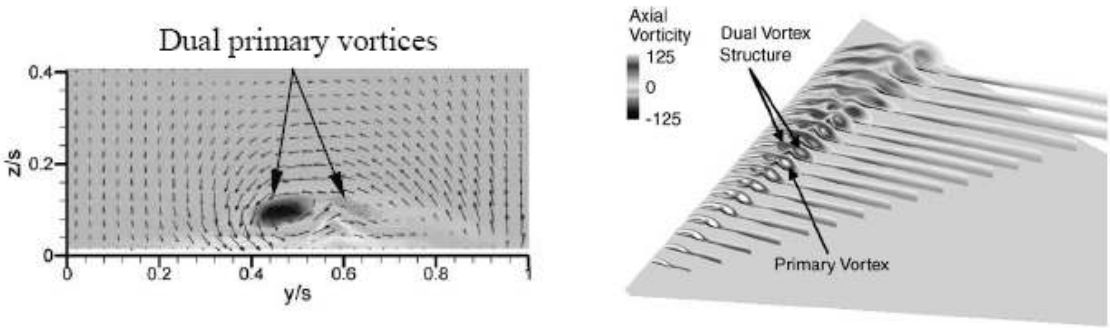

Figure 1.8 a) Experimental[16] and b) computational[17] examples of the dual vortex structure for 50^o sweep wings at $\alpha = 5^o$ and $\alpha = 7.5^o$ respectively.

a) b)

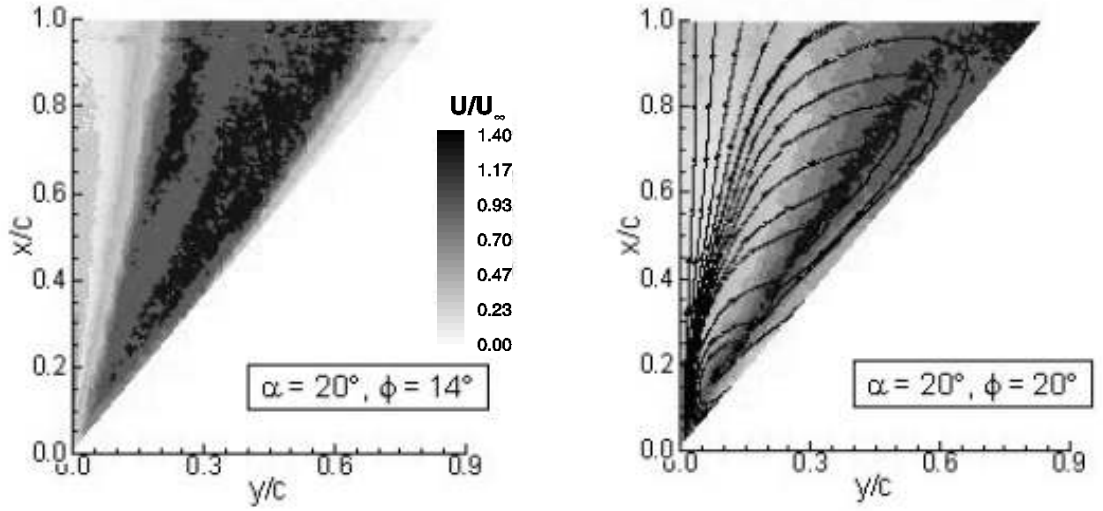

Figure 1.9 Magnitude of velocity in a) the vortex core and b) near the wing surface for 50^o sweep wing at $\alpha = 20^o$[16].

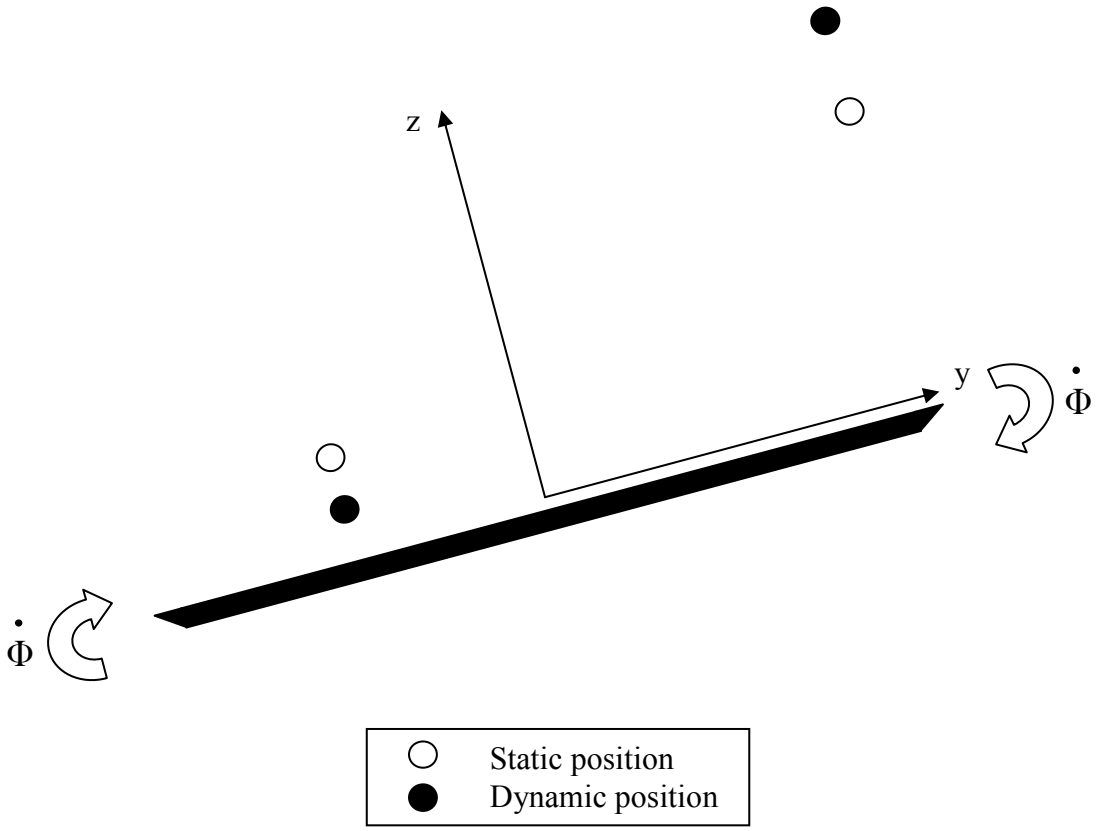

Figure 1.7 Sketch of static and dynamic vortex position during slender wing rock[23].

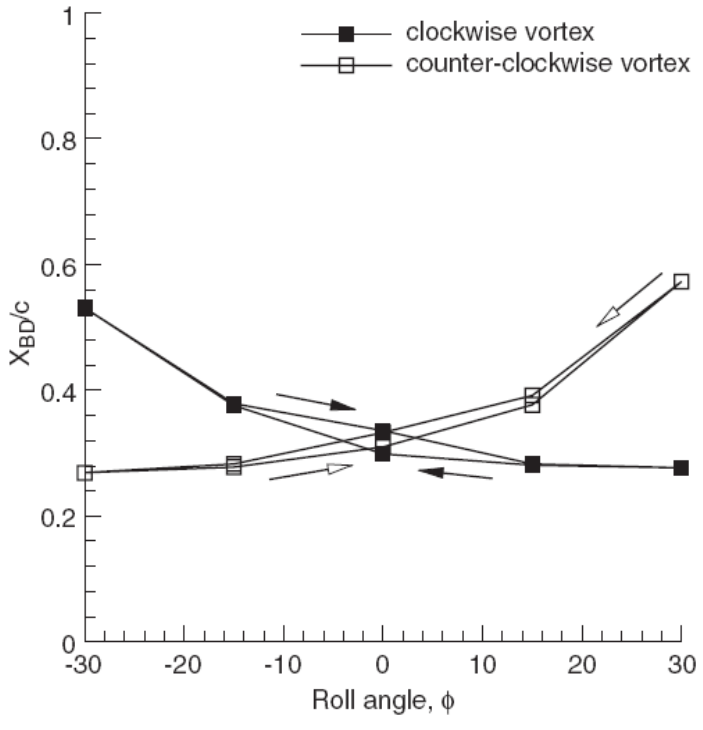

Figure 1.8 Variation of the vortex breakdown position with roll angle at $\alpha = 20^{o}$ for a non-slender delta wing[18].

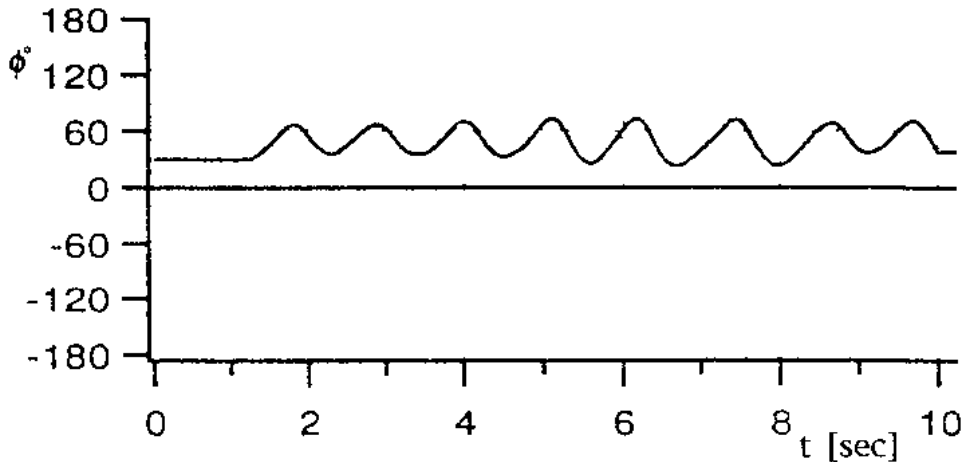

Figure 1.9 Roll angle time history of 45-deg delta wing model at $\alpha = 30^{o}$[50].

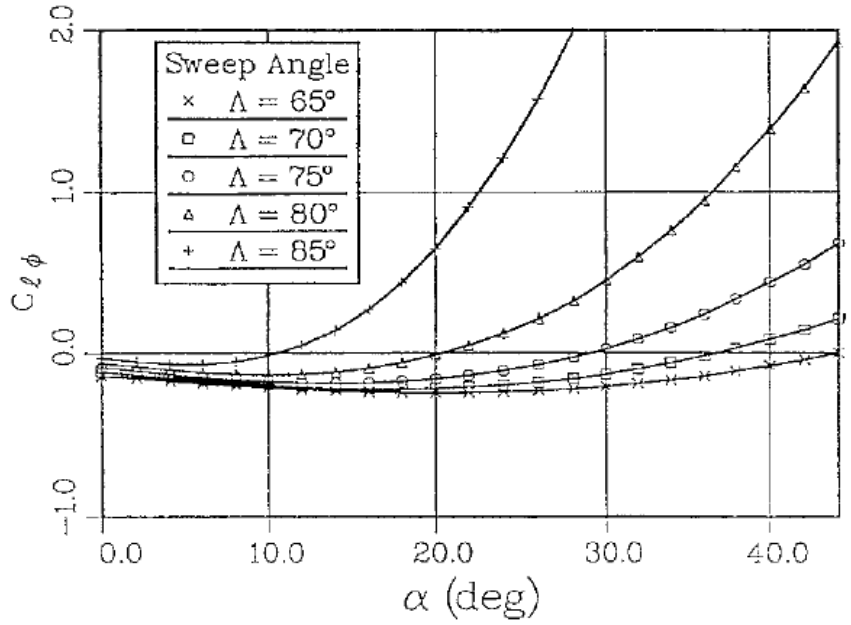

Figure 1.10 Effect of leading-edge sweep on the roll damping[33].

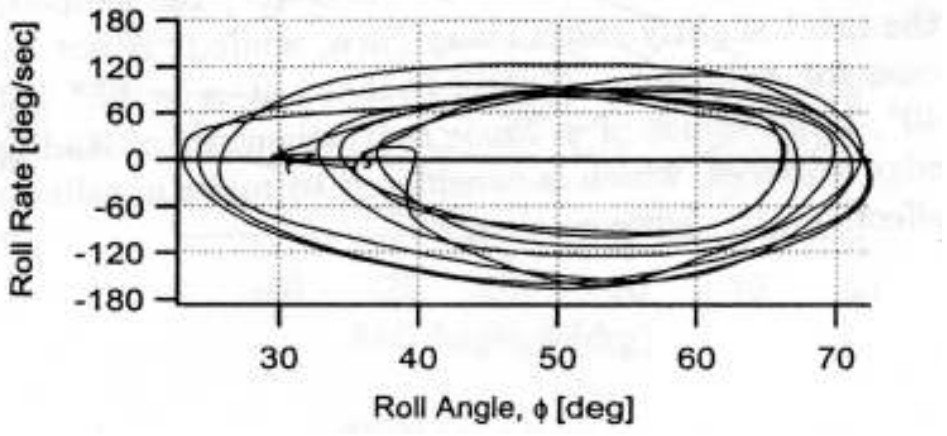

Figure 1.11 Unsteady characteristics of a wing with $\Lambda = 45^{o}$ at $\alpha = 30^{o}$ and round leading-edge performing self-excited roll oscillations[6].

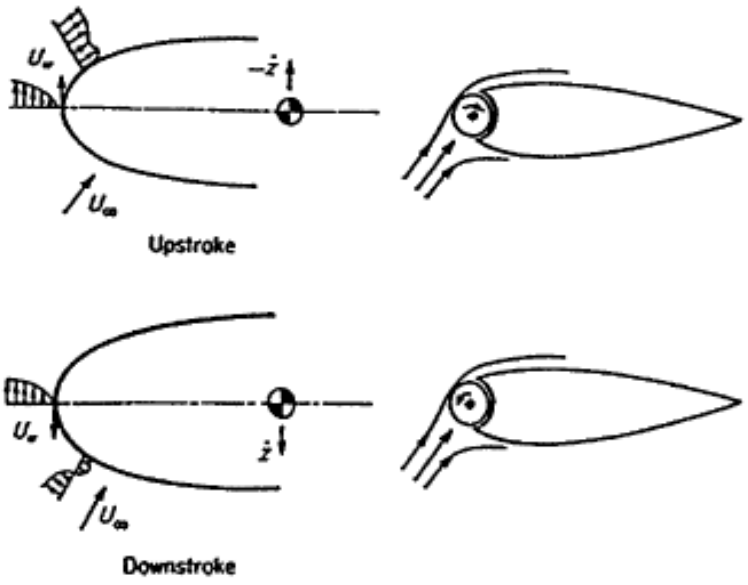

Figure 1.12 Moving-wall effect on a pitching or plunging aerofoil[33].

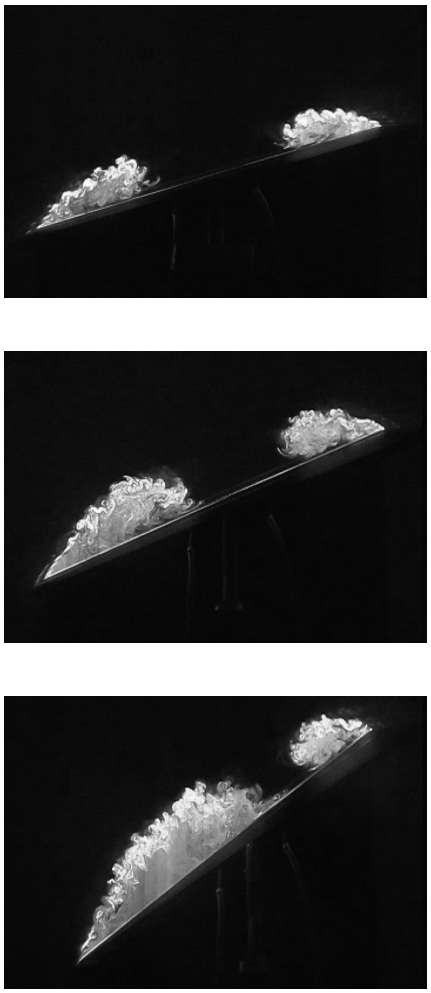

Figure 1.13 Laser fluorescence flow visualisation at equilibrium roll angles for incidences α = 10°, 15°, 20°[45].

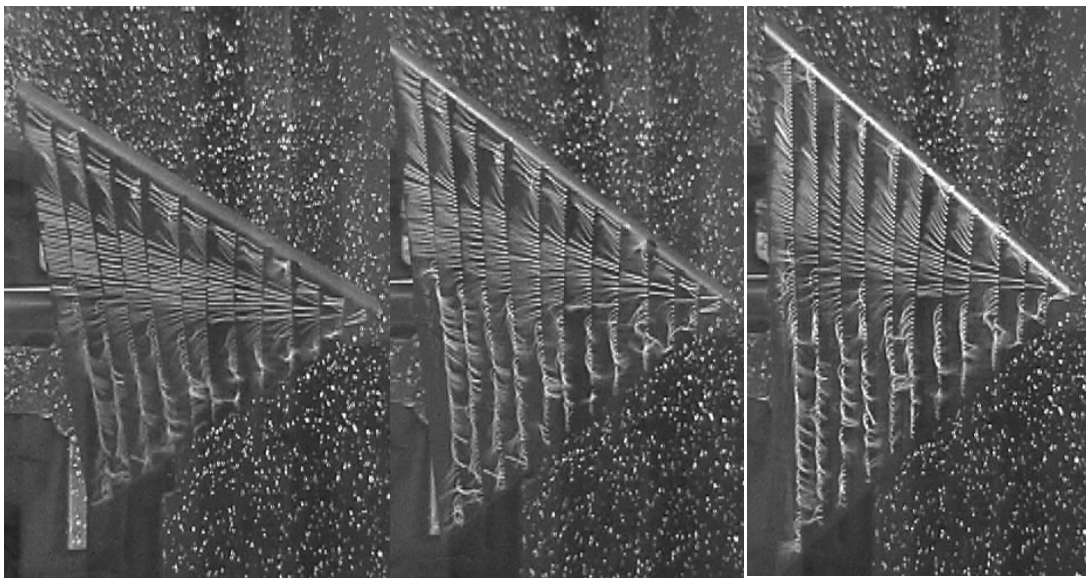

Figure 1.14 Tuft visualisation of surface flow pattern at three different instants, corresponding to maximum (left), average (centre) and minimum (right) roll angles during self-excited roll oscillations[15] at $\alpha = 28^{o}$.

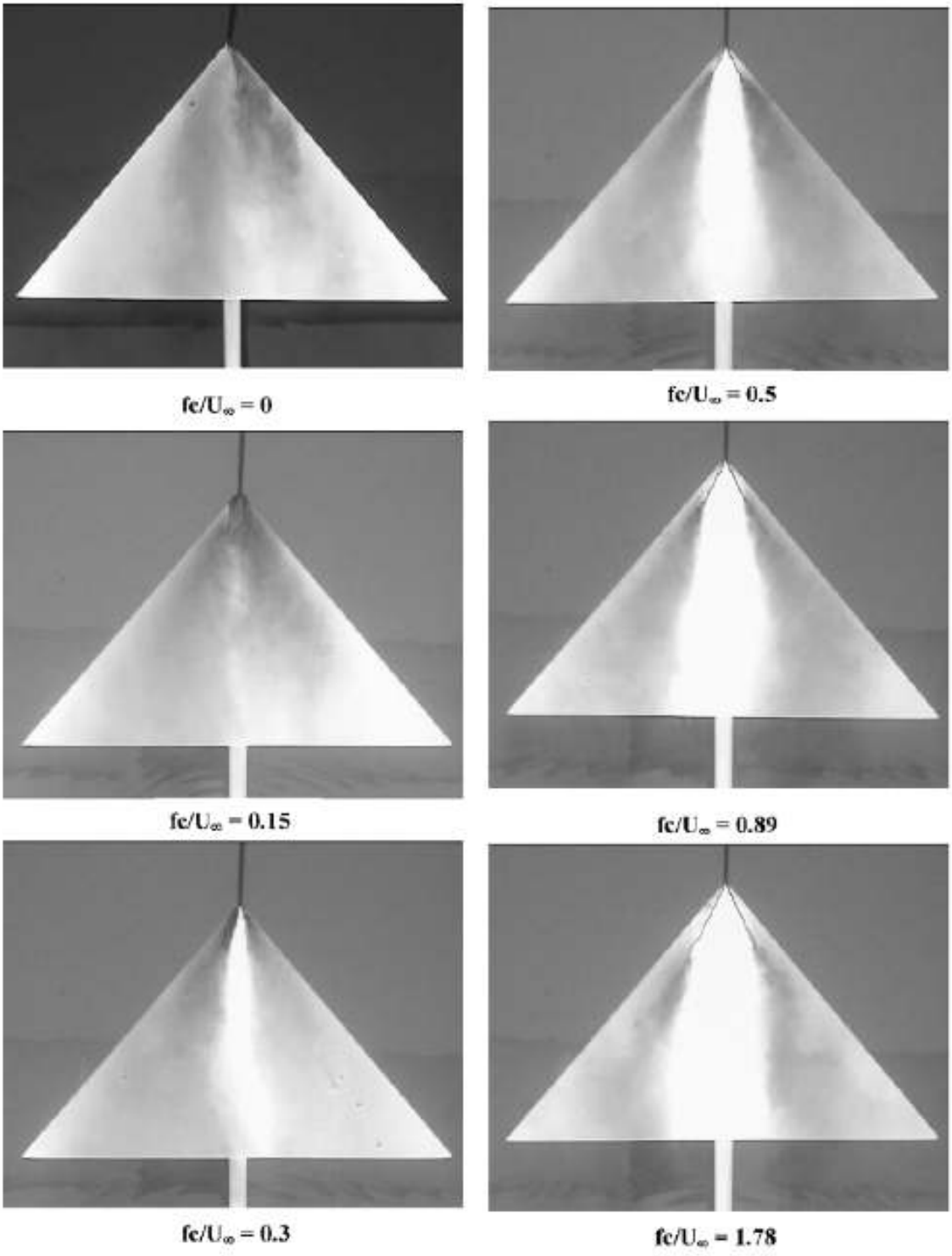

Figure 1.15 Flow visualisation for a stationary and small amplitude ($\Delta\Phi = 5^{o}$) rolling wing in water tunnel experiments[18].

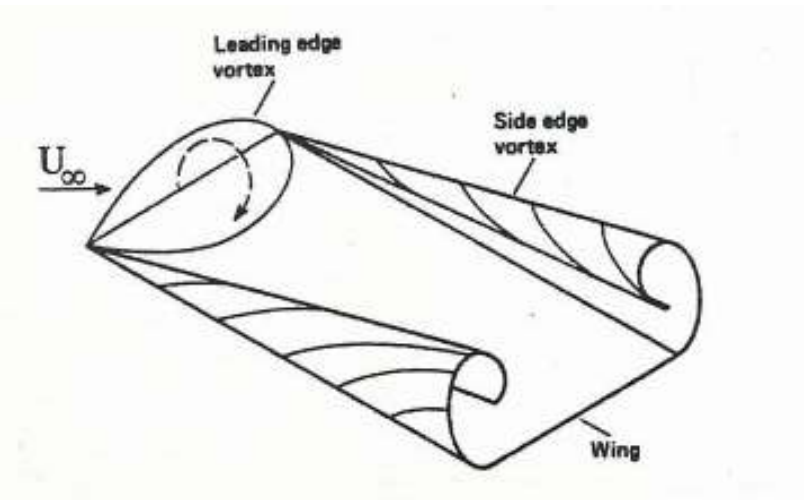

Figure 1.16 Leeward side flowfield of LARR wings at high angle of attack[63].

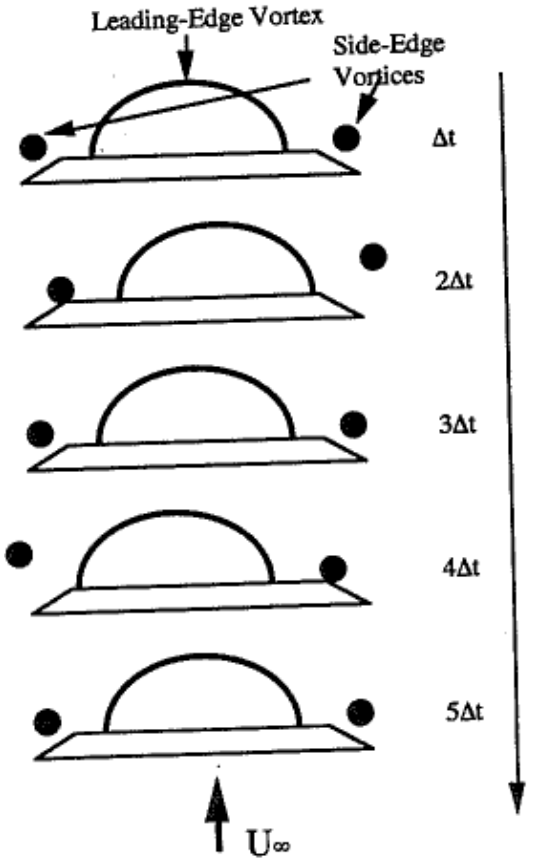

Figure 1.17 Sketch of unsteady vortical movement on LARR wing at 10 % chord location and standard position[65].

Chapter 2 Experimental Methods

2.1 Facilities

Wind tunnel experiments were conducted in the high speed working section of the 2.13 m x 1.52 m x 1.7 m closed circuit facility at the University of Bath, which enabled speeds up to 50 ms^{-1} to be achieved if necessary. This is shown in Fig. 2.1 in schematic and in Fig. 2.2 the working section is shown as a picture, together with the computer set-up and part of the wind tunnel; these were the facilities available.

Experiments were conducted at a constant free-stream velocity varying between U_∞ = 10 – 30 ms^{-1}, giving Reynolds numbers (based on chord length) of between 114,000 and 839,000, which is close to flight conditions for unmanned air vehicles operating at low/transitional Reynolds numbers.

2.2 Apparatus

2.2.1 Free-to-roll device

The wing and sting were attached to the high-α rig via a shaft free to rotate on greased bearings shown in Fig. 2.3a) (schematic). Roll damping was thus present, but minimised by changing the bearings often. One end of the shaft is attached to a potentiometer which outputs a varying voltage, linearly dependent on the roll angle, while the other end of the shaft is attached to the sting upon which the wing is supported. The minimum angle of attack achievable with the high alpha rig is around 1.5^o. Models were supported using the high-alpha rig as shown with the wing upside down in Fig. 2.3b) (photograph of the apparatus), which was controlled remotely so tests could be conducted into pitching. The stings used for all the models on the free-to-roll device were in line with the roll axis of the wings themselves, so there was no coning motion, just pure roll. A clamping system was designed so that there would be no centrebody mount on the wing surface influencing the flow and the suction surface was smooth, which did not upset the air flowing over the wing.

The standard deviation of the roll angle of the oscillations was calculated and the Strouhal number of the oscillations obtained using a Fast Fourier Transform.

2.2.2 Tuft visualisation

Surface flow visualisations were achieved using thin fluorescent thread taped to the wing suction surface. Images were captured using a digital video camera with a resolution of 2 million pixels for 60 s. Figure 2.4 shows an example of the set-up of the tufts for flow visualisation purposes, which was used as a first tool to determine the air flow over the wing in question

2.2.3 Digital PIV system

Quantitative flow measurements were undertaken using Digital Particle Image Velocimetry (DPIV). The system used was a TSI Solo DPIV system, which incorporates a pair of pulsed mini Nd : YAG lasers with a maximum energy of 120 mJ per pulse that illuminated desired plane via a laser mirror if necessary. A combination of cylindrical and spherical lenses was used to generate the required light sheet and the flow was seeded using a smoke generator placed in the low speed working section of the wind tunnel. Images were captured using an eight-bit PowerView CCD digital camera with a resolution of 2048 x 2048 pixels and a maximum capture rate of 7.5 frames per second, producing 3.75 frames per second in cross-correlation as two images were needed for each frame. The commercial software package TSI Insight version 6.0 and a Fast Fourier Transform (FFT) cross-correlation algorithm were used to analyse the images, with an interrogation window of 32 x 32 pixels and to produce velocity vectors for further processing. 16 x 16 fields were looked at but were found to be large in terms of data, while 64 x 64 were not significantly accurate.

For all the measurements, up to 2000 instantaneous images were captured to give a smooth phase-averaged flow field using an external trigger card. The time delay used was 7 μs and was found to give the best results at these tunnel velocities, and work has been performed on this by other authors[74]. For these speeds of the wind tunnel, 5 μs did not allow significant movement to be picked up and faster speeds enabled the smoke to leave the field under investigation, so results were worse. In the static tests, the wing was held stationary, while in the dynamic tests the wing was then released, allowed to roll and triggered measurements were taken. Two measurements, corresponding to roll angle increasing and roll angle decreasing, were taken for the mean roll angle to capture the flow physics of the whole motion. Two consecutive images of the smoke particles

and their associated positions were captured at a specified time separation by a digital camera placed behind the wing in the high-speed section of the wind tunnel. This was for cross-flow measurements and the camera was placed opposite the wing and outside the wind tunnel for the near-surface measurements. The PIV set up is shown in Fig. 2.1. The models were painted matt black in order to avoid reflections created from the laser and the working section was shrouded with curtains for safety.

In order to study the strength of the side-edge vortices from the PIV data, circulation was calculated using a line integral around the region of interest and normalised using the free-stream velocity (U_∞) and chord length (c). A 3D PIV system would have allowed for a w component as measurements of an oscillating wing were difficult, as will be discussed in Chapter 2.3.

2.2.4 Wing models for the effect of moment of inertia

The edges on all the following wings were manufactured as either round or sharp. To clarify this - for the delta wings, the leading-edge was the only one with the named profiles and at the rear of the wing the edge was a simple straight cut. An 'edge' for the rectangular wings signifies all the way around the wing sides. The moment of inertia about the roll axis for each wing was calculated using CAD software, which had been calibrated using the measured masses of the wings and includes the moment of inertia of the sting used.

The symmetric clamp used in carbon wing cases is shown in Fig. 2.5 and this clamp was necessary to hold the carbon wings due to their brittle nature. As stated, the free-to-roll moment of inertia is taken into account in the calibrations and calculations. Different materials were used in order to give different moments of inertia about the roll axis in order to determine the role of wing weight in the self-induced delta wing oscillation phenomenon. Each carbon delta wing had $\Lambda = 50^o$ and a single bevel leading-edge (wings 12 – 14 in Table 2.1, which shows the wings tested) as the material was too brittle to form a double-bevelled leading-edge with, particularly at the apex. This leading-edge shape ensured the separation point was fixed, so the results could be compared to the aluminium 50^o sweep wing (wing 4 in Table 2.1) with the same chord, upon which free-to-roll tests were also verified. One more delta wing (wing 11 in Table

2.1) was designed and made out of 2 mm thick steel, again with $\Lambda = 50^o$ but with double-bevelled leading-edge, to complement the results already obtained due to the higher moment of inertia about the roll axis.

2.2.5 Wing models for the effect of leading-edge shape

For these experiments, the wings were set free to roll at the smallest or largest angles of attack, and then the angle of attack was increased or decreased, without any setting of the initial roll angle. Prior to stall, the mean roll angle is non-zero and there were no roll oscillations. In a critical and small range of incidence the roll oscillations became large. Upon further increase in incidence, the roll oscillations died away before the mean roll angle suddenly snapped to zero. Comparison with the lift curves indicates that these self-excited roll oscillations occur around the stall angle. Note that stall occurs earlier for the sharp-edged wings[20].

To begin with, a 10 mm thick HDPE (high-density polyethylene) wing with 200 mm chord and round leading-edge (wing no. 1 – henceforth referred to as the thick wing) was tested in preparation for PIV measurements. It was desired to repeat the tests performed on wings with 8 mm thick HDPE (wings 15 - 18 in Table 2.1) to confirm previous results and check the equipment was operating in the same manner, and also to increase the resolution of the work previously done[15] by increasing the angle of attack in quarter-degree increments around the angles of attack where free-to-roll oscillations were expected. Each of these wings had different leading-edges, but similar moments of inertia, sweep angle (50^o) and thickness ratio (t/c = 4 %). The leading-edges were sharp, 4:1 elliptical, 2:1 elliptical and round to ascertain the role of separation on the oscillations.

2.2.6 Wing models for the effect of sweep angle

Twenty two different delta wings were tested, with the leading-edges and moments of inertia different, as well as the actual shape of the wing, be it delta or a cropped section with the same span. Wings were fabricated out of aluminium, steel, high density polyethylene (HDPE) or carbon fibre, depending on what was desired. A general delta wing shape, together with leading-edge shapes is shown in Fig. 2.6. These

leading-edges were also used for other wing shapes tested. Testing commenced with a round leading-edge (D), and then moved on once the effect of leading-edge was discovered. Shapes E and F were tested to confirm some previous data obtained in the wind tunnel and to further the knowledge of equipment capability. Previously at the University of Bath, tests on free-to-roll oscillations had been performed only on delta wings with $\Lambda = 50^o$. The boundary between slender (for which a lot more is known) and non-slender wings is usually taken as $\Lambda = 55^o$. Wings of $\Lambda = 40^o$, 45^o, 52.5^o, 55^o, 60^o, 65^o and 70^o (wing numbers 2 – 10 in Table 2.1) were manufactured out of aluminium and had sharp leading-edges, so separation was not an issue. The moment of inertia about the roll axis was different for each however, but it was thought for this data that this would only affect the frequency of oscillation, rather than again whether or not the oscillations occurred.

Cropped delta wings were also tested. These wings were fabricated out of 3 mm thick aluminium with sharp leading edges and the same span as one another. Wings 19 - 21 in Table 2.1 were made with a 55^o sweep leading-edge for the delta portion of the wing and 50, 100 and 150mm cropped lengths. Wing 22 was made with the same span, but using a 40^o sweep angle.

2.2.7 Pitching delta wings

Various parameters were investigated to see whether oscillations could be attenuated by varying moment of inertia, leading-edge shape, planform shape and ultimately by pitching. In addition to the passive attenuation of the oscillations, active attenuation of oscillating wings was attempted by varying the angle of attack of the wings at a constant rate, once they had settled into their motion.

2.2.8 Alternative planform shapes considered

Further tests were carried out on wings with other planforms once the delta wing field was finalised; the data for each shown in the Table 2.2. Five other wings were made out of aluminium and tested including a Zimmerman shape (wing 26), an ellipse (wing 27, made due to the greatest lift gain of any planform shape) and some rectangular shapes (wings 23 – 25). The four rectangular wings are shown in Fig. 2.7. Wings 23

and 25 (Table 2.2) had rectangular planforms and leading-edge D from Fig. 2.6. Wing 24 had leading-edge B.

2.3 Uncertainties

The effect of the Reynolds number is substantial for Re < 30,000[2,20], so is not thought to be an issue here as the Reynolds number is an order of magnitude higher. Maximum blockage for the wind tunnel was approximately 4.3 % at $\alpha = 16°$ for the rectangular wing with AR = 4, which is within the 5 % suggested by the wind tunnel fabricators[7]. The wing was supported on its pressure surface and also in a vertical plane for practical reasons. Errors in the measurements for the fabrication of apparatus were very small. Roll angle was measured with a potentiometer with an estimated uncertainty of ± 1° at a sampling frequency of 250 Hz, with measurements of between 30 s and 90 s in length once the wing had settled into motion. The angle of attack was varied in quarter-degree increments so the peak in the standard deviation plot could be smoothed and an angle of attack near the maximum could be chosen. The data could have been more specific with closer increments, but the high-alpha device would not show sufficient resolution.

Not every vector is shown in the PIV test results for clarity, only every other vector is shown so the contours are visible. According to TSI, measurements obtained by the PIV images are correct within 2 % of the free-stream velocity. Near-surface velocity measurements were performed with the laser in the PIV tests illuminating a plane parallel and close to the wing surface (1 mm from the surface, which is equivalent to a maximum of 0.6 % of the chord length). Such PIV measurements were previously used to give an indication of the near-surface topology on low sweep delta wings[16,75]. The effective grid size varied from 1.2 mm to 1.9 mm in these measurements. Further, for the near surface PIV measurements, errors were minimal as any significant roll angle error led to the laser sheet hitting the rear of the wing, thus the camera receiving no input due to the proximity to of the laser to the wing surface. An amount of 1000 pictures were needed for the PIV tests because of the noisy nature of these experiments, primarily due to the camera being housed in a large box in the unsteady wake of the wing when cross-flow measurements were taken. Up to four separate tests were needed to cover the extent of the wing span, depending on if the measurements were cross-flow

or near-surface. The data were taken at various chordwise positions depending on which wing was being tested and what was being looked at. The processing of Insight and Matlab was much more accurate than errors when obtaining the data, so errors here were neglected.

Data being lost as bad vectors (noise) was very minimal, bar next to the wing surface due to laser reflection in the cross-flow case. The reflections from the wing surface were strong as a result of the laser being fired directly at it in some cases, particularly at low roll-angles and from the leading-edge of the wing nearest the laser. This reflection is why reattachment points have not been tabulated. Even for slender delta wings the flow appeared to be attached in a cross-flow plane, though the limited near-surface PIV and knowledge says it is not. In order to overcome problems experienced because of blooming, a phenomenon similar to that found when taking photographs of bright objects such as the sun, the camera box had to be rotated to the same angle as the wing, which contributed to the instability of the camera box due to the larger moment arm. The reflections were minimised during the testing procedure.

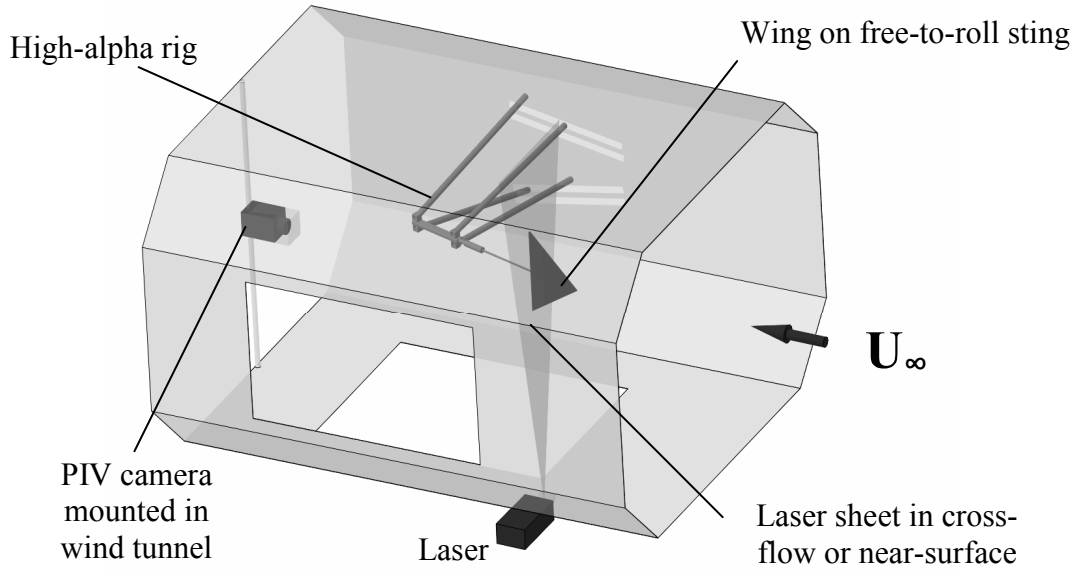

Figure 2.1 High-speed working section of the wind tunnel used in experiments, together with set-up for PIV tests.

Figure 2.2 Picture of the working section of the wind tunnel and apparatus.

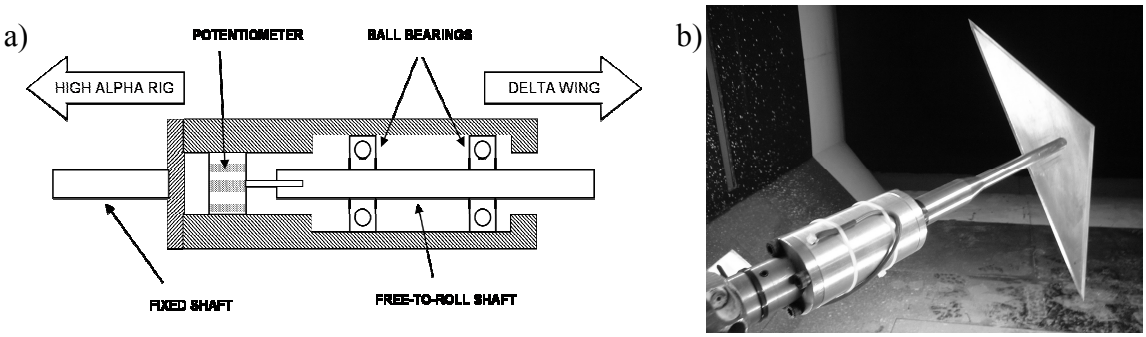

Figure 2.3 a) Schematic and b) picture of free-to-roll device.

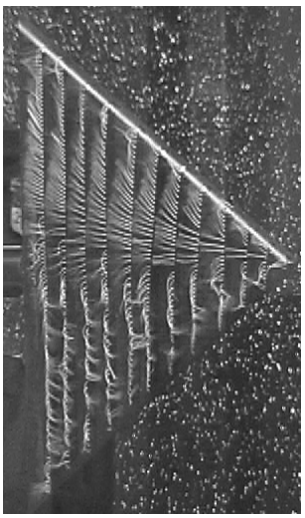

Figure 2.4 Tuft visualisation example.

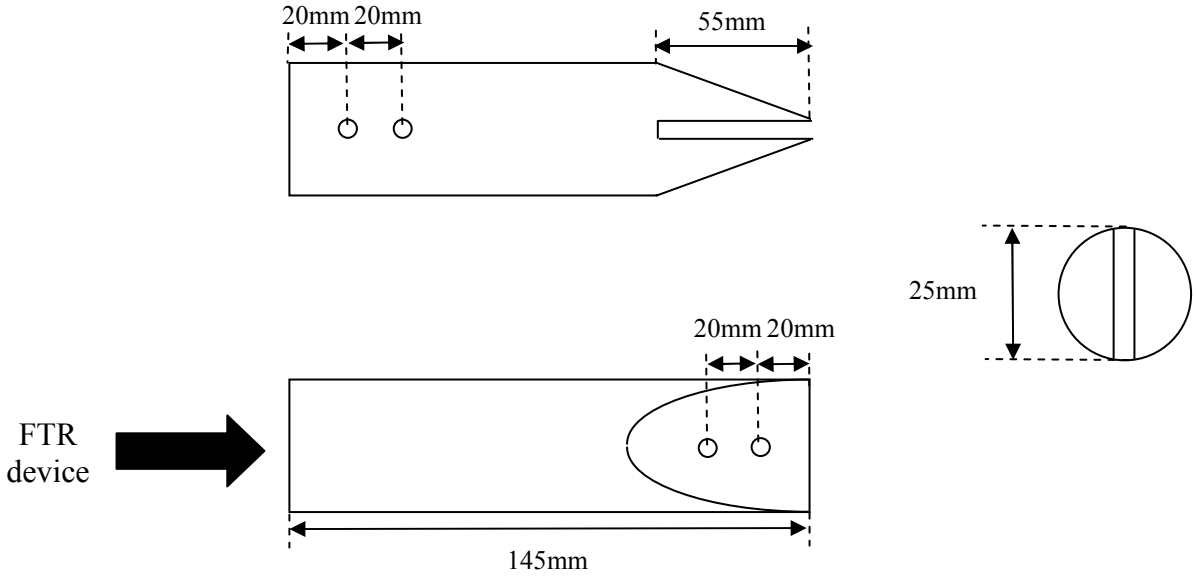

Figure 2.5 Symmetric clamp design (not to scale).

Wing number	Leading-edge sweep, ^{o}	Material	A, m^2	t/c, %	Type of leading-edge	I_{xx}, kgm^2	Re, $\rho U_{\infty} c / \mu$	Comment
1	50	HDPE	3.36×10^{-2}	10	D	3.0789×10^{-3}	411,000	Delta wing
2	40	Aluminium	2.37×10^{-2}	2.13	A	0.7925×10^{-3}	289,000	Delta wing
3	45	Aluminium	2.82×10^{-2}	1.79	A	0.9453×10^{-3}	345,000	Delta wing
4	50	Aluminium	3.36×10^{-2}	1.5	A	1.2075×10^{-3}	411,000	Delta wing
5	52.5	Aluminium	3.67×10^{-2}	1.37	A	1.2645×10^{-3}	449,000	Delta wing
6	55	Aluminium	4.02×10^{-2}	1.25	A	1.3735×10^{-3}	492,000	Delta wing
7	57.5	Aluminium	4.42×10^{-2}	1.14	A	1.4165×10^{-3}	530,000	Delta wing
8	60	Aluminium	4.88×10^{-2}	1.03	A	1.7563×10^{-3}	597,000	Delta wing
9	65	Aluminium	6.04×10^{-2}	0.83	A	2.0804×10^{-3}	739,000	Delta wing
10	70	Aluminium	7.74×10^{-2}	0.65	A	2.6582×10^{-3}	927,000	Delta wing
11	50	Steel	3.36×10^{-2}	1	A	2.1440×10^{-3}	411,000	Delta wing
12	50	Carbon	3.36×10^{-2}	1	B	0.6388×10^{-3}	411,000	Symmetric clamp used
13	50	Carbon	3.36×10^{-2}	1.5	B	0.8837×10^{-3}	411,000	Symmetric clamp used
14	50	Carbon/ foam sandwich panel	3.36×10^{-2}	1.7	B	0.2907×10^{-3}	411,000	Symmetric clamp used
15	50	HDPE	3.36×10^{-2}	4	C	1.1325×10^{-3}	411,000	Sharp leading-edges
16	50	HDPE	3.36×10^{-2}	4	D	1.1209×10^{-3}	411,000	Semi-circular leading-edges
17	50	HDPE	3.36×10^{-2}	4	E	1.2352×10^{-3}	411,000	2:1 elliptical leading-edges
18	50	HDPE	3.36×10^{-2}	4	F	1.1644×10^{-3}	411,000	4:1 elliptical leading-edges
19	55	Aluminium	8.81×10^{-2}	0.88	A	3.6826×10^{-3}	697,000	Cropped wing
20	55	Aluminium	11.2×10^{-2}	0.77	A	4.8295×10^{-3}	800,000	Cropped wing
21	55	Aluminium	13.6×10^{-2}	0.68	A	5.9942×10^{-3}	903,000	Cropped wing
22	40	Aluminium	4.377×10^{-2}	1.76	A	1.4671×10^{-3}	292,000	Cropped wing

Table 2.1 Specifications of delta wings tested.

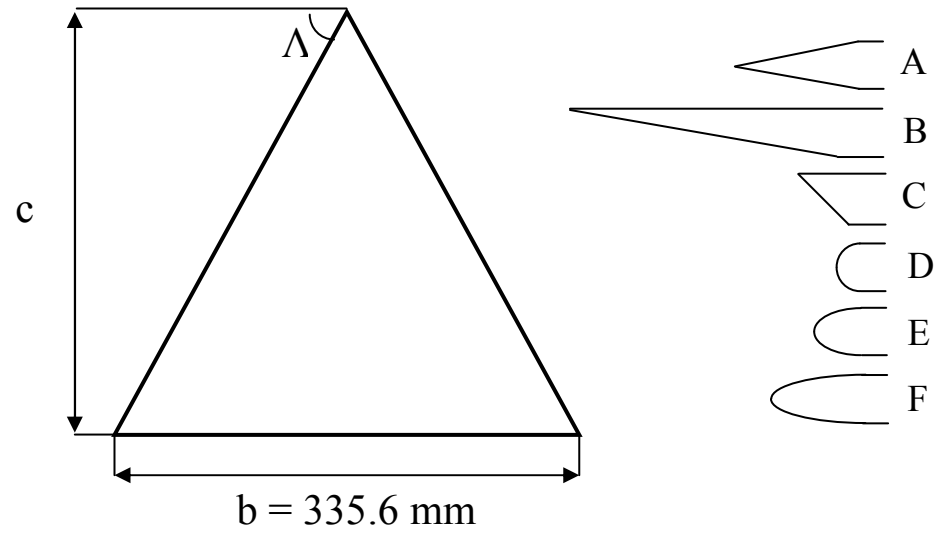

Figure 2.6 Generic delta wing planform and leading-edge profiles: A) Double bevel, 10° angle; B) Single bevel, 10° angle; C) Single bevel, 45° angle; D) Semi-circular; E) 2:1 elliptical and F) 4:1 elliptical.

Wing number	**Aspect ratio, b^2/S**	**Material**	**t/c, %**	**Type of leading-edge**	**I_{xx}, kgm^2**	**Re, $\rho U_\infty c / \mu$**	**Comment**
23	2	Aluminium	1.79	D	4.1290 x 10^{-3}	114,000 228,000 342,000	Rectangular
24	2	Aluminium	1.79	B	3.1576 x 10^{-3}	114,000	Rectangular
25	4	Aluminium	1.79	D	3.2592 x 10^{-2}	114,000	Rectangular
26	1.93	Aluminium	1.41	D	3.2330 x 10^{-3}	145,000 290,000 435,000	Zimmerman
27	2.55	Aluminium	1.79	D	2.5083 x 10^{-3}	114,000 228,000 342,000	Elliptical

Table 2.2 Specifications of other wings tested.

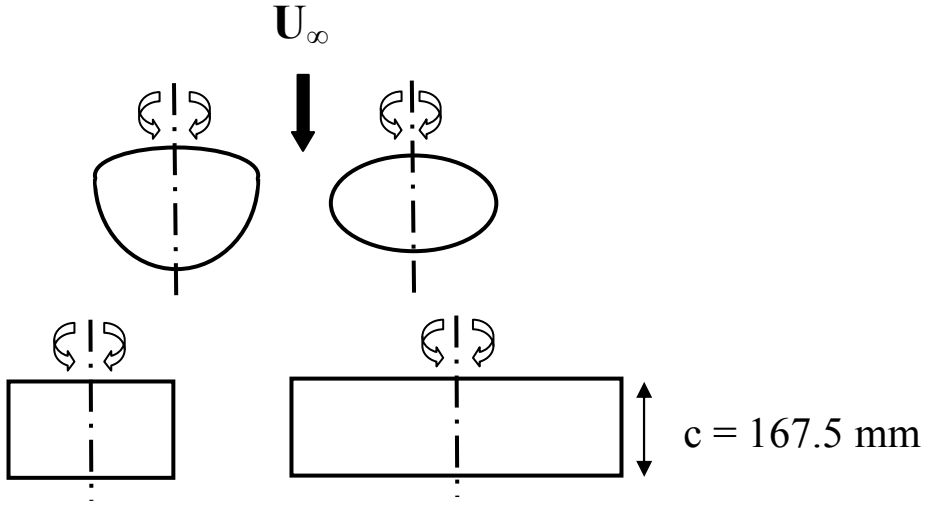

Figure 2.7 Planform shapes with Zimmerman (top left), elliptical (top right) and rectangular wings with AR = 2 and 4 (bottom, from left to right respectively).

Chapter 3 50^o Sweep Non-slender Delta Wings

Both zero and non-zero roll angles are possible for free-to-roll non-slender delta wings, depending on the angle of attack. Hence it is useful to consider the roll characteristics as a function of incidence in addition to presenting the roll angle time histories. The roll characteristics of the thick wing (t/c = 10 %) in the pre-stall, near-stall, and post-stall regions are investigated. Comparisons between different thicknesses of delta wings (still with 50^o sweep) are also discussed in this Chapter.

3.1 Thick delta wing

3.1.1 Pre-stall incidences

Figure 3.1a) presents an example of the time history of wing roll angle and shows that the roll angles reached during the motion for wing 1 are non-zero. At pre-stall angles of attack at which vortex breakdown was expected to be over the wing, several equilibrium positions at non-zero roll angles were found, depending on the initial roll angle[15]. In the present investigation, no initial roll angle was imposed upon any of the wings.

Figure 3.1b) shows that zero roll angle is not an equilibrium position at pre-stall angles of attacks, possibly due to the destabilising nature of vortex breakdown. The existence of multiple roll "attractors" is somewhat similar to the observations for a slender delta wing[24] ($\Lambda = 65°$). This will be discussed in Chapter 5; however, there is a significant difference in that zero roll angle is not an attractor for the non-slender delta wing at pre-stall incidences. Similar flow patterns (not shown) were found throughout the pre-stall region when the angle of attack was increased, with the continued asymmetric location of the reattachment lines. The flow physics behind the observation that zero roll angle is not a stable position is not clear, but is believed to be associated with flow reattachment[19,45] rather than vortex breakdown, as might be expected. Note that, at these pre-stall incidences, there was evidence of reversed flow on the leeward side of the wing, suggesting stall of this wing half though stall of non-slender delta wings was seen to be slower than that of slender delta wings[17].

3.1.2 Near stall: roll oscillations

Around the stall angle, self-excited roll oscillations are observed as shown in Fig. 3.1a). These large amplitude roll oscillations for the thick wing with round leading-edge differ from slender wing rock. They occur about a non-zero roll angle and do not exhibit constant amplitude, as has been previously noted for a non-slender delta wing and is discussed in the literature review[34]. The frequency and amplitude of these oscillations appeared to be independent from the initial roll angle, but probably depend on spring damping effects. Self-excited roll oscillations about a non-zero attractor are not well understood, as previously discussed in Chapter 1. As was discussed in the pre-stall region, the leeward shear layer appears to be stalled at all roll angles during the motion, with reversed flow again evident. The mean roll angle against angle of attack plot (Fig. 3.1b)) shows how the mean roll angle magnitude increases before reducing, then increasing again before the wing snaps back to zero roll angle at $\alpha = 32^{o}$, corresponding to full wing stall. Interestingly there is a range of angles of attack after which the wing has finished oscillating (low standard deviation), but before the wing snaps back to zero mean roll angle in Fig. 3.1b). This also shows the broad range of angles of attack at which roll oscillations are observed and the high amplitude of roll oscillation.

The wing was found to oscillate with a Strouhal number of St = 0.01 (Fig. 3.1c)), which is relatively low. Figure 3.1c) shows how the Strouhal number (frequency) of wing roll oscillations increases slightly with an increasing angle of attack. Insensitivity of the round leading-edge and the larger moment of inertia (Table 2.1) of the thick wing mean this increase is less than in the sharp leading-edge case. This will be discussed in the next Chapter and the effect of moment of inertia will be shown. The thick wing demonstrates insensitivity to angle of attack which has previously been observed by other researchers[49] for round leading-edges. This is thought to cause the broad peak in the standard deviation plot due to the insensitivity to angle of attack of the round leading-edge. Figure 3.1d) shows that the oscillation of the wing is not sinusoidal in this case; a sinusoidal oscillation would trace out an oval on the angular velocity plot. Figure 3.1e) shows that the rolling moment coefficient (from equation (4)) and the time variation of the rolling moment coefficient is calculated from:

$$C_r = (I_{xx} d^2\Phi/dt^2) / (qAb) \qquad (4)$$

The measured static rolling moment becomes zero at these non-zero roll trim angles and it is believed that asymmetric vortex breakdown is behind this behaviour. The non-zero mean roll angle this creates would cause the aircraft to lose lift and spin, thus it is not desirable.

It is interesting to note that cross-flow PIV velocity measurements indicate the presence of distinct reattachment lines at the maximum roll angle, whereas at the minimum roll angle the reattachment lines are closer together (Figs. 3.2 and 3.3). These reattachment lines are a non-slender delta wing characteristic. Figure 3.2 shows PIV data for the thick wing at an angle of attack at which roll oscillations occur, clamped (so no rotation) at near the minimum roll angle achieved during the free-to-roll motion. The data is presented at three different chordwise locations, with velocity contour plots and vectors on the left of the Figure, and standard deviation of velocity plots as a representation of turbulence on the right. At x/c = 0.25, there is little evidence of a windward (left-hand side) vortex or reattachment, suggesting that the flow is stalled. There is an interesting region of turbulent flow emanating from the leeward (right-hand side) shear layer in the turbulence plot. On the right-hand side of Fig. 3.2 at x/c = 0.25, this is evident, and may be due to the apex of the thick wing forming a sharp edge at this non-zero roll angle, as this effect diminishes further down the wing and for thin planforms with sharp leading-edges. The velocity fields at x/c = 0.5 and x/c = 0.75 show that there is interaction between the shear layers, particularly evident on the turbulence plots. As the flow progresses down the wing, the leeward shear layer moves further from the wing surface and the windward vortex becomes larger due to the continuous feeding of vorticity from the leading-edges.

Continuing to look at the minimum roll angle achieved in the rolling motion ($\Phi = 26^{o}$), it can be seen from Fig. 3.2 that the velocity magnitude associated with the left-hand vortex increases down the wing. However, in this case there is a considerable reduction in velocity magnitude in the region of the right-hand wing half at x/c = 0.75. The reattachment lines are close together at $\Phi = 26^{o}$, though cannot be exactly defined. Note that there is no evidence of a vortical flow structure formed by the right-hand shear layer. Whether this is because it is very close to the wing surface due to the round leading-edge or because the wing is stalled is unclear from this data. The turbulence

intensity graphs on the right-hand side of Fig. 3.2 show that the turbulence associated with the shear layer increases in size further down the wing. Another point to note, particularly at x/c = 0.75, is that the left-hand vortex has higher turbulence levels. This may be due to unquantifiable noise from the laser reflection on the wing surface, but could also be due to the proximity of the attachment lines from both shear layers and subsequent interaction. The vortices are seen to move further from the wing surface as the flow progresses down the wing in Fig. 3.2.

Figure 3.3 shows similar data to Fig. 3.2 but at near the maximum roll angle achieved during the rolling motion. Figure 3.3 suggests that there is a reattached region at all chordwise locations, and the turbulence intensity confirms that there is no interaction between the shear layers. Again, the leeward shear layer moves further from the wing surface and the windward (left-hand side) vortex becomes larger as the flow progresses down the wing. It is interesting to note that the windward vortex is now much more compact at $\Phi = 54^o$ than at $\Phi = 26^o$ (Fig. 3.2) due to the increased effective sweep and lower effective angle of attack (equations (1) and (2)) of this wing half at this higher roll angle. The other point to note is that the leeward shear layer is now much closer to the wing surface than at $\Phi = 26^o$ (Fig. 3.2). Reattachment lines of the left and right-hand shear layers are well separated at this roll angle and betray the presence of a vortical structure on either wing half at all stations (Fig. 3.3). There is an outboard velocity along the wing surface on the right-hand wing half and the vortices are seen to be particularly close to the wing surface. The turbulence intensity in Fig. 3.3 shows the same pattern, with the turbulent region associated with the right-hand side shear layer becoming larger in size further down the wing. The turbulence associated with the left-hand side shear layer grows in size down the wing and also moves further from the wing surface. Previous work has believed that this vortex is what causes the non-zero trim angles and non-linearity. The vortices are suspected to create non-linearity in the C_L vs. α curve as the linear portion is due to potential flow (thin aerofoil theory[7]).

Comparing the velocity fields at the maximum and minimum magnitudes of roll angle (Figs. 3.2 and 3.3) particularly at x/c = 0.75, it can be seen that there is a large difference in the size of the windward (left-hand side) vortex. The lower effective angle of attack mean a more compact vortex is formed at the higher magnitude of roll angle. It appears that no leeward vortex is formed by the right-hand shear layer at the lowest

magnitude of roll angle (no reversed flow), possibly due to stall, while there is evidence for the two larger magnitudes of roll angles that a leeward vortex forms in this region. At the highest roll angle it is evident that the vortical flows are closer to the wing surface. In all cases the shear layers move further from the wing surface as the flow progresses down the wing due to continuous feeding of vorticity from the leading-edges. The velocity fields show how the reattachment line of the right-hand side shear layer moves further outboard with increasing magnitude of roll angle. Velocity fields at x/c = 0.75 demonstrate an outboard flow along the right-hand side wing surface, though the outboard flow for the left-hand vortex is hard to see due to proximity to the wing surface. The turbulence intensity levels associated with increasing magnitude of roll angle are seen to increase, while the presence of this turbulence gets closer to the wing surface, showing that the increasing roll angle causes the shear layers to be closer to the wing surface.

Figures 3.4 and 3.5 present the normalised velocity profiles and streamline patterns respectively, for the thick wing in motion at $\alpha = 28^{o}$ (near maximum standard deviation from Fig. 3.1b)) and x/c = 0.25. Figures 3.4 and 3.5 show the movement of the leeward shear layer reattachment point, and how an area of reattached flow exists at near the maximum roll angle, but is not evident at near minimum roll angle or at the mean roll angle as the roll angle increases. Figure 3.4 indicates that the maximum roll angle (part (i)) and the mean roll angle for decreasing roll (part (ii)); the right-hand shear layer is very close to the wing surface. It moves farther away from the wing surface at the minimum roll angle (part (iii)) and the mean roll angle for increasing roll (part (iv)). Figure 3.4 also shows the movement of the right-hand shear layer reattachment point, and how an area of reattached flow exists near Φ_{max} (part (i)), but is not evident near Φ_{min} (part (iii)) or at Φ_{mean} (part (iv)) as the roll angle increases. As near Φ_{max} the leeward shear layer is much closer to the wing surface, this presumably generates the lift on that wing half to drive the wing back in the other direction. There appears to be a time lag in the development of the flow. A leeward vortical structure also appears to form at near the maximum roll angle, and the shear layer is much closer to the wing surface (Fig. 3.5), which presumably drives the wing back in the other direction. There appears to be a time lag effect, with the leeward shear layer stalling after the lowest roll angle, evident in Fig. 3.4 (iii) and (iv). In all cases the windward vortex is too close to the wing surface to be distinguished.

The phase-averaged velocity fields at x/c = 0.5 (Figs. 3.6 and 3.7) are similar to those at x/c = 0.25 (Figs. 3.4 and 3.5). Figures 3.6 and 3.7 confirm that a large area of reattached flow is present at near the maximum roll angle and that the leeward shear layer appears to stall after the minimum roll angle. This corresponds to the leeward shear layer being furthest from the wing surface at point (iv) but closest at point (i), where it has more effect on the wing dynamics. An interesting point to note is how the size of the windward vortex changes throughout the motion, visible in Fig. 3.6. At instance (i), it is compact, in contrast to (iii) where it appears to be much larger. Whether this is due to vortex breakdown or not is unclear and would require near-surface PIV measurements to determine. At this chordwise location a leeward vortical structure is evident in all cases.

This hysteresis effect is more pronounced at a streamwise station further downstream (x/c = 0.5) as shown in Fig. 3.8 (every other vector is omitted for clarity). This Figure shows the three different flow structures possible at the mean roll angle depending on whether the wing is static, Φ is increasing or Φ is decreasing. These different flow structures indicate the presence of a time lag, without which the motion would not occur. In the instance of b), the left-hand vortex is generating the lift driving the motion and vice versa in c). Figs. 3.8a) and 3.8c) show that the structures in these two cases are very similar, though with a slightly larger area of reattached flow in (c). In this case, the right-hand vortical structure must be generating more lift than the left-hand wing half. According to equations (1) and (2), for this wing at $\alpha = 28^o$ and $\Phi_{max} = 54^o$, $\Lambda_{eff} = 73.3^o$ and $\alpha_{eff} = 17.4^o$, which would place vortex breakdown beyond the trailing-edge[10], while at $\Phi_{min} = 26^o$, values of $\Lambda_{eff} = 63.1^o$ and $\alpha_{eff} = 25.5^o$ would place breakdown on the wing surface in the static case. However, it has not been previously investigated how the time lags present affect breakdown on this rolling wing. A significant difference exists for Φ increasing, with the right-hand shear layer being much further from the wing surface. In this instance, the left-hand vortex must be generating more lift to drive the motion. At this streamwise station, the vortical flow developing on the left hand side is more visible. For all cases in Fig. 3.8, the left-hand vortex is compact and approximately the same size. The right-hand vortical flow is expected to have breakdown at the apex at all roll angles. Although a general understanding of the vortical flow during the roll oscillations is achieved, role of the round leading-edges, if

any, is not clear. Comparison of the velocity field with that of wings with sharp leading-edge will be presented later on in the Chapter.

3.1.3 Post-stall incidences

In Fig. 3.1b) the model can be seen to reach equilibrium not too far from zero mean roll angle at low angles of attack. When the angle of attack is increased sufficiently away from the stall angle, there is only one trim position at zero roll angle (Fig. 3.1b)). There were some initial oscillations which rapidly died away because the wing motion is damped in this case, which corresponds to full wing stall, with reversed flow on both wing halves.

3.2 Other leading-edge shapes

Self-excited roll oscillations were also observed for a thin (t/c = 1.5%) delta wing with the same planform shape but with sharp leading-edge, which will be discussed in Chapter 4. This is the first experimental observation of such oscillations for non-slender delta wings with sharp leading-edges. It suggests that even when the separation point is fixed as it is for the sharp leading-edge, these oscillations occur. As the amplitude of the motion is amplified for a round leading-edge, characteristics of flow separation at the leading-edge are a contributing, but not a necessary factor. In both cases these oscillations are observed around the stall angle, where the reattachment of asymmetric flows is the most important factor on non-slender delta wings[19,45]. If the leading-edge is round (hence the separation line is not fixed) unsteady separation at the leading-edge might also contribute to the roll oscillations.

The mean roll angle and standard deviation of roll oscillations are shown as a function of incidence for wings with various leading-edge profiles in Fig. 3.9. Trends are similar to those of the thick delta wing with round leading-edge (Fig. 3.1b)), with the wing stalling suddenly after the oscillations. The standard deviation of the roll oscillations for the round leading-edge wing is smaller for the t/c = 4 % wing (number 16 in Table 2.1, results in Fig. 3.9c) than for the 10 % thick wing in Fig. 3.1b), which is due to the wing thickness. It is interesting to note that at a given thickness, the wing with 2:1 elliptical leading-edge (number 17 in Table 2.1) exhibits the largest oscillations

of these 4 wings (Fig. 3.9a)). Perhaps this compromise between a blunter leading-edge of the semi-circular profile in Fig. 3.9c) and the sharper 4:1 elliptical leading-edge in Fig. 3.9b) allows the separation point to move, thus causing the oscillations to become larger. The 4 % thick delta wing with 4:1 elliptical leading-edge (number 18 in Table 2.1) again demonstrated free-to-roll oscillations, as shown in Figure 3.9b) (time history of roll angle). The stall angle obtained from the mean roll angle plot was around $\alpha = 26.5^{o}$, which is again near what was observed previously[45]. Unlike for the thick, round leading-edge version of this wing, the magnitude of the roll angle did not reduce just before stall for the 4 % thick version. The oscillations were of lower amplitude than for the 2:1 elliptical case, as shown in Fig. 3.9c). The leading-edge shape of 2:1 elliptical gave larger oscillation amplitudes than even the round leading-edge, possibly because it is easier for the separation point to move in this case than on the sharper leading-edges and there is less curvature than in the round leading-edge case, suggesting that the flow can stay attached for longer. The data for the sharp leading-edged version (number 15 in Table 2.1, results shown in Fig. 3.9d)) confirms this.

3.3 Summary

A mechanism is postulated whereby at the maximum roll angle a large area of reattached flow damps the motion on the leeward wing half and overcomes the lift provided by the compact windward vortex. This drives the wing around. The leeward shear layer (because of the changing effective angles) stalls as the roll angle decreases and the dominant driving mechanism is now the windward vortex. This windward vortex may break down at the minimum roll angle due to increasing effective angle of attack. This could explain the differing amplitude of the motion, as it is well known for the breakdown location on non-slender delta wings to fluctuate by up to 40-50 % of the chord length[76], compared to around 10% for slender delta wings[77]. This breakdown would damp the motion at the smallest roll angle.

Upon analysis of the evidence, the following points are observed:

- The oscillations may be triggered by the increasing proximity of the reattachment points as the angle of attack is increased, causing an interaction between the two reattaching shear layers. They cannot be caused by vortex breakdown because at the mean roll angle vortex breakdown is beyond the

trailing-edge on the windward wing half, whereas it is at the apex for the leeward wing half. This assumes no time-lag effects;

- At the maximum magnitude of roll angle, there is enough lift on the right-hand wing half to cause the wing to roll back towards the minimum magnitude of roll angle. This may be because the right-hand vortical structure has formed closer to the wing surface, which could also explain the earlier reattachment;

- The left-hand side vortex at this maximum roll angle is compact (because of high effective sweep and low effective angle of attack) and generates less lift. This is shown by the lower velocities, thus circulation, associated with this vortex at high roll angles when compared with low magnitudes of roll angle in the dynamic PIV data at $\alpha = 28^{o}$;

- As the roll angle magnitude decreases through its mean roll angle the reattachment points move closer together, which may affect the damping properties of the wing;

- At the minimum roll angle, the left-hand side vortex increases in strength, caused by the increase in effective angle of attack. Vortex breakdown may also be present on the wing at this point and the oscillation of this breakdown point cause the irregular amplitude of the motion. If breakdown occurs closer to the apex, less lift will be generated by the left-hand side wing half, suggesting that the driving force for the motion is reduced, thus the amplitude is less. This relatively strong vortex causes the wing to roll in the other direction, and may be what provides the damping to stop the motion at this roll angle. Here the reattachment points are very close together, but the left-hand side vortex is still present and generates enough lift to make the wing rotate in the other direction. The PIV data shows that the right wing half may be stalled as the roll angle increases through the mean value again;

- The aforementioned oscillations are not seen to such an extent for the wings with sharp leading-edges, which suggest that the motion is probably related to the separation phenomenon. The round leading-edge amplifies the effect of the motion because the separation point is free to move; this is what gives the thick wing its insensitivity to angle of attack and broad standard deviation peak;

- In summary, a round leading-edge is good in terms of increasing stall angle, thus manoeuvrability of an air vehicle, but a sharp leading-edge can attenuate oscillations better at this sweep angle. Hysteresis and time-lag effects are significant even though typical dimensionless frequencies are very low.

a)

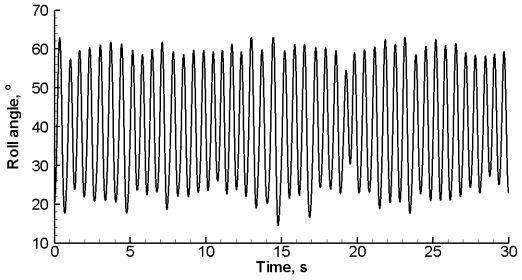

b)

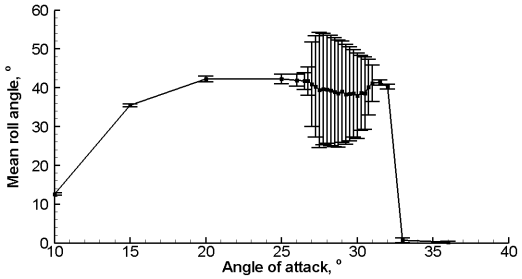

c)

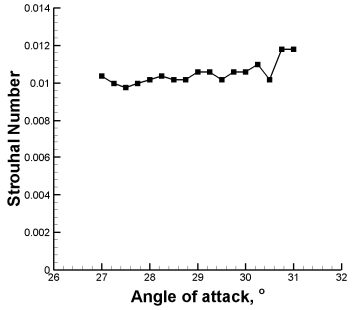

d)

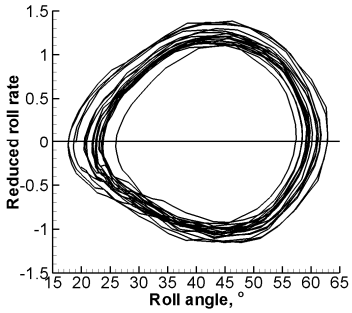

e)

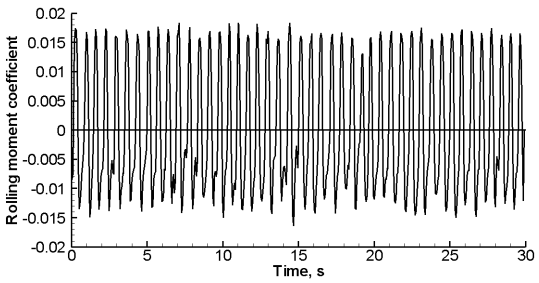

Figure 3.1 Free-to-roll results for non-slender delta wing with $\Lambda = 50^o$, t/c = 10% and round leading-edge, showing a) time history of roll angle at $\alpha = 28^o$; b) mean roll angle with standard deviation as error bars versus angle of attack; c) Strouhal number versus angle of attack at angles of attack for which large oscillations occur; d) reduced roll rate versus roll angle and e) time history of rolling moment coefficient obtained from $\Phi(t)$ at $\alpha = 28^o$.

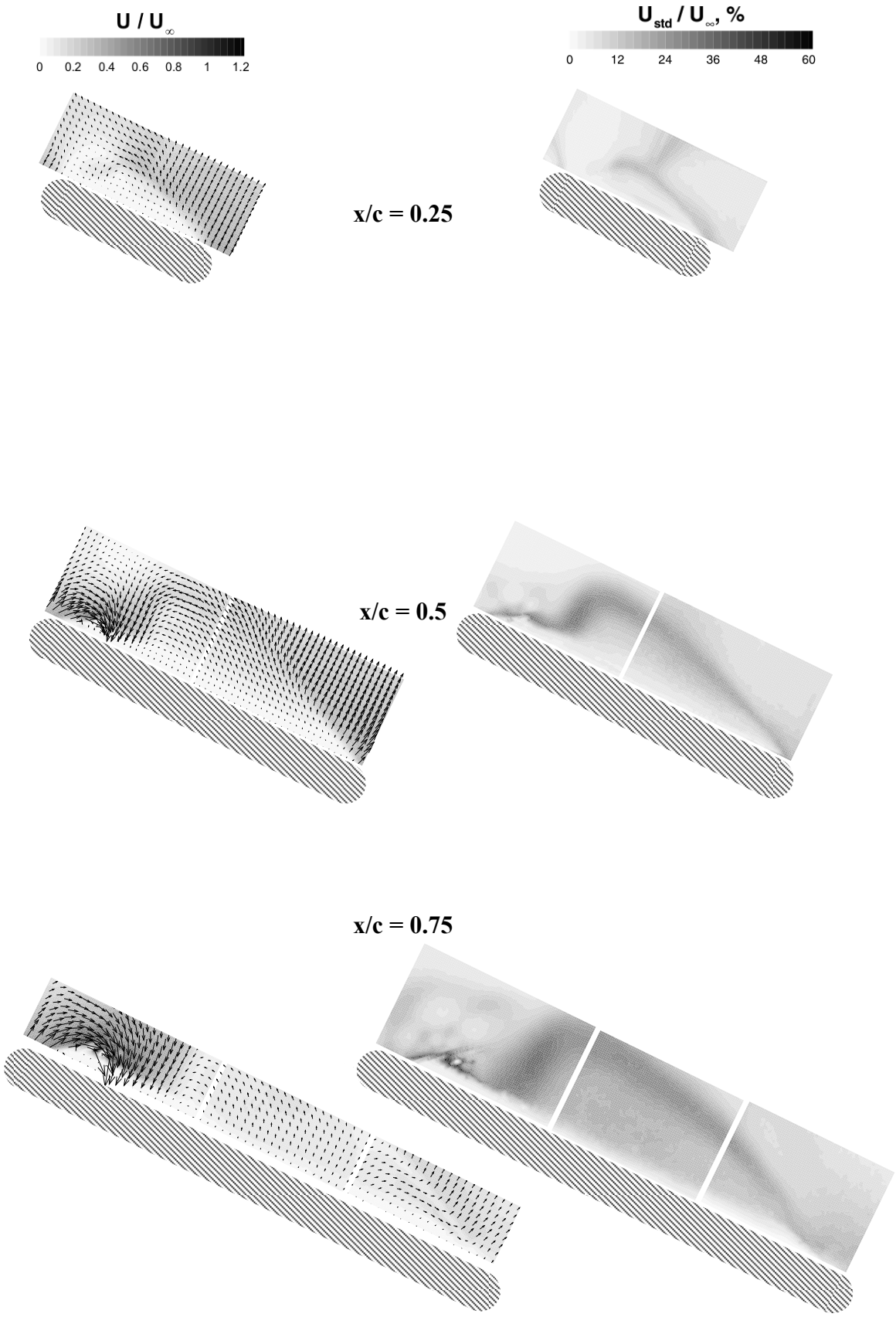

Figure 3.2 Cross-flow velocity magnitude (left) and turbulence intensity (right) at x/c = 0.25, 0.5 and 0.75 respectively, $\alpha = 28°$ and $\Phi = 26^{o}$ (signified by roll angle of diagram) for stationary non-slender delta wing with $\Lambda = 50^{o}$, t/c = 10% and round leading-edge.

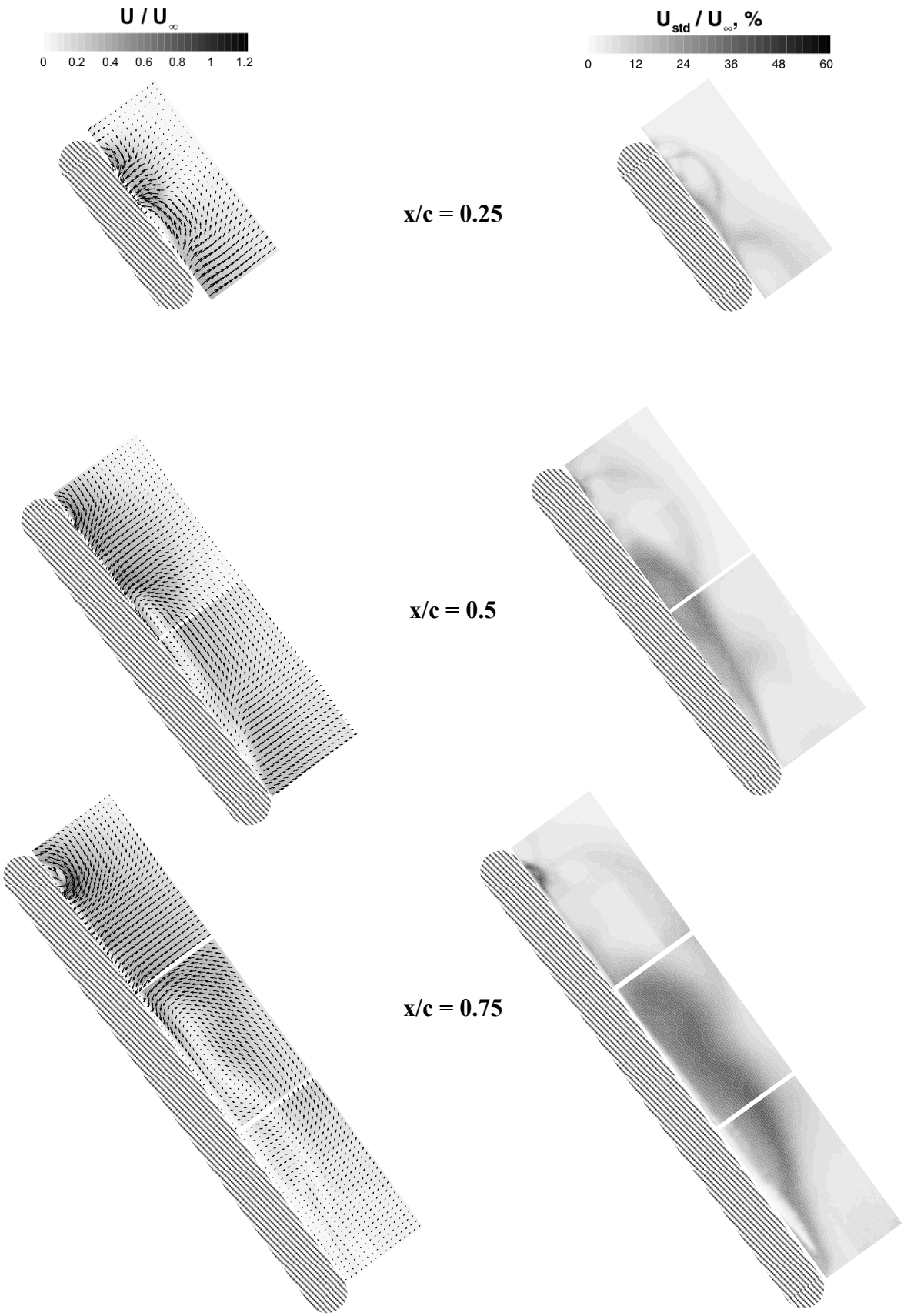

Figure 3.3 Cross-flow velocity magnitude (left) and turbulence intensity (right) at x/c = 0.25, 0.5 and 0.75 respectively, $\alpha = 28°$ and $\Phi = 54^o$ for stationary non-slender delta wing with $\Lambda = 50^o$, t/c = 10% and round leading-edge.

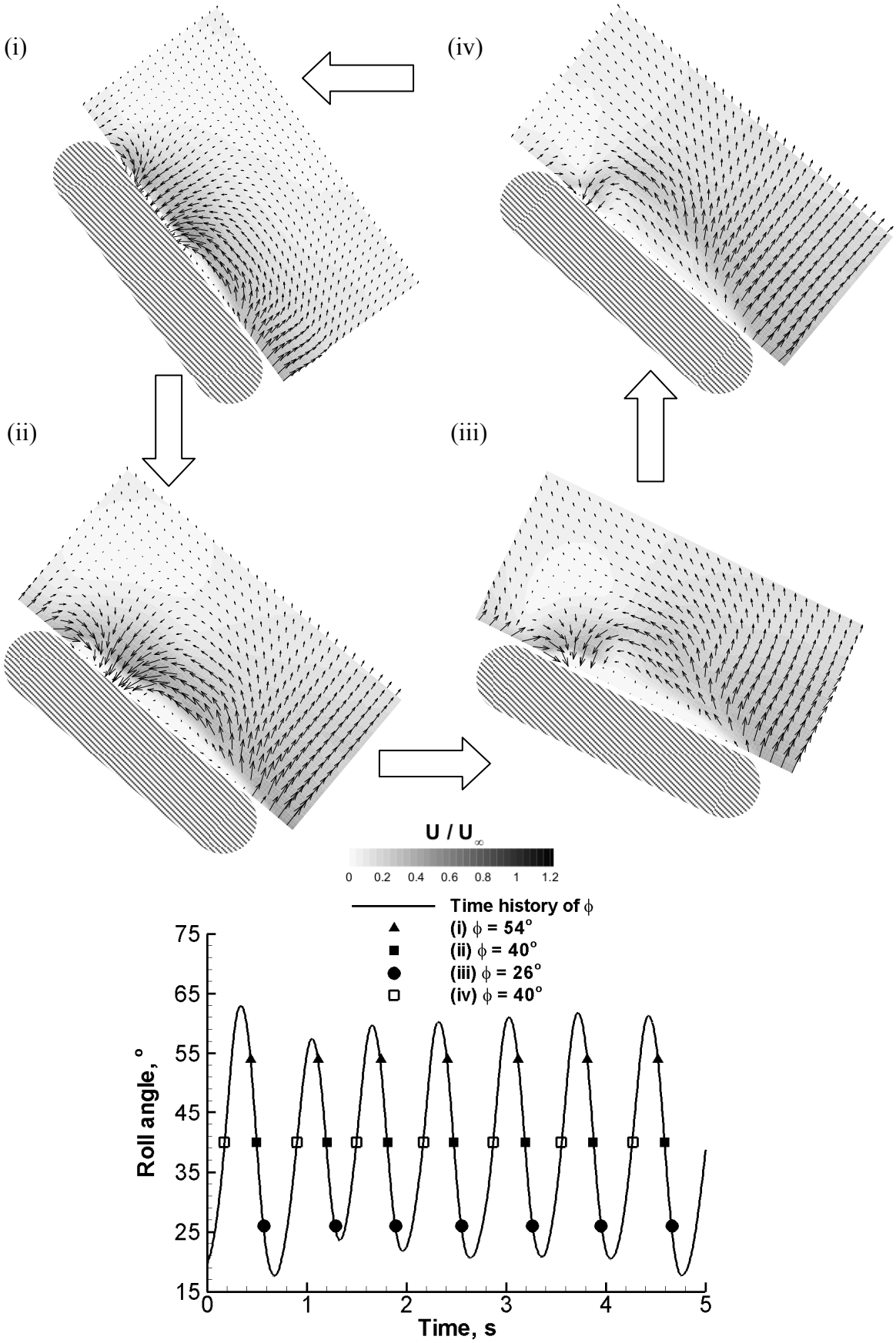

Figure 3.4 Phase-averaged velocity fields with timing diagram corresponding to images, with (i) at $\Phi = 54^{o}$; (ii) at $\Phi = 40^{o}$; (iii) at $\Phi = 26^{o}$ and (iv) at $\Phi = 40^{o}$ for free-to-roll non-slender delta wing with $\Lambda = 50^{o}$, t/c = 10% and round leading-edge at x/c = 0.25 and $\alpha = 28^{o}$.

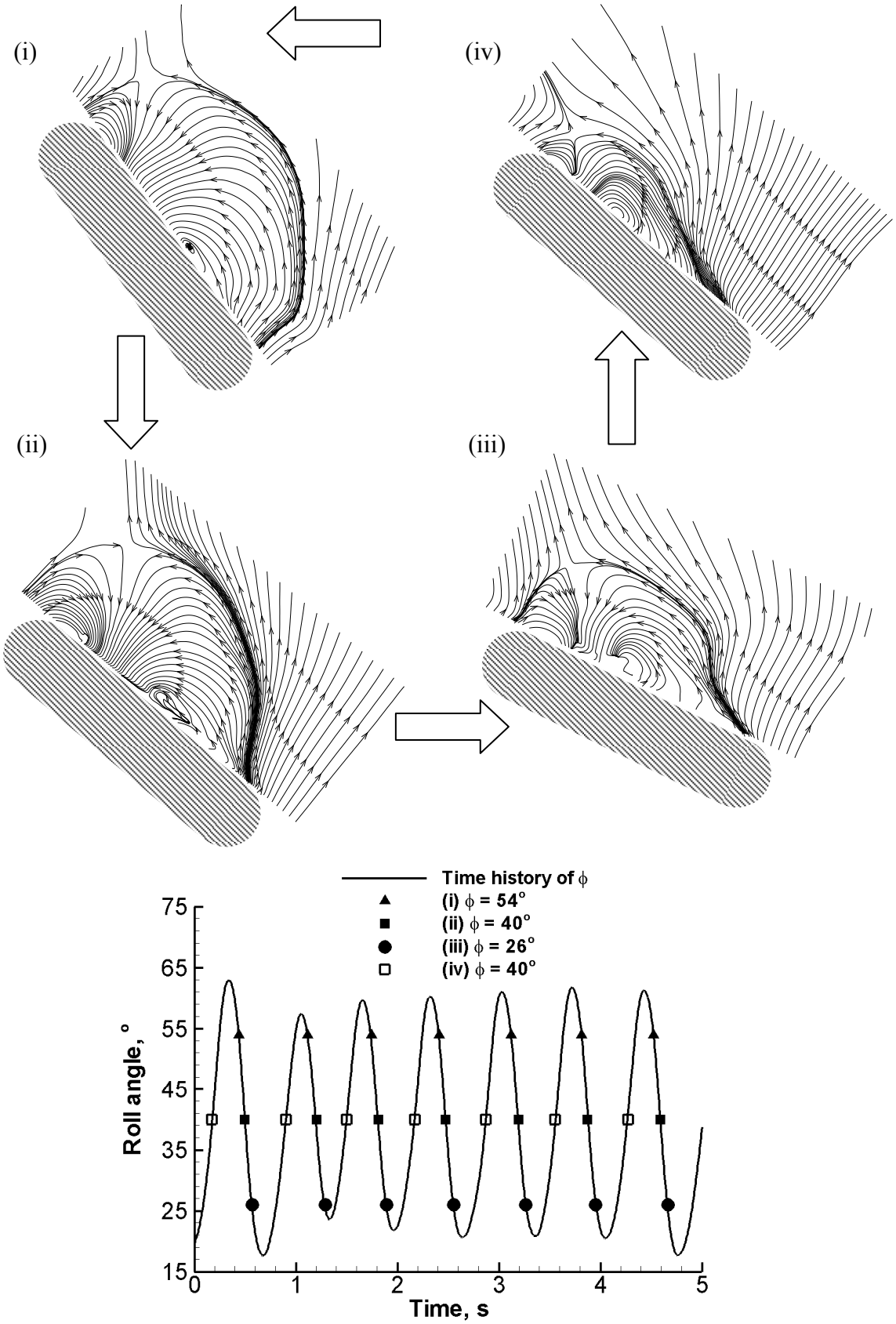

Figure 3.5 Phase-averaged streamline patterns with timing diagram corresponding to images, with (i) at $\Phi = 54^{o}$; (ii) at $\Phi = 40^{o}$; (iii) at $\Phi = 26^{o}$ and (iv) at $\Phi = 40^{o}$ for free-to-roll non-slender delta wing with $\Lambda = 50^{o}$, t/c = 10% and round leading-edge at x/c = 0.25 and $\alpha = 28^{o}$.

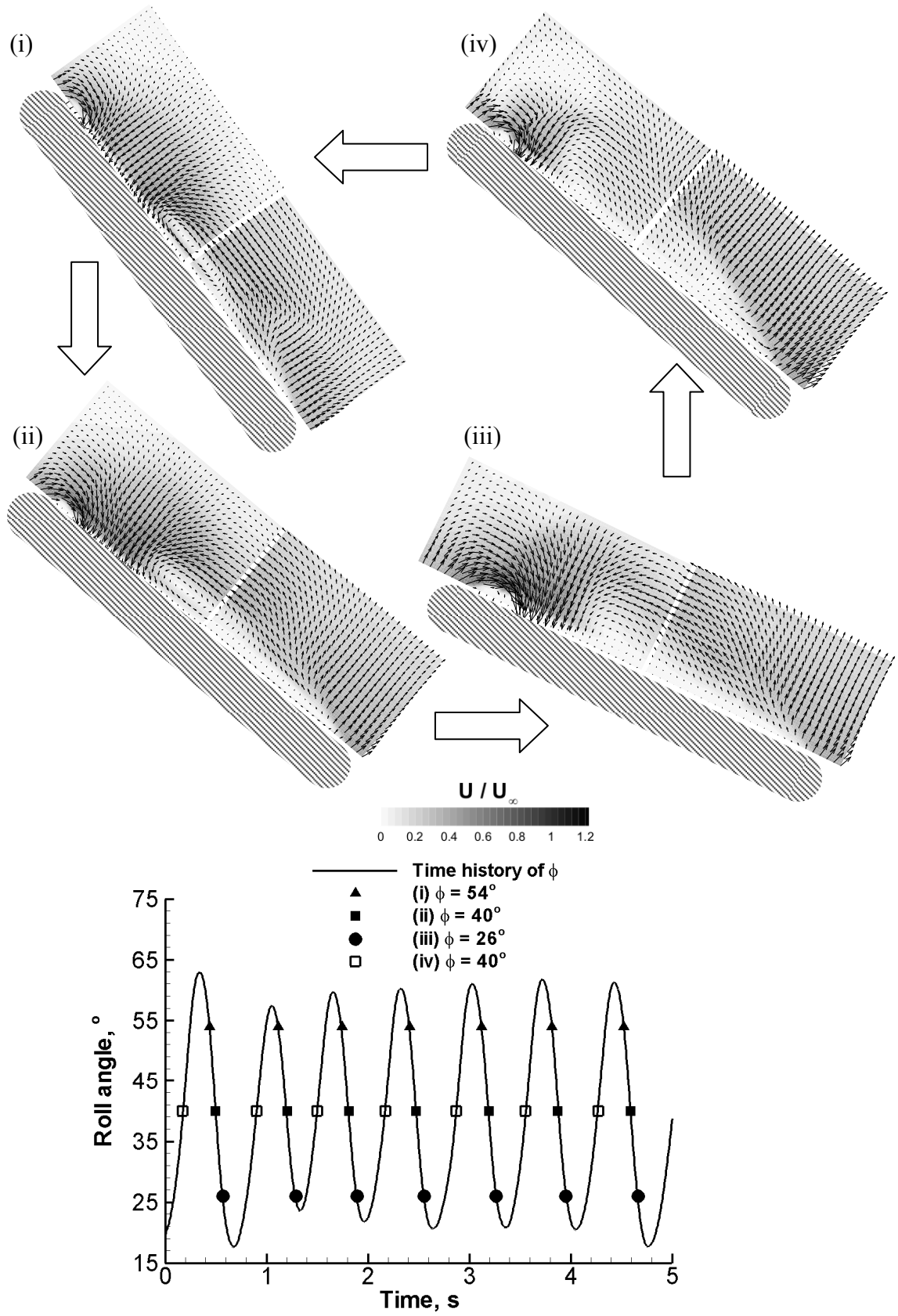

Figure 3.6 Phase-averaged velocity fields with timing diagram corresponding to images, with (i) at $\Phi = 54^{o}$; (ii) at $\Phi = 40^{o}$; (iii) at $\Phi = 26^{o}$ and (iv) at $\Phi = 40^{o}$ for free-to-roll non-slender delta wing with $\Lambda = 50^{o}$, t/c = 10% and round leading-edge at x/c = 0.5 and $\alpha = 28^{o}$.

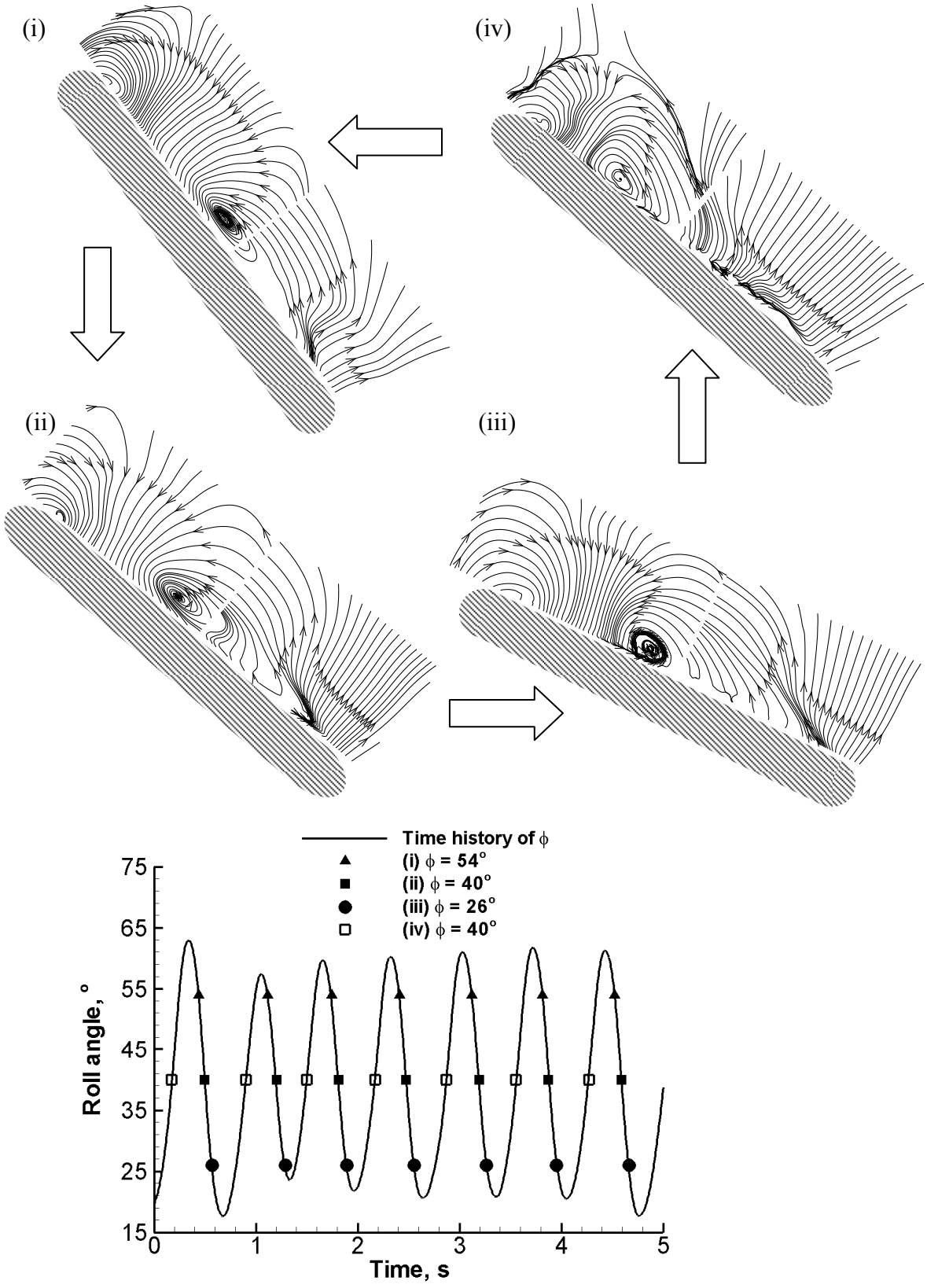

Figure 3.7 Phase-averaged streamline patterns with timing diagram corresponding to images, with (i) at $\Phi = 54^{o}$; (ii) at $\Phi = 40^{o}$; (iii) at $\Phi = 26^{o}$ and (iv) at $\Phi = 40^{o}$ for free-to-roll non-slender delta wing with $\Lambda = 50^{o}$, t/c = 10% and round leading-edge at x/c = 0.5 and $\alpha = 28^{o}$.

a) **Stationary**

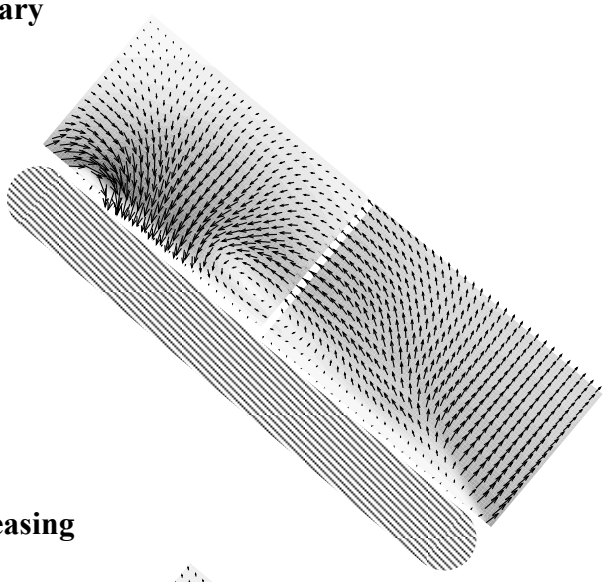

b) **Φ increasing**

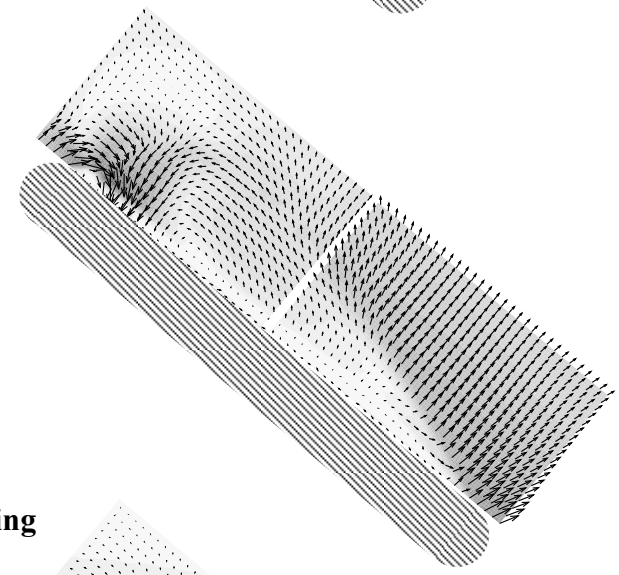

c) **Φ decreasing**

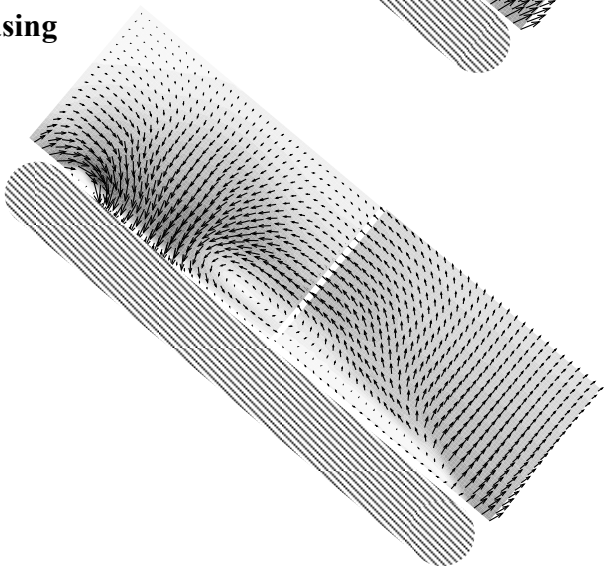

Figure 3.8 Cross-flow velocity fields at x/c = 0.5 for a) stationary wing; b) Φ increasing and c) Φ decreasing, at α = 28° and Φ = 40° respectively, for non-slender delta wing with Λ = 50°, t/c = 10 % and round leading-edge.

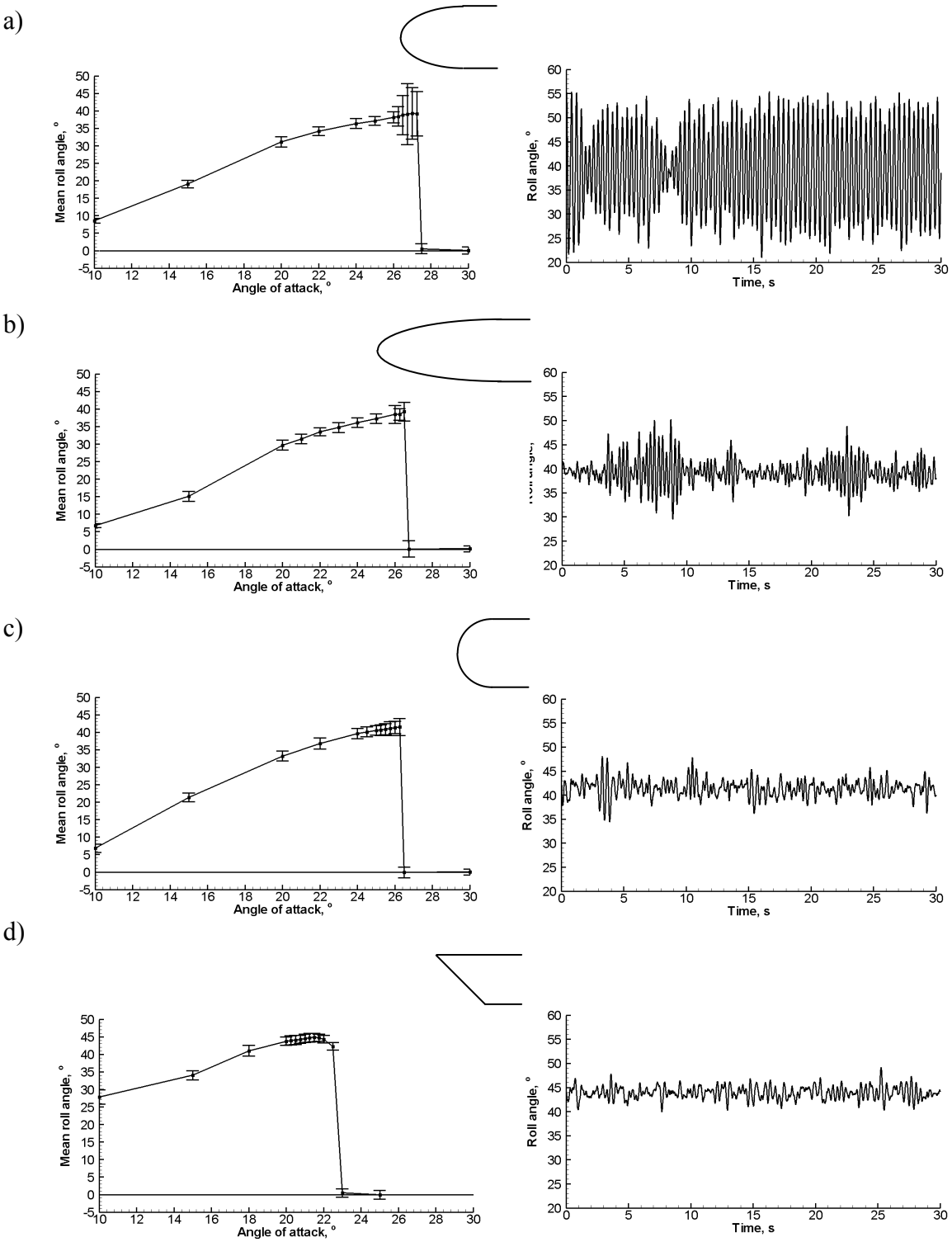

Figure 3.9 Graphs showing mean roll angle versus angle of attack with standard deviation as error bars (left), time histories of roll angle corresponding to maximum standard deviation (right, α = 26.75°, 26.5°, 26.25° and 20.5°, respectively) and schematics of each leading-edge (centre) for non-slender delta wings with $\Lambda = 50^{o}$, t/c = 4% and a) 2:1 elliptical; b) 4:1 elliptical; c) semi-circular and d) sharp leading-edges.

Chapter 4 Non-slender Delta Wings

All delta wings being tested, apart from the 70^o sweep wing, exhibited significant non-zero roll trim angles, which is similar to what has been observed previously (Chapter 1). The delta wings tested could be put into two categories, dependent on their observed stalling characteristics. Firstly, wings of $\Lambda \leq 55^o$ snapped suddenly from a non-zero mean roll angle to zero mean roll angle as angle of attack was increased, which is assumed to be where the wing stalls. Secondly, wings of higher sweep angles reduced to zero mean roll angle more gently, thus were considered to be stalling more gradually, and will be discussed in the next Chapter. This Thesis goes along with the tradition of calling delta wings of $\Lambda \leq 55^o$ non-slender and those of greater sweep angle slender. Note that all wings discussed in this Chapter have sharp leading-edges, to take the roundness of the leading-edge out as a factor.

4.1 Effect of moment of inertia

Since the wings in this Chapter had sharp leading-edges, the separation point was fixed and they all had the same span. It was desired to know the effect of various parameters as well as fixing the separation point.

Figure 4.1 demonstrates the effect of the moment of inertia of a non-slender delta wing planform of $\Lambda = 50^o$ (heavier wings with increasing Figure number). The moment of inertia about the roll axis includes that of the two slightly different stings used. On the left-hand side, plots are shown of the mean roll angle against the angle of attack; with the standard deviation of the oscillations shown as error bars. On the right-hand side, a 15 s trace of the roll oscillations at the maximum standard deviation is shown at a point near stall in all cases. Increasing the moment of inertia of the wing (Fig. 4.1) is seen to delay the stalling characteristics. This is in terms of making the angle of attack where the wings snap to zero mean roll angle larger on the left-hand plots as the moment of inertia increases. This is presumably because the oscillations of the wing take it to a state where it oscillates in and out of stall, while the heavier wings are seen to reach lower roll angles and thus not necessarily achieve stall conditions. From the oscillations it can be seen that all wings exhibit oscillations of some description with reducing frequency with increasing moment of inertia.

Figure 4.2 presents the maximum standard deviation achieved and the variation of the stall angle of the wing against the non-dimensionalised moment of inertia. Non-dimensionality was achieved using dimensional analysis:

$$F = ma \text{ thus by similarity, } T = I_{xx}d^2\Phi / dt^2 \text{ (the equation of motion for a rolling wing)}$$
$$T \sim St^2$$

$$\text{Therefore } d^2\Phi / dt^2 = 0.5\rho U_\infty{}^2 sbC_L / I_{xx}$$
$$St^2 \sim \rho U_\infty{}^2 cbC_L / I_{xx}$$

Now, to non-dimensionalise, use the above formula's dimensions (St is non-dimensional):

St depends on **ρ**		U_∞	c	b	I_{xx}
Units	$\mathbf{ML^{-3}}$	LT^{-1}	L	L	ML^2

From Buckingham's Pi theorem, we have 5 variables with 3 dimensions, thus $n \geq 2$ dimensionless groups. Remove variables by dimensional consistency and target ρ:

St depends on $\mathbf{\rho b^5}$		c	b	I_{xx}
Units	$\mathbf{ML^2}$	L	L	ML^2

St depends on $\mathbf{\rho b^5 / I_{xx}}$	b / c
Units	-

Thus $\mathbf{St \sim \rho b^5 / I_{xx}}$ and St ~ b / c.

It can be observed that the maximum standard deviation occurs for a non-dimensional moment of inertia of about 0.17 (Fig. 4.2a)). Increasing the moment of inertia (I_{xx}) can be seen to delay the stall angle in Fig. 4.2b), with the stall angle seemingly increasing with angle of attack continuously. This is also evident from the standard deviation graphs on the left-hand side of Fig. 4.1. Here there is evidence of the wing snapping to zero mean roll angle later with increasing angle of attack as the moment of inertia is increased (i.e. stall angle, looking down from Figs. 4.1a) to e)).

The Strouhal number of the largest oscillations is presented against the non-dimensional moment of inertia in normal and logarithmic cases. Figure 4.3a) indicates that the Strouhal number decreases with increasing non-dimensional moment of inertia as expected due to the same tunnel velocity or driving force. In Fig. 4.3b), this is confirmed with a virtually straight line suggesting direct proportionality, which goes along with the adopted formula for Strouhal number on the previous page. This suggests a quadratic relationship, with the line shown in Fig. 4.3b) presenting non-dimensional data.

4.2 Non-slender delta wing roll oscillation behaviour

The left-hand side of Fig. 4.4 shows how the mean roll angle varied with angle of attack for non-slender delta wings with increasing sweep angle, with error bars showing the standard deviation of the roll angle time history shown on the right-hand side. The first point to note is that the stalling of the wings was delayed with increasing sweep angle, and that all the wings experienced an increasing non-zero mean roll angle with increasing angle of attack nearly up to stall. The trim angle for the 45^o wing at $\alpha = 20^o$ was $\Phi_{mean} = 38^o$, which correlates well with the data for a sharp leading-edged 45^o delta wing[50]. For this wing, a trim angle of $\Phi_{mean} = 40^o$ was obtained, albeit at a slightly lower Reynolds number of 2.2×10^5 in comparison to the 3.42×10^5 used here. Secondly, it can be seen that as the sweep angle of the wing increases, there is a region of high standard deviation corresponding to self-excited roll oscillations. As the angle of attack is increased, the oscillations die out just before the wing stalls and the mean roll angle snaps to zero. The roll angle time histories (on the right-hand side) at the angle of attack of the highest standard deviation indicate that delta wings of sweep angle of less than 50^o did not demonstrate oscillatory behaviour. However, for $\Lambda = 50^o$, small oscillations were present. These oscillations were much larger for the cases of 52.5^o and 55^o sweep angle, as shown in Figs. 4.4d) and e). The self-excited roll oscillations in these cases were of slightly varying amplitude, as previously seen[45] for a wing with round leading-edge (the thick wing), and of a constant frequency. Slender wing rock is known to exhibit constant amplitude[34], again highlighting a difference.

Comparing the current results that have been obtained in Table 4.1, it can be seen that a round leading-edge is not a necessity for free-to-roll oscillations to occur, as was previously thought[33]. These oscillations do not exhibit characteristics akin to slender wing rock, and the combination of angles of attack and roll angles mean that at least one wing half is in a state of dynamic stall during the motion. This can be seen in Table 4.1, which shows the effective sweep angles for either wing half, effective sideslip angle and effective angle of attack for wings of 50^o, 52.5^o, 55^o and 60^o sweep angles. These calculations are at angles of attack where roll oscillations occur, and roll angles are near to the maximum and minimum roll angles of the motion. It is expected for the more slender wing half to have a coherent vortex attached to the surface, while the other wing half is invariably non-slender with a high enough angle of attack to cause stall. These vortices with the associated lifts, a time delay and movement of the reattachment point cause the motion, which will be explained in more detail in Chapters 4 and 5.

4.3 Vortex topology

Figure 4.5 shows how the velocity field changed in a cross flow plane as the angle of attack was increased for the stationary 55^o sweep delta wing at x/c = 0.25, with the wing clamped at the equilibrium roll angle obtained from the free-to-roll time histories in Fig. 4.4e). The corresponding streamline patterns and vorticity magnitudes are shown in Figs. 4.6 and 4.7. At $\alpha = 21.25^o$ in (i), which is significantly before the self-excited oscillations, two high-velocity regions can be seen in Fig. 4.5 near to the wing surface corresponding to the reattachment points. When the angle of attack was increased to 22.25^o in (ii), which is just before the self-excited roll oscillations begin, the leeward (right-hand side) reattachment point was seen to move inboard. The increasing proximity of the shear layers may be what triggers these oscillations, in a similar manner to that thought to start slender wing rock[1], though the data is insufficiently accurate to determine exact points. At $\alpha = 23.75^o$ in (iii), which would correspond to where large oscillations would be observed in the free-to-roll case, the reattachment points and thus shear layers were seen to be very close together, with a possibility of interaction between them in Fig. 4.6 (iii). At these first three points the windward (left-hand) vortex appears to be of a similar size, visible in Fig. 4.7. Finally, at $\alpha = 23.75^o$ in (iv), which was just before the wing snapped to zero mean roll angle, the leeward shear layer was seen to be stalled and the windward vortex has weakened slightly (again, visible from Fig. 4.7).

Figure 4.8 shows the time-averaged velocity fields and streamline patterns at x/c = 0.5, before ($\alpha = 21.25^o$) and after ($\alpha = 26^o$) the oscillations. Again, the streamlines from both shear layers show that the reattachment points can be seen to be closer to one another at the higher angle of attack (also higher roll angle). These were taken from the mean roll angle plots, so the angle of attack and roll angles are those which the wing would achieve in normal flight conditions. It can be seen from the velocity field at $\alpha = 26^o$ and $\phi = 38^o$ that at in (ii) the right-hand shear layer appears smaller than the other, and that the area of reattached flow is small too. The streamlines confirm this; with a vortex being present near to the wing surface, though as the results are a lot of takes averaged, this vortex is likely to be small, though the data is of insufficient accuracy for measurements. The streamlines in (ii) also confirm that the right-hand shear layer forms a vortex closer to the wing surface than that in part (i), which is to be expected at this higher roll angle. It can be seen that in the case of (i), the windward shear layer is indeed further away from the wing surface too.

Now, moving on to look at the dynamic cases, it can be seen from Fig. 4.9 what is occurring in real images triggered by the oscillations of the wing itself. As the PIV images will show, the area of reattached flow forming the leeward (bottom) shear layer is small at (ii) and (iii). The area of reattached flow is seen to increase for (iv), which corresponds to Φ_{max}, and is still large at Φ_{mean} with Φ decreasing in (i). The time delay is highlighted here, with a lag in flow structures evident in (i) and (iii); though the roll angles and angles of attack are the same. The movement of the wing leads to delays in the flow structure, which undoubtedly causes the roll oscillations.

In Figs. 4.10 - 4.13 dynamic PIV tests are presented at $\alpha = 23.75^o$ (corresponding to near maximum standard deviation in Fig. 4.4e)) at x/c = 0.25 and 0.5 respectively for the 55^o sweep delta wing. It was desired to gain an understanding of how the flow structure over the whole wing changes as the wing undergoes self-excited roll oscillations.

Figures 4.10 and 4.12 show the velocity fields at the two stations and Figs. 4.11 and 4.13 show the corresponding streamline layouts. In each case a timing diagram is included to clarify where the images were taken. Measurements near Φ_{max} ((i) $\Phi = 47^o$)

and near Φ_{min} ((iii) $\Phi = 23^o$) are shown, together with two more measurements at Φ_{mean} ($\Phi = 35^o$), one with roll angle increasing and the other with roll angle decreasing. At (i) a large reattached region exists, with two distinct areas of high velocity in Figs. 4.10 and 4.11 corresponding to the reattachment points visible. A large portion of reattached flow is visible in Fig. 4.13, which presumably stabilises the wing from oscillating further. The windward vortex in Figs. 4.10 and 4.11 appears to be compact and the leeward vortical structure was closest to the wing surface, generating sufficient lift on the corresponding wing half to drive the motion in the opposite direction.

As the roll angle decreases to (ii), the reattachment points on the delta wing surface were seen to move closer to one another and closer still at (iii), most evident in Fig. 4.10. This was where the wing was near the minimum roll angle. There appears to be interaction between the shear layers at this point, with the windward vortex also appearing much larger and stronger, causing the restoring moment, perhaps because of the breakdown of the windward vortex. As the roll angle again increases towards Φ_{max}, at (iv), the leeward shear layer seems to be closer to the wing surface than at (iii) in Figs. 4.10 and 4.12, though the leeward reattachment point does not seem to have an area of high velocity associated with it in this case. Whether this is due to vortex breakdown, increased vortex strength because of increased effective angle of attack, or a combination of the two is not clear. Referring back to equations (1) and (2) (Chapter 1), the effective angles at $\Phi = 47^o$ are $\Lambda_{eff} = 72.8^o$ and $\alpha_{eff} = 16.7^o$ for the windward wing half, which would mean vortex breakdown was expected to be beyond the trailing-edge in this case[11] as shown in Fig. 1.3. However, at $\Phi = 23^o$, the effective angles are $\Lambda_{eff} = 64.8^o$ and $\alpha_{eff} = 22.0^o$, which, for the static case, would correspond to vortex breakdown being on the wing surface. The leeward wing half is expected to have breakdown at the apex all the time.

4.4 Possible mechanism of oscillations

The oscillations may be initiated by the increasing proximity of the shear layers and associated instabilities such as vortex wandering as the angle of attack is increased. At Φ_{min} the shear layer reattachment points move close together and the subsequent motion is driven by the stronger windward vortex generating lift, which may be caused by the high value of α_{eff}, causing an increase in roll angle. As the roll angle increases,

the windward vortex becomes more compact, possibly caused by decreasing α_{eff} and increasing Λ_{eff}. This could be quantified with obtaining clearer, higher definition data and performing vorticity calculations. Also, the reattachment points of both shear layers, which are hard to quantify, move further apart, and the leeward shear layer moves closer to the wing surface. At Φ_{max} the early reattachment of the leeward shear layer means the area of reattached flow is larger and this may damp the motion. The presence of the leeward vortex close to the wing surface generates more lift than the compact windward vortex, evident from the data and changing effective angles (equations (1) and (2)), and this provides a restoring moment, which drives the wing in the other direction. The reattachment points move closer together as the wing passes through the mean roll angle until the wing approaches Φ_{min} when the sequence starts again. The motion may be damped at Φ_{min} by vortex breakdown. Overall, the mechanism appears the same as for the thick wing, the mechanism of which was discussed in Chapter 3.

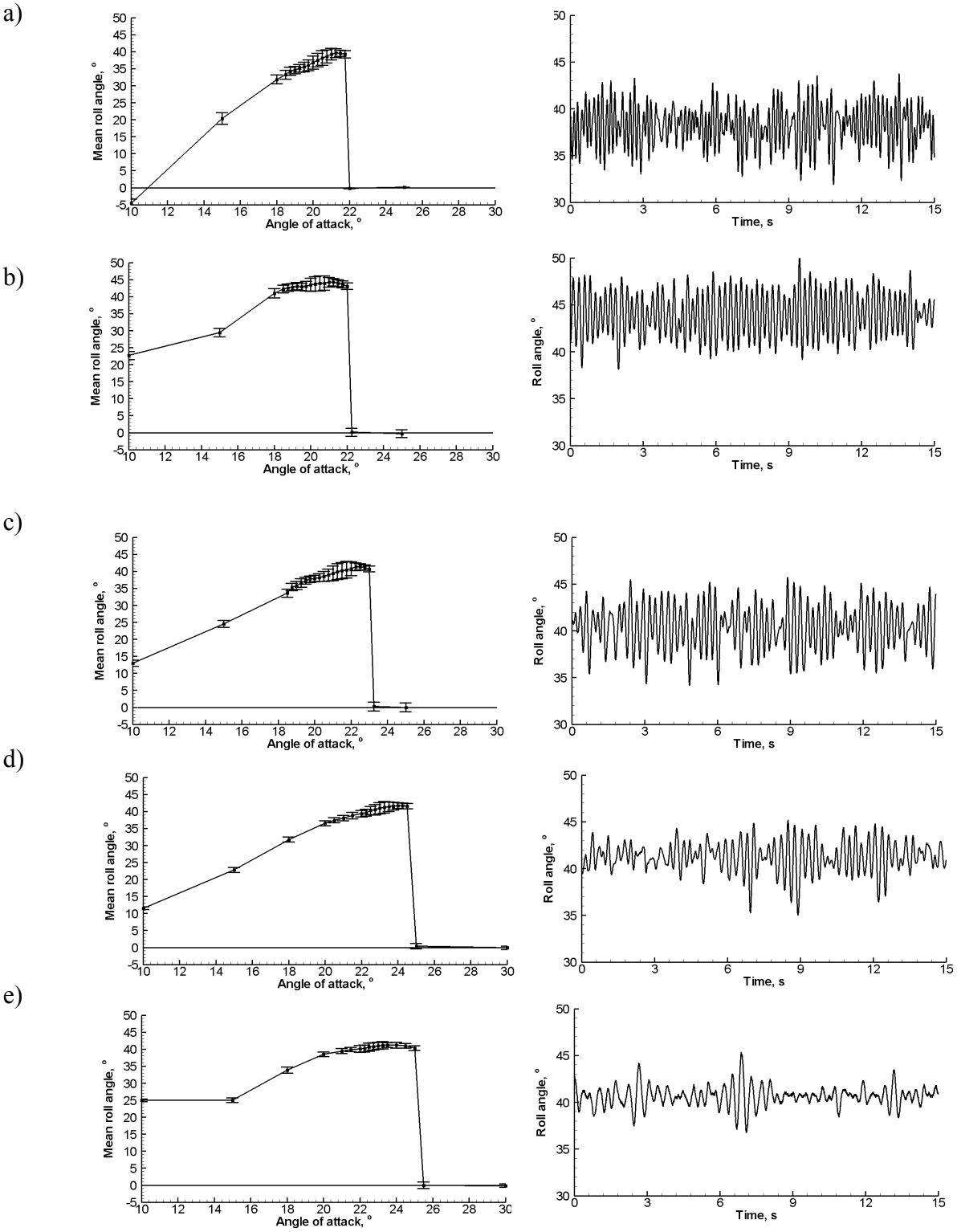

Figure 4.1 Graphs showing mean roll angle against angle of attack with standard deviation as error bars (left) and time histories of roll angle corresponding to maximum standard deviation (right, at $\alpha = 20.5^o$, 20.5^o, 21.75^o, 23.25^o and 22.5^o respectively) for delta wings with increasing second moment of area made from a) carbon/foam sandwich panel, with t/c = 1.7%; b) carbon sheet, with t/c = 1%; c) carbon sheet, with t/c = 1.5%, d) aluminium, with t/c = 1.5% and e) steel, with t/c = 1%, all with $\Lambda = 50^o$ and sharp leading-edges.

a) b)

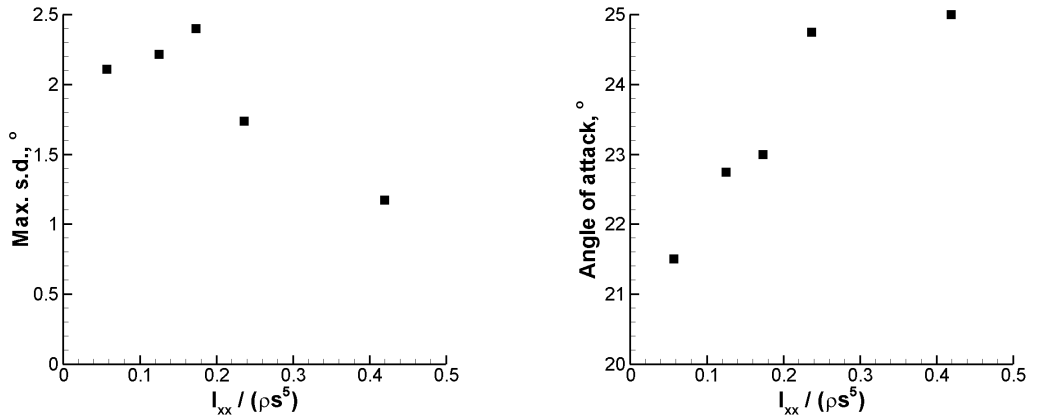

Figure 4.2 Graphs showing a) variation of maximum standard deviation and b) variation of stall angle with non-dimensional moment of inertia for delta wings with $\Lambda = 50^o$ and sharp leading-edges.

a) b)

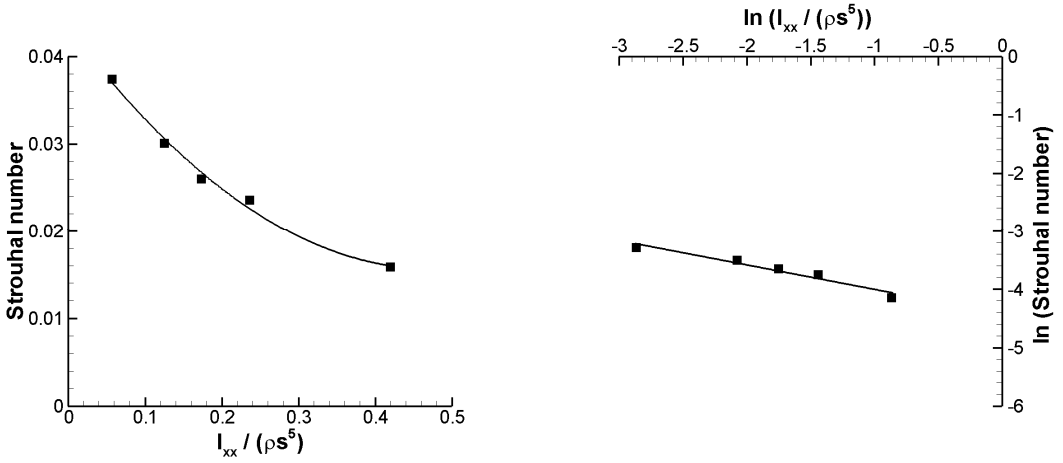

Figure 4.3 Graphs showing a) variation of Strouhal number at maximum standard deviation against non-dimensional moment of inertia and b) variation of Strouhal number at maximum standard deviation against non-dimensional moment of inertia with natural logs taken for delta wings with $\Lambda = 50^o$ and sharp leading-edges.

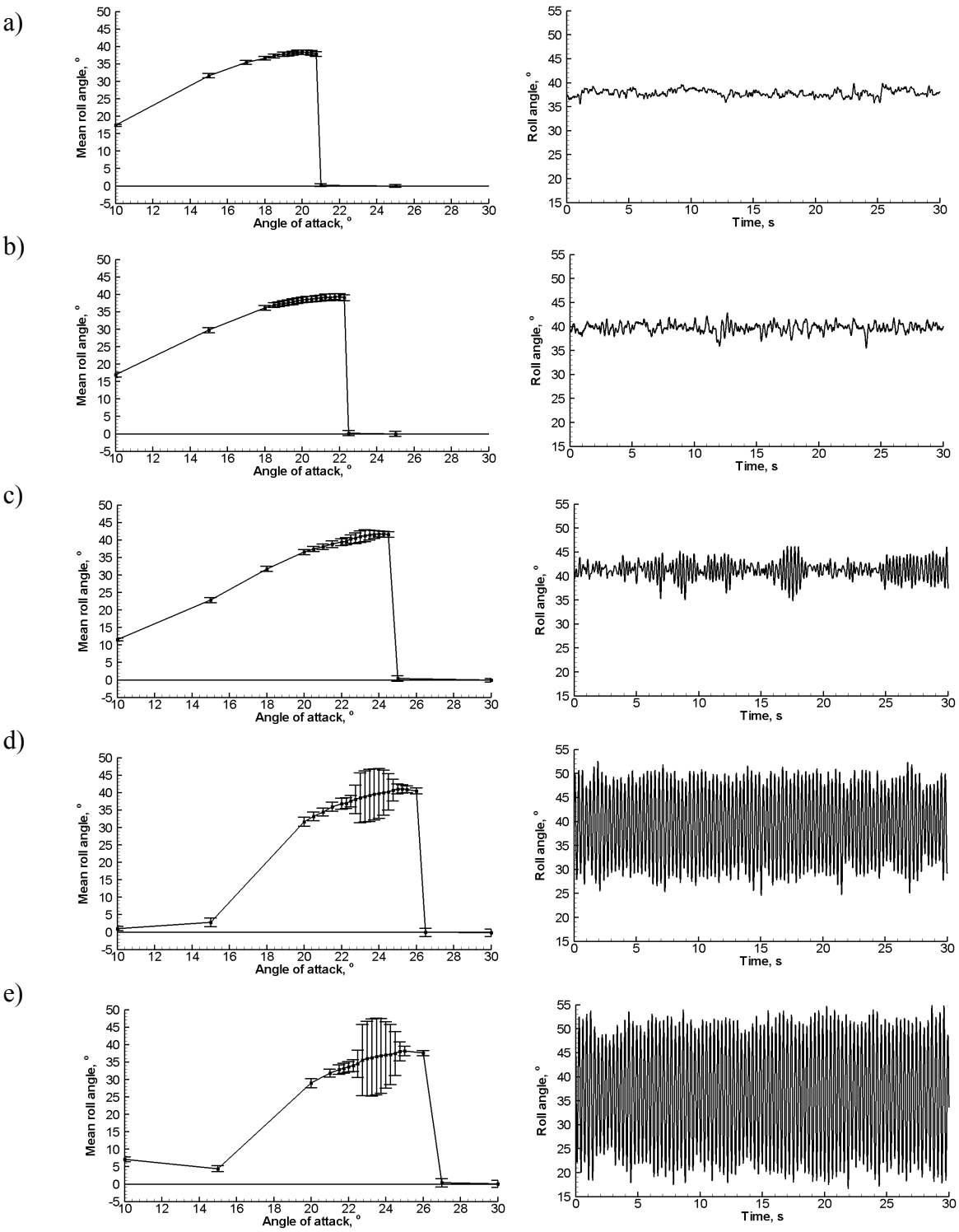

Figure 4.4 Graphs showing mean roll angle against angle of attack with standard deviation as error bars (left) and time histories of roll angle corresponding to maximum standard deviation (right, at $\alpha = 20.75^{o}$, 22^{o}, 23.25^{o}, 23.5^{o} and 23.25^{o} respectively) for delta wings with a) $\Lambda = 40^{o}$; b) $\Lambda = 45^{o}$; c) $\Lambda = 50^{o}$ d) $\Lambda = 52.5^{o}$ and e) $\Lambda = 55^{o}$, all with sharp leading-edges and same thickness.

Λ / ^{o}	α / ^{o}	Φ / ^{o}	$\Lambda_{eff,\ max}$ / ^{o}	$\Lambda_{eff.\ min}$ / ^{o}	α_{eff} / ^{o}
50	28	26	63.1	36.9	25.5
50	28	54	73.3	26.7	17.3
52.5	23.5	30	64.8	40.2	20.6
52.5	23.5	48	70.4	34.6	16.2
55	23.75	20	63.6	46.4	22.5
55	23.75	52	74.1	35.9	15.2
60	26.5	14	66.9	53.1	25.8
60	26.5	38	77.1	42.9	21.4
60	33	0	60	60	33
60	33	10	66.4	53.6	32.6

Table 4.1 Effective sweep angle and angle of attack calculated from equations (1) and (2) for delta wings of varying sweep angle.

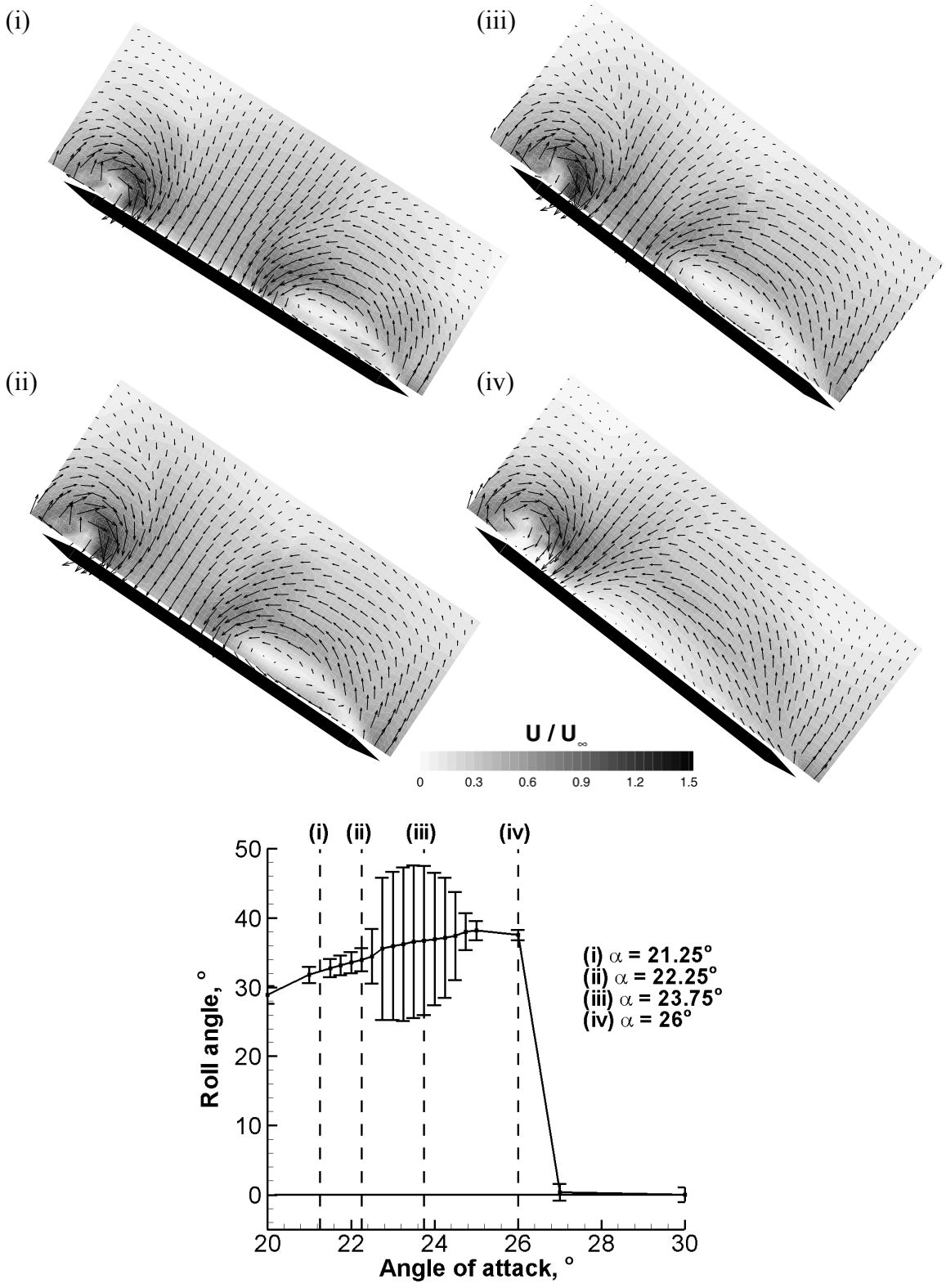

Figure 4.5 Cross-flow time-averaged velocity fields for stationary delta wing and graph of mean roll angle with standard deviation as error bars against angle of attack corresponding to images, with (i) at α=21.25° and Φ=32°; (ii) at α = 22.25° and Φ = 34°; (iii) at α = 23.75° and Φ = 37° and (iv) at α = 26° and Φ = 38°, for thin wing with Λ = 55° at x/c = 0.25.

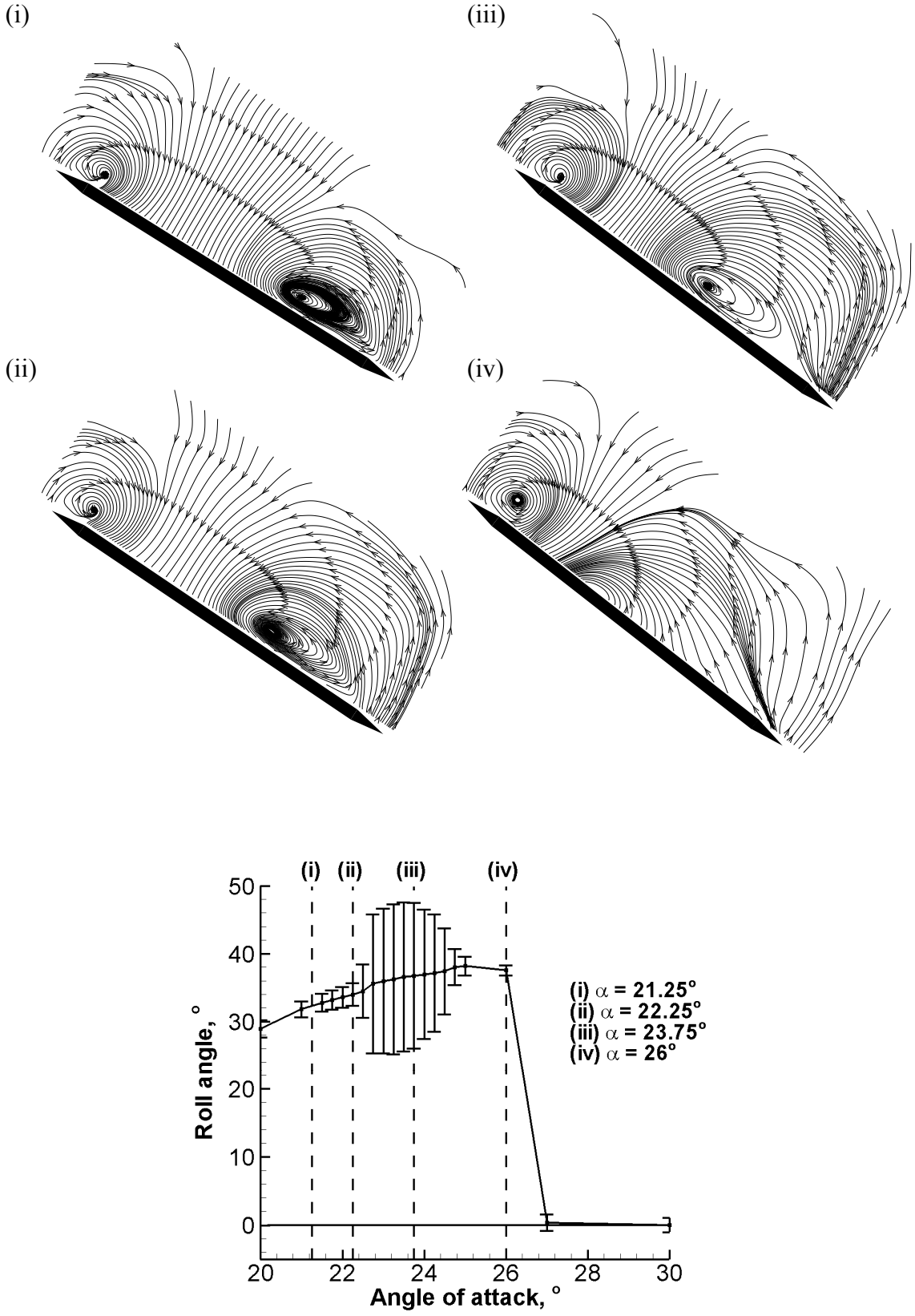

Figure 4.6 Cross-flow time-averaged streamline patterns for stationary delta wing, and graph of mean roll angle with standard deviation as error bars against angle of attack corresponding to images, with (i) at $\alpha = 21.25^{o}$ and $\Phi = 32^{o}$; (ii) at $\alpha = 22.25^{o}$ and $\Phi = 34^{o}$; (iii) at $\alpha = 23.75^{o}$ and $\Phi = 37^{o}$ and (iv) at $\alpha = 26^{o}$ and $\Phi = 38^{o}$ for wing with $\Lambda = 55^{o}$ and sharp leading-edges at x/c = 0.25.

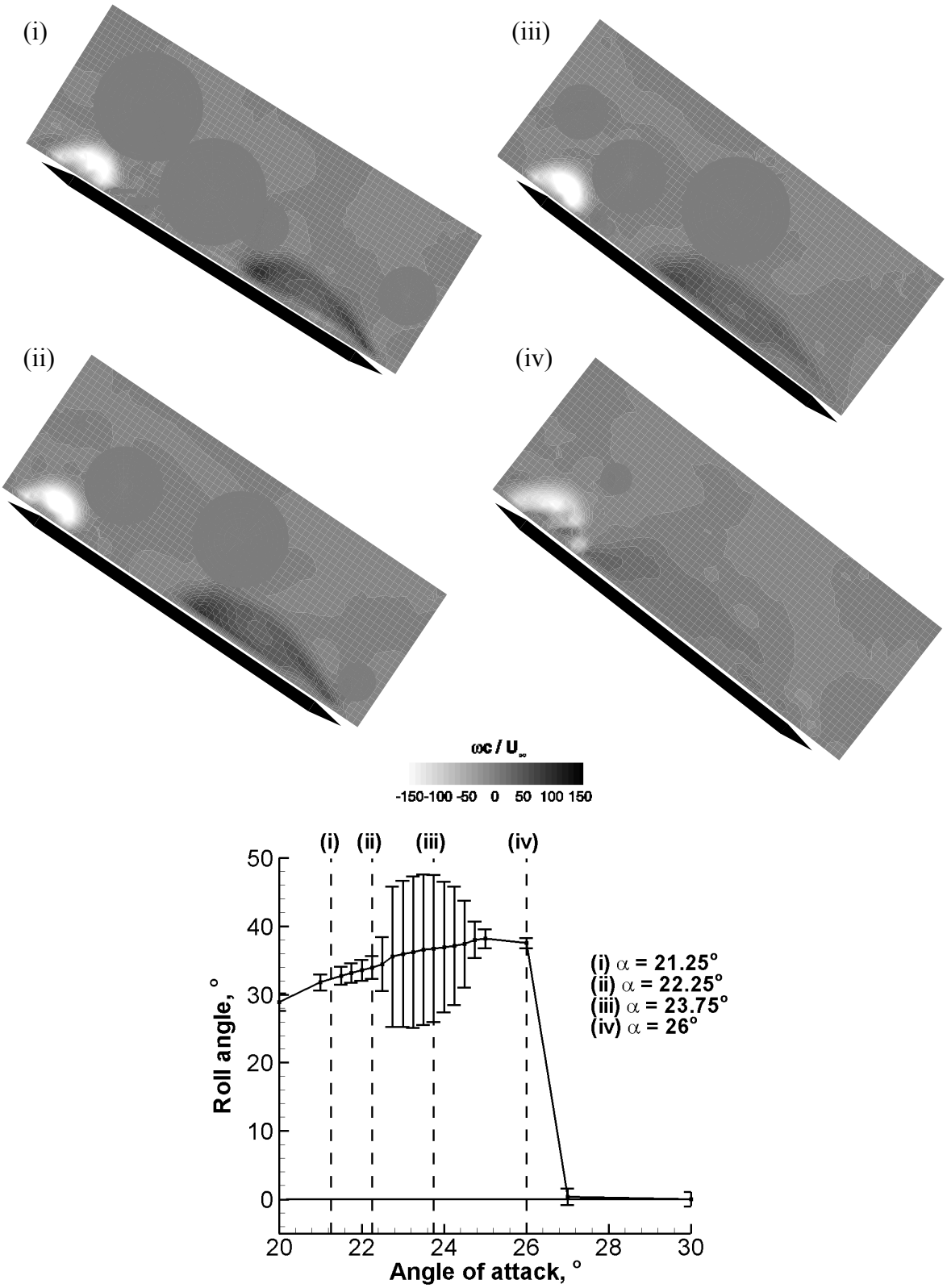

Figure 4.7 Cross-flow time-averaged vorticity patterns for stationary delta wing and graph of mean roll angle with standard deviation as error bars against angle of attack corresponding to images, with (i) at $\alpha = 21.25^{o}$ and $\Phi = 32^{o}$; (ii) at $\alpha = 22.25^{o}$ and $\Phi = 34^{o}$; (iii) at $\alpha = 23.75^{o}$ and $\Phi = 37^{o}$ and (iv) at $\alpha = 26^{o}$ and $\Phi = 38^{o}$ for wing with $\Lambda = 55^{o}$ and sharp leading-edges at x/c = 0.25.

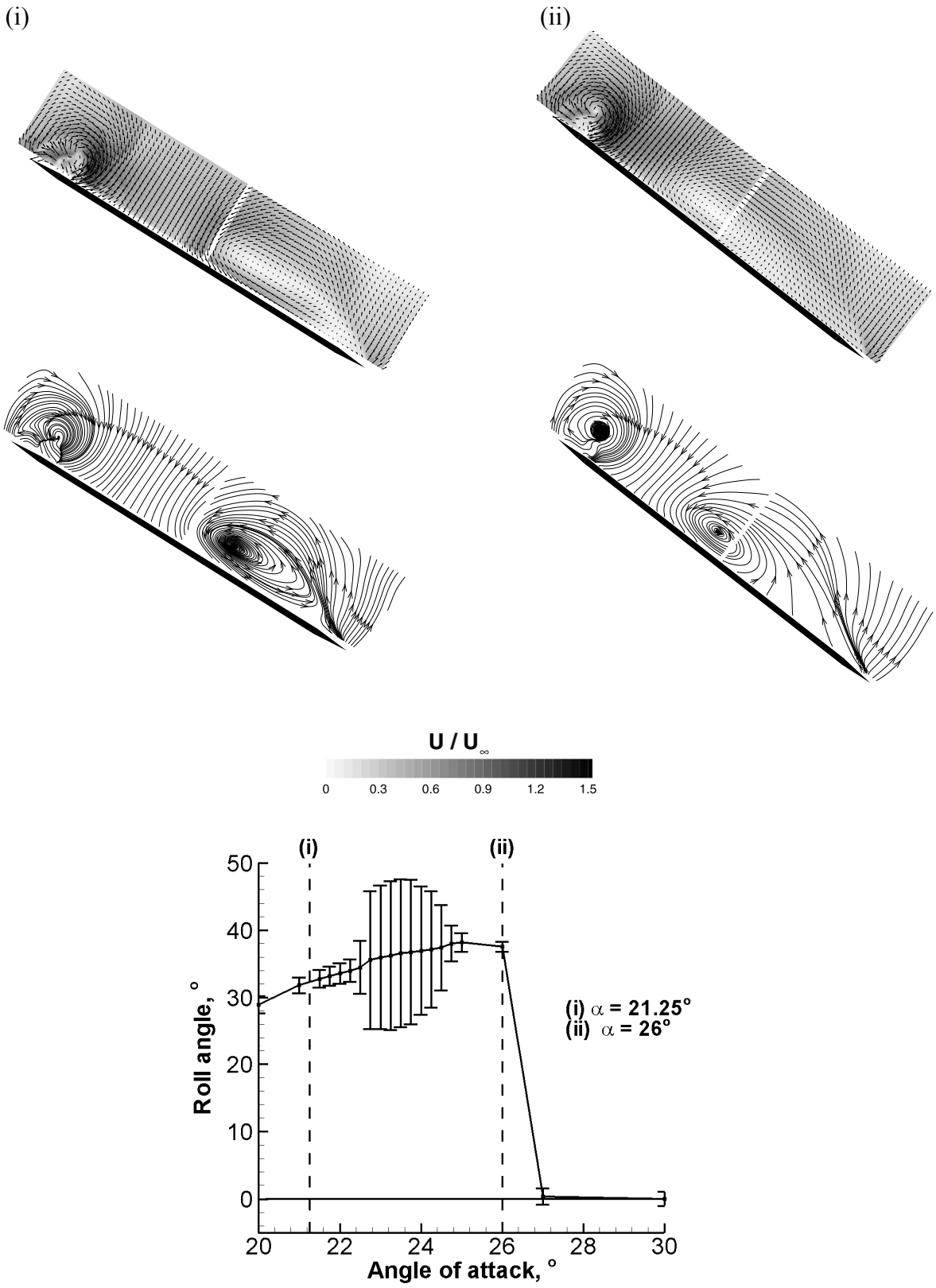

Figure 4.8 Cross-flow time-averaged velocity fields (top) and streamline patterns (bottom) on stationary wing together with graph of mean roll angle with standard deviation as error bars against angle of attack corresponding to images, with (i) at $\alpha = 21.25^{o}$ and $\Phi = 32^{o}$ and (ii) at $\alpha = 26^{o}$ and $\Phi = 38^{o}$ for delta wing with $\Lambda = 55^{o}$ and sharp leading-edges at x/c = 0.5.

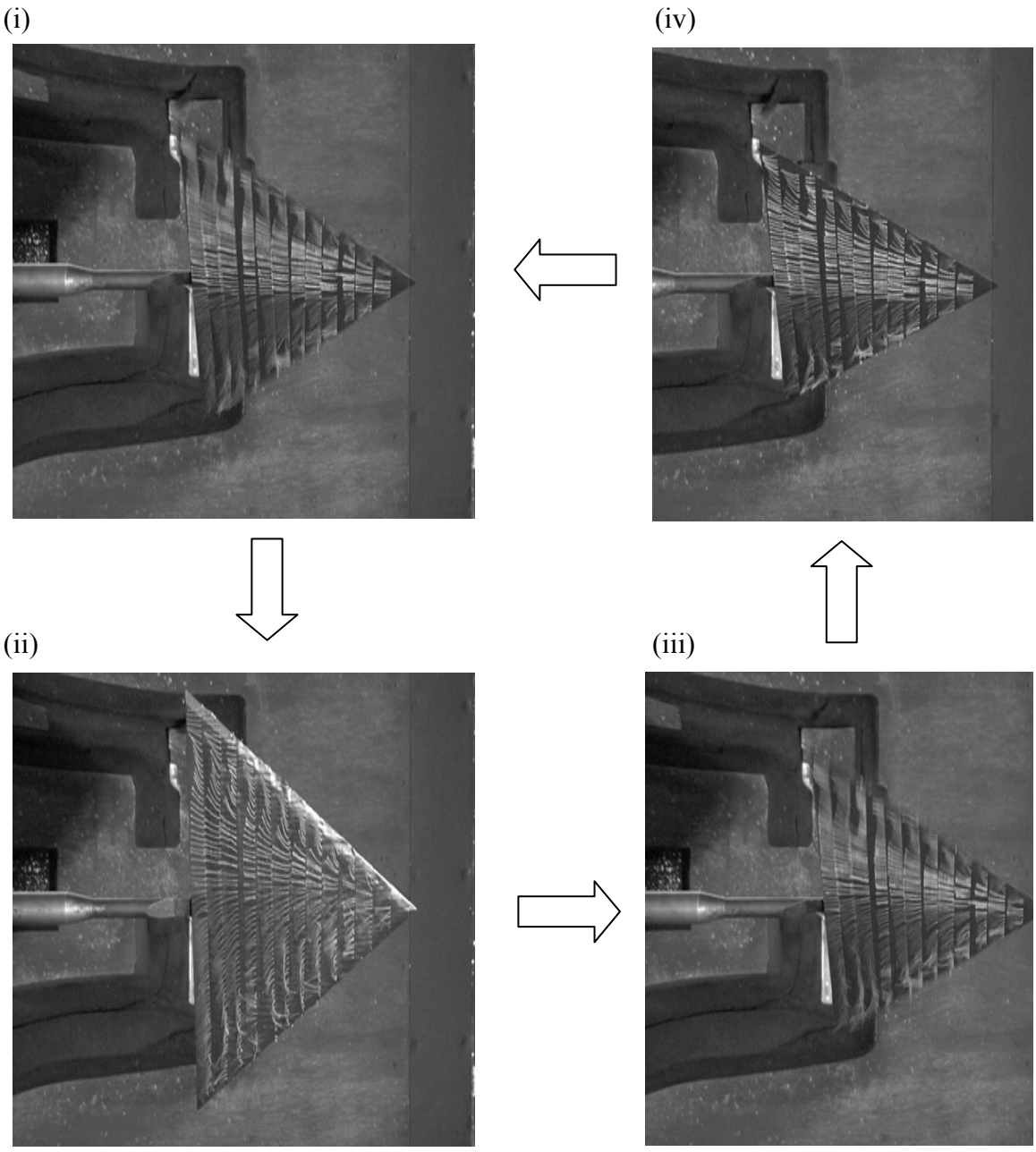

Figure 4.9 Tuft visualisation of rolling delta wing at (i) Φ_{mean} with Φ decreasing; (ii) Φ_{min}; (iii) Φ_{mean} with Φ increasing and (iv) Φ_{max} for delta wing with $\Lambda = 55^{o}$ and sharp leading-edges at $\alpha = 23.75^{o}$.

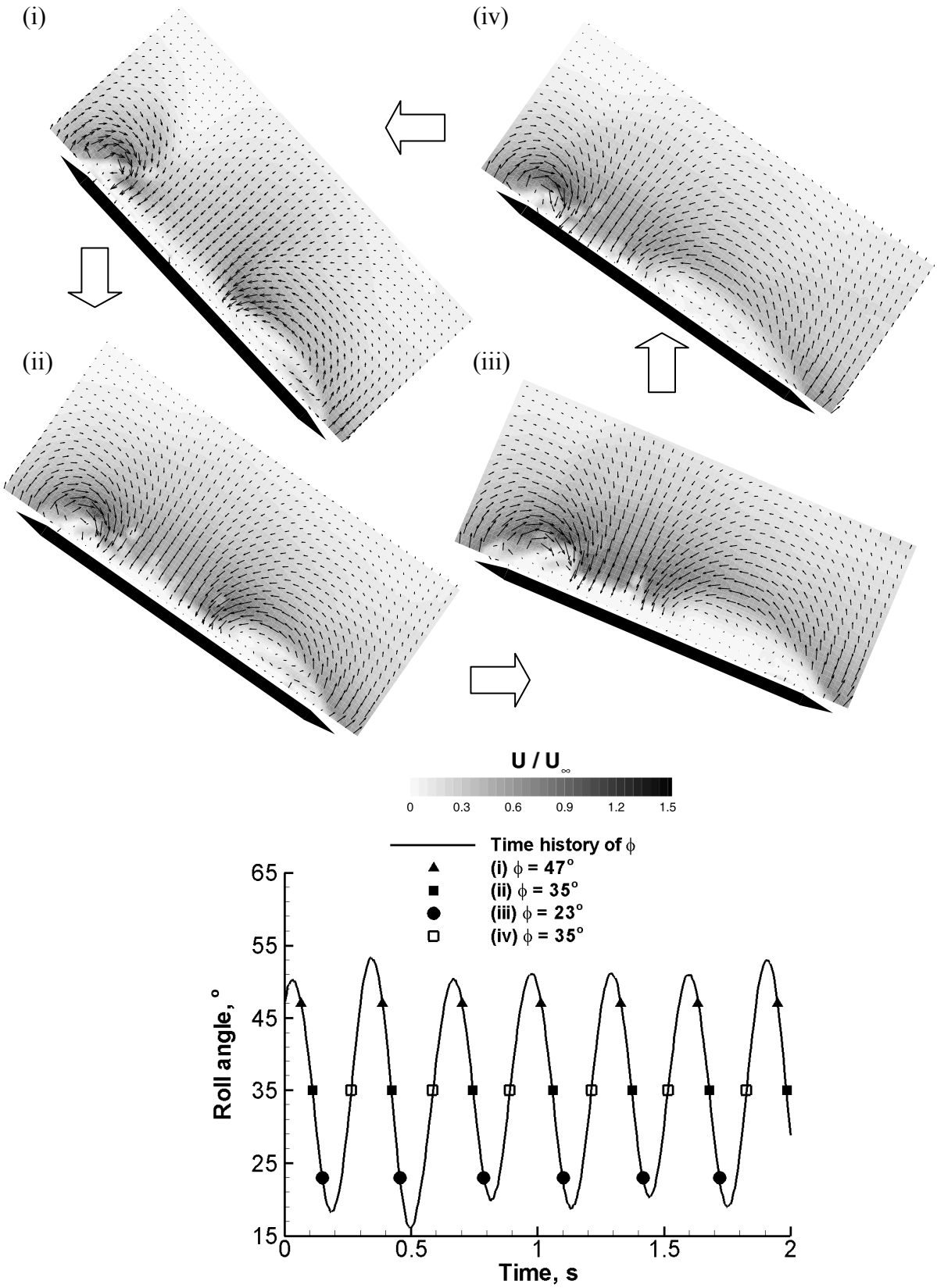

Figure 4.10 Phase-averaged velocity fields on rolling delta wing and timing diagram corresponding to images, with (i) at $\Phi = 47^{o}$; (ii) at $\Phi = 35^{o}$; (iii) at $\Phi = 23^{o}$ and (iv) at $\Phi = 35^{o}$ for wing with $\Lambda = 55^{o}$ and sharp leading-edges at x/c = 0.25 and $\alpha = 23.75^{o}$.

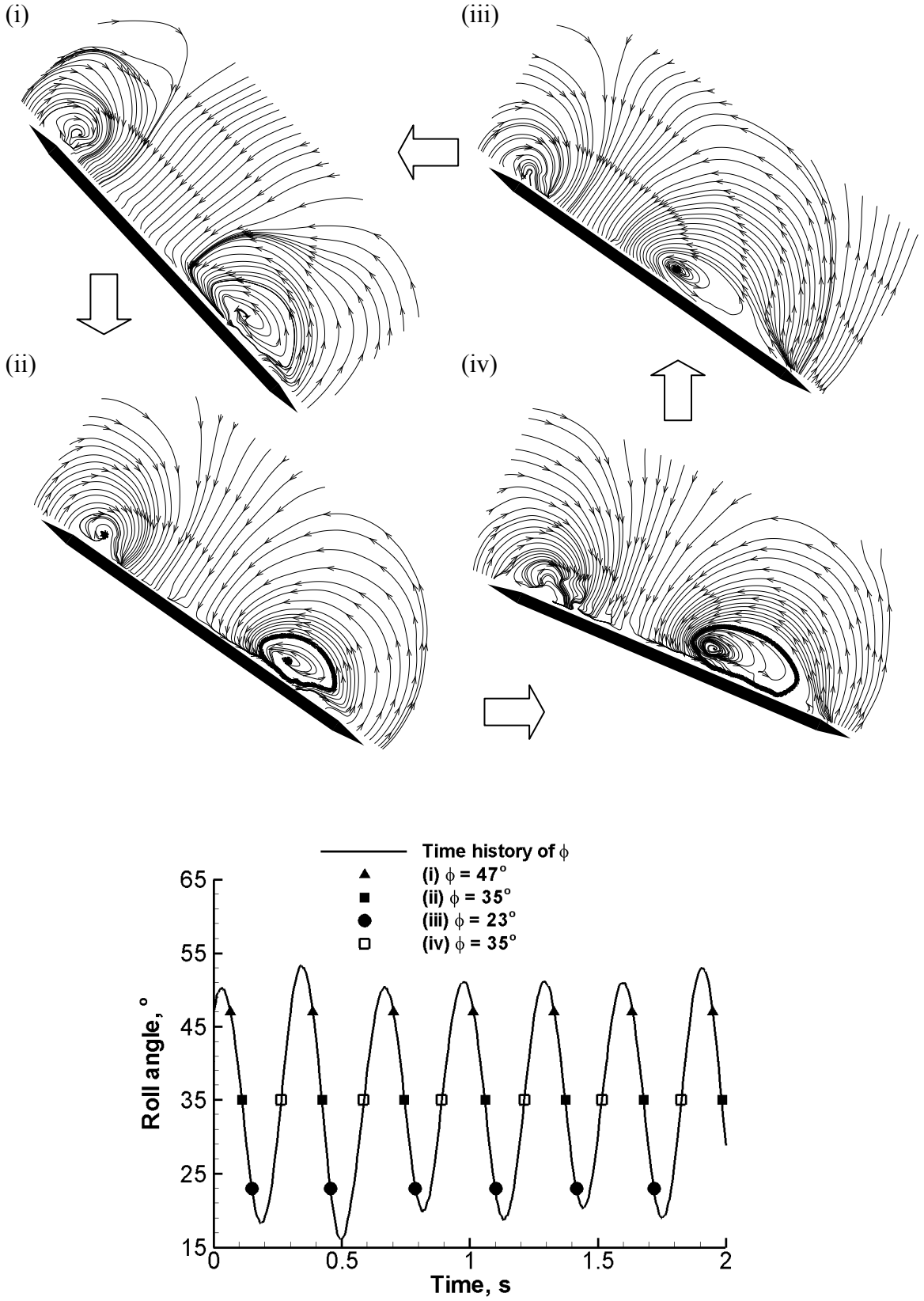

Figure 4.11 Phase-averaged streamline patterns on rolling delta wing and timing diagram corresponding to images, with (i) at $\Phi = 47^{o}$; (ii) at $\Phi = 35^{o}$; (iii) at $\Phi = 23^{o}$ and (iv) at $\Phi = 35^{o}$ for wing with $\Lambda = 55^{o}$ and sharp leading-edges at x/c = 0.25 and $\alpha = 23.75^{o}$.

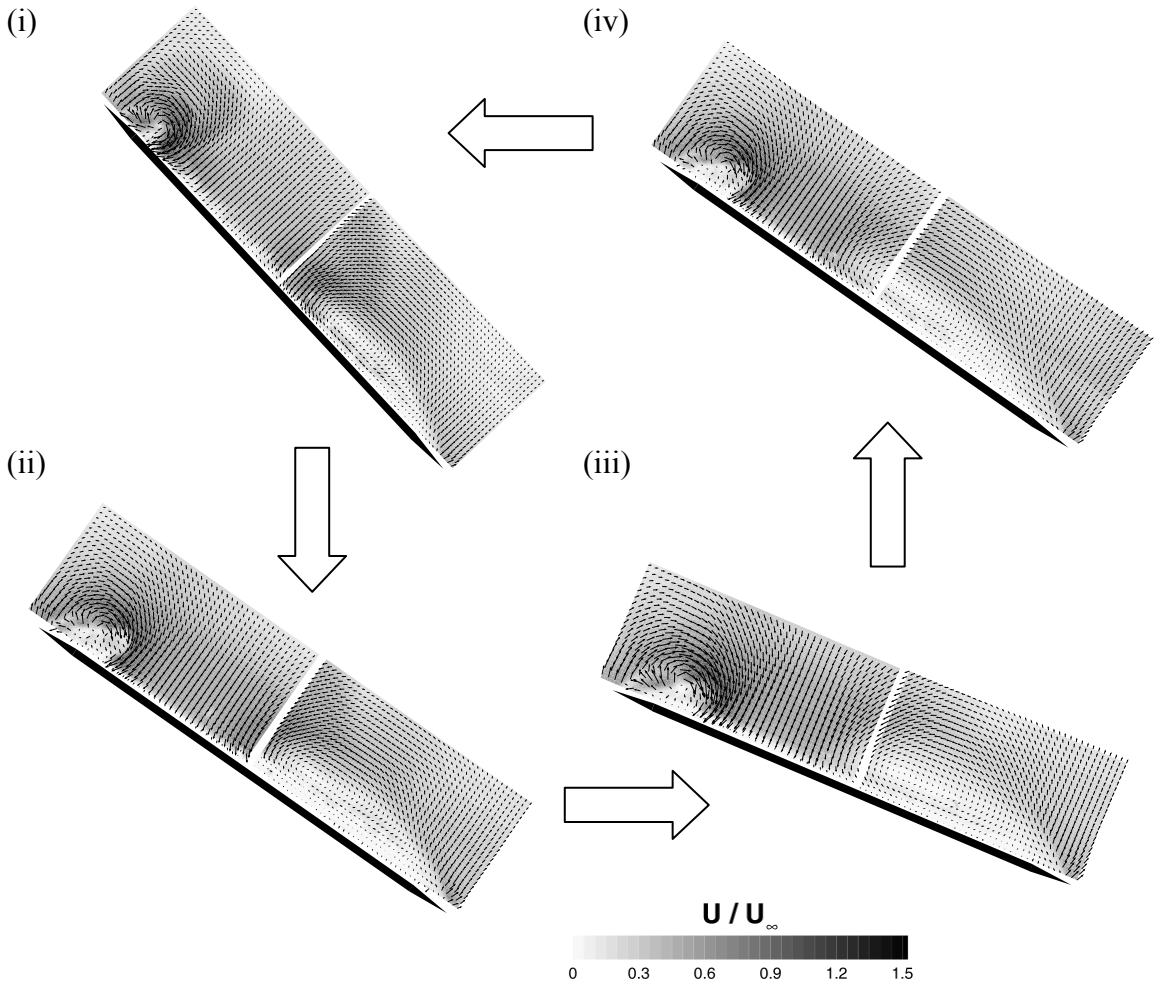

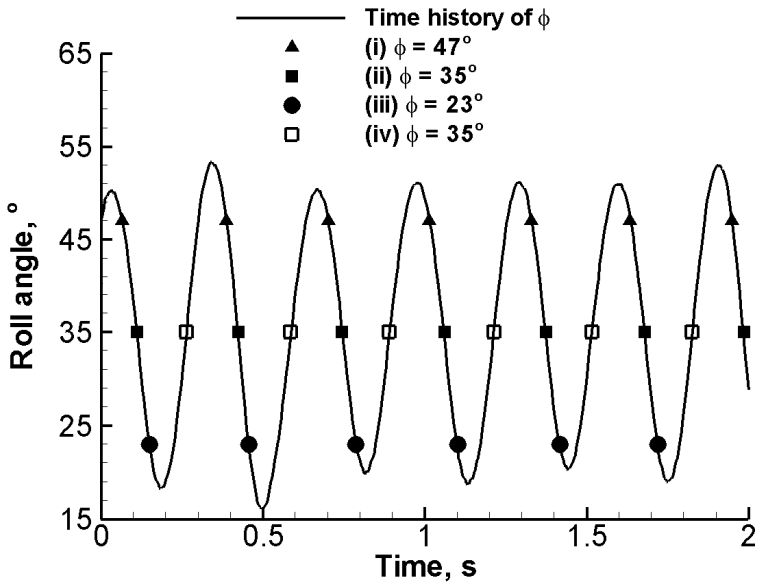

Figure 4.12 Phase-averaged velocity fields on rolling delta wing and timing diagram corresponding to images, with (i) at $\Phi = 47^{o}$; (ii) at $\Phi = 35^{o}$; (iii) at $\Phi = 23^{o}$ and (iv) at $\Phi = 35^{o}$ for wing with $\Lambda = 55^{o}$ and sharp leading-edges at x/c = 0.5 and $\alpha = 23.75^{o}$.

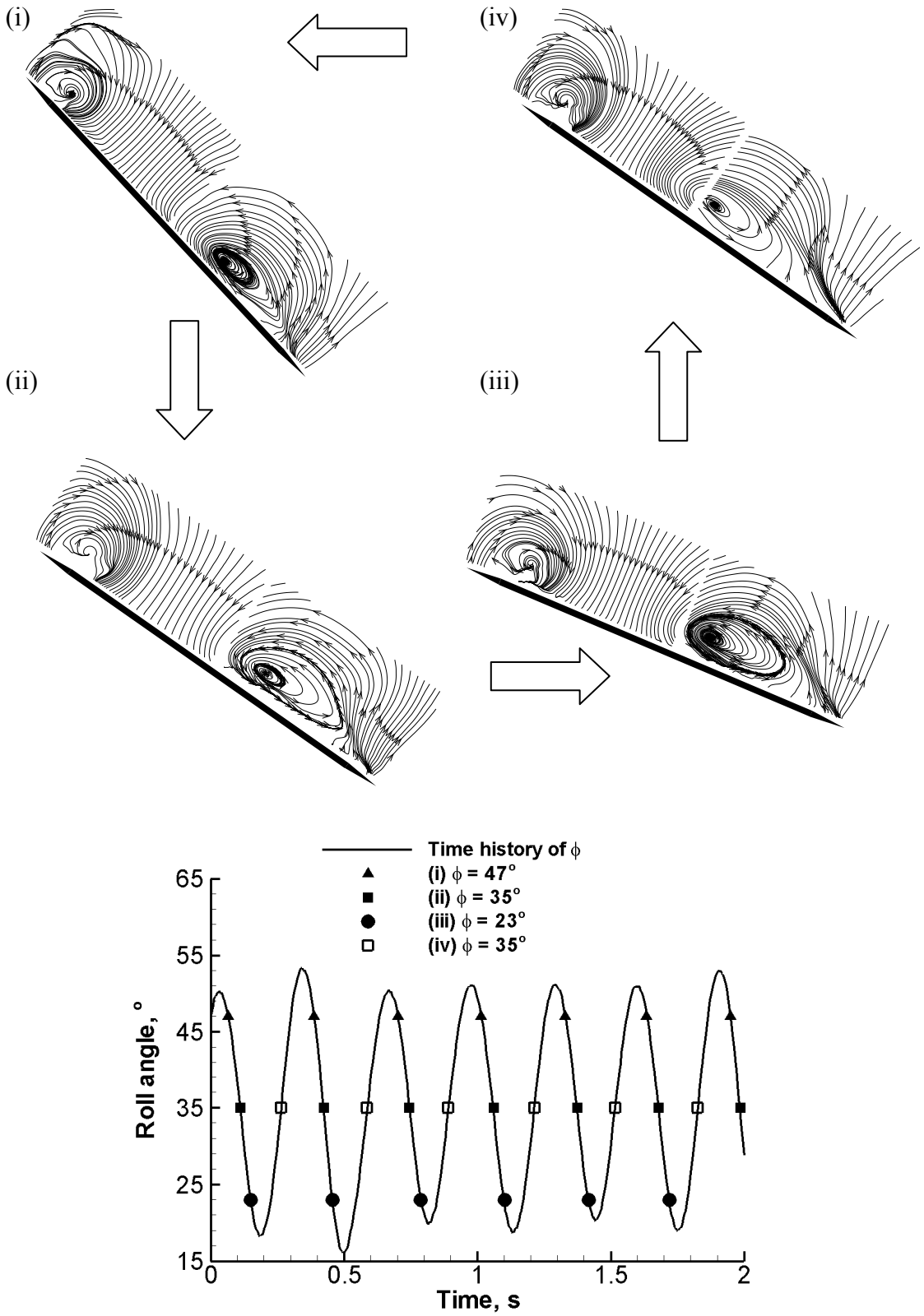

Figure 4.13 Phase-averaged streamline patterns on rolling delta wing and timing diagram corresponding to images, with (i) at $\Phi = 47^{o}$; (ii) at $\Phi = 35^{o}$; (iii) at $\Phi = 23^{o}$ and (iv) at $\Phi = 35^{o}$ for wing with $\Lambda = 55^{o}$ and sharp leading-edges at x/c = 0.5 and $\alpha = 23.75^{o}$.

Chapter 5 Slender Delta Wings

The results for the 55° delta wing are presented in Chapter 4 because, although slender wings are classed as $\Lambda \geq 55^{o}$, the sudden stalling characteristics led it to be classed as non-slender for this Thesis.

5.1 Slender delta wing behaviour

The left-hand side of Fig. 5.1 shows how the mean roll angle varied with angle of attack for wings with sweep of 57.5° and above, again with error bars showing the standard deviation of the roll time history.

It was found that the stalling of the wings was delayed with increasing sweep angle and that all the wings experienced an increasing non-zero mean roll angle with increasing angle of attack up to and just beyond the peak oscillations. It can be observed that the mean roll angle reduced to zero much more gradually with increasing angle of attack than with the lower sweep angled wings (Chapter 4). In Figs. 5.1a) and b), corresponding to delta wings with sweep of 57.5° and 60° respectively, a region with large self-excited oscillations can again be seen just before the mean roll angle started decreasing, suggesting they might be caused by the same mechanism as in the sudden stall/non-slender delta wing case. These oscillations die away with increasing angle of attack, before an interesting second region of high standard deviation, after which the wing becomes fully stalled. This second region will be discussed further later in this Chapter. The mean roll angles of the 60° and 65° sweep wing at $\alpha = 30^{o}$ in this case were both 18°, while literature[24,30] found slightly larger trim angles at the same angle of attack, with $\Phi_{mean} = 21^{o}$ for both sweep angles. This may be due to different Reynolds numbers, or more likely different levels of friction in the free-to-roll devices as this was found to be important to the wing behaviour; slight friction could prevent roll oscillations. Increasing the sweep angle further, as shown in Figs. 5.1c) and d) ($\Lambda = 65^{o}$ and 70° respectively), led to the roll oscillations stopping and the maximum mean roll angle reducing. The characteristics of the first region of oscillations for the 57.5° and 60° delta wings were similar to the thick, 50°, 52.5° and 55° delta wings' oscillations. Differing amplitude of the oscillations were observed and seen to die away with increasing sweep angle.

5.2 Effect of sweep angle

The variation of mean roll angle is plotted against sweep angle in Fig. 5.2a) and the standard deviation of roll angle has been plotted against sweep angle in Fig. 5.2b). The maximum mean roll angle of the wings was found for $\Lambda = 50^o$ and was seen to reduce with Λ increasing or decreasing. A peak standard deviation was seen for a wing of 57.5^o sweep angle, with again the maximum standard deviation reducing with increasing or decreasing sweep angle. This is presumably the case with the best comparison between side-edge vortices strengths and reattachment on the wing surface, which is known to be unstable[45]. Figure 5.3 shows how the Strouhal number of the wings with large oscillations varied with angle of attack. Slight increases in St were seen with increasing angle of attack as is known to occur for slender wing rock[34]. Note that the oscillations have St ~ $O(10^{-2})$, thus these oscillations fall in the region of aerodynamic manoeuvres.

5.3 First region of oscillations

Figures 5.4 - 5.6 show cross-flow velocity fields, streamline and vorticity patterns at x/c = 0.25 for the stationary 60^o sweep delta wing. For (i), which is before the oscillations commence, the reattachment points of both shear layers were separated with two distinct areas of higher velocity close to the wing surface signifying these points in Fig. 5.4(i). It is worth pointing out that in Fig. 5.5(ii), the leeward shear layer appears to be closer to the wing surface. This will be returned to in other cases, but for now it is significant to note that this leeward shear layer is about to stall. As the angle of attack was increased to 25.5^o in (ii), the reattachment points appeared to be very close (Fig. 5.6). Finally, at (iii), which corresponds to the largest standard deviation, the leeward shear layer now appears to be stalled, with definite interaction between the shear layers, shown in Fig. 5.5. This is slightly different to what was observed over the 55^o sweep delta wing (Chapter 4) and can be attributed to the larger sweep angle.

Looking at the dynamic cases it can be seen from Fig. 5.7 what is occurring in images, triggered by the oscillations of the wing itself as in Fig. 4.9 (images captured for the moving wing). As for the 55^o sweep delta wing, the area of reattached flow forming the leeward (bottom) shear layer is small at (ii) and (iii), with reversed flow visible at (iii) suggesting that the corresponding wing half is stalled. The area of reattached flow

is seen to increase for (iv), which corresponds to Φ_{max}, and is still large at Φ_{mean} with Φ increasing in (i). This observation is similar to those for the 55^o sweep delta wing. The time delay is again highlighted here, with different flow structures evident in (i) and (iii); though the roll angles and angle of attack are the same. The movement of the wing leads to delays in the flow structure, which undoubtedly causes the oscillations in a similar manner to the 55^o sweep delta wing.

Figures 5.8 - 5.11 present the phase-averaged cross-flow velocity fields (similar to Chapter 4) for the 60^o sweep delta wing at x/c = 0.25 (Figs. 5.8 and 5.9) and x/c = 0.5 (Figs. 5.10 and 5.11) and α = 26.5^o. Again, in Fig. 5.9, it is evident that the leeward shear layer is close to the wing surface at (iv) (α = 28^o), which suggests the shear layer is about to stall. This proximity of the shear layer to the wing surface is again evident in Fig. 5.11, though not as obvious in position (iv) as at x/c = 0.25. At (i) in Figs. 5.8 and 5.10, near the maximum roll angle, the reattachment points are separated, with distinct areas of high velocity showing the reattachment points of either shear layer. It can also be seen from Figs. 5.8 - 5.11 that the windward vortex was compact in this case and the same theme of flow structure is carried on down the wing, with no significant differences. As the roll angle decreased to the mean value in (ii), the leeward shear layer reattachment point is seen to move closer to the windward reattachment point. It moves closer still at (iii), which is near the minimum roll angle achieved during the motion. However, at the mean roll angle with roll angle increasing, the leeward shear layer stalls (Fig. 5.8), suggesting that a time lag exists between the minimum roll angle and wing stall. The wing recovers from this stall, and the leeward shear layer reattaches before point (v) and again a time lag exists, shown by a slightly different flow structure here to at point (i).

According to equations (1) and (2), for α = 26.5^o and Φ = 39^o, Λ_{eff} = 77.4^o and α_{eff} = 21.2^o, which would place vortex breakdown beyond the trailing-edge, while at Φ = 17^o, values of Λ_{eff} = 68.3^o and α_{eff} = 25.5^o would place vortex breakdown on the wing surface in the static case, which this may correspond to due to the low Strouhal number of these oscillations. This appears to be the case in all the delta wings cases. For the leeward wing half breakdown is expected to be at the apex and none on the other wing half from the effective angles calculated in Table 4.1. This suggests that at the minimum roll angle for the 55^o sweep delta wing and the 60^o sweep delta wing vortex breakdown may

be on the wing surface and this may damp the motion, though no conclusions can be drawn without further experimental data.

5.4 Possible mechanism of oscillations

Based on the evidence from this Chapter, the oscillations seem to be similar in mechanism to those in Chapter 4, regardless of the sweep angle. To clarify, the oscillations may be initiated by the increasing proximity of the shear layers as the angle of attack is increased for the thick and 50^o to 60^o sweep delta wings. Separation points are fixed for these sharp leading–edged wings. In all cases as the roll angle increases through the mean roll angle there appears to be interaction between the windward and leeward shear layers, with the leeward wing half appearing to be stalled in Figs. 5.8 and 5.10. At Φ_{min} the shear layer reattachment points move close together and the subsequent motion is driven by the stronger windward (or left-hand side in the cross-flow plane) vortex generating lift. This may be caused by the high value of α_{eff} at this roll angle. In all cases, a compact windward vortex is present near Φ_{max}, while higher velocities associated with the windward vortex are present at Φ_{min}. As Φ increases, the windward vortex becomes more compact, possibly caused by decreasing α_{eff} and increasing $\Lambda_{eff.}$ At Φ_{max} the early reattachment of the right-hand shear layer indicates that the area of reattached flow is larger and this, together with the compact left-hand vortex, may damp the motion. Vortex breakdown, which is known to damp slender wing rock, is present at Φ_{min} though the effect of the time lag is not known in this case. The presence of the leeward vortex close to the wing surface generates more lift than the compact windward vortex and provides a restoring moment, which drives the wing in the other direction. The reattachment point of the leeward shear layer moves away from the reattachment point of the windward shear layer and the vortex also gets closer to the wing surface and hence has more of an effect. The wing approaches Φ_{min} and the sequence starts again.

5.5 Different modes of oscillations

Upon closer scrutiny of the left-hand side of Fig. 5.1a) and b), a second region of high standard deviation is seen to exist at high angles of attack for the 57.5^o and 60^o sweep delta wings. This is different to the region suggested[9], where a slender delta wing

of $\Lambda = 85^o$ undergoes unsteadiness at high roll angles. In the slender wing case, there is no regularity to the oscillations, while there is here. Interestingly, Fig. 5.12 shows differing behaviour of the 57.5^o sweep delta wing, with it flipping between roll angles at angles of attack well below the expected stall condition. As this was not seen for any of the other wings it was not investigated further, but as the literature for non-slender wings suggests, it does show the existence of other critical states[32], this time for a slender delta wing.

Figure 5.13 shows the behaviour of the 57.5^o sweep delta wing through various angles of a attack in the second region of oscillations. Initially, at $\alpha = 29^o$, large oscillations are seen for this planform, and are shown in the Figure on the left of Fig. 5.1a). Upon increasing the angle of attack, the oscillations are seen to make the wing flip between positive and negative states; the oscillations themselves presumably causing this. This frequency of flipping between positive and negative states is seen to become more frequent with increasing angle of attack, as shown in Fig. 5.13c)

Figure 5.14a) shows a roll angle time history of the 60^o sweep delta wing in this region at $\alpha = 33^o$ in a similar manner to those for the 57.5^o sweep delta wing (Fig. 5.13). Self-excited oscillations are seen to develop, again about a non-zero mean roll angle with a low Strouhal number of 0.031. When the angle of attack was increased to 35^o (Fig. 5.14b)), the wing is seen to flip occasionally between two mirror images of mean roll angle. This flipping between states is what causes the peak in the standard deviation, though the oscillations alone at $\alpha = 33^o$ have a reasonably high standard deviation of around 4^o, which is why PIV tests were performed at this angle of attack. This flipping increased in frequency as the angle of attack was increased further (Fig. 5.1b)) and the mirror image mean roll angles become closer to zero until the wing was fully stalled.

Now, looking at the increase of angle of attack shown in Fig. 5.15 for the 60^o sweep wing, it can be seen that, perhaps surprisingly, the leeward (right-hand) shear layer is seen to be stalled at (i) and (ii), while there seems to be vortices in (iii) and (iv). This is confirmed in Fig. 5.16, with vortical structures evident at (iii) and (iv), but not at the other two angles of attack. Based on previous work, these two points ($\alpha = 33.5^o$ in (iii) and $\alpha = 34.75^o$ in (iv)) are just before the shear layer stalls, which fits with the

explanations. Basically put, when the oscillations are occurring, the shear layers are separate, while they meet when stable and at different effective angles. The oscillations themselves do have some similarities to non-slender delta wing roll oscillations as they occur about a non-zero roll angle and the windward (left-hand) shear layer does not appear to move. The vorticity shown in Fig. 5.17 confirms the lack of interaction between the shear layers at (iii) and (iv).

If one looks at the near-surface PIV measurements for the 60^o sweep delta wing for an unstable roll angle (left-hand side of Fig. 5.18), and a stable roll angle (right-hand side of Fig. 5.18), it can be seen that in the unstable case there are two separated vortices present. However, for the stable case, it can be seen how the lower shear layer has stalled completely with reversed flow evident and a vortex is only present on the upper wing-half. The right-hand velocity plot shows a 3D vortex and the core can be seen. Similarities can be drawn to the data in Chapter 4 here, as the reattachment of the separated vortices appears unstable.

Now, going on to look at the oscillations themselves in this region, video evidence can be seen in Fig. 5.19. Stalled, reversed flow is again evident in all cases, but it can be seen that at Φ_{min} (in position (ii)) there are two vortices present, as the PIV data in Fig. 5.21 suggests, while at Φ_{max} (in position (iv)) the lower wing-half is stalled as reversed flow is evident. The attachment process again drives the motion rather than for usual slender delta wing rock, when the side-edge vortices are seen to move the wing as in Fig. 1.10.

Figures 5.20 - 5.23 show the phase-locked velocity fields and streamline patterns near Φ_{mean} at (i) and (iii), Φ_{min} at (ii) and Φ_{max} at (iv). At (i) and (iv) it can be seen from Fig. 5.20 that there is interaction between the reattachment points of the vortices near Φ_{mean} with Φ increasing and Φ_{max}. Another point to note from the velocity plots in Fig. 5.20 and 5.22 is the comparative size of the windward vortices. To get an idea of the air flow over the wing surface, it is worth considering the movement of the leeward shear layers in Fig. 5.21. At position (ii), the leeward vortex appears close the wing surface so just about to stall, while at (iii) normal airflow has been resumed. It is much larger near Φ_{min}, shown in Fig. 5.22, suggesting possible vortex breakdown, though further work needs to be done to confirm this. The streamlines in Fig. 5.23 show the interaction

between the shear layers near Φ_{max} and x/c = 0.5, and also the formation of a leeward vortex at x/c = 0.5. Again, the proximity of the leeward shear layer to the wing surface is highlighted as evidence of a wing half about to stall fully. Near Φ_{min}, the presence of vortices on both wing halves at both stations is seen, as is the area of reattachment. It is also interesting to note that the leeward vortex is further from the wing surface at x/c = 0.5 for Φ_{min} than at Φ_{max}. It is worth noting that the changing of reattachment location in this region of oscillations seems to be out of phase with the first region. There appears to be reattachment at Φ_{min} and stalled leeward flow at Φ_{max}, while in the first region of oscillations, the larger area of reattached flow was evident at Φ_{max} and stalled leeward flow was found at Φ_{min}.

For the case of the 60^o sweep delta wing around the second standard deviation peak, the data in Fig. 5.20 suggests that at Φ_{min} ($\Phi = 0^o$) both windward and leeward shear layers form large vortical structures, with a distinct area of reattached flow, shown in Fig. 5.21. There is an asymmetry in strength of the vortices with the windward vortex being slightly stronger because of a time lag, and this creates more lift on the corresponding wing half, causing the wing to rotate. The formation of a leeward vortical structure close to the wing surface, as shown in Fig. 5.23 at x/c = 0.5, creates the lift on the corresponding wing half, with the value being greater than the lift created by the compact windward vortex.

In summary, the streamlines (Fig. 5.21) confirm the interaction between the shear layers near Φ_{max} at (iv) and x/c = 0.25 and also the formation of a leeward vortex at x/c = 0.5 in Fig. 5.23, which highlights the wing not being stalled. Near Φ_{min} the presence of vortices on both wing halves at both maximum and minimum stations is confirmed, as is the area of reattachment. It is also interesting to note that the leeward vortex is further from the wing surface at x/c = 0.5 for Φ_{min} than at Φ_{max}. There appears to be reattachment at Φ_{min}, evident from Fig. 5.19, and stalled leeward flow at Φ_{max}, while in the first region of oscillations, the larger area of reattached flow was evident at Φ_{max} and stalled leeward flow was found at Φ_{min}. The evidence suggests that the whole wing stalls at Φ_{max}, which makes the wing rotate to its stalled position at $\Phi_{min} = 0^o$, where the vortices re-form. This is shown in Fig. 5.19 (ii). A slight time lag means again the wing rotates until it is fully stalled again, at position (iv) (Φ_{max}), though this suggests that the attaching of the shear layer is opposite to what has been seen at early

angles of attack, so conclusions of this motion are difficult to draw. Going on to look at α_{eff} and Λ_{eff}, the results are shown in Table 4.1 and by using Fig. 1.3, it can be seen that at $\alpha = 0^o$, vortex breakdown is beyond the trailing-edge due to the high α_{eff}. However at $\alpha = 10^o$, $\Lambda_{eff} = 66.4^o$, which means that vortex breakdown is expected on the wing surface, towards the trailing-edge at $\alpha_{eff} = 32.6^o$. Perhaps this leads to the instability necessary to drive the motion.

The data is plotted in Fig. 5.24 to show the contours of a) mean and b) standard deviation of roll angle at different angles of attack and sweep angles for the pure delta wings. Dashed lines are also drawn showing how the stall angle and vortex breakdown position change[45]. From Fig. 5.24a) it can be seen that a region of higher mean roll angle (darker contours) exists where the roll oscillations happen. For slender delta wing rock the mean roll angles would be zero. The mean roll angle increases slightly before the wing stalls.

5.6 Free-to-roll behaviour – cropped delta wings

It is worth noting that these cropped wings are considered slender because of their relatively high root chord. Figure 5.25a) shows how the mean roll angle, with standard deviation of roll angles as error bars, varies with angle of attack, as previously seen for other wings in Fig. 4.4. From Fig. 5.25a), it can be seen that the 40^o sweep cropped delta wing (wing 22 in Table 2.1) does not oscillate in roll, as is to be expected from the non-slender delta wing data in Fig. 4.4a). Figure 5.25b) shows the free-to-roll time history of this wing and there are no free-to-roll oscillations whatsoever, even at this highest standard deviation achieved (just before stall, known to be unsteady). The mean roll angles were generally less than for the pure delta wing, as will be seen for the 55^o sweep delta wing. Hence cropping the delta wing, despite having the same span, does not make the wing perform any more insignificantly apart from stalling slightly earlier.

Figures 5.26 – 5.31 present data for various cropped delta wings all with the same span (wings 19 – 21 in Table 2.1). It can be seen from Fig. 5.26 that increasing the cropped proportion of the wing leads to the maximum mean roll angle reducing as well as more gradual stalling characteristics. The oscillations present for the pure delta wing

in Fig.5.26a) are larger in amplitude and occur at higher angle of attack than for the wing in Fig. 5.26b) and these oscillations are not present for the other two cropped wings (Figs. 5.26c) and d)). It appears that the cropped section can prevent the wing attaining the necessary mean roll angle to initiate oscillations, with the wings in c) and d) not going to a mean roll angles above 5^o.

Figure 5.27 confirms what is shown by the mean roll angles plots in Fig. 5.26, with oscillations not present in Fig. 5.27c) and d) but present for the delta and shorter cropped wing in Figs. 5.27a) and b); all wings at the highest standard deviation achieved in the free-to-roll tests. The effect of cropping on the oscillations can be seen from Fig. 5.27a) and b), with even a small cropped section leading to fewer, and increasing the cropped length further means no oscillations. Interestingly the mean roll angle is seen to decrease for each case, creating stability.

Moving on to look at the cause of the oscillations in a stationary cross-flow plane, Fig. 5.28 shows the cross-flow velocity fields in two planes for the delta wing with $\Lambda = 55^o$. The trim angle being non-zero is why one plane at an angle across the wing; this plane was chosen because it was the maximum chordwise distance which still covered the wing extent i.e. it went through the corner of the wing and did not take in the trailing-edge. Circulations calculations on the 55^o sweep wing at $\alpha = 20^o$ and $\Phi = 0^o$ suggest that the circulation is similar on both wing halves, with the left-hand vortex having $\Gamma/cU_\infty = -0.60$, while the right hand vortex shows $\Gamma/cU_\infty = 0.61$. This similarity shows there is instability of the shear layer attachment present to cause the non-zero roll angles, shown in Fig. 4.4e). From Fig. 5.28, it can be seen that the trim angle is probably caused by the large leeward and compact windward vortices. The lift from both wing halves must be the same, thus the compact vortex must be strong, and the leeward vortex is large to cope with the low velocities associated with it (inducing weakness). At the same angle of attack, $\alpha = 20^o$, data was obtained for the stationary cropped wing, the time history of which is shown in Fig. 5.27c) at the maximum standard deviation and shown in Fig. 5.29. This was found to be a trim angle despite the similarities in the flow structure to the $\Lambda = 55^o$ pure delta wing (data shown in Fig. 5.28 at the trailing-edge) at x/c = 39.5 %. This must mean that the rear portion of the wing now provides this stability, presumably due to the cropped section, as the front portion of the cropped delta wing showed similarities in the flow to the pure delta wing.

From Figs. 5.29b), it can be seen that the vortices are now far from the wing surface and diffuse (thus have less of an effect) and must damp the wings' roll movement, which is accentuated by increasing the cropped portion. This leads to fewer free-to-roll oscillations as in Fig. 5.27c). Circulation calculations at x/c = 0.395 %, $\alpha = 20^o$ and $\Phi = 0^o$ reveal that $\Gamma/cU_\infty = -0.51$ on the left-hand side and $\Gamma/cU_\infty = 0.59$ on the right-hand side, shown in Fig. 5.26c). At the trailing-edge, circulation calculations of $\Gamma/cU_\infty = -0.50$ and 0.59 suggest that this rear portion of the wing does not add vortical lift, merely keeps what exists. The circulations are dissimilar on both wing halves, suggesting the non-zero roll trim angle present.

To compare the results, time-averaged PIV measurement were taken of the slender, stable 70^o sweep delta wing and these are shown in Fig. 5.30 together with two other wings of 55^o sweep. Again, circulation calculations at $\alpha = 20^o$ and $\Phi = 0^o$ show $\Gamma/cU_\infty = -0.43$ for the left-hand side, and $\Gamma/cU_\infty = 0.41$ for the right-hand side, suggesting a trim angle of near zero, and shown in Fig. 5.1d). The streamlines themselves in Fig. 5.30c) do not really show it, but in Fig. 5.30a) it can be seen that the vortices interact with one another and the velocities over the wing surface are much higher than in the other cases, proven by the fact that in Fig. 5.30b) the vortices are very compact and strong. If one compares this Figure to Fig. 5.28, it can be seen that the velocities are much more significant and Fig. 5.31 shows that reattached flow is not present on the wing surface, but is in the other two cases. Figure 5.31b) confirms that despite the reattached flow at the start of the wing, the rear portion must damp the motion in the same way as Fig. 5.31c).

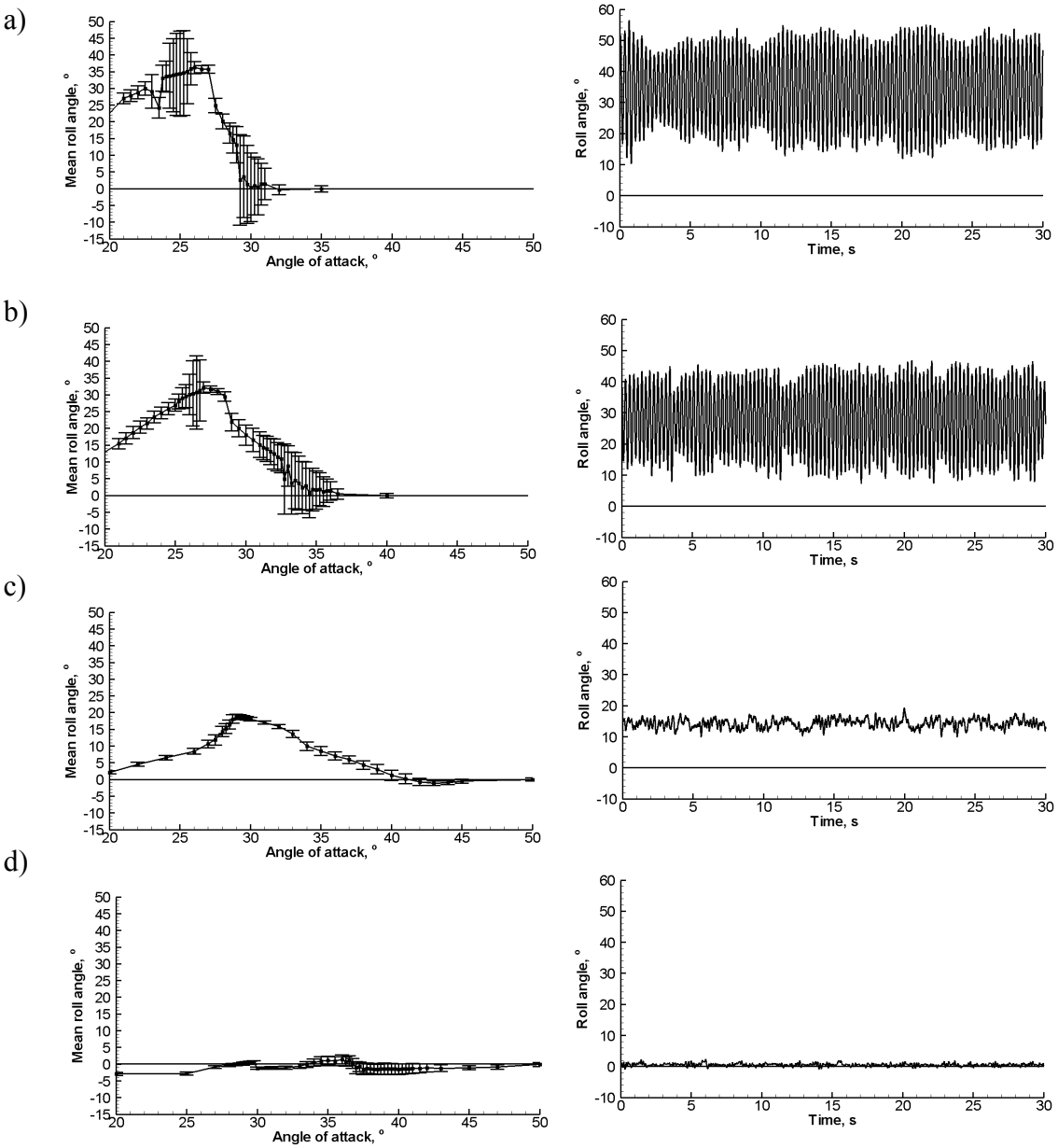

Figure 5.1 Graphs showing (left) mean roll angle against angle of attack with standard deviation as error bars and (right) time histories of roll angle corresponding to maximum standard deviation (at $\alpha = 25^o$, 26.5^o, 28^o and 29.75^o respectively) for delta wings with a) $\Lambda = 57.5^o$; b) $\Lambda = 60^o$, c) $\Lambda = 65^o$ and d) $\Lambda = 70^o$, all with sharp leading-edges.

a) b)

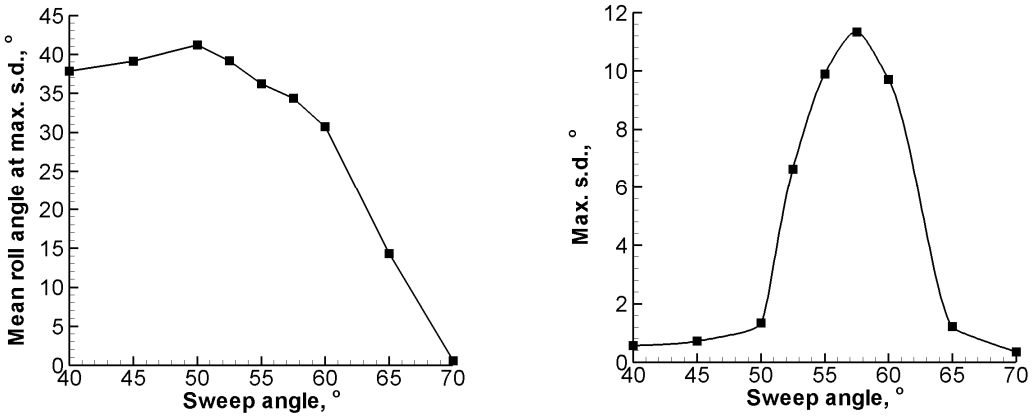

Figure 5.2 Results for delta wings with sharp leading-edges showing a) mean roll angle at maximum standard deviation against sweep angle and b) maximum standard deviation against sweep angle for wings with large free-to-roll oscillations.

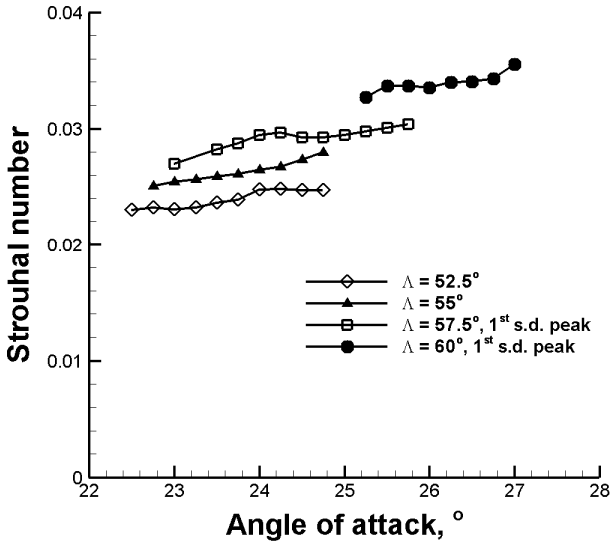

Figure 5.3 Results for delta wings with sharp leading-edges showing Strouhal number against angle of attack for wings with large free-to-roll oscillations.

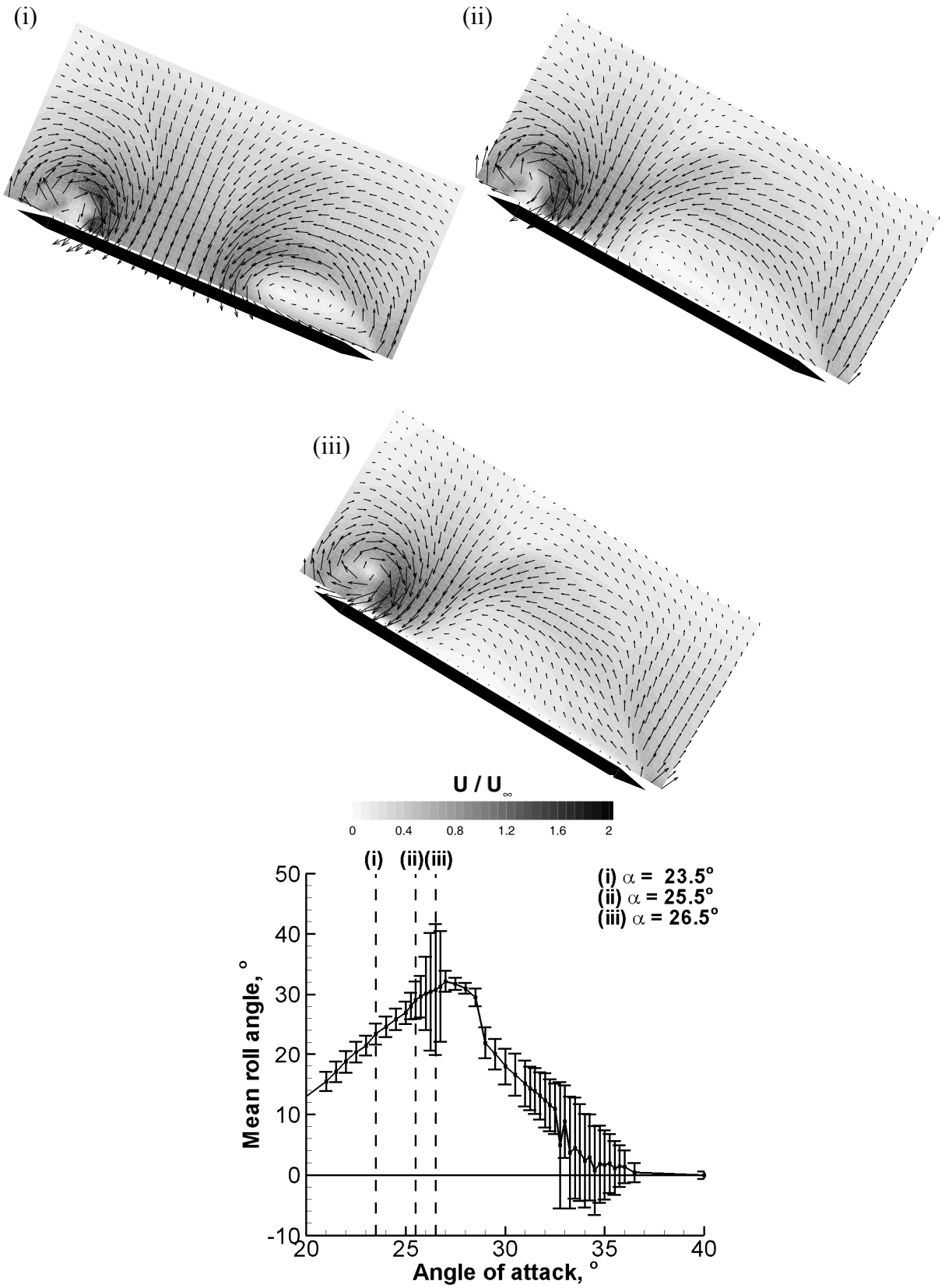

Figure 5.4 Cross-flow time-averaged velocity fields on stationary delta wing and graph of mean roll angle with standard deviation as error bars against angle of attack corresponding to images, with (i) at $\alpha = 23.5^{o}$ and $\Phi = 23^{o}$; (ii) at $\alpha = 25.5^{o}$ and $\Phi = 29^{o}$ and (iii) at $\alpha = 26.5^{o}$ and $\Phi = 31^{o}$ for wing with $\Lambda = 60^{o}$ and sharp leading-edges at x/c = 0.25.

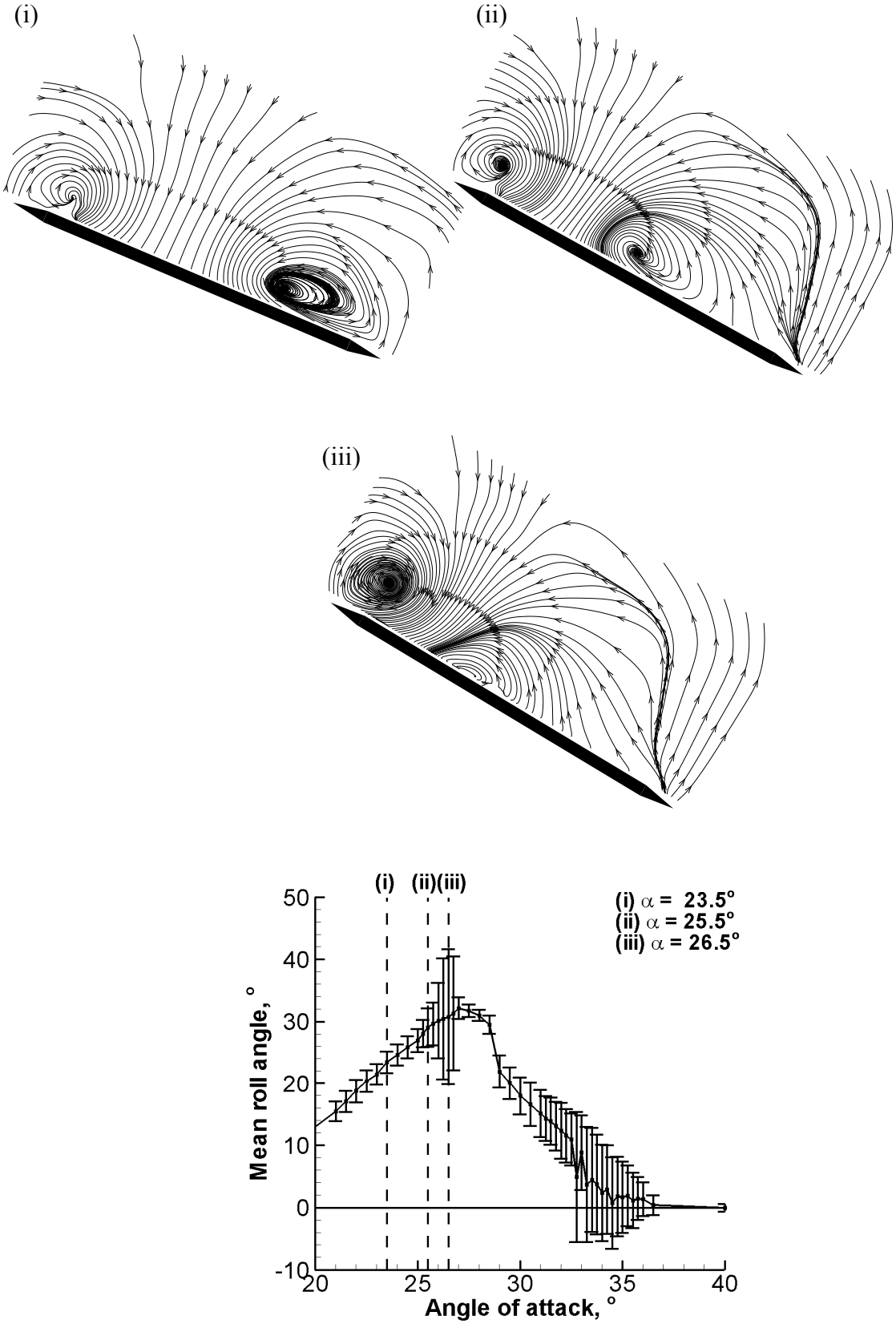

Figure 5.5 Cross-flow time-averaged streamline patterns on stationary wing and graph of mean roll angle with standard deviation as error bars against angle of attack corresponding to images, with (i) at $\alpha = 23.5^{o}$ and $\Phi = 23^{o}$; (ii) at $\alpha = 25.5^{o}$ and $\Phi = 29^{o}$ and (iii) at $\alpha = 26.5^{o}$ and $\Phi = 31^{o}$ for wing with $\Lambda = 60^{o}$ and sharp leading-edges at x/c = 0.25.

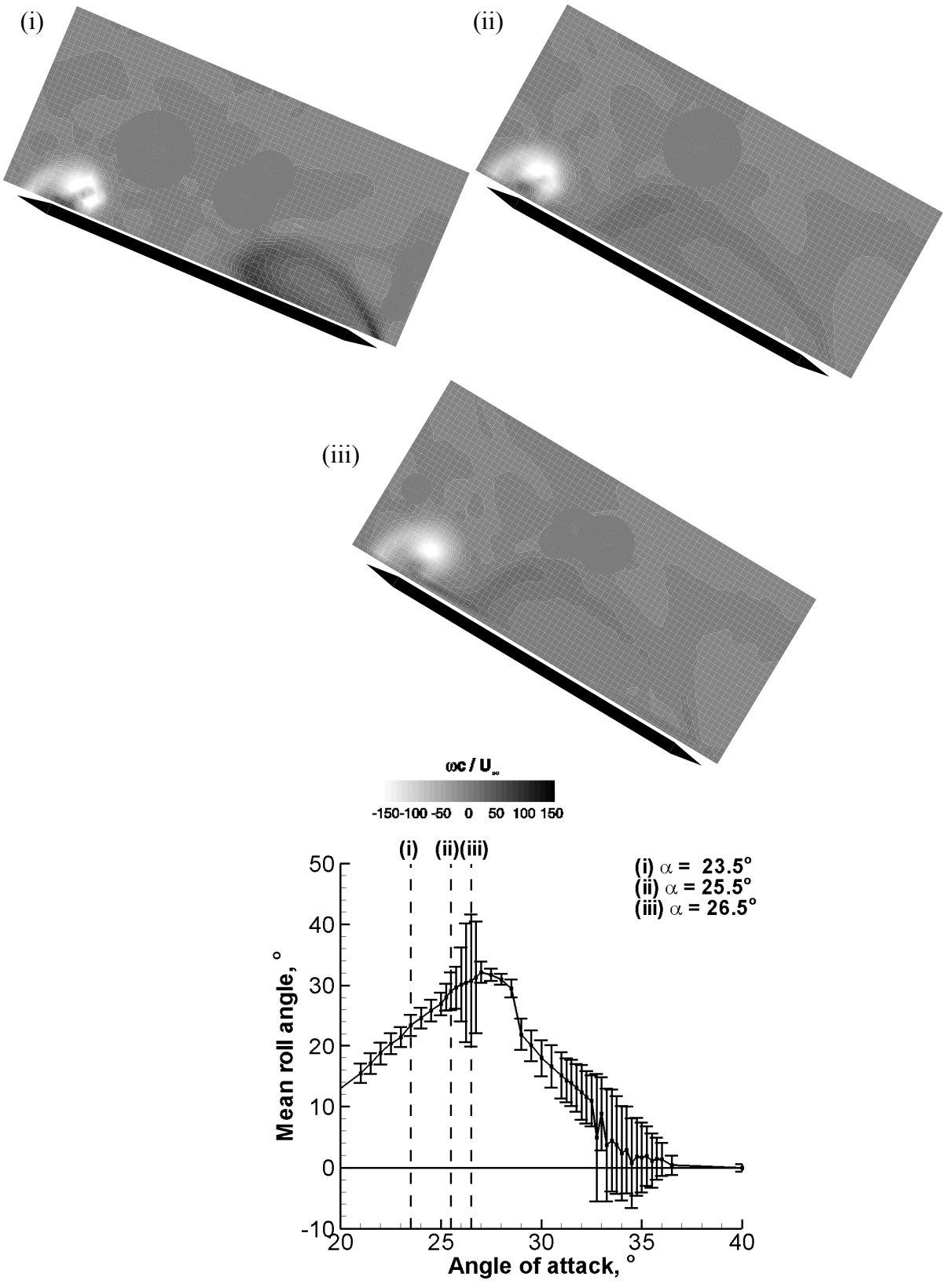

Figure 5.6 Cross-flow vorticity patterns on stationary delta wing and graph of mean roll angle with standard deviation as error bars against angle of attack corresponding to images, with (i) at $\alpha = 23.5^{o}$ and $\Phi = 23^{o}$; (ii) at $\alpha = 25.5^{o}$ and $\Phi = 29^{o}$ and (iii) at $\alpha = 26.5^{o}$ and $\Phi = 31^{o}$ for wing with $\Lambda = 60^{o}$ and sharp leading-edges at x/c = 0.25.

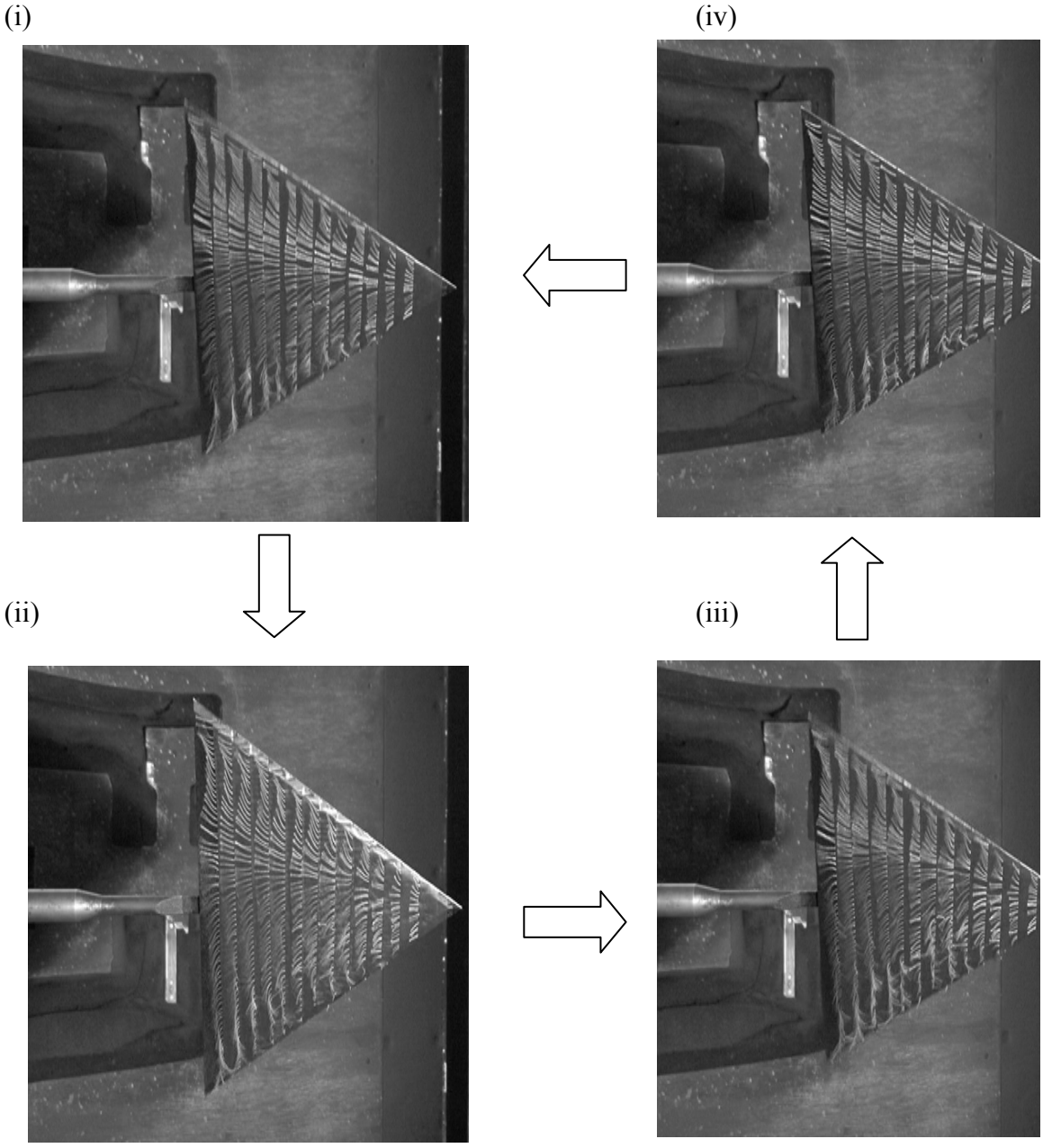

Figure 5.7 Tuft visualisation of rolling delta wing at (i) Φ_{mean} with Φ decreasing; (ii) Φ_{min}; (iii) Φ_{mean} with Φ increasing and (iv) Φ_{max} for delta wing with $\Lambda = 60^o$ and sharp leading-edges at $\alpha = 26.5^o$.

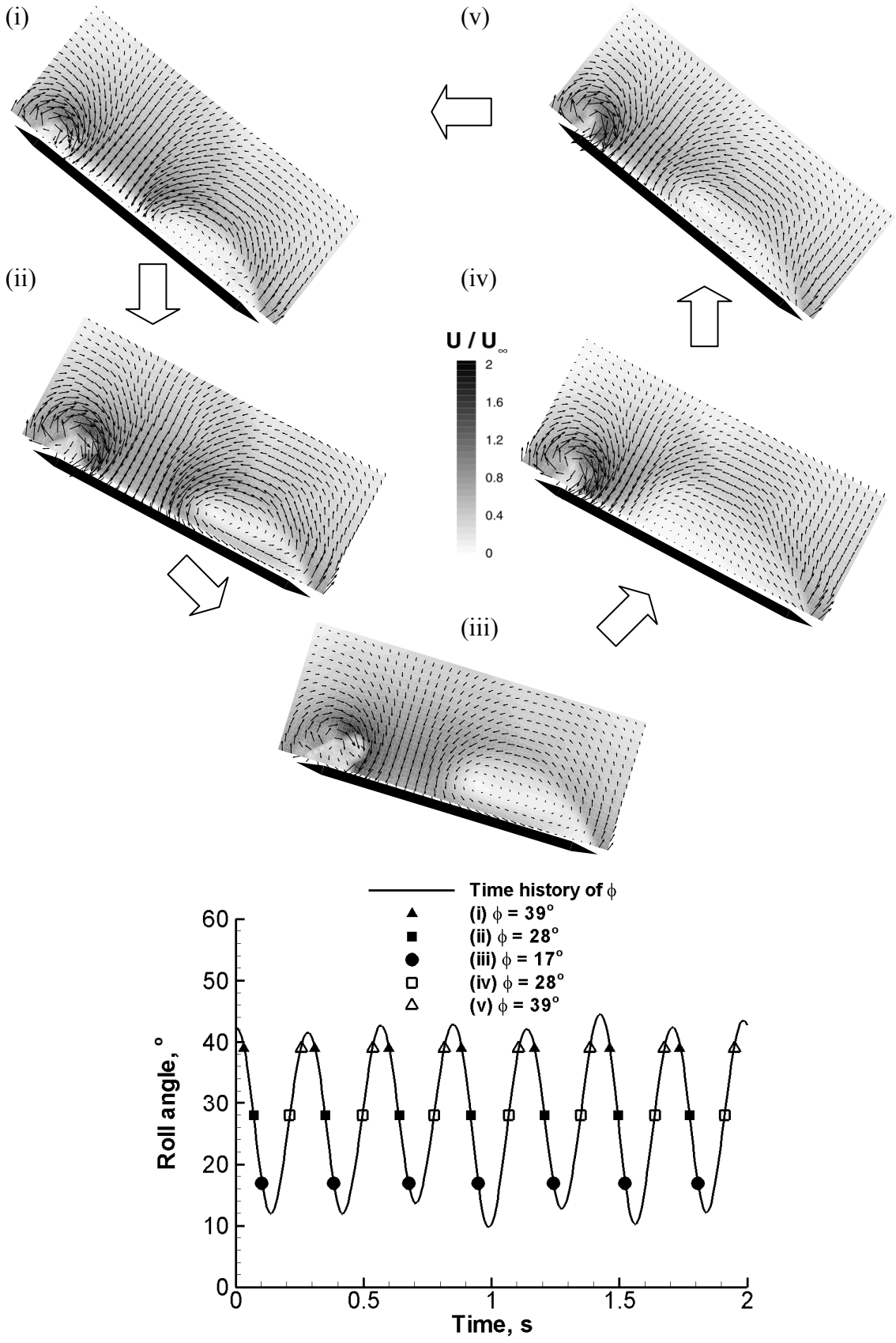

Figure 5.8 Cross-flow phase-averaged velocity fields on rolling delta wing and timing diagram corresponding to images, with (i) at $\Phi = 39^{o}$; (ii) at $\Phi = 28^{o}$; (iii) at $\Phi = 17^{o}$; (iv) at $\Phi = 28^{o}$ and (v) at $\Phi = 39^{o}$ for wing with $\Lambda = 60^{o}$ and sharp leading-edges at $x/c = 0.25$ and $\alpha = 26.5^{o}$.

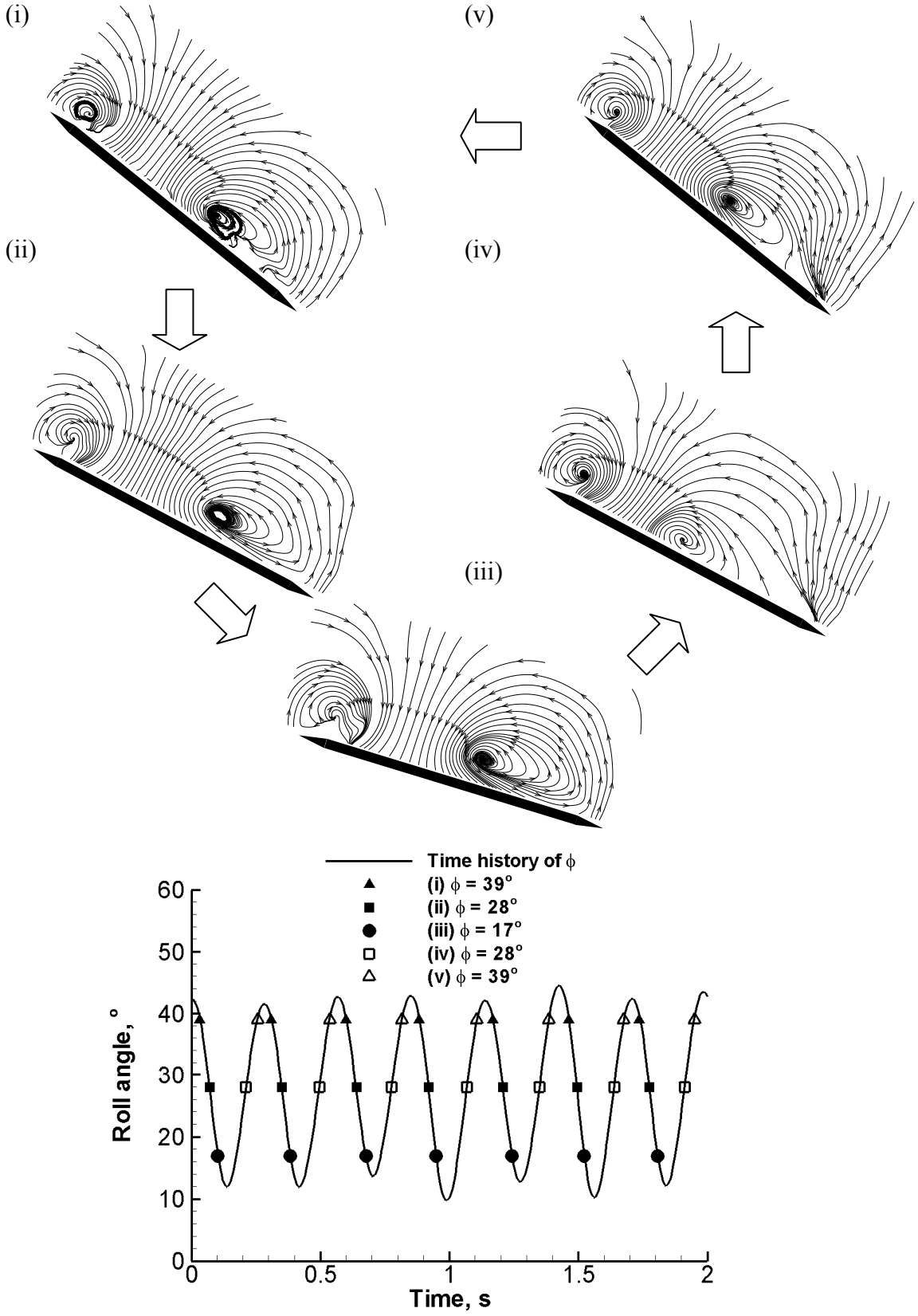

Figure 5.9 Cross-flow phase-averaged streamline patterns on rolling delta winga and timing diagram corresponding to images, with (i) at $\Phi = 39^o$; (ii) at $\Phi = 28^o$; (iii) at $\Phi = 17^o$; (iv) at $\Phi = 28^o$ and (v) at $\Phi = 39^o$ for wing with $\Lambda = 60^o$ and sharp leading-edges at $x/c = 0.25$ and $\alpha = 26.5^o$

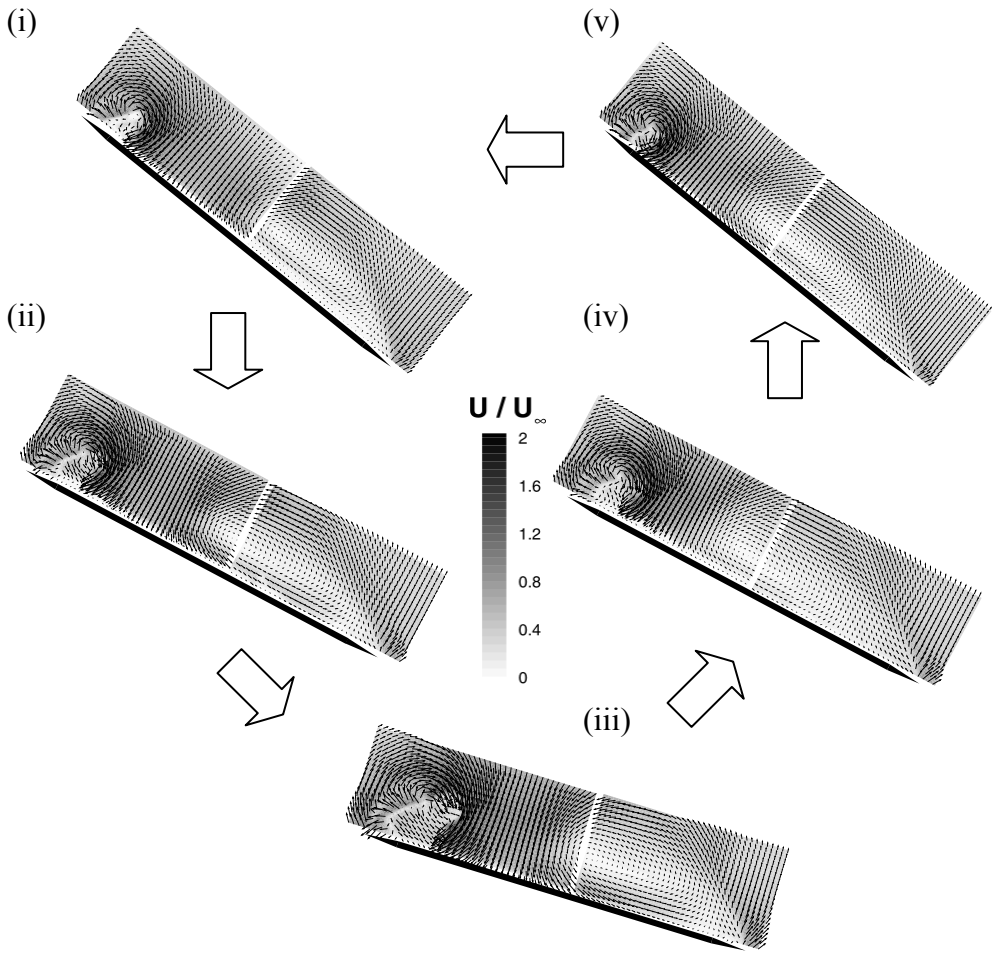

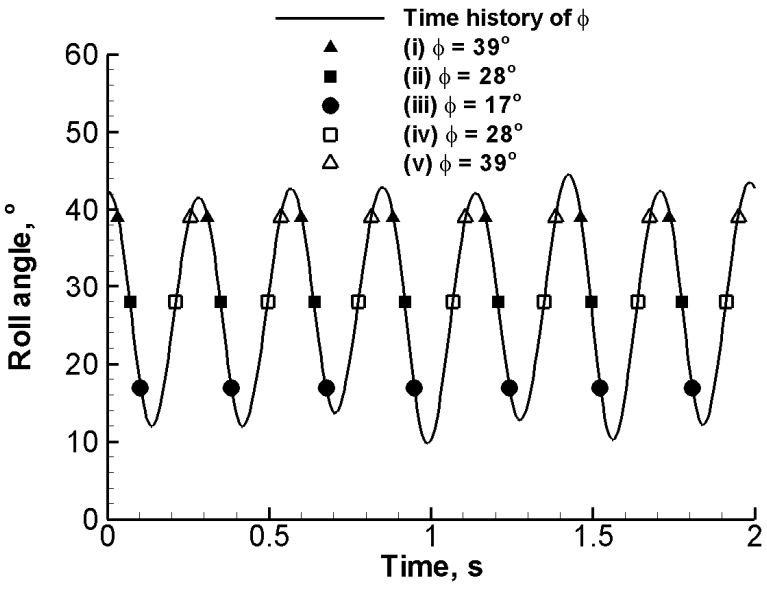

Figure 5.10 Cross-flow phase-averaged velocity fields on rolling delta wing and timing diagram corresponding to images, with (i) at $\Phi = 39^o$; (ii) at $\Phi = 28^o$; (iii) at $\Phi = 17^o$; (iv) at $\Phi = 28^o$ and (v) at $\Phi = 39^o$ for wing with $\Lambda = 60^o$ and sharp leading-edges at $x/c = 0.5$ and $\alpha = 26.5^o$.

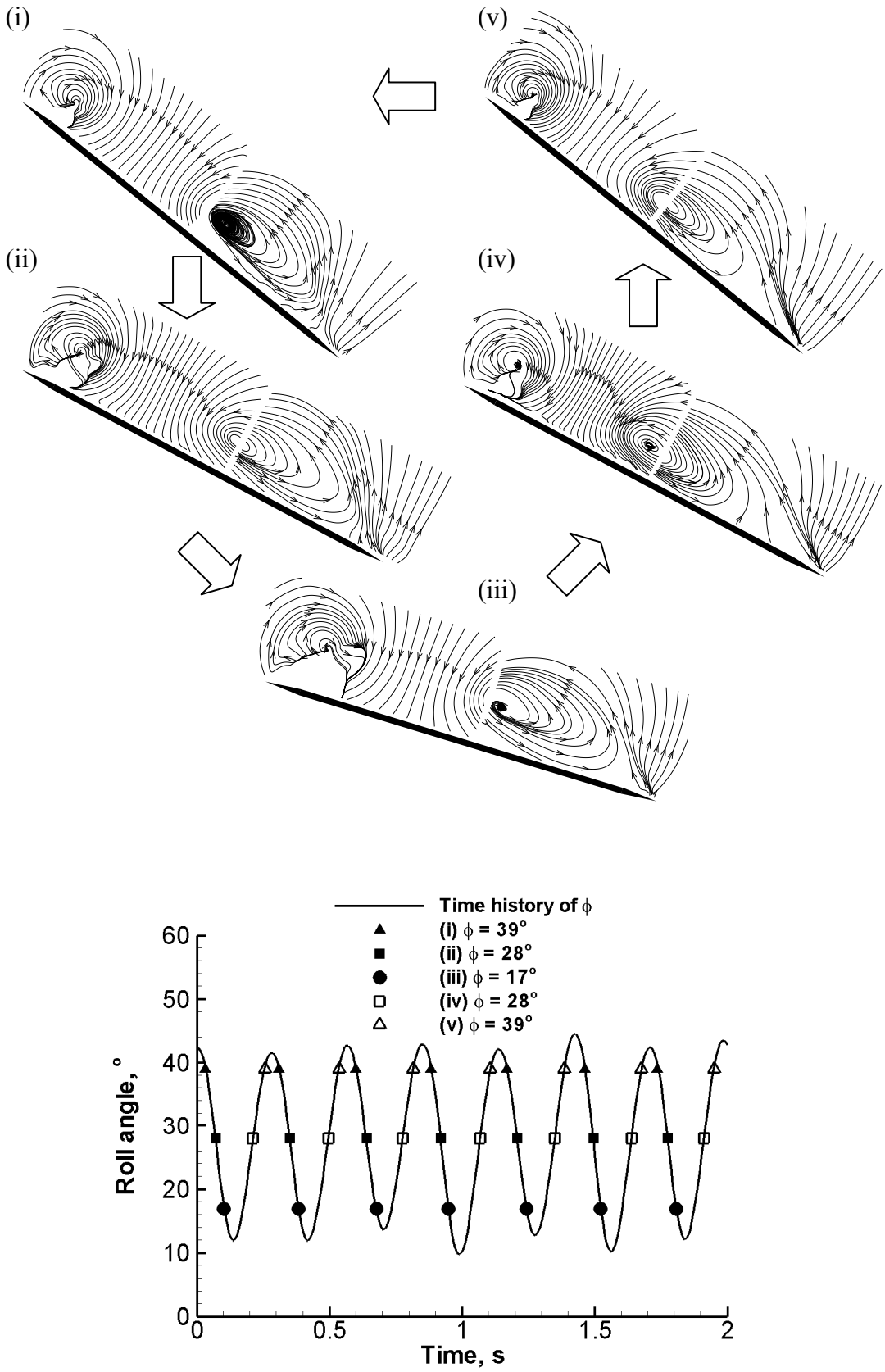

Figure 5.11 Cross-flow phase-averaged streamline patterns on rolling delta wing and timing diagram corresponding to images, with (i) at $\Phi = 39^o$; (ii) at $\Phi = 28^o$; (iii) at $\Phi = 17^o$; (iv) at $\Phi = 28^o$ and (v) at $\Phi = 39^o$ for wing with $\Lambda = 60^o$ and sharp leading-edges at $x/c = 0.5$ and $\alpha = 26.5^o$.

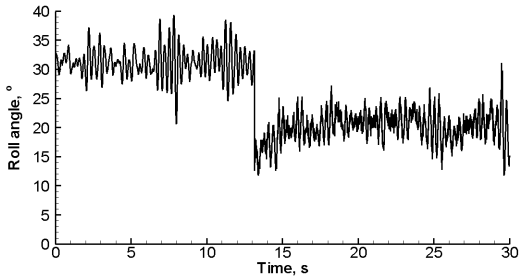

Figure 5.12 Graph showing time history of roll angle at $\alpha = 23^{o}$ for delta wing with $\Lambda = 57.5^{o}$ and sharp leading-edges.

a)

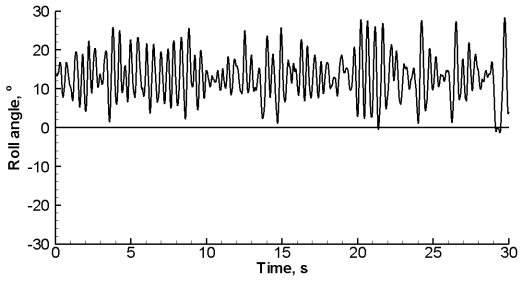

b)

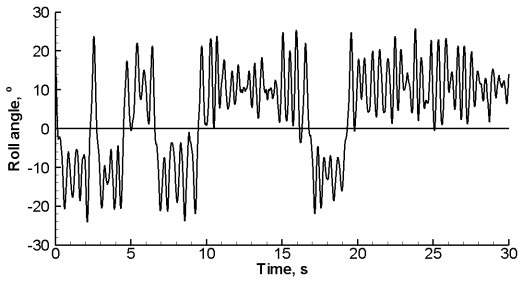

c)

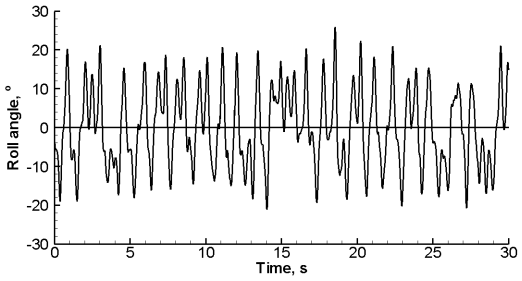

Figure 5.13 Graphs showing time histories of roll angle at a) $\alpha = 29^{o}$; b) $\alpha = 29.5^{o}$ and c) $\alpha = 30^{o}$ for delta wing with $\Lambda = 57.5^{o}$ and sharp leading-edges.

a)

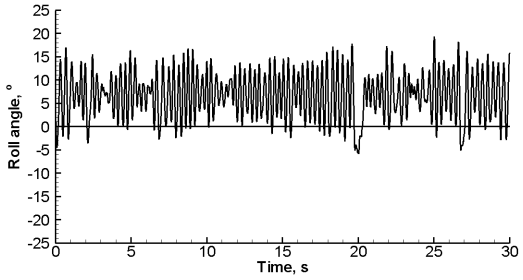

b)

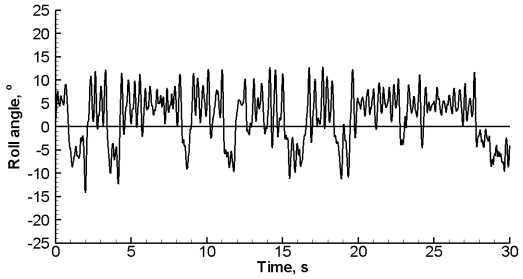

Figure 5.14 Graphs showing time histories of roll angle at a) $\alpha = 33^{o}$ and b) $\alpha = 35^{o}$ for delta wing with $\Lambda = 60^{o}$ and sharp leading-edges.

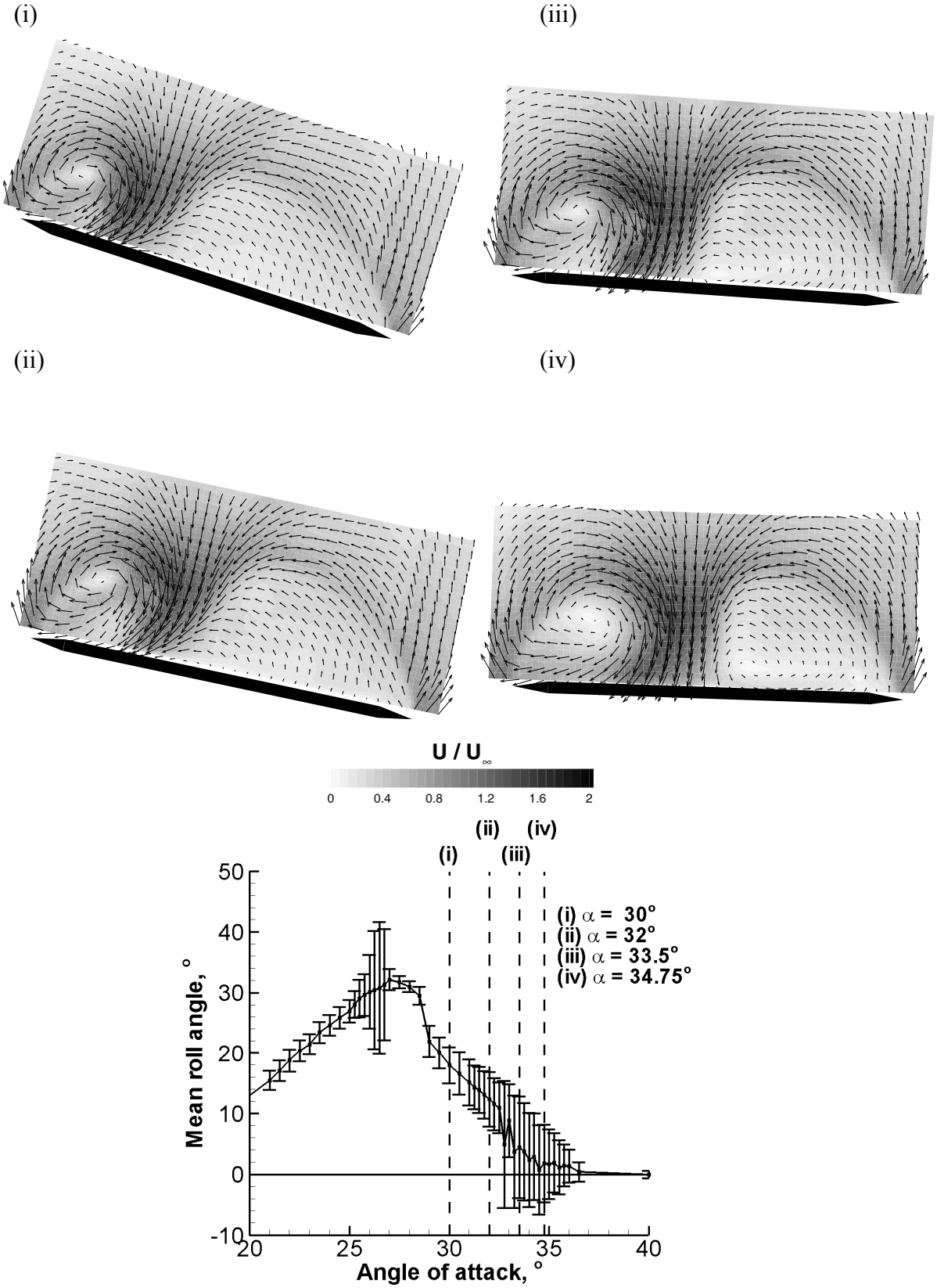

Figure 5.15 Cross-flow time-averaged velocity fields on stationary delta wing and graph of mean roll angle with standard deviation as error bars against angle of attack corresponding to images, with (i) at $\alpha = 30^o$ and $\Phi = 18^o$; (ii) at $\alpha = 32^o$ and $\Phi = 12^o$; (iii) at $\alpha = 33.5^o$ and $\Phi = 6^o$ and (iv) at $\alpha = 34.75^o$ and $\Phi = 2^o$ for wing with $\Lambda = 60^o$ and sharp leading-edges at x/c = 0.25.

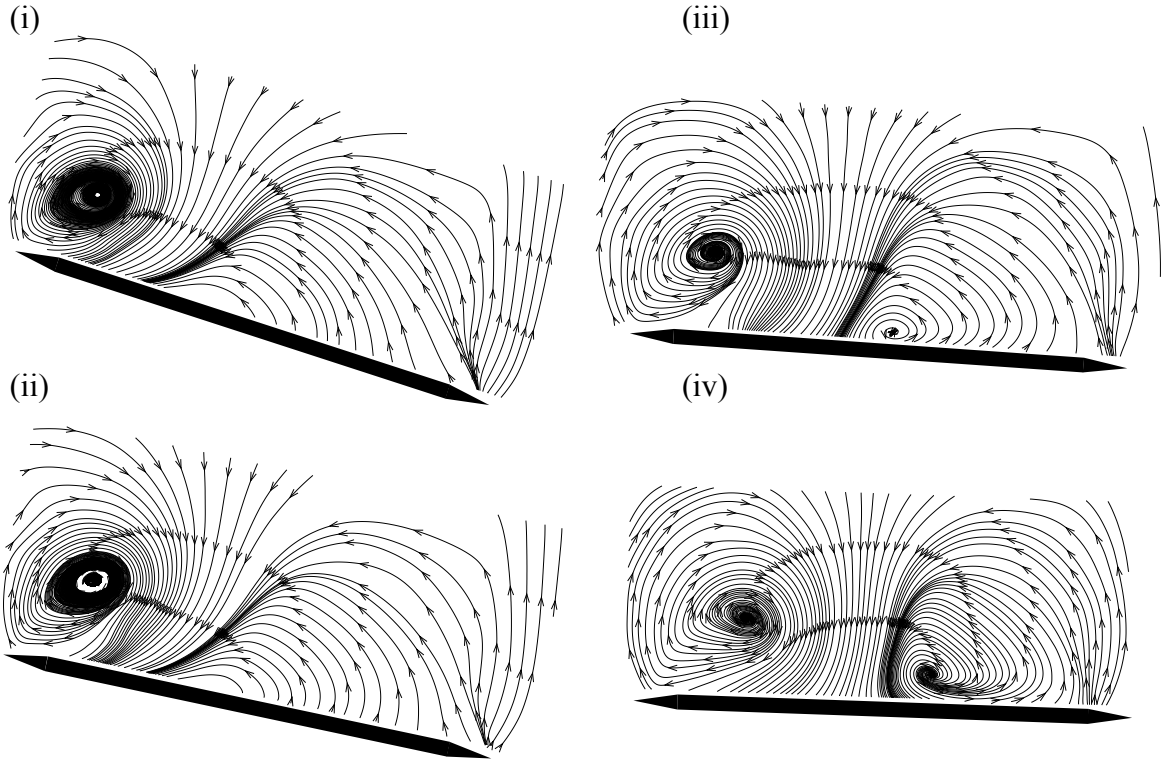

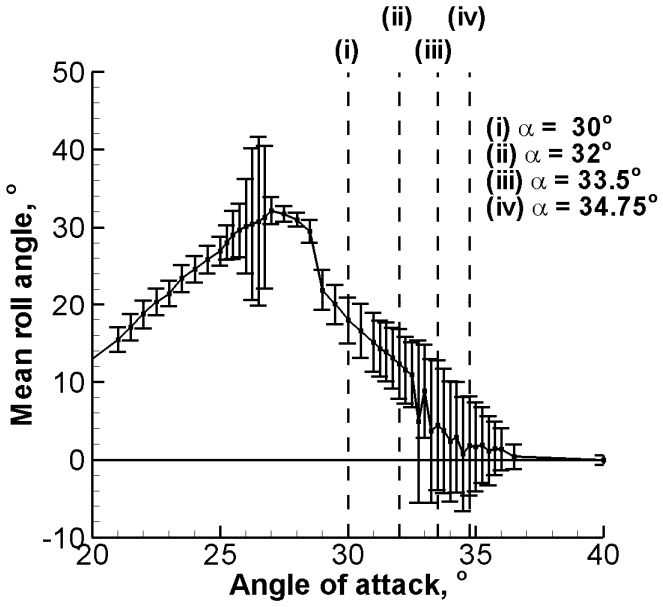

Figure 5.16 Cross-flow time-averaged streamlines on a stationary delta wing and graph of mean roll angle with standard deviation as error bars against angle of attack corresponding to images, with (i) at $\alpha = 30^o$ and $\Phi = 18^o$; (ii) at $\alpha = 32^o$ and $\Phi = 12^o$; (iii) at $\alpha = 33.5^o$ and $\Phi = 6^o$ and (iv) at $\alpha = 34.75^o$ and $\Phi = 2^o$ for wing with $\Lambda = 60^o$ and sharp leading-edges at x/c = 0.25.

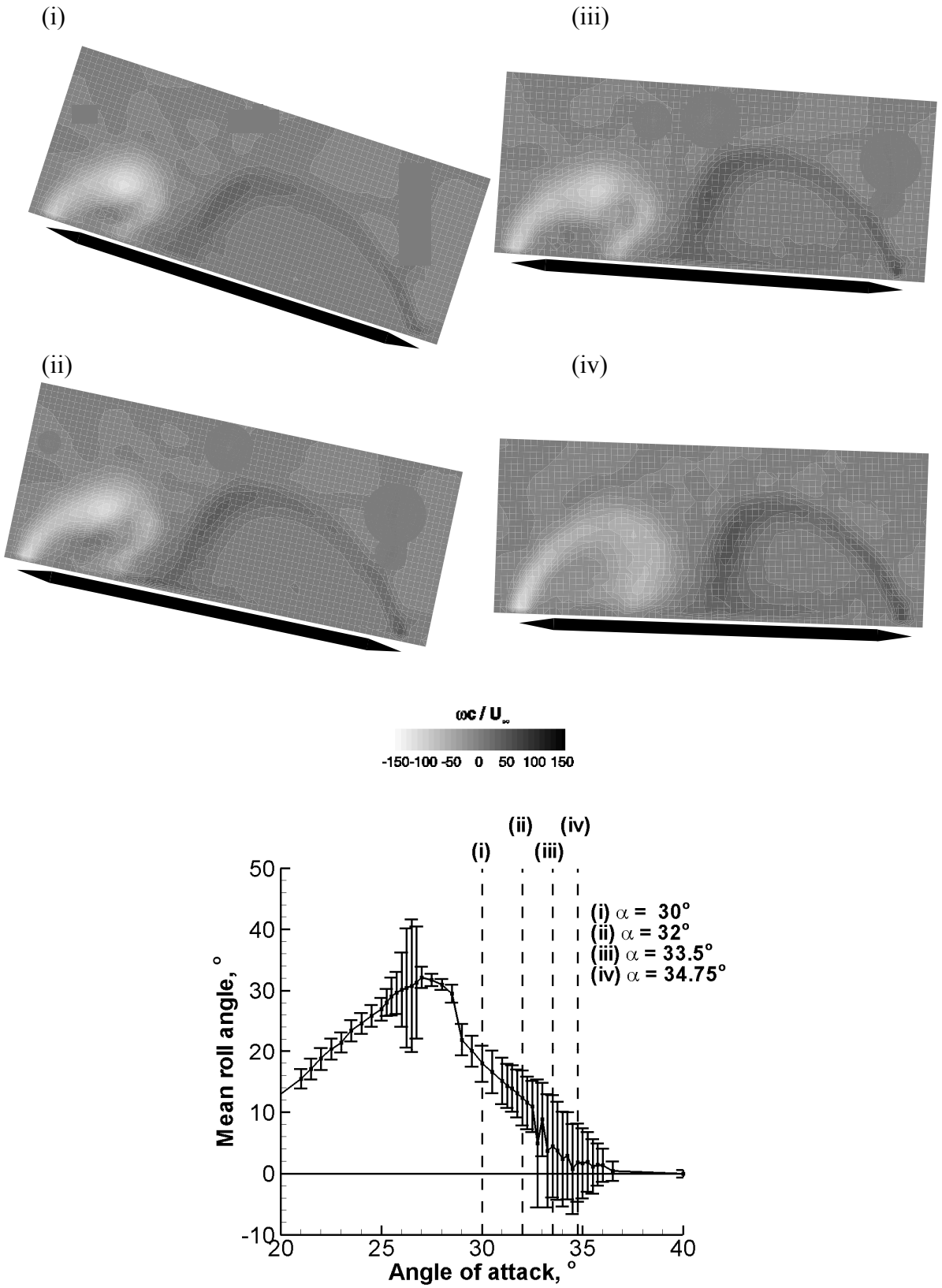

Figure 5.17 Cross-flow time-averaged vorticity patterns on stationary delta wing and graph of mean roll angle with standard deviation as error bars against angle of attack corresponding to images, with (i) at $\alpha = 30^o$ and $\Phi = 18^o$; (ii) at $\alpha = 32^o$ and $\Phi = 12^o$; (iii) at $\alpha = 33.5^o$ and $\Phi = 6^o$ and (iv) at $\alpha = 34.75^o$ and $\Phi = 2^o$ for wing with $\Lambda = 60^o$ and sharp leading-edges at x/c = 0.25.

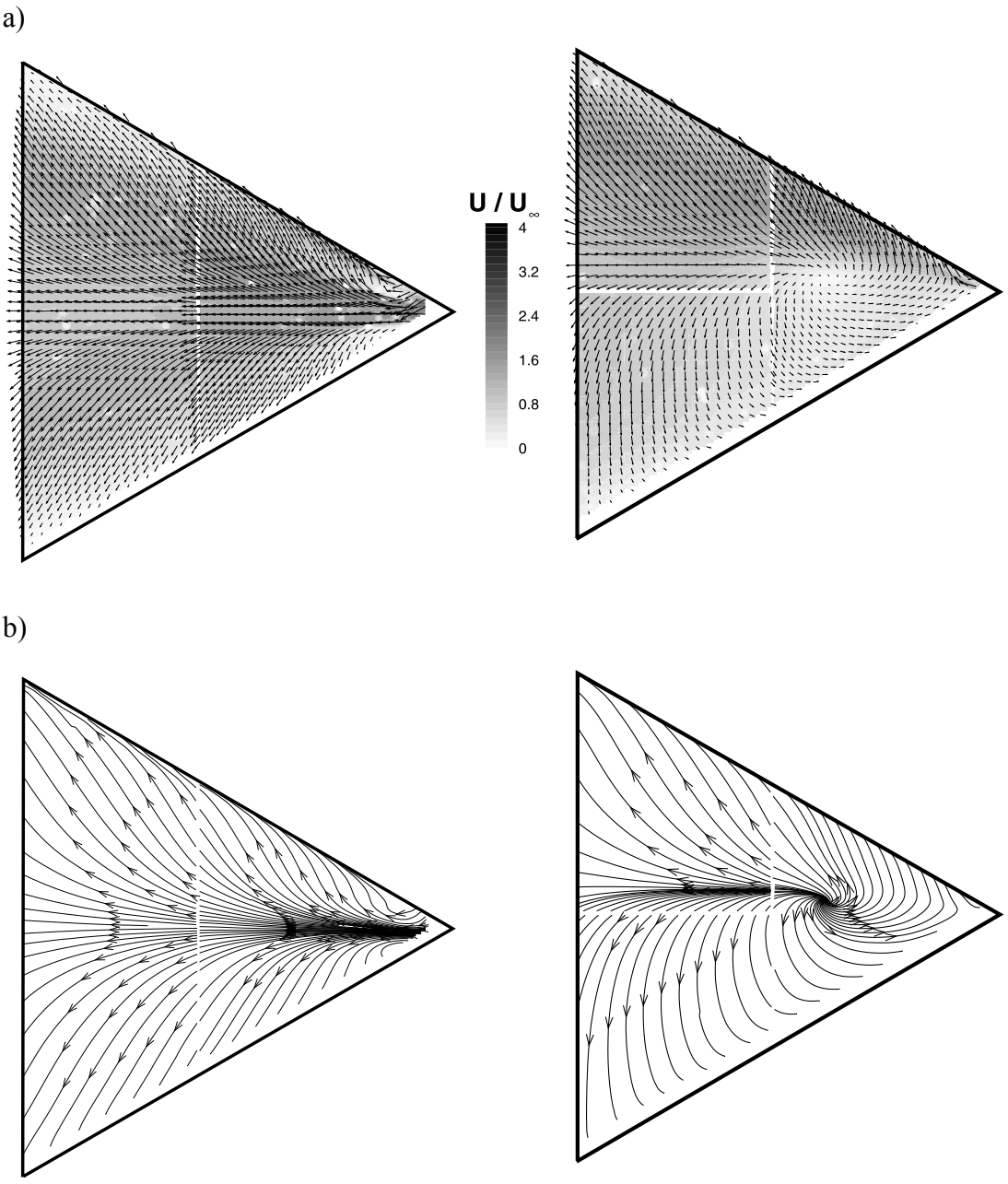

Figure 5.18 Near-surface PIV measurements, showing a) velocity field and b) streamline pattern for $\Phi = 0^o$ (left) and $\Phi = 12^o$ (right) at $\alpha = 33°$, for delta wing with sharp leading-edges and $\Lambda = 60^o$.

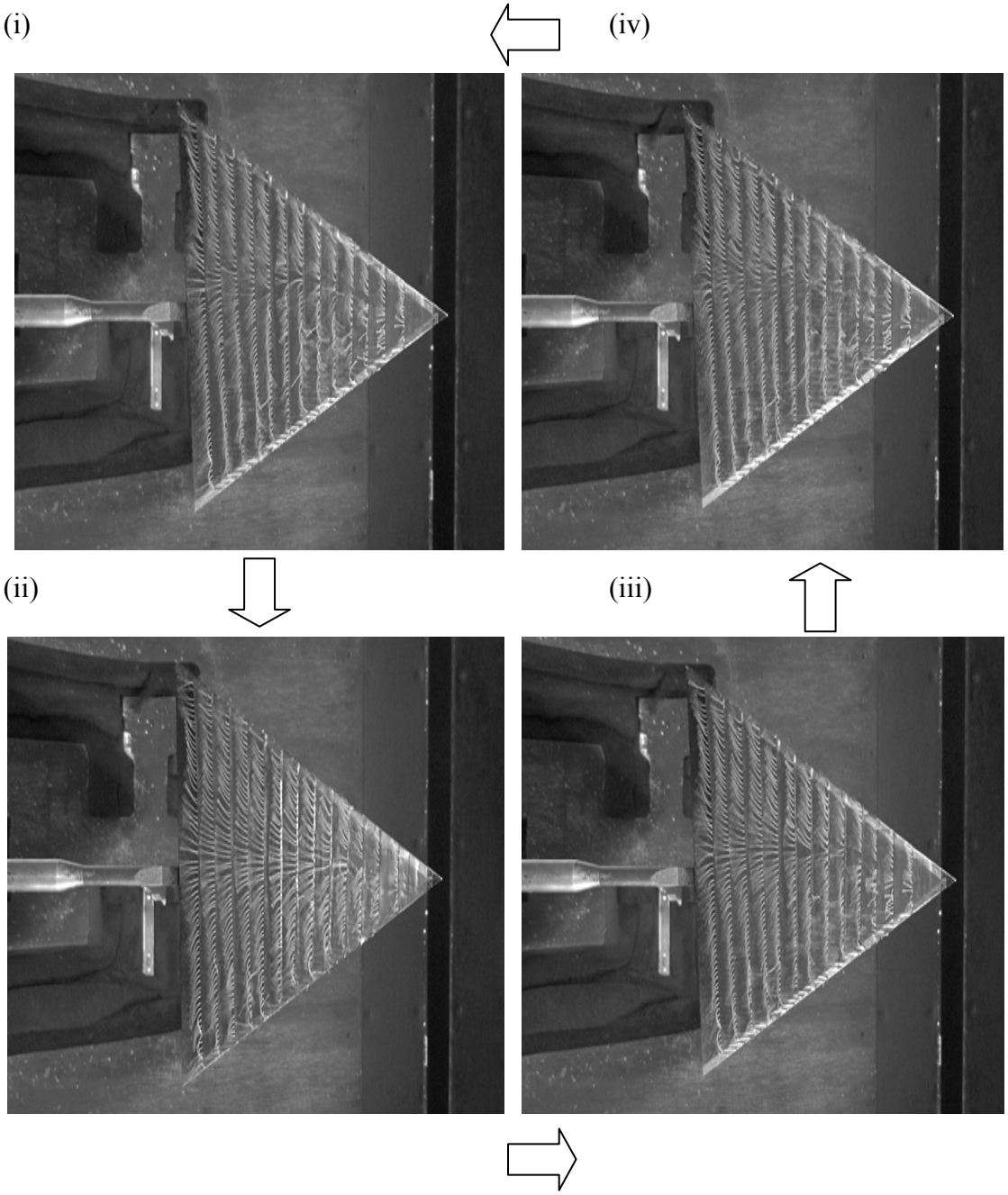

Figure 5.19 Tuft visualisation of rolling delta wing at (i) Φ_{mean} with Φ decreasing; (ii) Φ_{min}; (iii) Φ_{mean} with Φ increasing and (iv) Φ_{max} for wing with $\Lambda = 60^{o}$ and sharp leading-edges at $\alpha = 33^{o}$.

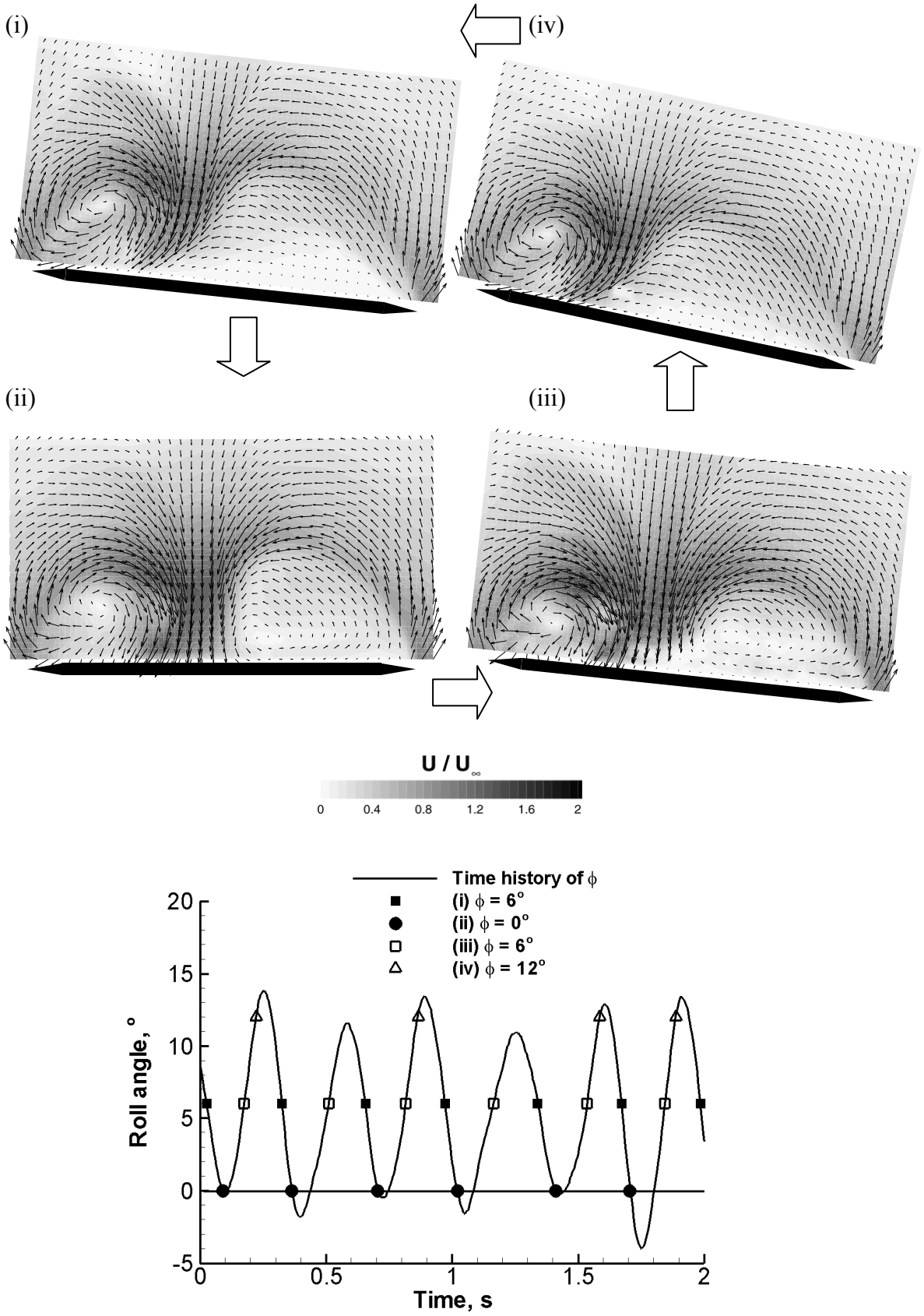

Figure 5.20 Cross-flow phase-averaged velocity fields on rolling delta wing and timing diagram corresponding to images, with (i) at $\Phi = 6^o$; (ii) at $\Phi = 0^o$; (iii) at $\Phi = 6^o$ and (iv) at $\Phi = 12^o$ for wing with $\Lambda = 60^o$ and sharp leading-edges at x/c = 0.25 and $\alpha = 33^o$.

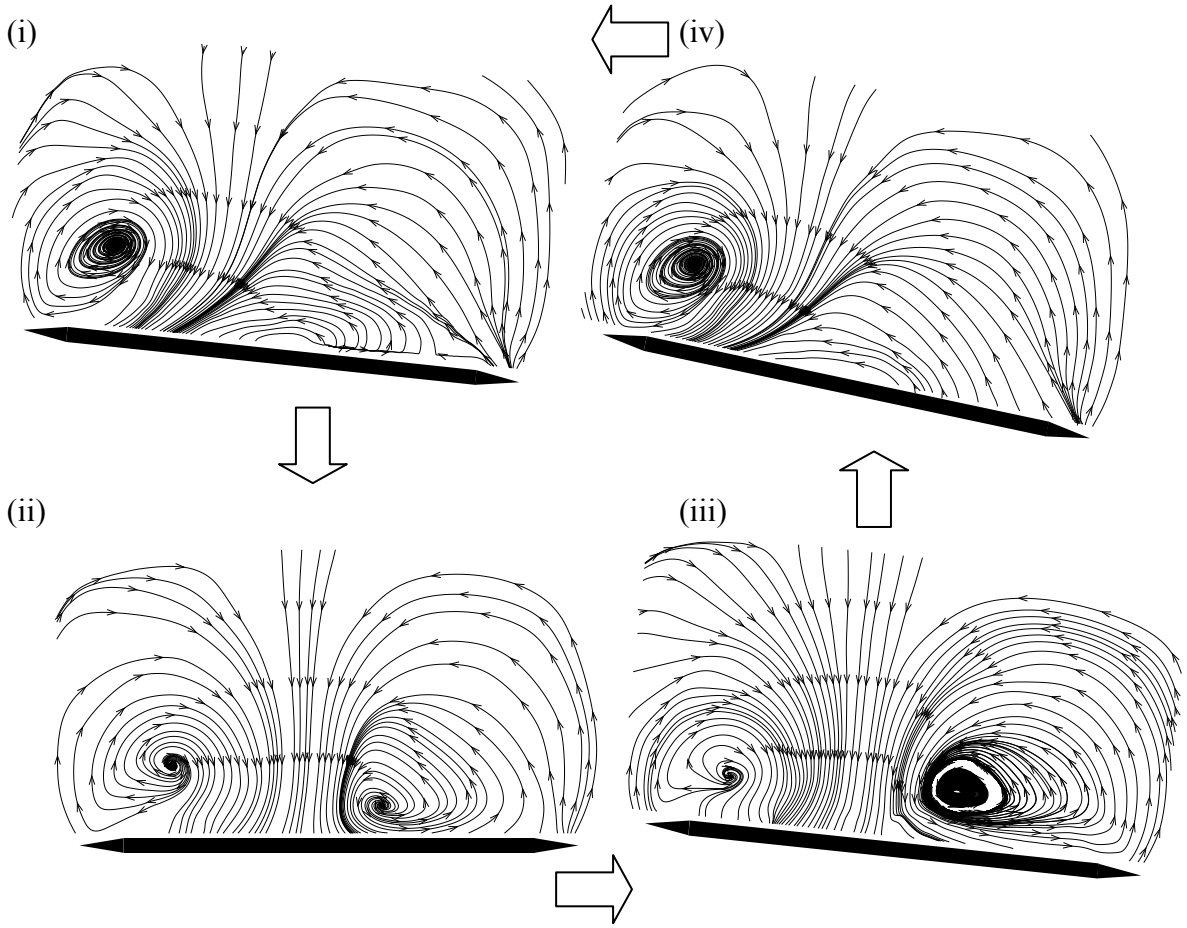

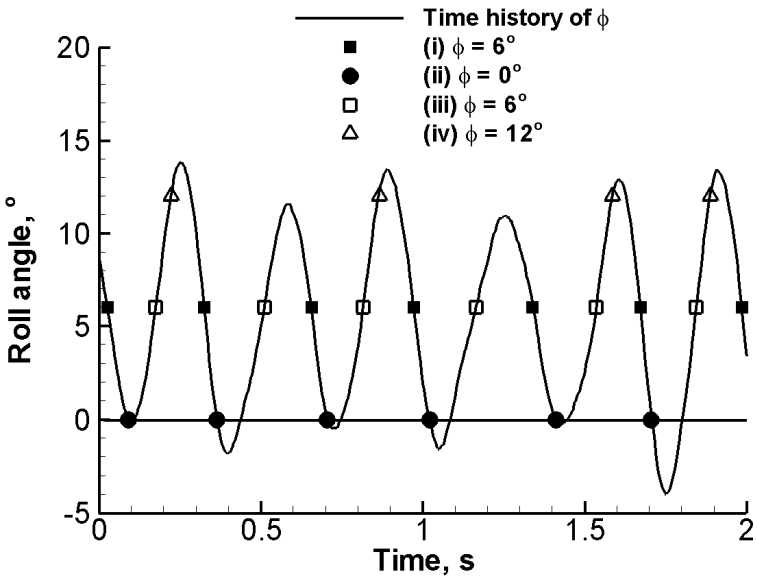

Figure 5.21 Cross-flow phase-averaged streamlines on rolling delta wing and timing diagram corresponding to images, with (i) at $\Phi = 6^o$; (ii) at $\Phi = 0^o$; (iii) at $\Phi = 6^o$ and (iv) at $\Phi = 12^o$ for wing with $\Lambda = 60^o$ and sharp leading-edges at x/c = 0.25 and $\alpha = 33^o$.

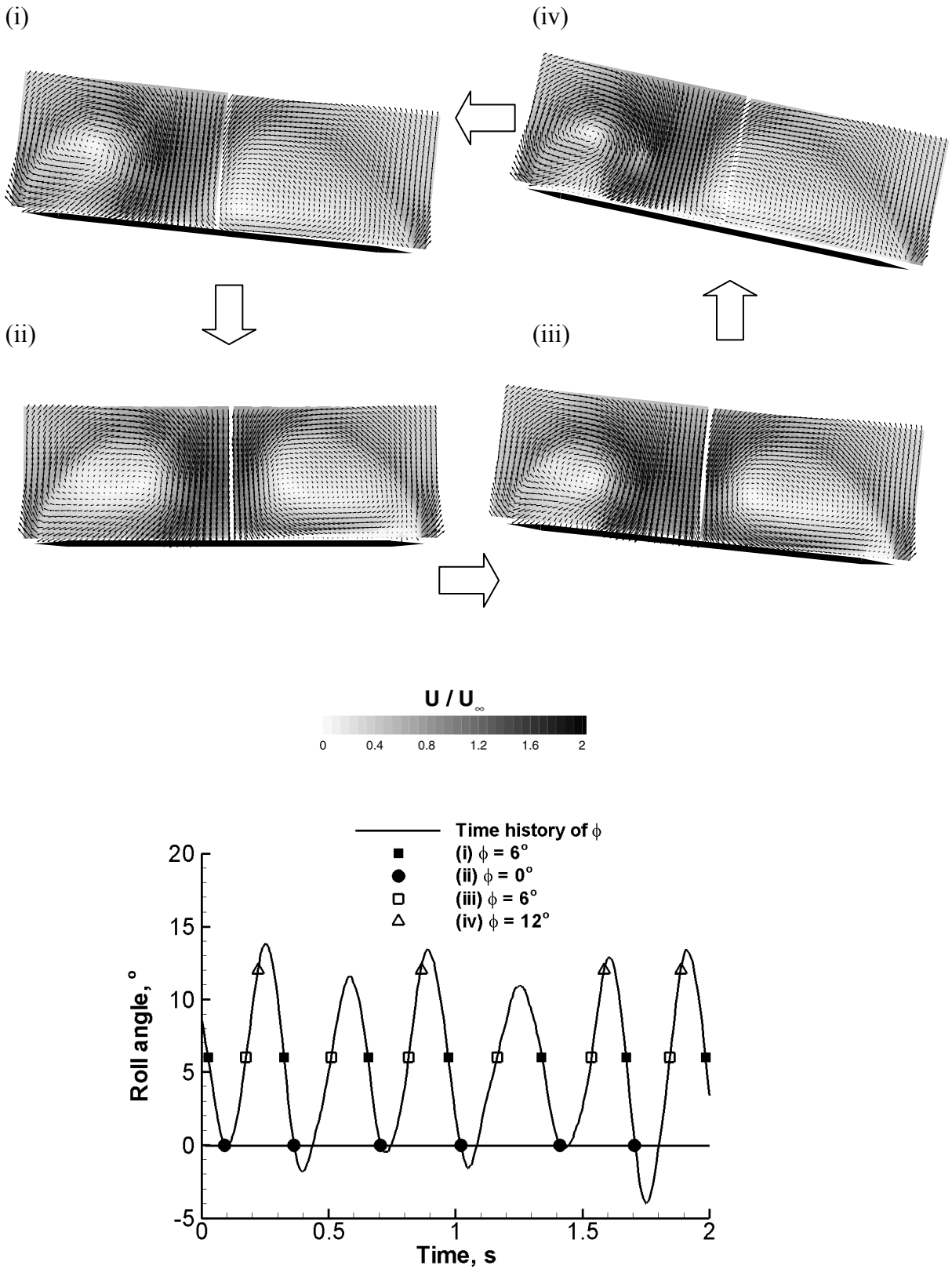

Figure 5.22 Cross-flow phase-averaged velocity fields on rolling delta wing showing timing diagram corresponding to images, with (i) at $\Phi = 6^o$; (ii) at $\Phi = 0^o$; (iii) at $\Phi = 6^o$ and (iv) at $\Phi = 12^o$ for wing with $\Lambda = 60^o$ and sharp leading-edges at x/c = 0.5 and $\alpha = 33^o$.

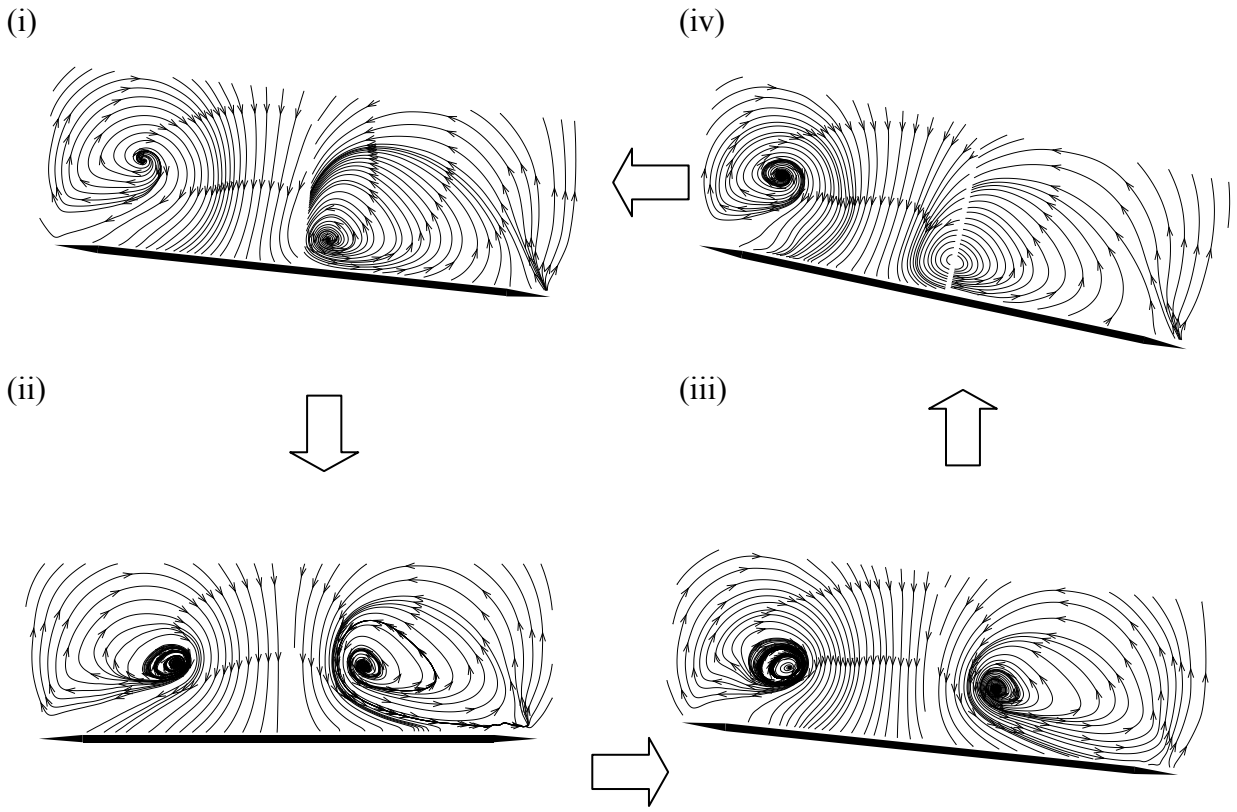

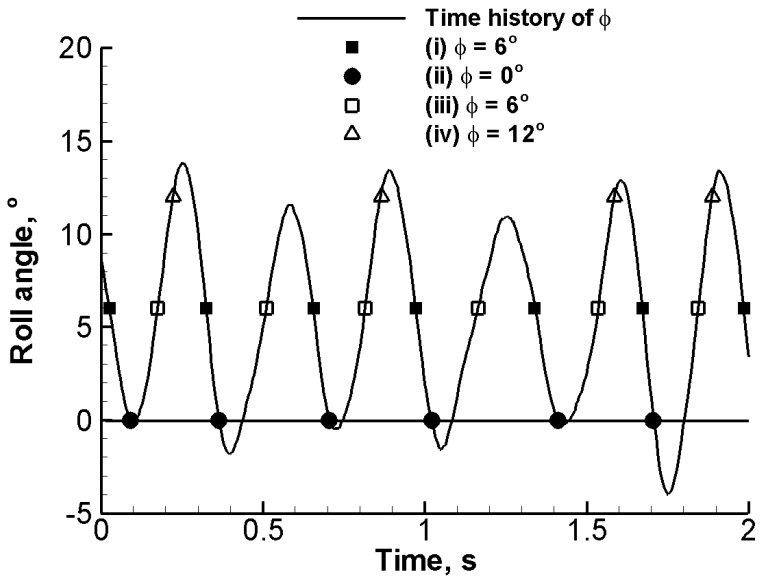

Figure 5.23 Cross-flow phase-averaged streamlines on rolling delta wing and timing diagram corresponding to images, with (i) at $\Phi = 6^o$; (ii) at $\Phi = 0^o$; (iii) at $\Phi = 6^o$ and (iv) at $\Phi = 12^o$ for wing with $\Lambda = 60^o$ and sharp leading-edges at x/c = 0.5 and $\alpha = 33^o$.

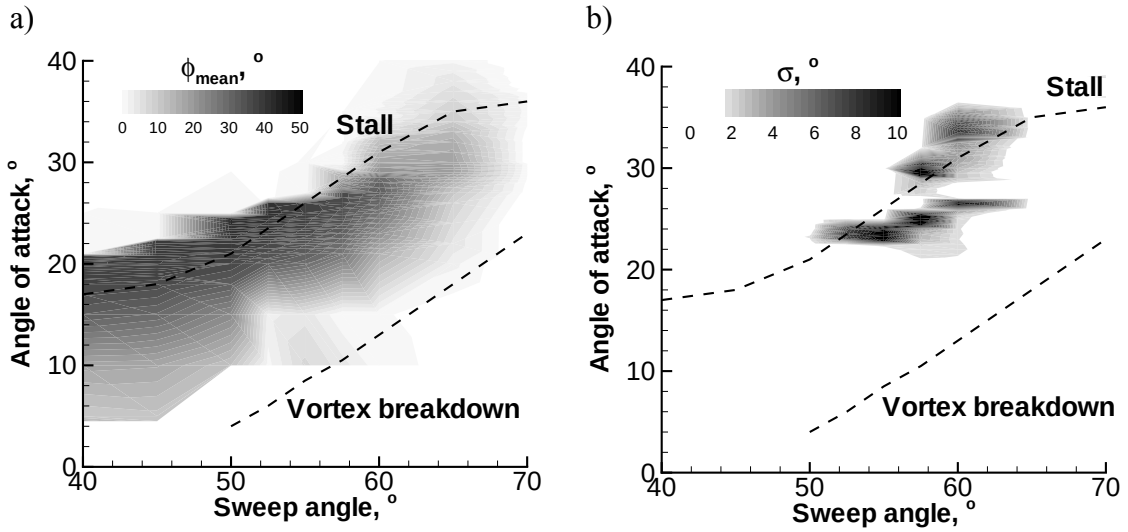

Figure 5.24 Graphs of angle of attack against delta wing sweep angle showing contours of a) mean roll angle and b) standard deviation of free-to-roll wings, together with stall and vortex breakdown locations for different sweep angles.

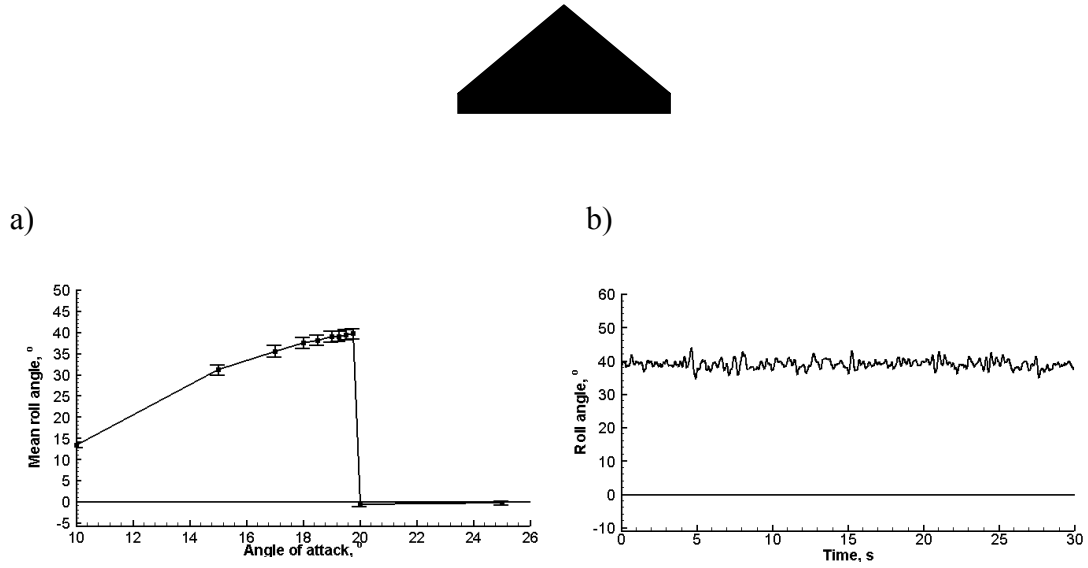

Figure 5.25 Graphs showing a) mean roll angle against angle of attack with standard deviation as error bars and b) free-to-roll time history at $\alpha = 19^o$ for a cropped delta wing $\Lambda = 40^o$, which schematic shown.

a)

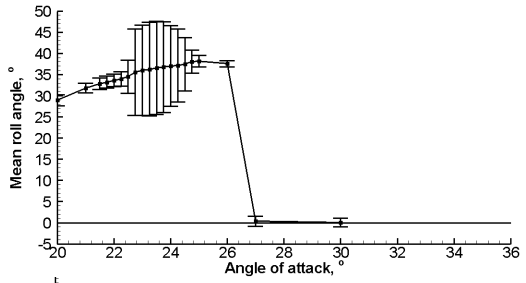

b)

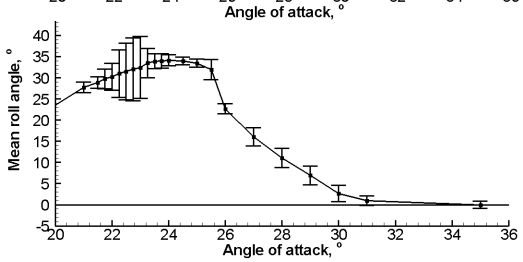

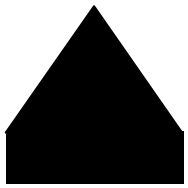

c)

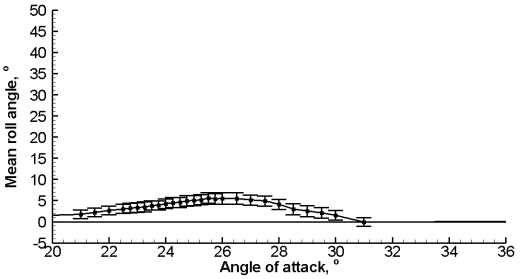

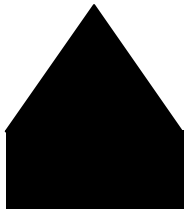

d)

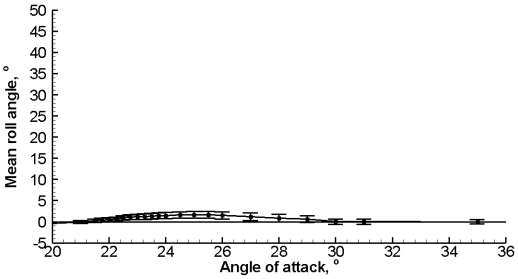

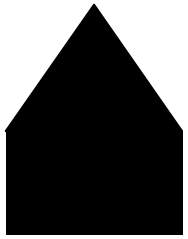

Figure 5.26 Graphs showing mean roll angle against angle of attack with standard deviation as error bars and schematics of each wing (right) for a) simple delta wing and b) - d) cropped delta wings with different cropped section lengths, all with $\Lambda = 55^{o}$ and sharp leading-edges.

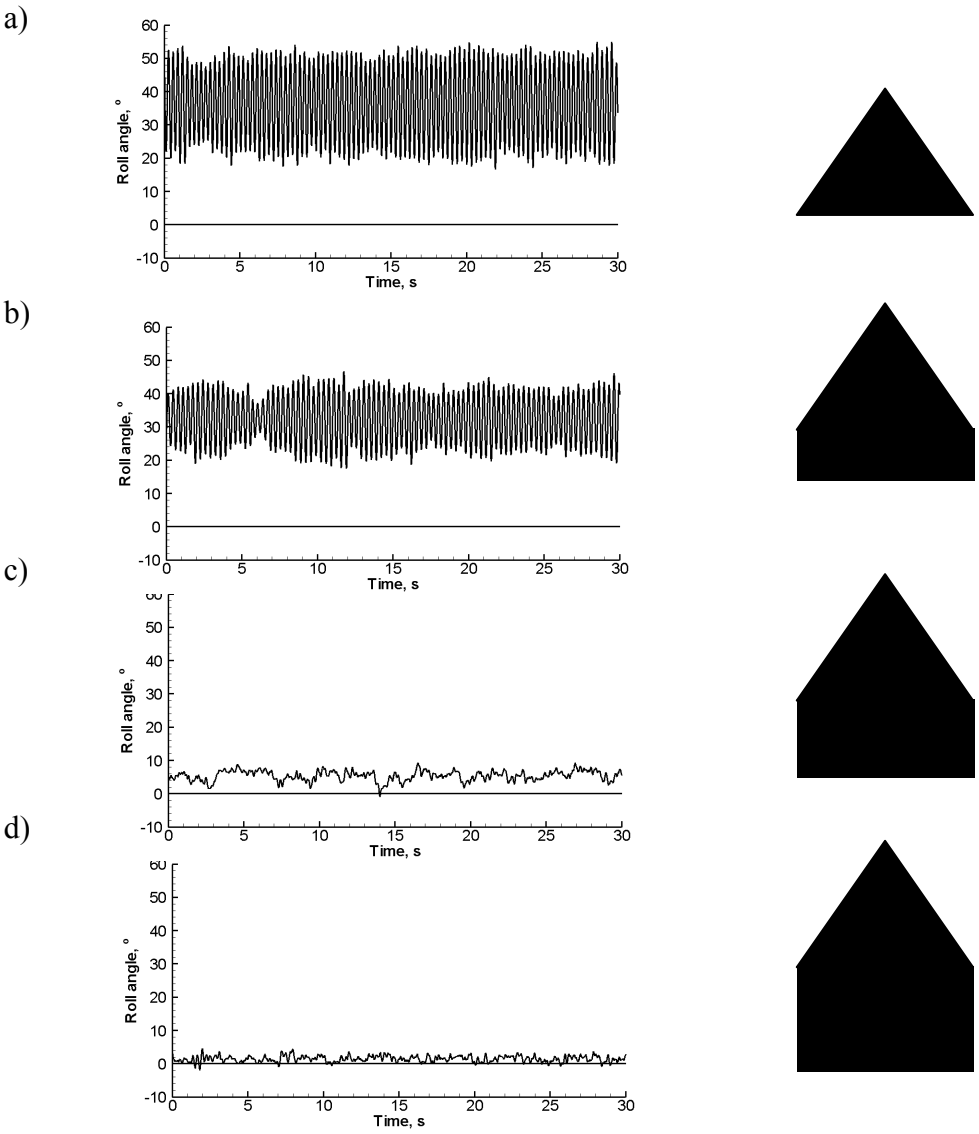

Figure 5.27 Graphs showing time histories of roll angle corresponding to maximum standard deviation (left, at $\alpha = 23.25^{o}$, 22.75^{o}, 26^{o} and 26^{o} respectively) and schematics of each wing (right) for a) simple delta wing and b) - d) cropped delta wings with different cropped section lengths, all with $\Lambda = 55^{o}$ and sharp leading-edges.

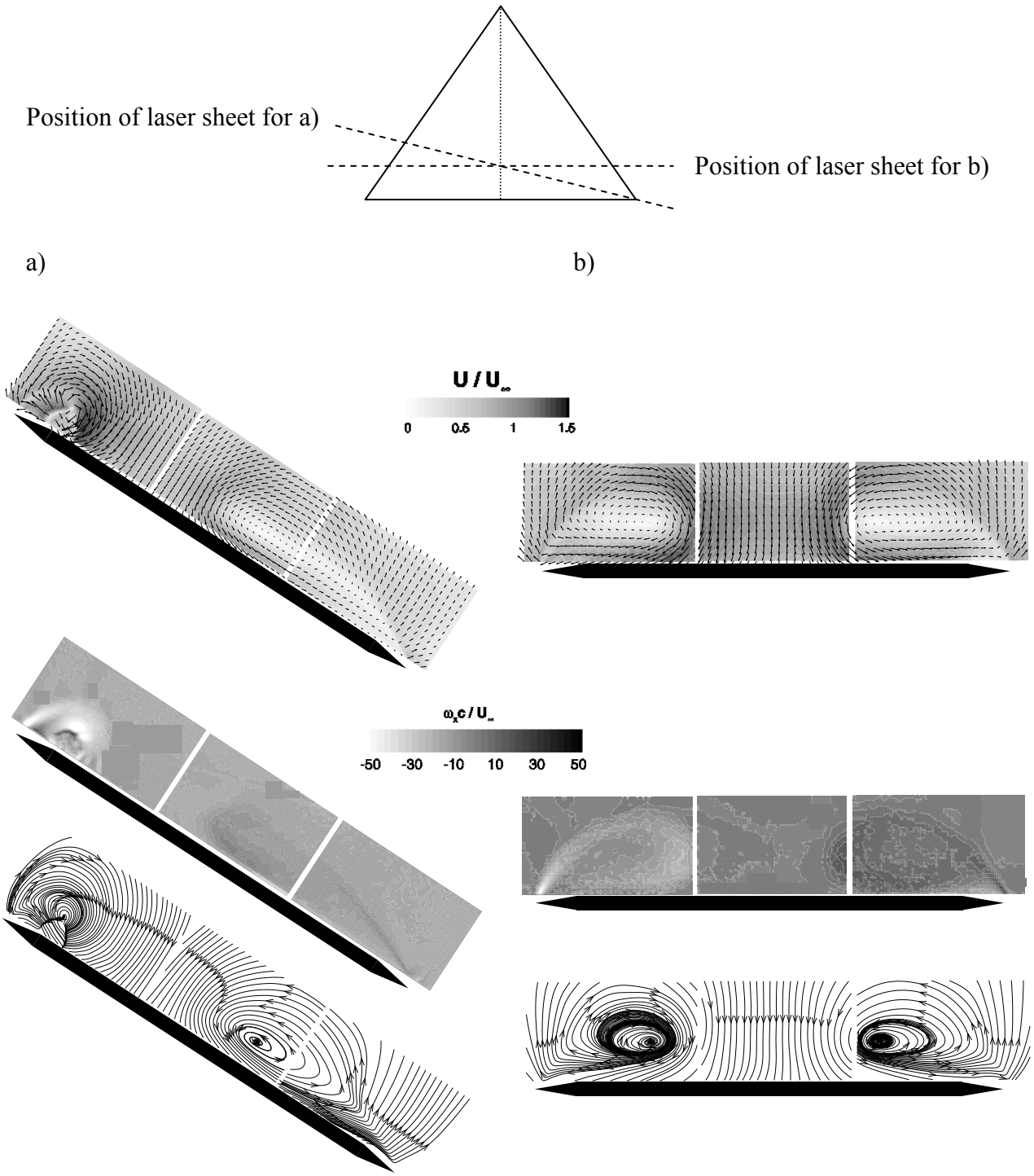

Figure 5.28 Cross-flow time-averaged velocity fields, vorticity and streamline patterns for stationary delta wing at a) $\Phi = 33^o$ (stable) and b) $\Phi = 0^o$ (unstable – will not stay at this roll angle in free-to-roll case) cases at x/c = 0.84 and $\alpha = 20^o$ for wing with $\Lambda = 55^o$ and sharp leading-edge together with schematic of laser sheet locations (top).

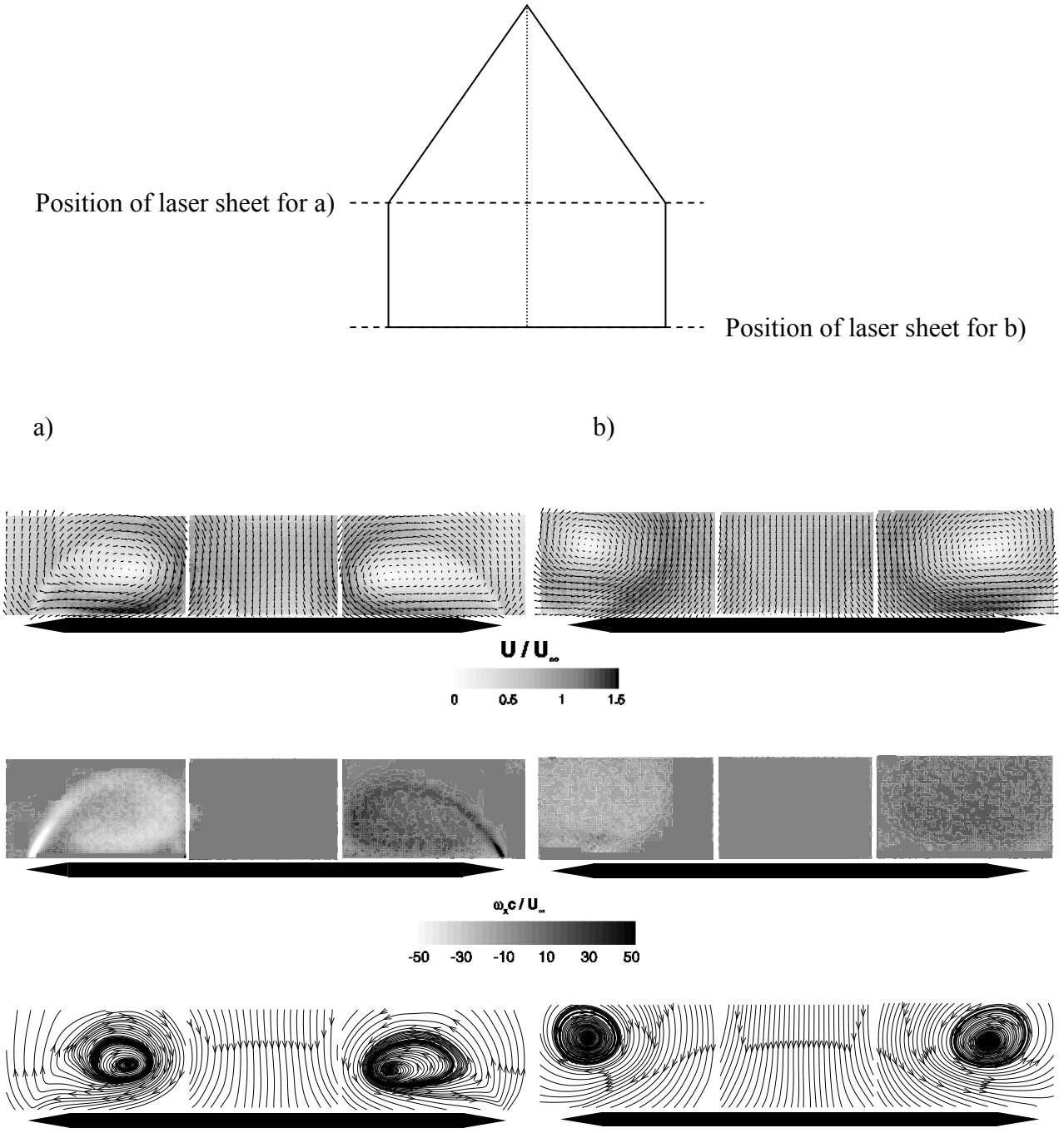

Figure 5.29 Cross-flow time-averaged velocity fields, vorticity and streamline patterns for stationary wing a) x/c = 39.5% and b) trailing edge, at $\alpha = 20^o$ and $\Phi = 0^o$ for cropped delta wing with $\Lambda = 55^o$ and sharp leading-edge, together with schematic of laser sheet locations (top).

a)

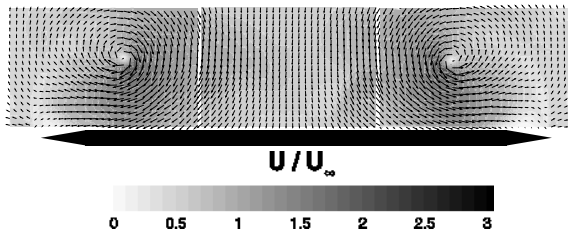

b)

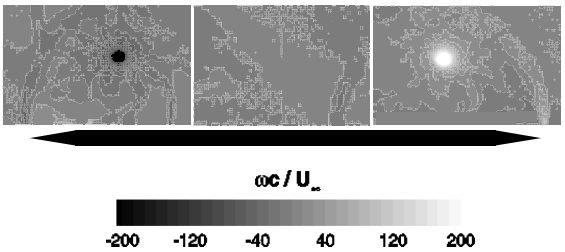

c)

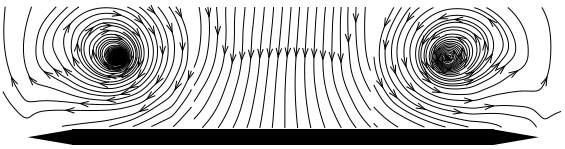

Figure 5.30 Cross-flow time-averaged velocity field, vorticity and streamline patterns for stationary delta wing at trailing-edge, at $\alpha = 20^o$ and $\Phi = 0^o$ for wing with $\Lambda = 70^o$ and sharp leading-edge.

a)

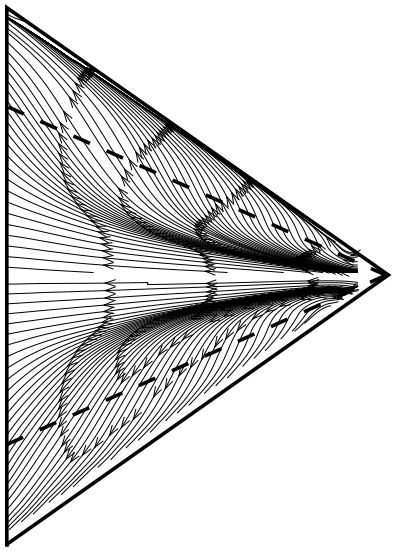

b)

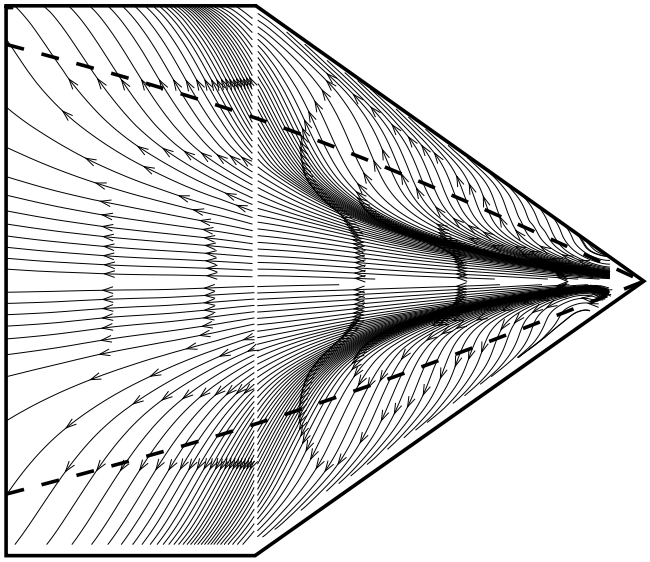

c)

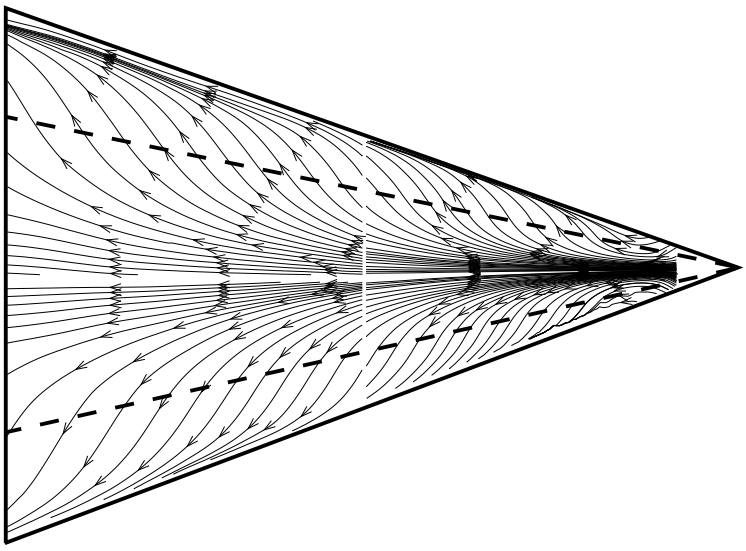

Figure 5.31 Near-surface time-averaged streamline patterns with vortex trajectory at $\alpha = 20^o$ and $\Phi = 0^o$ for delta wings with sharp leading-edges and a) $\Lambda = 55^o$; b) $\Lambda = 55^o$ with cropped section and c) $\Lambda = 70^o$.

Chapter 6 Effect of Pitching Manoeuvre

Transient pitching tests were performed on different wings using the free-to-roll sting shown in Fig. 2.3, and the roll angle was logged at a sampling rate of 250 Hz to determine what might happen to a MAV with non-slender delta wing planform during a gust encounter or manoeuvre. This gust response is serious because it would theoretically affect the actual flight path of the aircraft in question. The range of reduced frequency, designated k, was between 0.06 and 0.22, which again is quite low.

6.1 Thick wing with round leading-edges

Figure 6.1a) shows the pitching range for the thick wing (wing number 1 in Table 2.1) as it pitches from an angle of attack where there are no roll oscillations ($\alpha = 20^o$) to one where self-excited roll oscillations are experienced ($\alpha = 27^o$). The variation of angle of attack with time and the free-to-roll response is shown in Fig. 6.1b). This type of Figure is used for each case in this Chapter. A significant delay can be seen when the wing has finished pitching to increased angle of attack before the oscillations start building up; this is caused by the insensitivity of the round leading-edge to angle of attack. It is observed with the angle of attack both increasing and decreasing, but the time delay is greater with the angle of attack increasing.

If the wing is pitching from a flight condition to a stall condition the delay is still present, albeit smaller. On pitching into a stall condition as in Fig. 6.2b)(i), the wing is slower than it should be to stall, while coming out of the stall condition in (ii) it is slow too, having to achieve a lower angle of attack to get back to normal flight conditions. In this flight regime, especially Fig. 6.2b)(ii), oscillations can be seen to die down rapidly. The current observations suggest that, due to the round leading-edge of this planform, there is a delay and also insensitivity of the wing response to pitching manoeuvres.

Figure 6.3 shows the response of the wing to pitching from angles of attack of roll oscillations to stall. Going into stall (Fig. 6.3b)(i)), an angle of attack of $\alpha \sim 35^o$ needs to be achieved before normality is resumed, this angle being slightly higher than expected from the error bars in the plot from the full free-to-roll case in Fig. 6.3a). There is more of a delay coming out of the stall condition with the wing needing to achieve $\alpha \sim 29^o$ (shown in Fig. 6.3b)(ii)) before the wing oscillates. The oscillations do

seem to build up rapidly though and the period while the wing settles into or out of an oscillatory mode is only small - a couple of oscillations in magnitude.

Finally for the thick wing, tests were attempted pitching the wing from a condition after the oscillations and before the stall, to a condition with the wing stalled. The results are shown in Fig. 6.4 and show a significant time delay. In Fig. 6.4b)(i), it can be seen that the wing responds rapidly to the angle of attack going into stall, after some initial oscillations while the wing settles. However, if the same pitching is tried with the wing going from $\alpha = 36^o$ to $\alpha = 33^o$ in part (ii), there is no response from the wing, highlighting the delay for this planform shape, and presumably the round leading-edges. Thus if an aircraft with this planform were trying to pull out of a stall condition, it would have to reduce the angle of attack further than expected first.

6.2 50^o sweep angle delta wing with sharp leading-edges

Figures 6.5 to 6.7 show the results of a 50^o sweep angle delta wing with sharp leading-edges (wing number 4 in Table 2.1) going between various conditions. This is the same as the wing in Fig. 6.1 and is wing number 4 in Table 2.1, though with sharp leading-edges instead of round, different wing weight and exactly the same dimensions (apart from thickness). The moments of inertia about the roll axis (I_{xx}) are different too, again shown in Table 2.1, though this was thought to affect the frequency of the oscillations, rather than whether the oscillations occurred or not.

Three different regions were tested for this wing. The first, shown in Fig. 6.5, was from normal flight conditions to stall. As expected, the wing responded rapidly, with again a few oscillations on reaching its target angle of attack while the wing settled, shown in Figs. 6.5b)(i) and 6.5b)(ii). These oscillations are presumably down to the moment of inertia of the wing about the roll axis taking it beyond the expected flight condition. Thus the wing rapidly settled into a slightly different condition once the oscillations have died off. Again, in Fig. 6.5b)(ii), the wing is slightly slower to respond when one considers the angles of attack that needs to be achieved before the oscillations begin as expected. It requires an angle of attack of $\alpha \sim 22^o$ to come out of stall, which is slightly lower than expected.

Upon pitching from a normal flight regime into a region with oscillations, Fig. 6.6b)(i) shows the slow response of the wing. Upon stalling, Fig. 6.6b)(ii) shows the wing rapidly stalling, with no roll oscillations evident this time. This is presumably because the low roll angle change does not allow the wing to build up its dynamic moment of inertia about the roll axis, so momentum in a rolling motion is minimal.

Finally for this wing, if the plane were going from an angle of attack with roll oscillations to a stall condition as in Fig. 6.7a), Fig. 6.7b)(i) shows a rapid response of the wing upon stalling. There are also some oscillations due to the moment of inertia about the roll axis as previously seen, but these soon die away. Coming out of the stall condition is, however, slower, but still much more rapid than for the thick wing with the same shape, bar the leading-edges and slightly different weight (shown in Table 2.1). This highlights the insensitivity of the thick, round leading-edge.

6.3 55^o sweep angle delta wing with sharp leading-edges

Figures 6.8 – 6.10 show the transient performance of the 55^o sweep delta wing with sharp leading-edges (wing number 6 in Table 2.1) pitching between similar conditions as in Figs. 6.1 - 6.3. In this case the response of the wing is rapid, with oscillations building up quickly.

Figure 6.8 presents the response of the wing going from a normal flight condition (albeit at a high angle of attack) to an oscillatory angle of attack. The delays of the wing roll oscillations in this case, Figs. 6.8b)(i) and (ii), are very small, with oscillations building up or down according to the angle of attack. There is a slight time delay for the oscillations to build up, though this is again thought to be due to the wing having a finite weight and moment of inertia about the roll axis.

Figure 6.9 shows the same wing going from a normal flight regime to a stall condition, presumably because of a gust due to the aircraft being MAVs. Upon going from a stall condition to a normal flight mode in Fig. 6.9b)(ii), the response is slightly slower than expected, and again we have oscillations which die out rapidly due to the finite wing weight. Response of the wing, however, is good due to the sharp leading-edges and delays are short in time.

Finally, Fig. 6.10 shows the response of the 55^{o} wing moving from a region where it is stalled to a region of oscillations. Again, the response of the wing is rapid, with the oscillations building up with little time delay, thus of consequence for a MAV with such planform pulling out of a stall condition such as in Fig. 6.10b)(ii). This continues to insinuate that the sharp-edge makes the wing much more responsive, with minimal delays.

In summary, the thick wing does not come out of its stall position upon a small reduction in angle of attack. This is shown in Fig. 6.4b)(ii) and is due to the insensitivity to angle of attack of the round leading-edge and thicker wing being used, allowing the separation point to move. The wings always have a time delay coming out of the stall position, shown in Figs. 6.2, 6.5, 6.7 and 6.10 in part (ii). This will affect the wing performance in flight when manoeuvring or because of a gust. However, Fig. 6.9b)ii) shows that movement over the oscillations at a fairly slow rate does not allow the oscillations to build up, which is good from an aircraft designer's point of view.

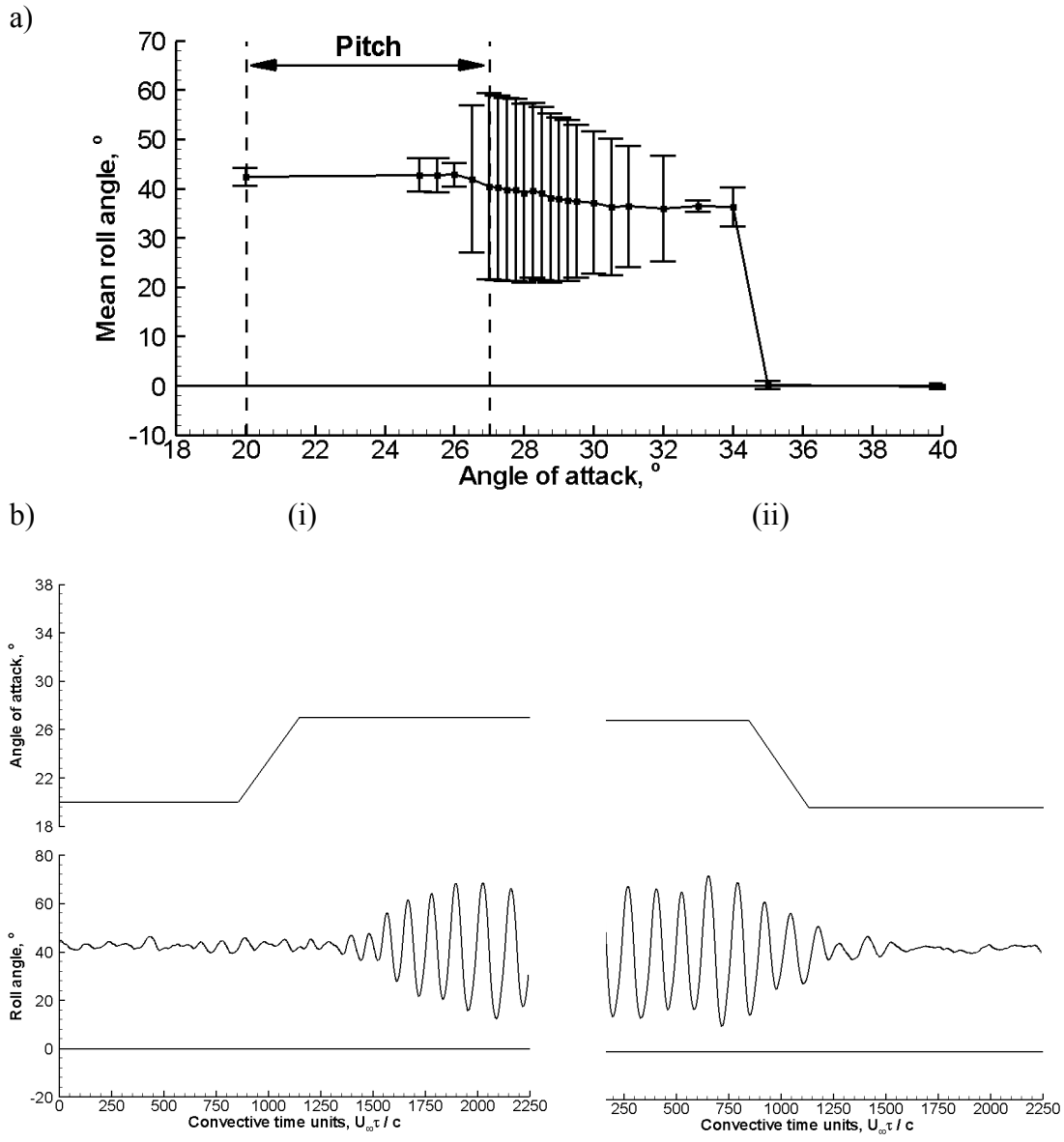

Figure 6.1 a) Mean roll angle plot showing pitching range together with error bars from a static (with regards to angle of attack) experiment showing standard deviation of oscillations and b) transient performance of wing with $\Lambda = 50^o$, t/c = 10 % and round leading-edge going from (i) $\alpha_0 = 20^o$ to $\alpha_1 = 27^o$ and (ii) $\alpha_0 = 27^o$ to $\alpha_1 = 20^o$ at constant rate.

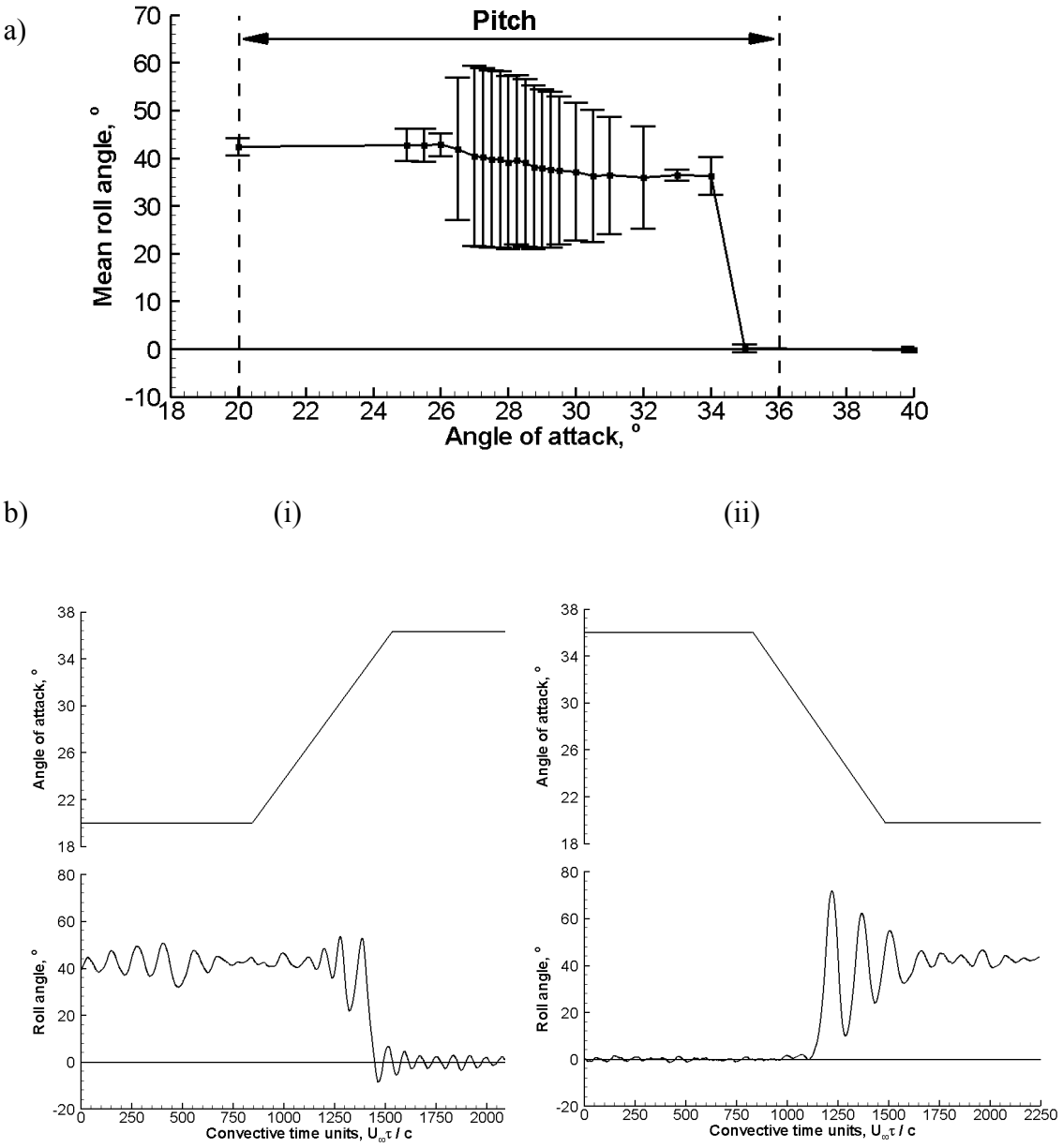

Figure 6.2 a) Mean roll angle plot showing pitching range together with error bars from a static (with regards to angle of attack) experiment showing standard deviation of oscillations and b) transient performance of wing with $\Lambda = 50^o$, t/c = 10 % and round leading-edge going from (i) $\alpha_0 = 20^o$ to $\alpha_1 = 36^o$ and (ii) $\alpha_0 = 36^o$ to $\alpha_1 = 20^o$ at constant rate.

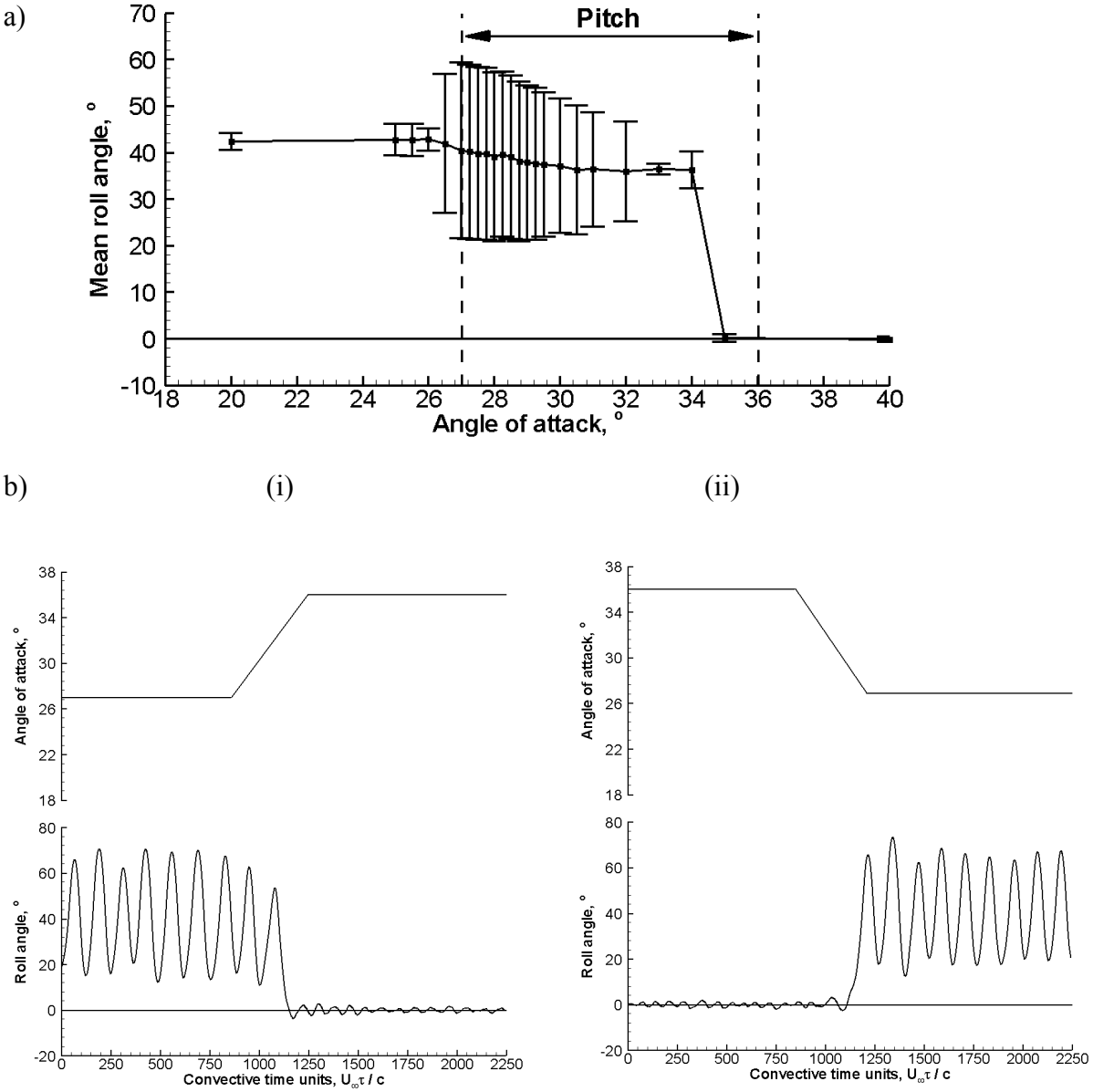

Figure 6.3 a) Mean roll angle plot showing pitching range together with error bars from a static (with regards to angle of attack) experiment showing standard deviation of oscillations and b) transient performance of wing with $\Lambda = 50^o$, t/c = 10 % and round leading-edge going from (i) $\alpha_0 = 27^o$ to $\alpha_1 = 36^o$ and (ii) $\alpha_0 = 36^o$ to $\alpha_1 = 27^o$ at constant rate.

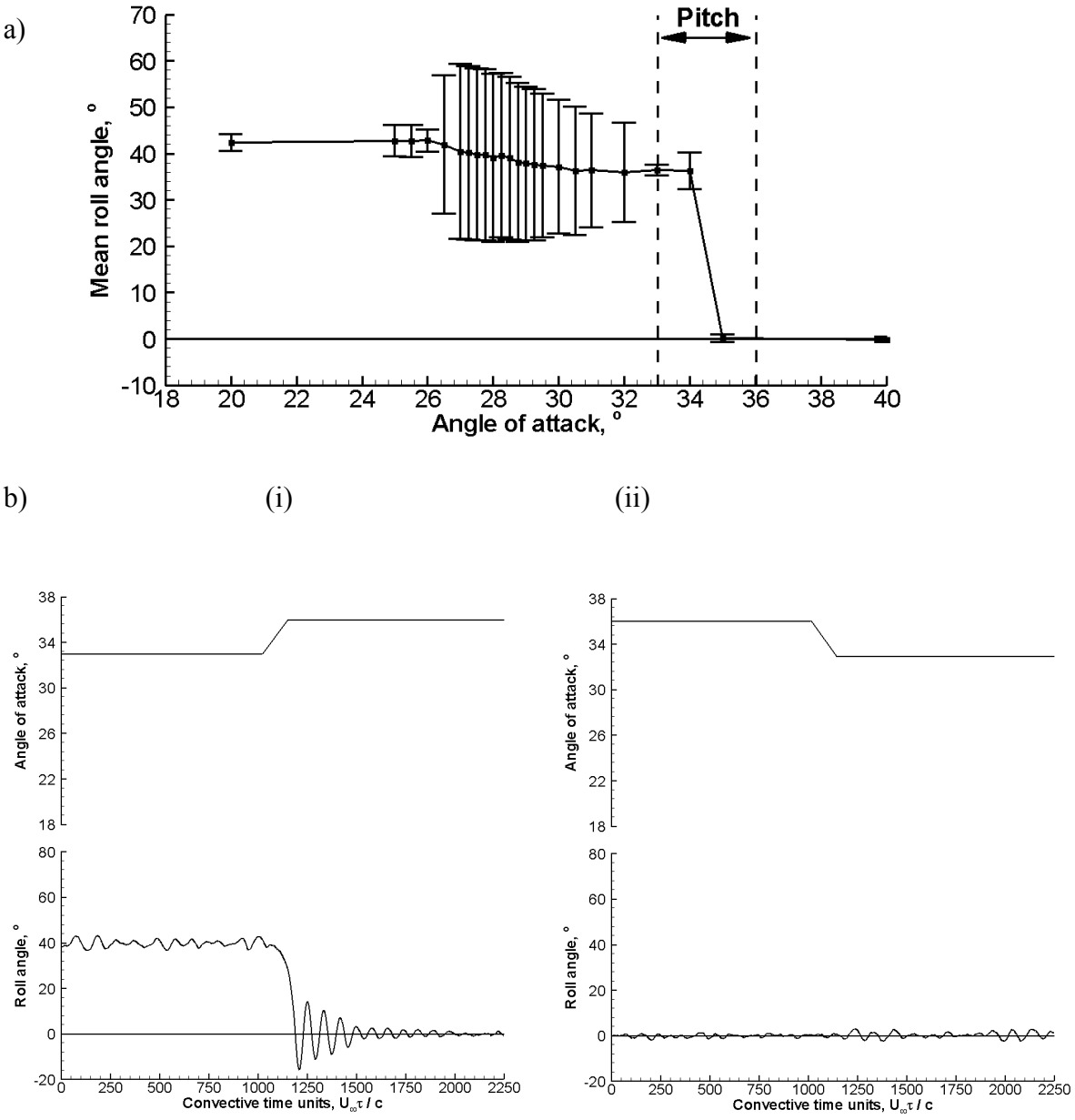

Figure 6.4 a) Mean roll angle plot showing pitching range together with error bars from a static (with regards to angle of attack) experiment showing standard deviation of oscillations and b) transient performance of wing with $\Lambda = 50^o$, t/c = 10 % and round leading-edge going from (i) $\alpha_0 = 33^o$ to $\alpha_1 = 36^o$ and (ii) $\alpha_0 = 36^o$ to $\alpha_1 = 33^o$ at constant rate.

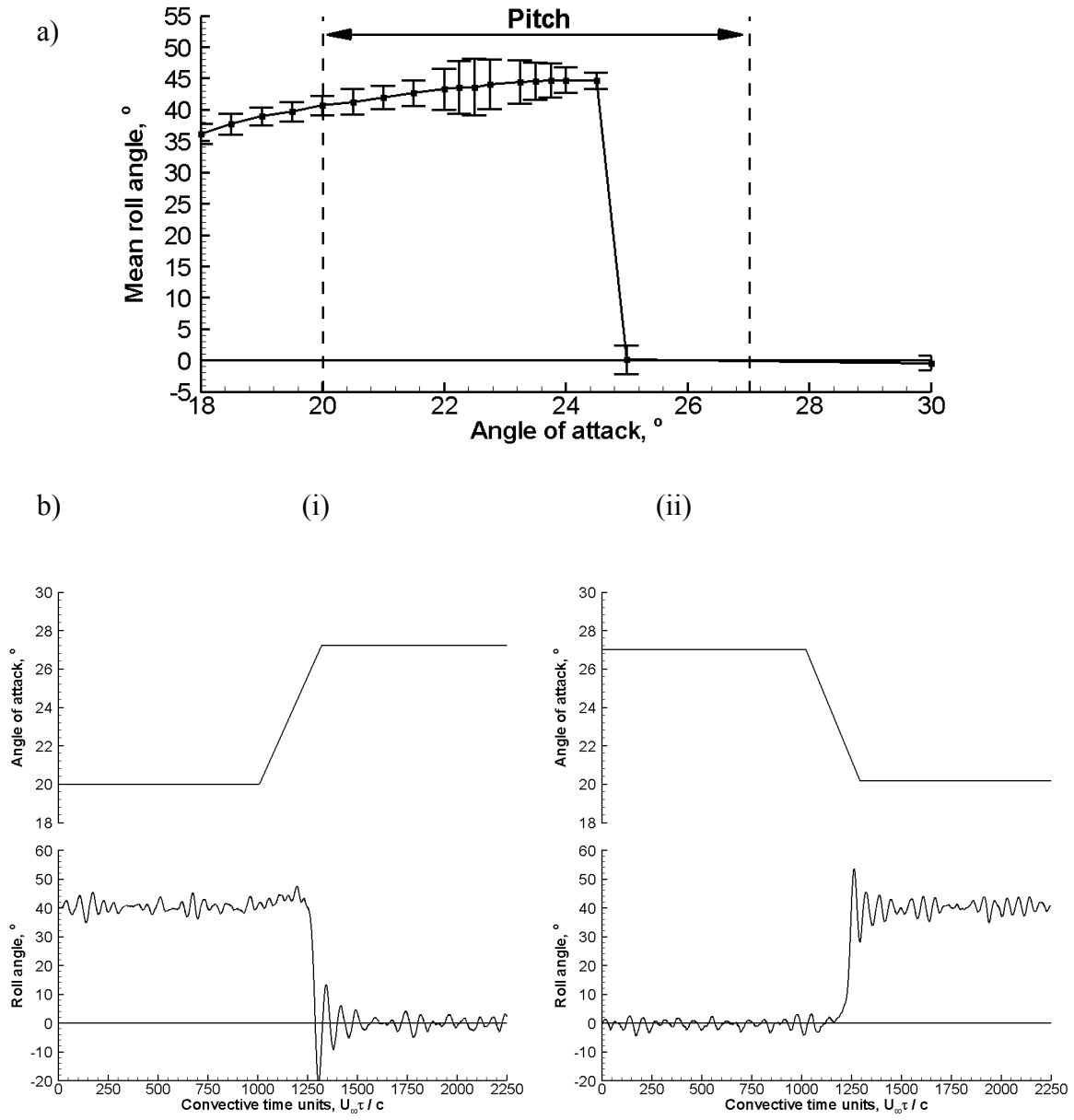

Figure 6.5 a) Mean roll angle plot showing pitching range together with error bars from a static (with regards to angle of attack) experiment showing standard deviation of oscillations and b) transient performance of wing with $\Lambda = 50^o$, t/c = 1.5 % and sharp leading-edge going from (i) $\alpha_0 = 20^o$ to $\alpha_1 = 27^o$ and (ii) $\alpha_0 = 27^o$ to $\alpha_1 = 20^o$ at constant rate.

a)

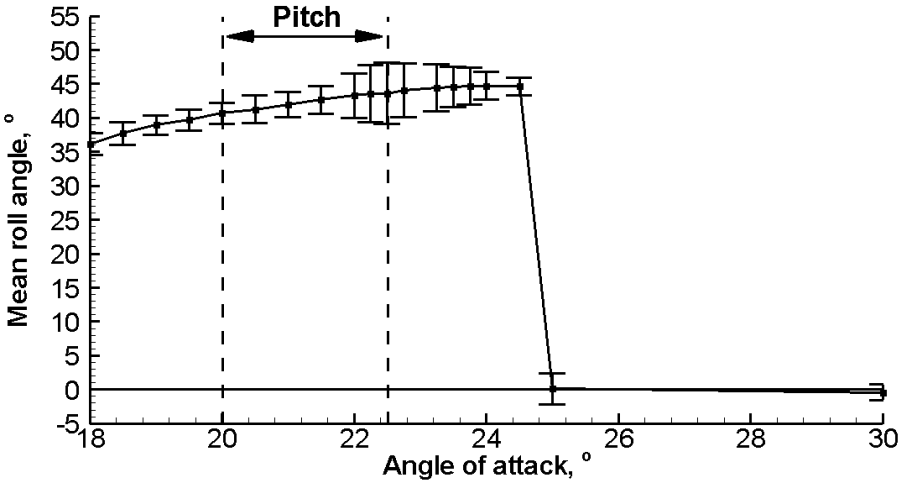

b) (i) (ii)

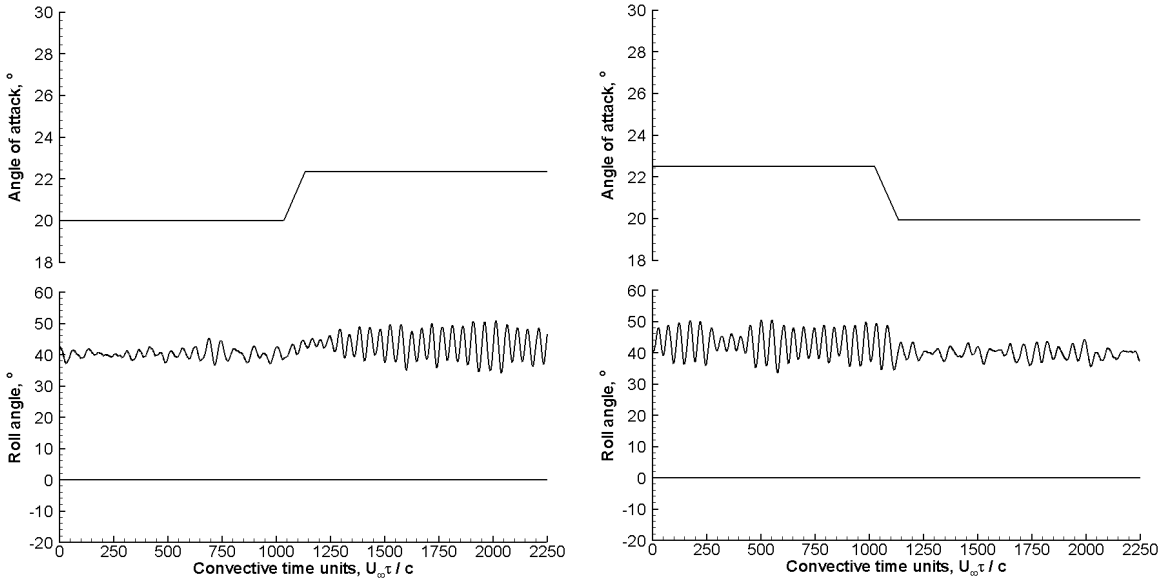

Figure 6.6 a) Mean roll angle plot showing pitching range together with error bars from a static (with regards to angle of attack) experiment showing standard deviation of oscillations and b) transient performance of wing with $\Lambda = 50^o$, t/c = 1.5 % and sharp leading-edge going from (i) $\alpha_0 = 20^o$ to $\alpha_1 = 22.5^o$ and (ii) $\alpha_0 = 22.5^o$ to $\alpha_1 = 20^o$ at constant rate.

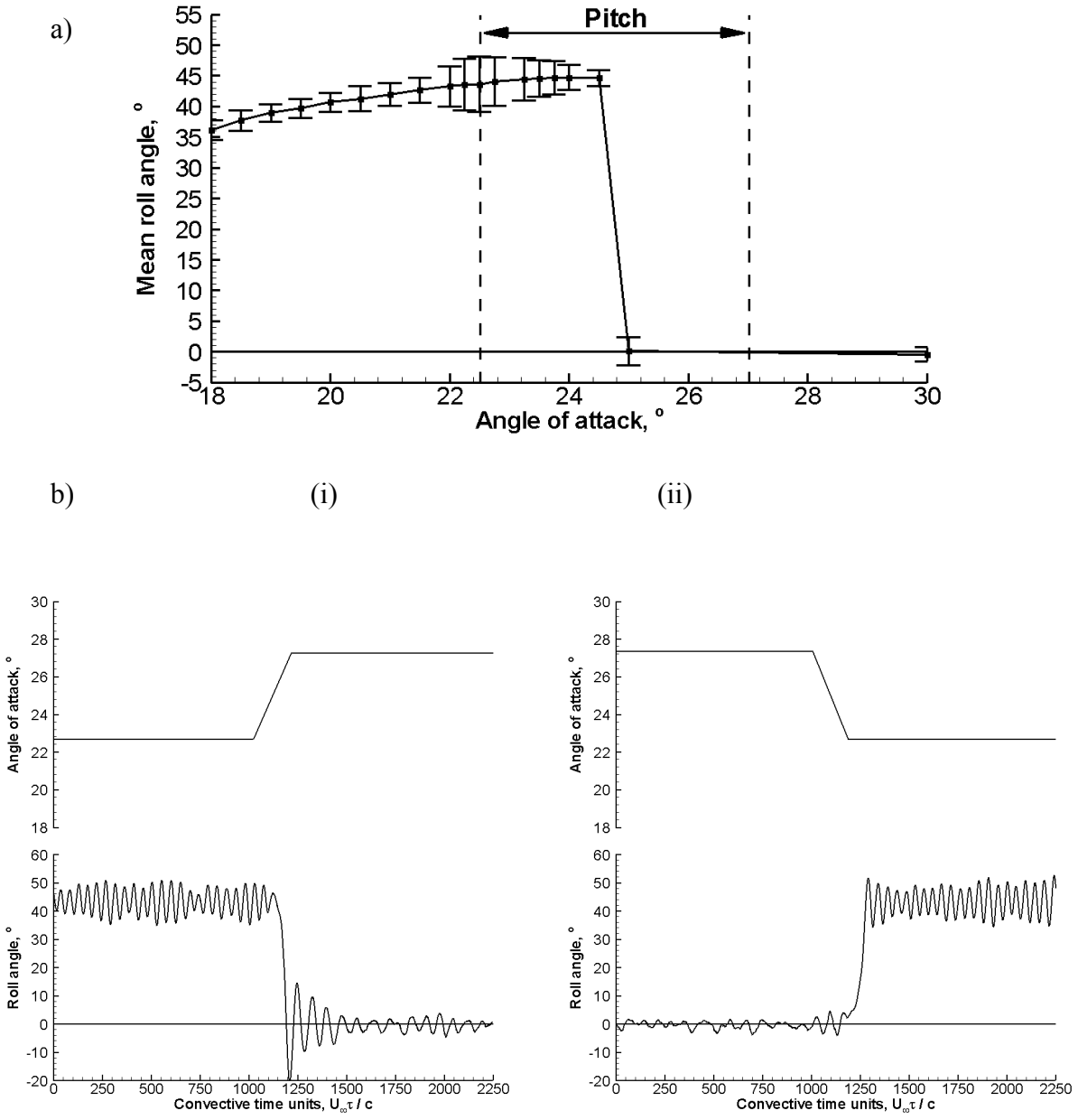

Figure 6.7 a) Mean roll angle plot showing pitching range together with error bars from a static (with regards to angle of attack) experiment showing standard deviation of oscillations and b) transient performance of wing with $\Lambda = 50^o$, t/c = 1.5 % and sharp leading-edge going from (i) $\alpha_0 = 22.5^o$ to $\alpha_1 = 27^o$ and (ii) $\alpha_0 = 27^o$ to $\alpha_1 = 22.5^o$ at constant rate.

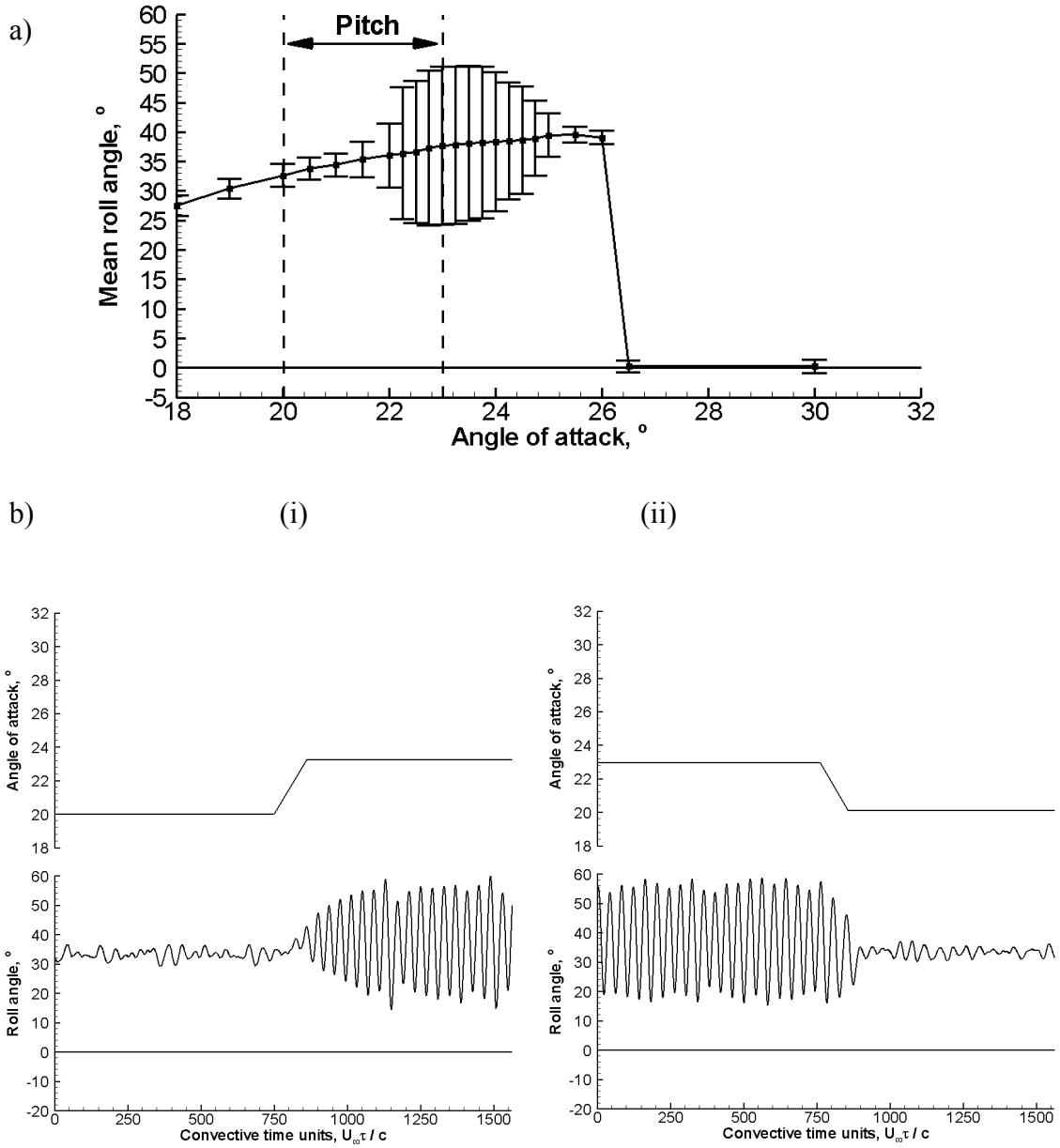

Figure 6.8 a) Mean roll angle plot showing pitching range together with error bars from a static (with regards to angle of attack) experiment showing standard deviation of oscillations and b) transient performance of wing with $\Lambda = 55^o$, t/c = 1.25 % and sharp leading-edge going from (i) $\alpha_0 = 20^o$ to $\alpha_1 = 23^o$ and (ii) $\alpha_0 = 23^o$ to $\alpha_1 = 20^o$ at constant rate.

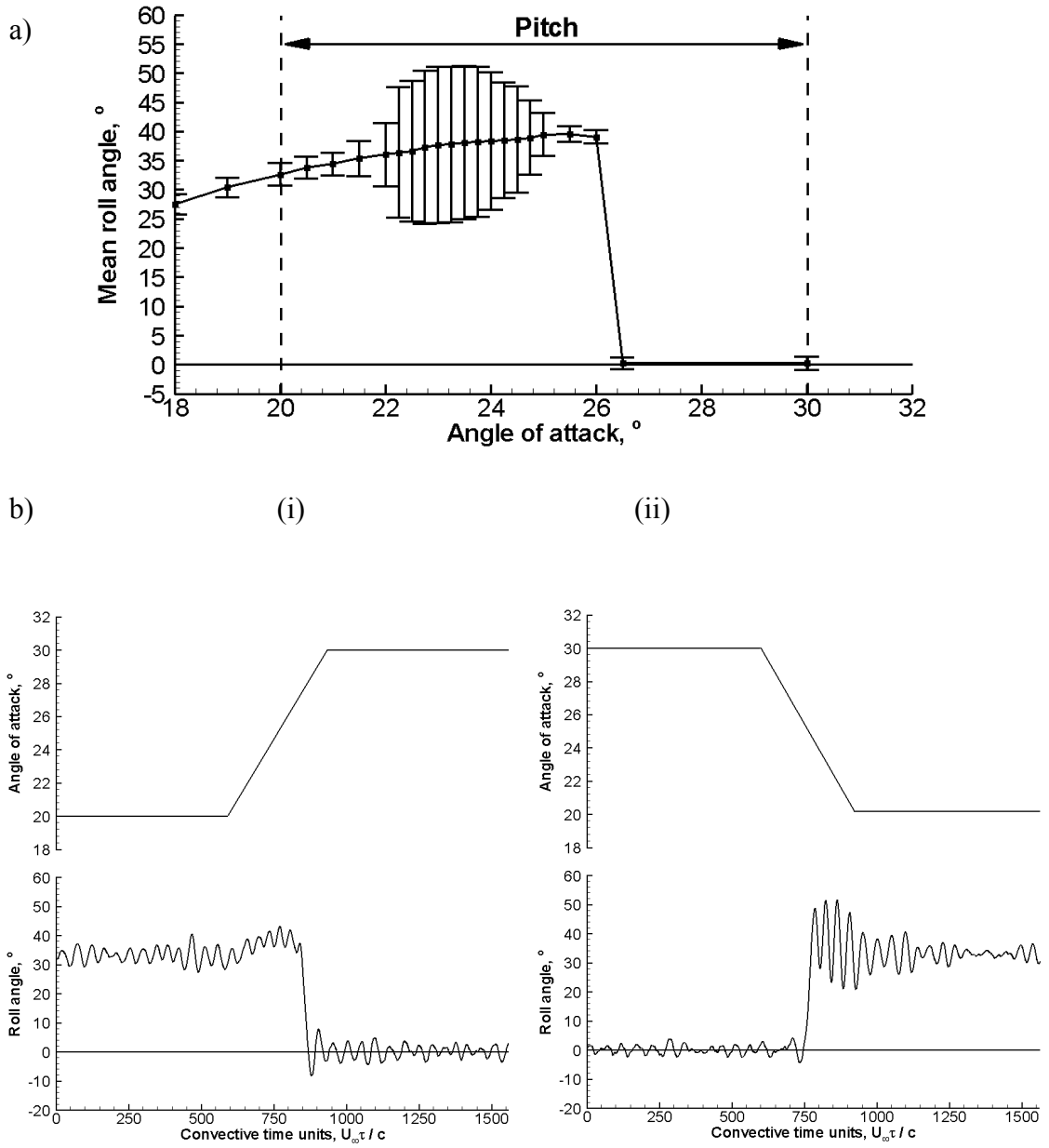

Figure 6.9 a) Mean roll angle plot showing pitching range together with error bars from a static (with regards to angle of attack) experiment showing standard deviation of oscillations and b) transient performance of wing with $\Lambda = 55^o$, t/c = 1.25 % and sharp leading-edge going from (i) $\alpha_0 = 20^o$ to $\alpha_1 = 30^o$ and (ii) $\alpha_0 = 30^o$ to $\alpha_1 = 20^o$ at constant rate.

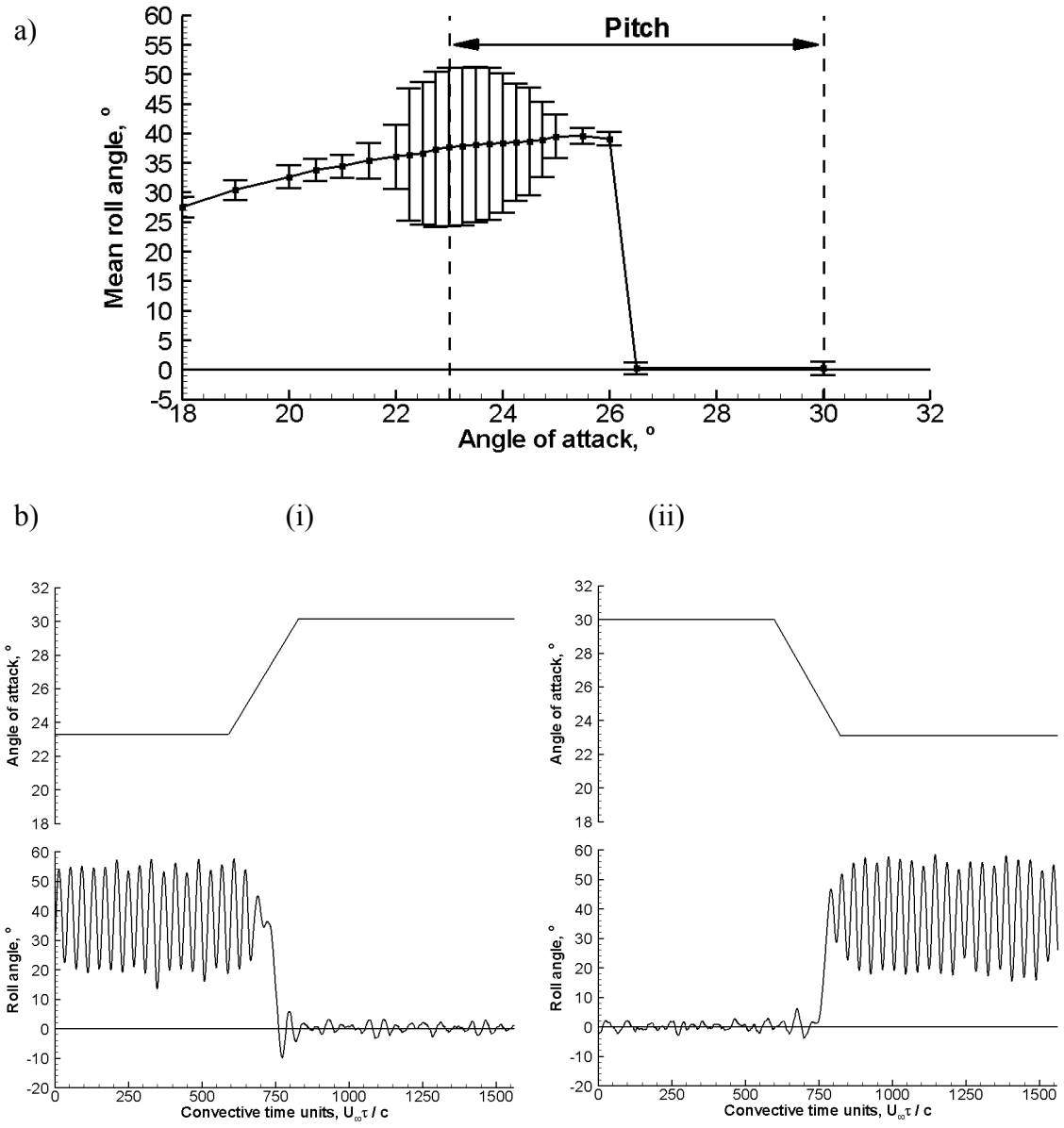

Figure 6.10 a) Mean roll angle plot showing pitching range together with error bars from a static (with regards to angle of attack) experiment showing standard deviation of oscillations and b) transient performance of wing with $\Lambda = 55^o$, t/c = 1.25 % and sharp leading-edge going from (i) $\alpha_0 = 23^o$ to $\alpha_1 = 30^o$ and (ii) $\alpha_0 = 30^o$ to $\alpha_1 = 23^o$ at constant rate.

Chapter 7 Other Planform Shapes

Investigations were performed to look at the free-to-roll behaviour of other, more common non-delta planforms.

7.1 Free-to-roll behaviour of rectangular wings

Figure 7.1a) shows a summary of the behaviour of the rectangular wing with aspect ratio AR = 2 and round edges at a Reynolds number of Re = 1.14 x 10^5. In addition, mean positive peak and mean negative peak values are given as the roll oscillations often exhibit some amplitude modulation. At low angles of attack, up to $\alpha = 10^o$, the mean roll angle is seen to be non-zero. This suggests asymmetry in the flow structure, which will be discussed later on in this Chapter. The lift measurements of Torres and Mueller[4] give the stall angle as $\alpha_{Clmax} = 18^o$ for a similar flat wing at a similar Reynolds number. This stall angle is significantly higher than where self-excited roll oscillations are first observed. As it will be shown later, complete flow separation without any reattachment takes place around $\alpha = 12°$, even though the lift may continue to increase for larger incidences, due to the increasing strength of the tip vortices. It is interesting that the onset of the roll oscillations coincides with the full separation from the wing at $\alpha = 12°$, as will be shown in the coming Figures.

As the angle of attack is increased in Fig. 7.1a), the amplitude of the oscillations is seen to increase, with the absolute maximum and minimum roll angles achieved during the 90 s also increasing. Maximum or minimum roll angle eventually reaches 90^o, after which the wing exhibits intermittent or continuous autorotation, dependent on the angle of attack α. Figure 7.1b) shows a wing undergoing self-excited roll oscillations, and a free-to-roll time history at the maximum angle of attack that the wing achieved without autorotation. The oscillations can be seen to be periodic and of large amplitude with a slightly non-zero mean roll angle in this case, which we will come back to in the discussion of the PIV data. The wing is at an angle of attack of $\alpha = 21°$ in the post-stall regime (this was confirmed with tuft visualisation, but not shown here). The data presented here is the first documented case of a wing of such aspect ratio exhibiting these oscillations. No free-to-roll experiments on wings with larger aspect ratios, such as AR = 2 or 4, have been reported in the literature, hence the discovery of oscillations for this wing, and also for AR = 4, is interesting and unexpected.

Figures 7.2 and 7.3 show similar data to Fig. 7.1, but at Re = 2.28 x 10^5 and Re = 3.42 x 10^5 respectively. In all these cases (including those to be mentioned), non-zero mean roll angles at low angles of attack were seen, all of a similar magnitude to Re = 1.14 x 10^5. It can be seen that the oscillations build up more rapidly as Reynolds number is increased, with autorotation starting earlier for larger Reynolds number (at $\alpha = 21.25^o$ for 1.14 x 10^5, $\alpha = 15.75^o$ for Re = 2.28 x 10^5 and $\alpha = 15.25^o$ for Re = 3.42 x 10^5). The free-to-roll time histories show that the mechanism for the autorotation starting is the same in all cases, beginning when the maximum or minimum roll angle surpasses the 90^o roll angle threshold.

Flow patterns over the stationary wing at zero roll angle were investigated using near-surface PIV measurements at various angles of attack for the wing with round edges at Re = 1.14 x 10^5. The results are shown in Fig. 7.4, which reveal the formation of a separation bubble at low angles of attack. This type of separation bubble is referred to as a long bubble because of it increasing in length with angle of attack[64]. Rectangular wings of relatively low aspect ratio have a very three-dimensional flow structure due to the effect of the tip vortices, and significant variations in the bubbles due to the tip vortices. At $\alpha = 5^o$ in both Figs. 7.4 and 7.5 the leading-edge separation bubble is not formed along the entire leading-edge and is not symmetrically located, thus different amounts of attached flow on each wing half are present, generating different loading. This explains the non-zero roll trim angle if the wing is set free-to-roll. As the angle of attack is increased, this asymmetry on the stationary wing disappears and the separation bubble is seen to grow; this corresponds to the mean roll angle becoming closer to zero in Fig. 7.1a) for the free-to-roll wing. At around $\alpha = 12^o$, there is little evidence of the separation bubble as the reattachment has passed the trailing-edge. The roll oscillations begin for the free-to-roll wing at this angle of attack. For $\alpha > 6^o$, the swirling flow structures on each wing half near the tip regions can be observed. These foci are an outcome of three-dimensional separation caused by the interaction between the side-edge vortices and stalled flow within the separation bubble[70,71]. As the separation bubble becomes larger, this interaction becomes greater due to the increasing proximity of the separation bubble to the side-edges. The swirling flow structures are seen to move downstream with increasing angle of attack, until they pass the trailing-edge between $\alpha = 25^o$ and $\alpha = 35^o$, which was where the autorotation ceased.

In order to investigate why the wings trimmed to non-zero roll angles, near-surface PIV measurements were performed at the trim angle ($\Phi = 14.4^o$) for the wing with round edges at $Re = 1.14 \times 10^5$ and $\alpha = 5^o$. This data, and the data for $\Phi = 0^o$ at the same angle of attack from Fig. 7.4, are shown in Fig. 7.5 for comparative purposes. It can be seen that at the trim angle, the leading-edge separation bubble extends over a much larger portion of the span, and it is more symmetrical, which confirms why the wing is trimmed at this roll angle. For the zero roll angle case the leading-edge separation bubble is not symmetrically formed, which might be due to small, non-visible manufacturing imperfections for the round leading-edge and free-stream non-uniformity.

The above data suggest that, despite having a low thickness-to-chord ratio, the round leading-edge does not fix the separation point, which is of importance for practical purposes. To investigate the effect of leading-edge separation, a sharp-edged version of the same wing was fabricated and the free-to-roll results presented in Fig. 7.6. The effects of Reynolds number and sharp edges for the rectangular wings with AR = 2 are not significantly different to Fig. 7.1. From Fig. 7.6, it can be seen that at low angles of attack, the tendency of the wing to find non-zero trim angles is significantly reduced, thus highlighting the sensitivity of the separation bubble to any imperfections in the leading-edge. Figure 7.7 shows the corresponding near-surface streamlines at $\alpha = 5^o$ and $\Phi = 0^o$, and it can be seen that with a fixed separation line, the separation bubble extends over a larger portion of the wing span than for the round leading-edge and appears more symmetrically located. This stabilises the wing and causes the roll trim angle to remain near zero. Also, at higher angles of attack, the autorotation is seen to begin slightly earlier than for the round leading-edge.

Results for all the rectangular wings are summarised in Fig. 7.8, which shows the variation of Strouhal number, fc/U_∞, where U_∞ is the free-stream velocity and f is the frequency of the roll oscillations. Here, the data for the rectangular wing with AR = 4 were also included for comparison with the results for the rectangular wing which had AR = 2 and round edges. These show that the oscillations become larger with increasing Reynolds number. It is noted that all the Strouhal numbers are low, of the order of 10^{-2}, which are similar to those expected for MAVs encountering typical atmospheric gusts.

In all cases the Strouhal number is seen to decrease with angle of attack. This is contrary to what was seen[63,65,67] for self-induced roll oscillations of low aspect ratio rectangular wings where the reduced frequency either remained the same or increased. It is also different to the increase seen for slender wing rock[34]. The rectangular wing with AR = 4 shows the lowest Strouhal number of oscillations, presumably because of its higher moment of inertia about the roll axis.

Figure 7.9a) shows the free-to-roll behaviour of the rectangular wing with AR = 4 and again a non-zero roll trim angle was observed at low angles of attack. The build-up of the oscillations can be seen in Figs. 7.9b) - d), increasing in amplitude with angle of attack until autorotation began at $\alpha = 16.25^{o}$. In a similar fashion to Fig. 7.4, a progression of near-surface streamlines for the stationary wing at $\Phi = 0^{o}$ for different angles of attack are shown in Fig. 7.10. Initially, at $\alpha = 3^{o}$, the separation bubble can be seen to be asymmetric, which explains the non-zero roll trim angle for the free-to-roll wing and is thought to be due to the round side-edges. This bubble spreads across the extent of the wing with increasing angle of attack as the reattachment line moves downstream. Again the oscillations were seen to begin once the bubble had left the trailing-edge and the side-edge vortices had increased in strength sufficiently. For all the rectangular wings, whether of AR = 2 or AR = 4, the distance between the side-edge vortices was large. This is shown that there is a lack of interaction between the tip vortices, as demonstrated in Figs. 7.11 and 7.12 for the AR = 2 wing case and regardless of the edge geometry.

7.2 Possible mechanism of rectangular wing oscillations

Now, to look at the actual mechanism of oscillations and the movement in a cross-flow plane of the side-edge vortices, it is necessary to look at the cross-flow PIV measurements during the oscillations on the rectangular wing with AR = 2 and round edges at $Re = 1.14 \times 10^{5}$ and $\alpha = 15^{o}$. Figures 7.11 and 7.12 show the phase-averaged cross-flow velocity and how the position of the vortices varies for: a) a stationary wing; b) the wing rolling in an anticlockwise direction and c) the wing rolling in a clockwise direction. From these data, it can be seen that the lift is driven by a small, compact vortex near the wing surface, while the opposing vortex is further from the wing surface (consequently having less of an effect) and also of smaller magnitude. Going on to look

at the effect of the vortices on one other, Fig. 7.12 shows the well defined separation of the side-edge vortices, so the effect on one another is expected to be negligible, unlike for slender wing rock. Thus it is confirmed that it must be a delay of some sort driving the motion, as in non-slender delta wing rock in the previous Chapters.

The mean roll angle is slightly larger than zero in this case. Figure 7.13a) shows the static case (at a slightly non-zero mean roll angle of $\phi = 3°$), and the salient feature to note is the symmetry of the flow structure, with each side-edge vortex being of similar size. The non-dimensional circulation in the stationary case, $\Gamma/U_\infty c$ of the left hand vortex is –0.20, while that of the right hand vortex is 0.23, the difference being due to the slightly non-zero mean roll angle (all circulation data from Fig. 7.12). This symmetry is lost in the dynamic case of Fig. 7.13 at the same roll angle. When the wing rolls in the clockwise direction (bottom of Fig. 7.13), the tip vortex is stronger on the left-hand side ($\Gamma/U_\infty c = –0.23$), which is larger than in the static case and also closer to the wing surface than the one on the right-hand side of the wing ($\Gamma/U_\infty c = 0.19$, smaller than in the static case). When the wing reaches the maximum roll angle ($\phi = 36°$), the right-hand vortex is strong ($\Gamma/U_\infty c = 0.32$), and has been seen to move inboard, while the left-hand vortex is small and weak ($\Gamma/U_\infty c = –0.08$). The stronger vortex on the right-hand side provides the restoring moment. As the wing rolls in the opposite (anticlockwise) direction, at the mean roll angle of $\phi = 3°$ (centre of Fig. 7.13), there is an asymmetry in the vortical flow, with the right hand vortex in this case providing the driving motion; the non-dimensional circulations are -0.16 for the left-hand vortex, smaller than in the static case and 0.24 for the right-hand vortex, which is slightly larger than in the static case.

For the case of Φ increasing at the mean roll angle, the right-hand vortex is now stronger ($\Gamma/U_\infty c = 0.24$) and closer to the wing surface than the left-hand vortex ($\Gamma/U_\infty c = -0.16$, Fig. 7.14 and 7.15); this theme is continued at the trailing-edge (Fig. 7.16), with the right-hand vortex having $\Gamma/U_\infty c = 0.41$ and the left-hand vortex $\Gamma/U_\infty c = -0.31$. This asymmetry in vortex strength provides the necessary rolling moment for the roll oscillations. In a similar fashion, for Φ decreasing at the mean roll angle, the motion is driven by the strong left-hand vortex (with $\Gamma/U_\infty c = -0.23$ in Fig. 7.14 and $\Gamma/U_\infty c = -0.42$ at the trailing-edge in Fig. 7.16) and weak right-hand vortex ($\Gamma/U_\infty c = 0.19$ at x/c = 0.5

and $\Gamma/U_\infty c = 0.35$ at the trailing-edge). In all dynamic cases, the stronger vortex above the wing is stronger than the corresponding stationary case and the less strong vortex is weaker than in the stationary case. For all dynamic cases, the vortices do not vary their position significantly in the spanwise direction, but do in the normal direction. The hysteresis shown in Figure 7.14 also indicates a time lag in the development of the vortices. The delay in the vertical vortex position is responsible for driving the wing rock of slender delta wings[22]. The left-hand vortex reaches its maximum strength not at the largest roll angle, but at the mean roll angle (Φ decreasing). Hence, the phase lag is at least 90^o.

Before moving on, Fig. 7.15 shows the phase-averaged non-dimensional standard deviation of the velocity present over the wing surface at half-chord in a cross-flow plane. From this, it is evident that when compared to other wings, the wing is fully stalled. However, in Fig. 7.12 it can be seen that the motion is driven by the side-edge vortices. Perhaps the stalling is what enables the motion to take place, as the side edge vortices now have more of an effect on the whole wing, without the damping nature of attached flow.

Moving on to look at the roll oscillations as a whole, Figs. 7.14 and 7.16 show the cross-flow velocity at the mean roll angles and near the maximum and minimum roll angles achieved during the motion, at half-chord and at the trailing-edge respectively. At (i) the strong right-hand vortex drives the motion, while at (ii) the left-hand vortex has increased in strength ($\Gamma/U_\infty c = -0.11$ at $x/c = 0.5$ and $\Gamma/U_\infty c = -0.39$ at the trailing-edge) relative to the right-hand one ($\Gamma/U_\infty c = 0.10$ at $x/c = 0.5$ and $\Gamma/U_\infty c = 0.18$ at the trailing-edge). The left-hand vortex core is also seen to move inboard and while one might expect this to reduce the moment arm of this vortex; this is more than compensated for by the increase in strength of the vortex. This left-hand vortex now drives the motion back through the mean roll angle at (iii) and to the minimum roll angle (iv). At this point, the right hand vortex is much stronger ($\Gamma/U_\infty c = 0.32$ at $x/c = 0.5$ and $\Gamma/U_\infty c = 0.35$ at the trailing-edge) than the left-hand vortex ($\Gamma/U_\infty c = -0.08$ at $x/c = 0.5$ and $\Gamma/U_\infty c = -0.22$ at the trailing-edge), which provides the restoring moment for the wing.

The different flow structures that are possible at the same roll angle demonstrate the hysteresis and time-lag effects that are present in the flow. These observations are similar to the hysteresis and time lag of the position of the vortices over slender delta wings during wing rock motion. In all these cases, it can be seen that there is no interaction between the side-edge vortices, showing that wing rock is not necessarily confined to slender delta wings only, and hence explaining Chapters 3 and 4. The vortices at the trailing-edge are stronger than at half-chord, which is to be expected due to the continuous feeding of vorticity into the vortex from the side edge along the chord, with the left vortex having $\Gamma/U_\infty c = -0.41$ and the right vortex $\Gamma/U_\infty c = 0.41$.

7.3 Free-to-roll behaviour – Zimmerman and elliptical

The elliptical and Zimmerman wings, the results of which are shown in Figs. 7.17 - 7.22, demonstrate previously unseen roll oscillations, shown by the increasing standard deviation with angle of attack in Fig. 7.17, though the oscillations were much smaller in amplitude than those for the delta and rectangular wings. The elliptical wing exhibited oscillations over a large range of angle of attack, starting at $\alpha = 10° - 11°$ as shown on the right-hand side of Fig. 7.17. Figure 7.18 shows the same data, but plotted in a different format. This highlights all the above points including a significant non-zero roll trim angle at low angles of attack (below about $\alpha = 10^o$) and also the difference between the mean and the maximum roll angles during the motion. This difference highlights the fact that the oscillations are not of constant amplitude.

The Zimmerman planform exhibited oscillations, though of smaller amplitude and with significant amplitude modulation, shown on the left-hand side of Fig. 7.19. Figure 7.19b) shows a time history taken at the angle of attack with maximum amplitude ($\alpha = 19.5°$ for the elliptical wing), and the oscillations can be seen to be large and periodic, and more so in Fig. 7.19c). The stall angle for this wing is expected to be $\alpha_{Clmax} = 16^o$, based on previous work[4]. This has implications[1,61] for the gust and manoeuvre response of MAVs employing these popular planform shapes. Looking at the actual Strouhal number of the oscillations of the elliptical wing that occur (they were generally greater in magnitude than the Zimmerman roll oscillations), it can be seen in Fig. 7.20 that they increase with angle of attack, albeit at a slightly lower Strouhal number for the higher velocity in Fig. 7.20b), with increased Reynolds number over the

wing. The Strouhal number is seen to increase for the Zimmerman and elliptical wings in Fig. 7.21, at Re = 4.35 x 10^4 and 3.42 x 10^4 respectively. The difference in Re is due to the different chord lengths of these wings. This wings' stall angle is expected to be $\alpha_{Clmax} \leq 13^o$ based on work previously performed[4,72]; hence the largest roll oscillations occur in the post-stall region.

Looking at Fig. 7.22a) it can be seen that the oscillations of the Zimmerman and elliptical wing planforms are much smaller than for the rectangular planforms. This range of angles of attack was chosen because with further increase, autorotation was experienced for the AR = 4 rectangular wing. Figure 7.22b) shows how the Strouhal number of the oscillations of these two wings varies with angle of attack. In both cases the Strouhal number increases with angle of attack, more in line with what one expects from wing rock of slender delta wings, and the elliptical wing is seen to oscillate with a lower Strouhal number at a given angle of attack. Interestingly, this plot shows that the rectangular wings reduce in St against α, so this other mechanism of wing rock is different in behaviour to non-slender wing rock.

a)

b)

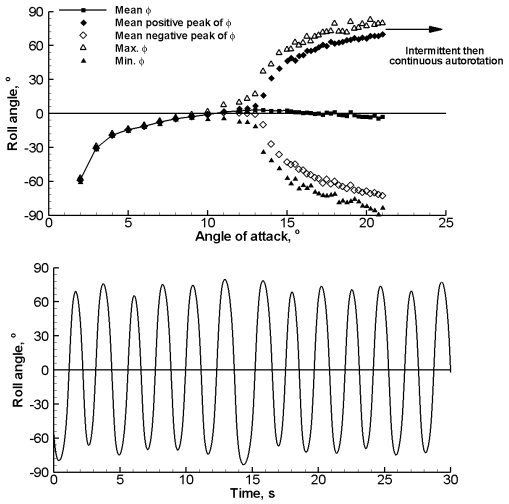

Figure 7.1 Graphs of a) mean roll angle variation with angle of attack and b) free-to-roll time history at $\alpha = 21^{o}$ for a rectangular wing with round edges and AR = 2 at Re = 1.14 x 10^{5}.

a)

b)

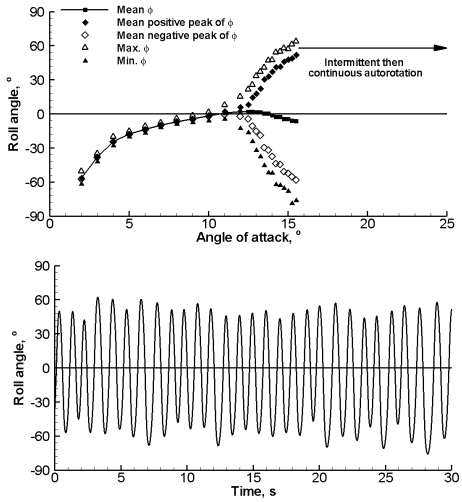

Figure 7.2 Graphs of a) mean roll angle variation with angle of attack and b) free-to-roll time history at $\alpha = 15.5^{o}$ for a rectangular wing with round edges and AR = 2 at Re = 2.28 x 10^{5}.

a)

b)

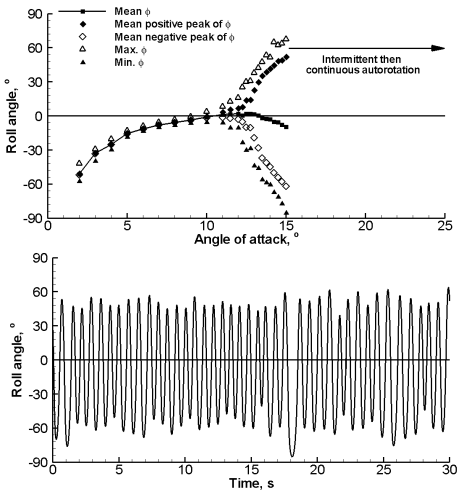

Figure 7.3 Graphs of a) mean roll angle variation with angle of attack and b) free-to-roll time history at $\alpha = 15^{o}$ for a rectangular wing with round edges and AR = 2 at Re = 3.42 x 10^{5}.

a) $\alpha = 5^o$

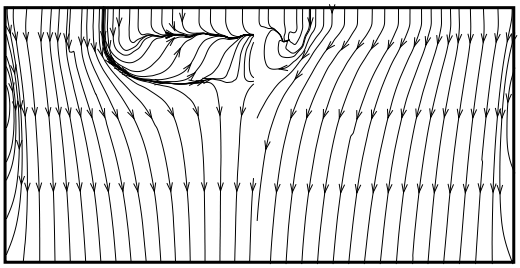

b) $\alpha = 6^o$

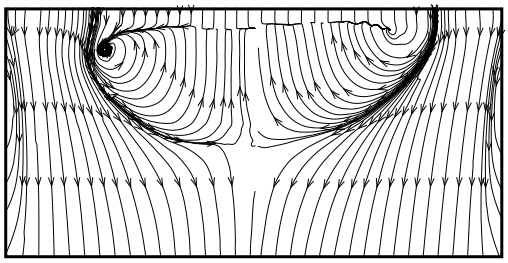

c) $\alpha = 7^o$

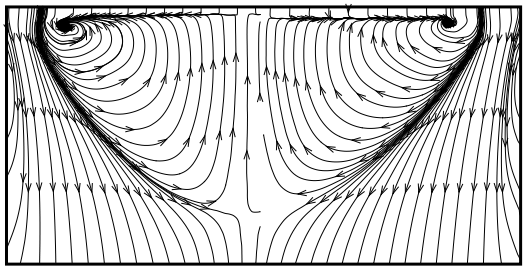

d) $\alpha = 10^o$

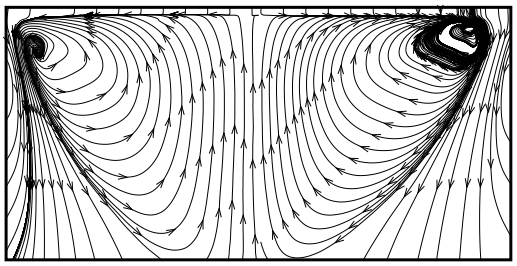

e) $\alpha = 12^o$

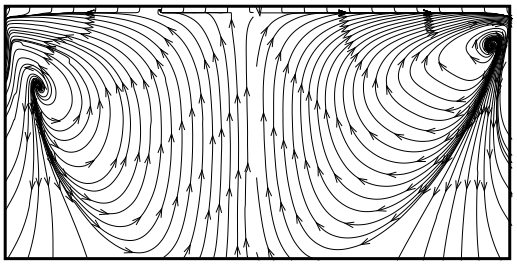

f) $\alpha = 15^o$

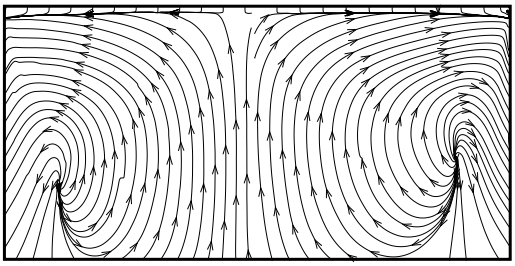

g) $\alpha = 20^o$

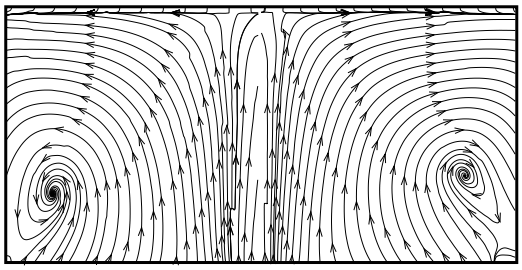

h) $\alpha = 25^o$

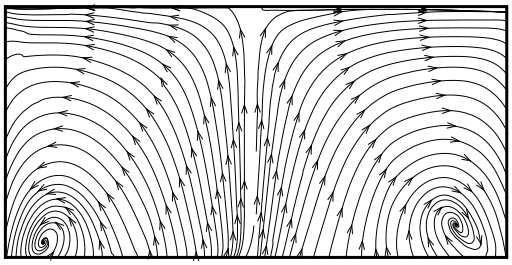

i) $\alpha = 35^o$

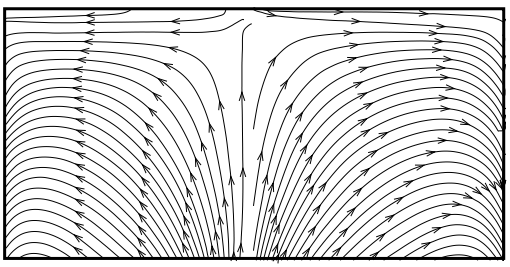

Figure 7.4 Near-surface time-averaged streamline patterns for a stationary rectangular wing with round edges and AR = 2 at Re = 1.14 x 10^5 at $\Phi = 0^o$ and a) $\alpha = 5^o$; b) $\alpha = 6^o$; c) $\alpha = 7^o$ d) $\alpha = 10^o$; e) $\alpha = 12^o$; f) $\alpha = 15^o$; g) $\alpha = 20^o$; h) $\alpha = 25^o$ and i) $\alpha = 35^o$.

a) b)

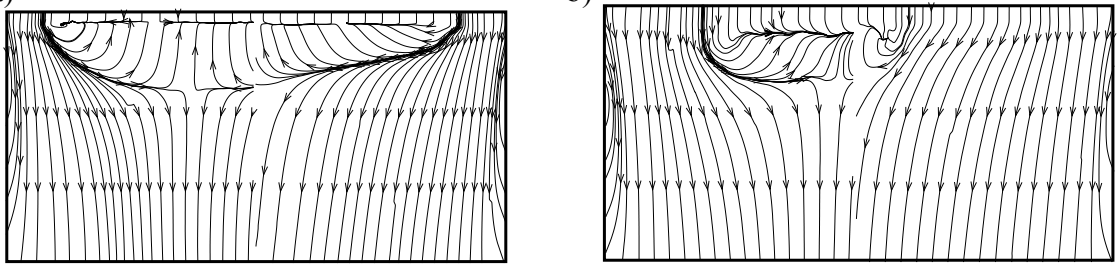

Figure 7.5 Near-surface time-averaged streamline patterns for a stationary rectangular wing with round edges and AR = 2 at Re = 1.14 x 10^5 and a) $\Phi = 14.4^o$ and b) $\Phi = 0^o$, both at $\alpha = 5^o$.

a)

b)

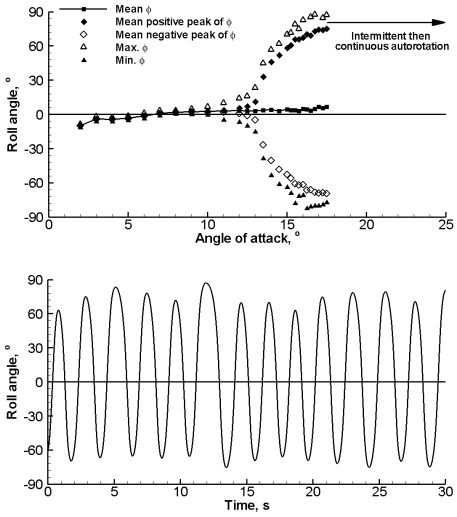

Figure 7.6 Graphs of a) mean roll angle variation with angle of attack and b) free-to-roll time history at $\alpha = 17.5^o$ for a rectangular wing with sharp edges and AR = 2 at Re = 1.14 x 10^5.

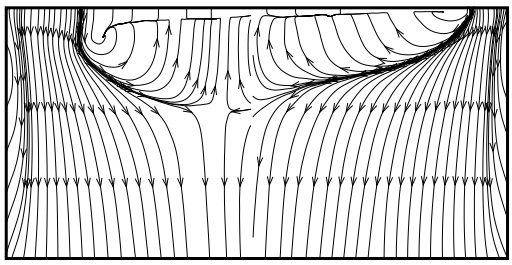

Figure 7.7 Near-surface time-averaged streamline patterns for a stationary rectangular wing with sharp edges and AR = 2 at Re = 1.14 x 10^5, $\Phi = 0^o$ and $\alpha = 5^o$.

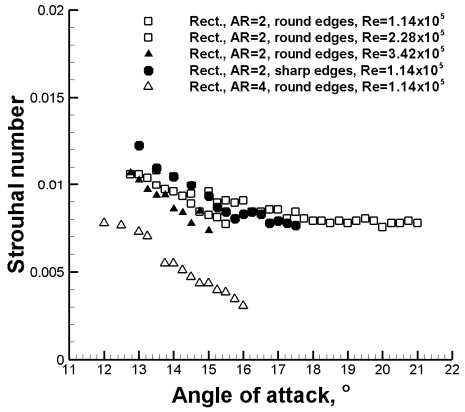

Figure 7.8 Strouhal number of oscillations as a function of angle of attack for rectangular wings.

a)

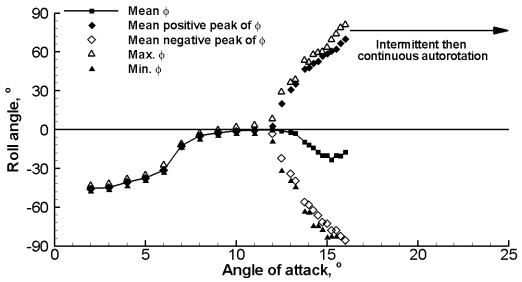

b)

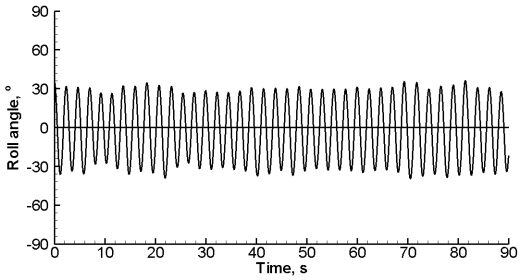

c)

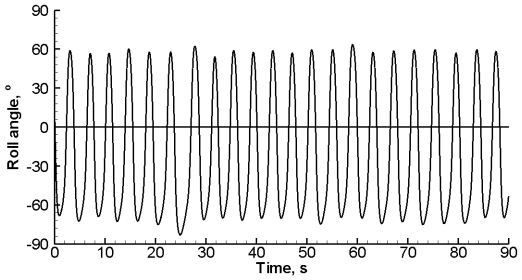

d)

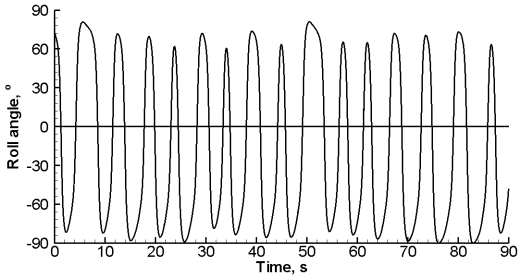

Figure 7.9 Graphs of a) mean roll angle variation with angle of attack and free-to-roll time histories at b) $\alpha = 13^{o}$; c) $\alpha = 15^{o}$ and d) $\alpha = 16^{o}$ for a rectangular wing with round edges and AR = 4 at Re = 1.14 x 10^{5}.

a) $\alpha = 3^o$

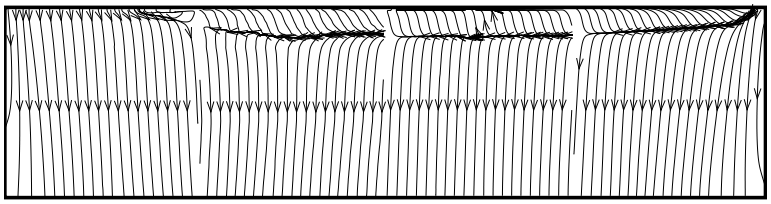

b) $\alpha = 5^o$

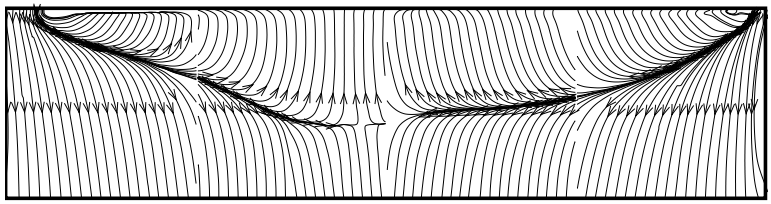

c) $\alpha = 6^o$

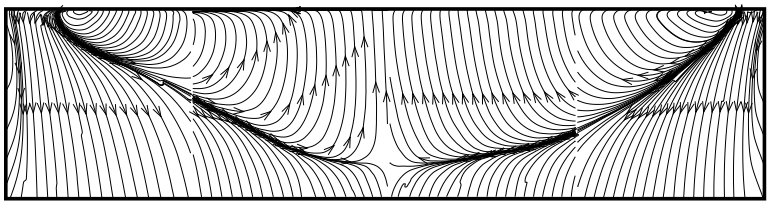

d) $\alpha = 7^o$

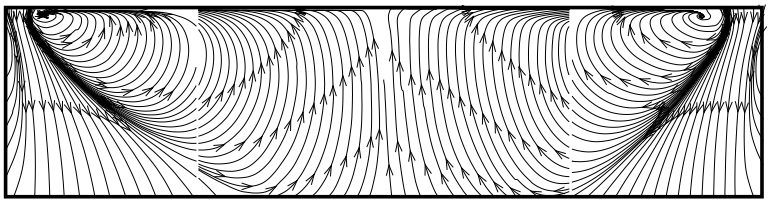

e) $\alpha = 8^o$

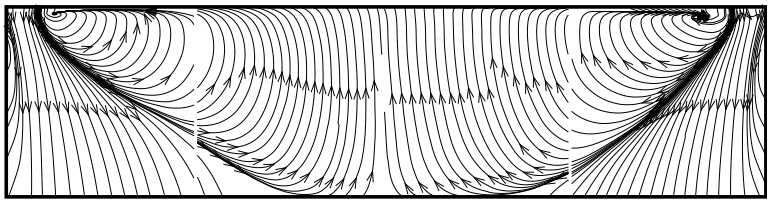

f) $\alpha = 10^o$

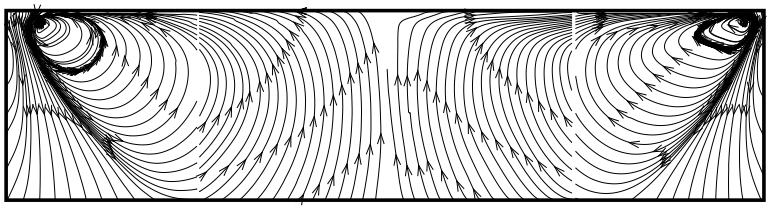

Figure 7.10 Near-surface time-averaged streamlines for a stationary rectangular wing with round edges and AR = 4 at Re = 1.14 x 10^5, $\Phi = 0^o$ and a) $\alpha = 3^o$; b) $\alpha = 5^o$; c) $\alpha = 6^o$; d) $\alpha = 7^o$; e) $\alpha = 8^o$ and f) $\alpha = 10^o$.

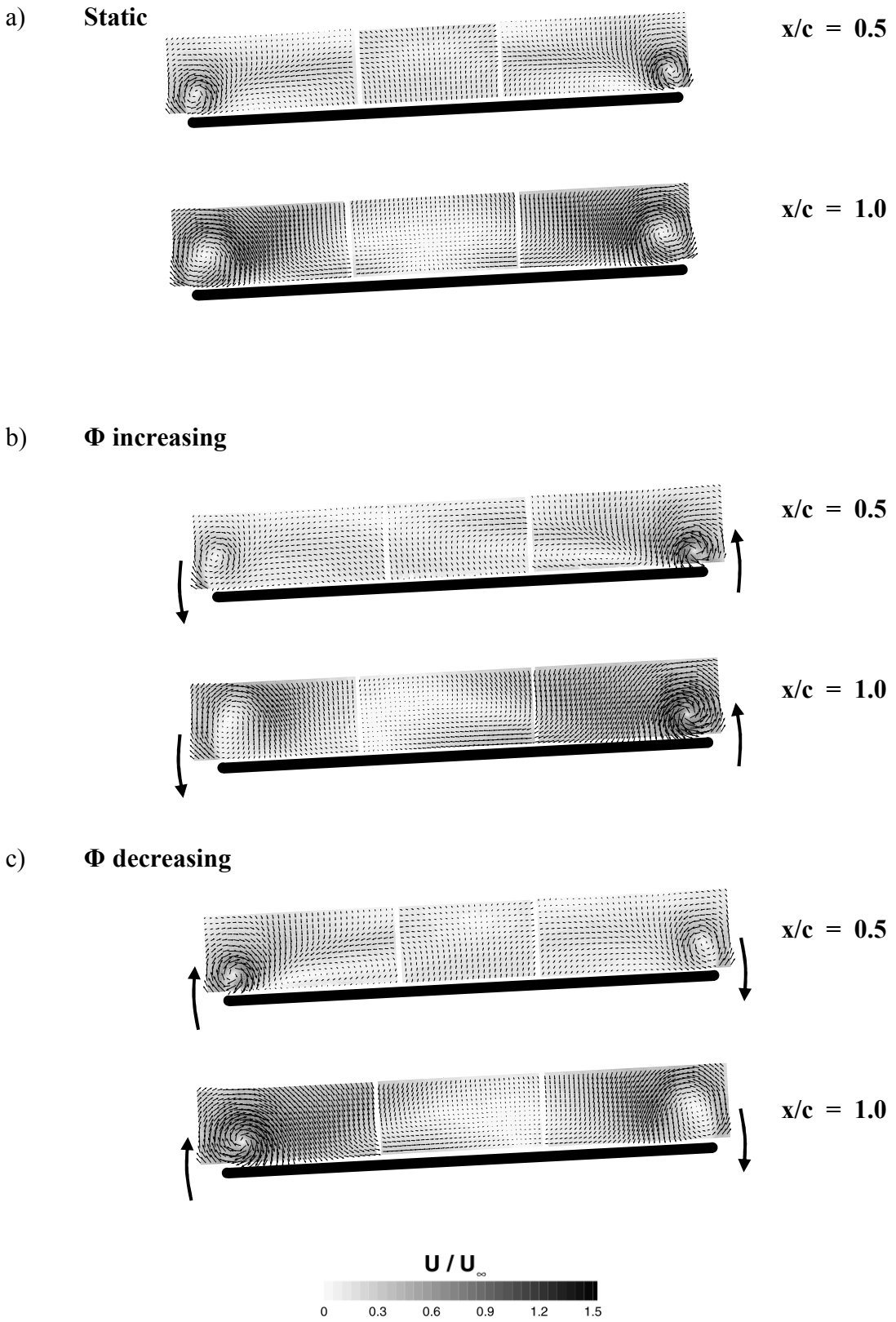

Figure 7.11 Cross-flow velocity fields at Re = 1.14 x 10^5 for a rectangular wing with AR = 2 and round edges at x/c = 0.5 (top in each case) and at the trailing-edge (bottom in each case) for a) stationary wing (time-averaged); b) Φ increasing (phase-averaged) and c) Φ decreasing (phase-averaged) at α = 15° and Φ = 3^o**.**

a) **Static**

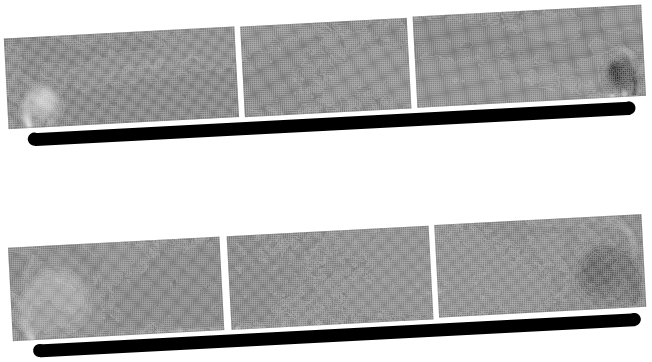

b) **Φ increasing**

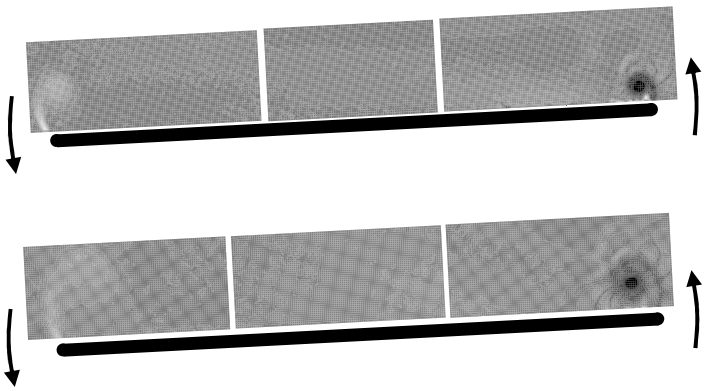

c) **Φ decreasing**

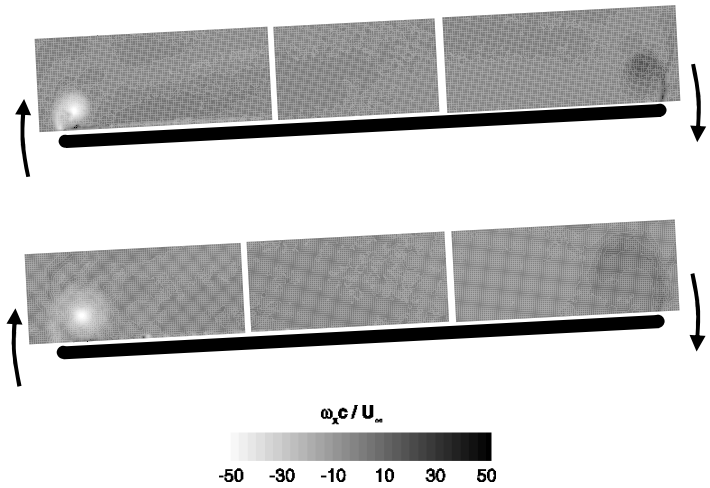

Figure 7.12 Cross-flow vorticity fields at Re = 1.14 x 10^5 for a rectangular wing with AR = 2 and round edges at x/c = 0.5 (top in each case) and at the trailing-edge (bottom in each case) for a) stationary wing (time-averaged); b) Φ increasing (phase-averaged) and c) Φ decreasing (phase-averaged) at α = 15° and Φ = 3^o.

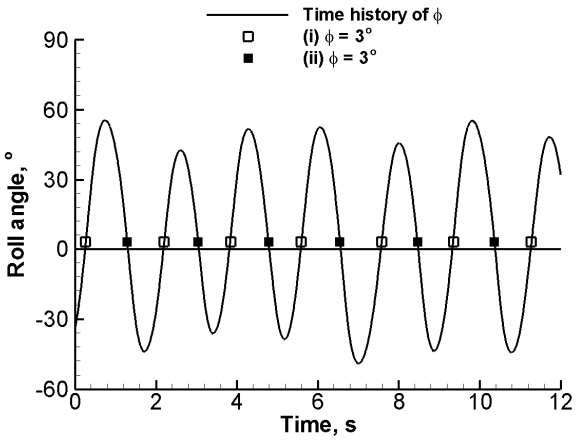

Static

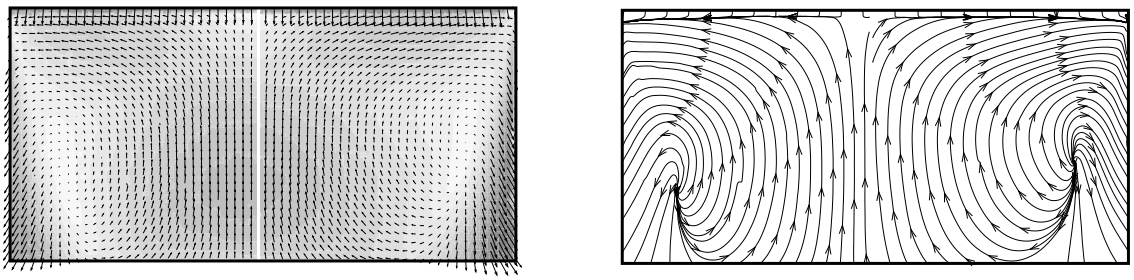

(i) Φ increasing

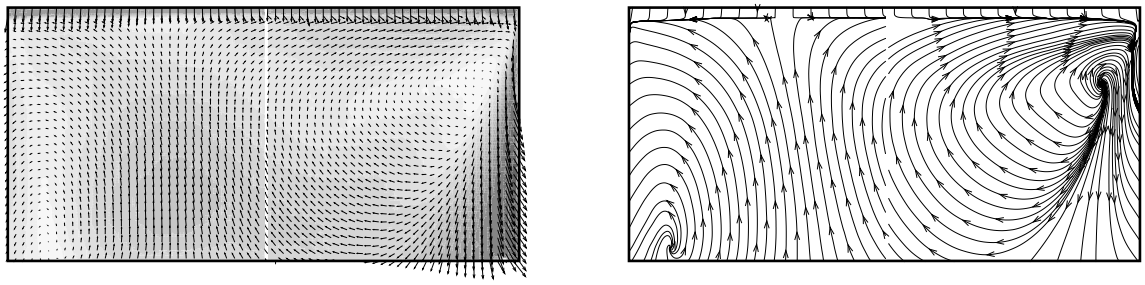

(ii) Φ decreasing

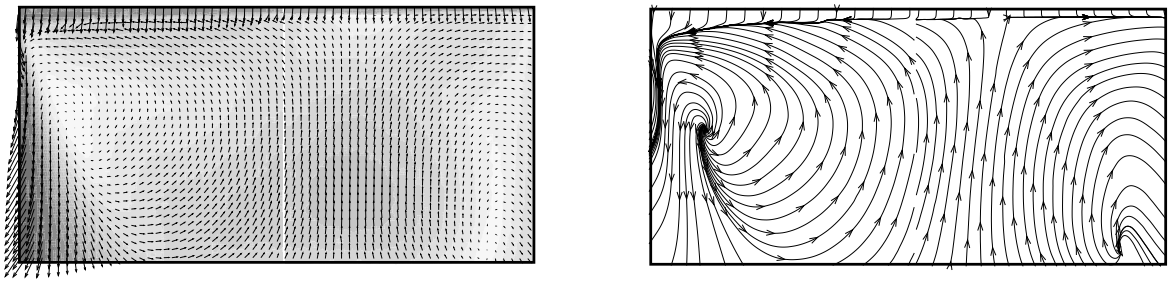

Figure 7.13 Near-surface PIV measurements at Re = 1.14 x 10^5 for a rectangular wing with AR = 2 and round edges, showing time-averaged velocity fields (left) and streamline patterns (right) for the stationary case, (i) Φ increasing and (ii) Φ decreasing at $\alpha = 15^o$ and $\Phi = 3^o$. The inset shows the roll angle at which measurements are taken for the rolling wing.

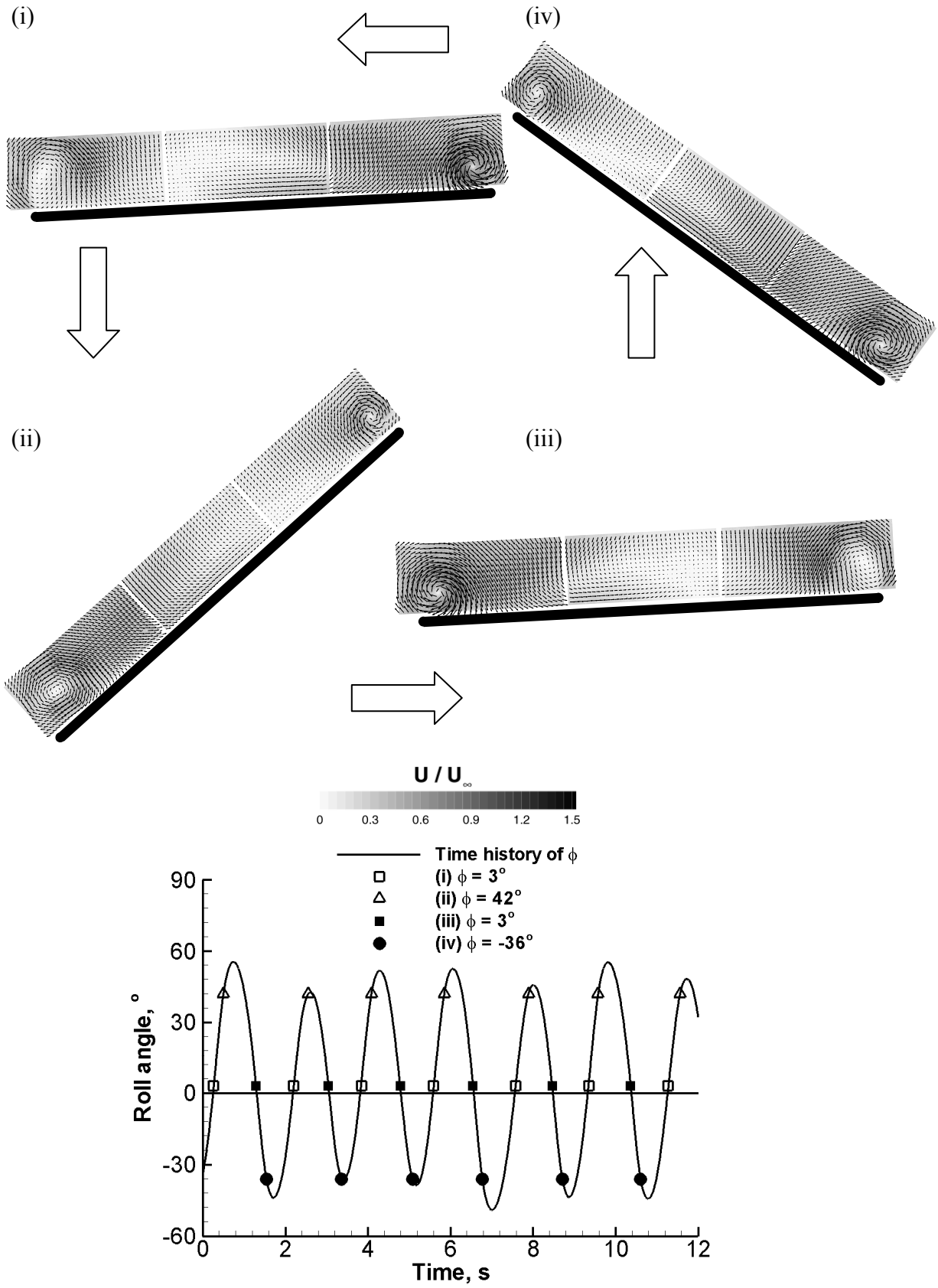

Figure 7.14 Cross-flow phase-averaged velocity fields at Re = 1.14 x 10^5 for (i) at $\Phi = 3^o$; (ii) at $\Phi = 42^o$; (iii) at $\Phi = 3^o$ and (iv) at $\Phi = -36^o$ for rectangular wing with AR = 2 and round edges at x/c = 0.5 and $\alpha = 15^o$. The inset shows the roll angle at which measurements are taken for the rolling wing.

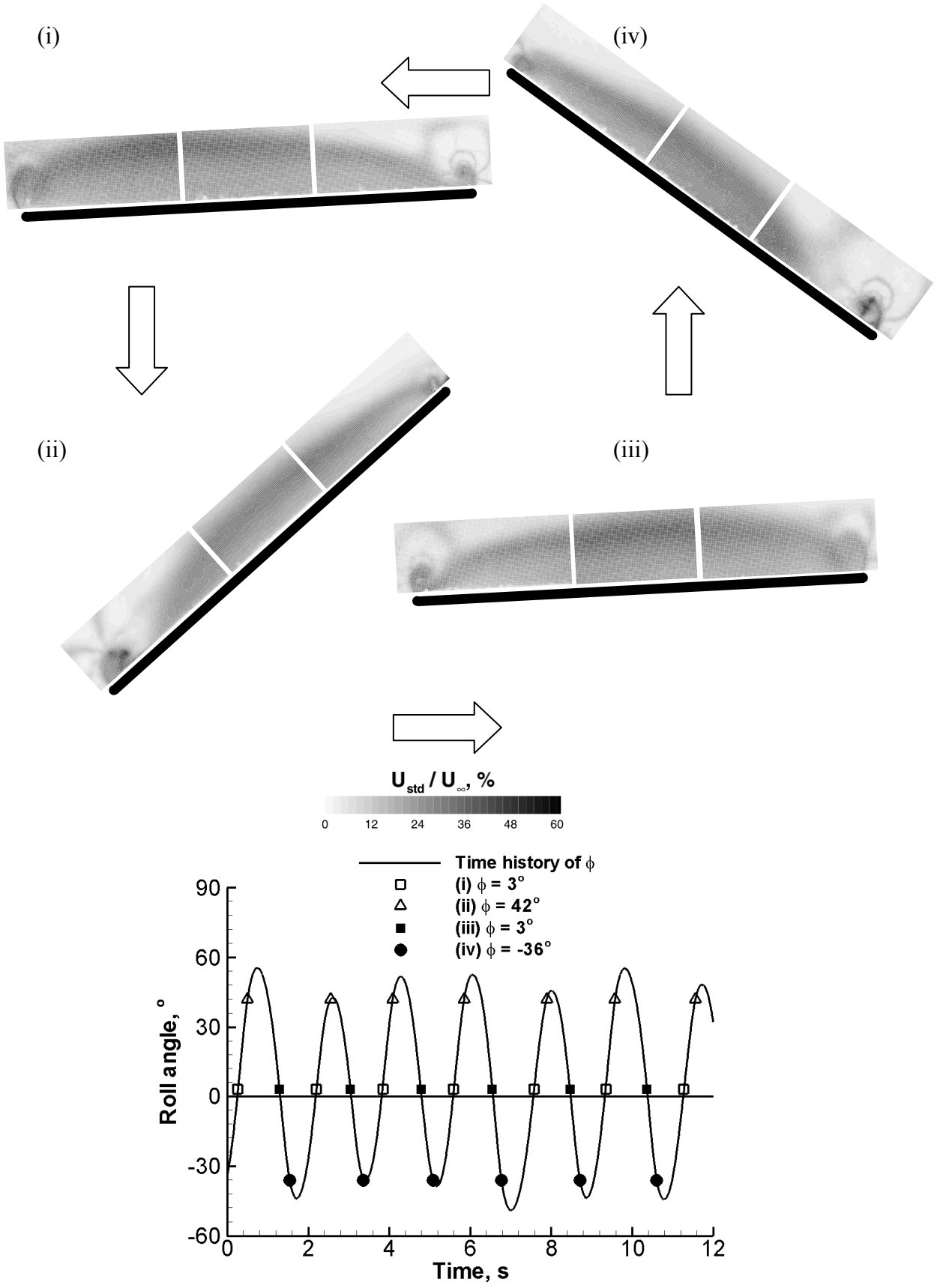

Figure 7.15 Cross-flow phase-averaged turbulence fields at Re = 1.14 x 10^5 for (i) at $\Phi = 3^o$; (ii) at $\Phi = 42^o$; (iii) at $\Phi = 3^o$ and (iv) at $\Phi = -36^o$ for rectangular wing with AR = 2 and round edges at x/c = 0.5 and $\alpha = 15^o$. The inset shows the roll angle at which measurements are taken for the rolling wing.

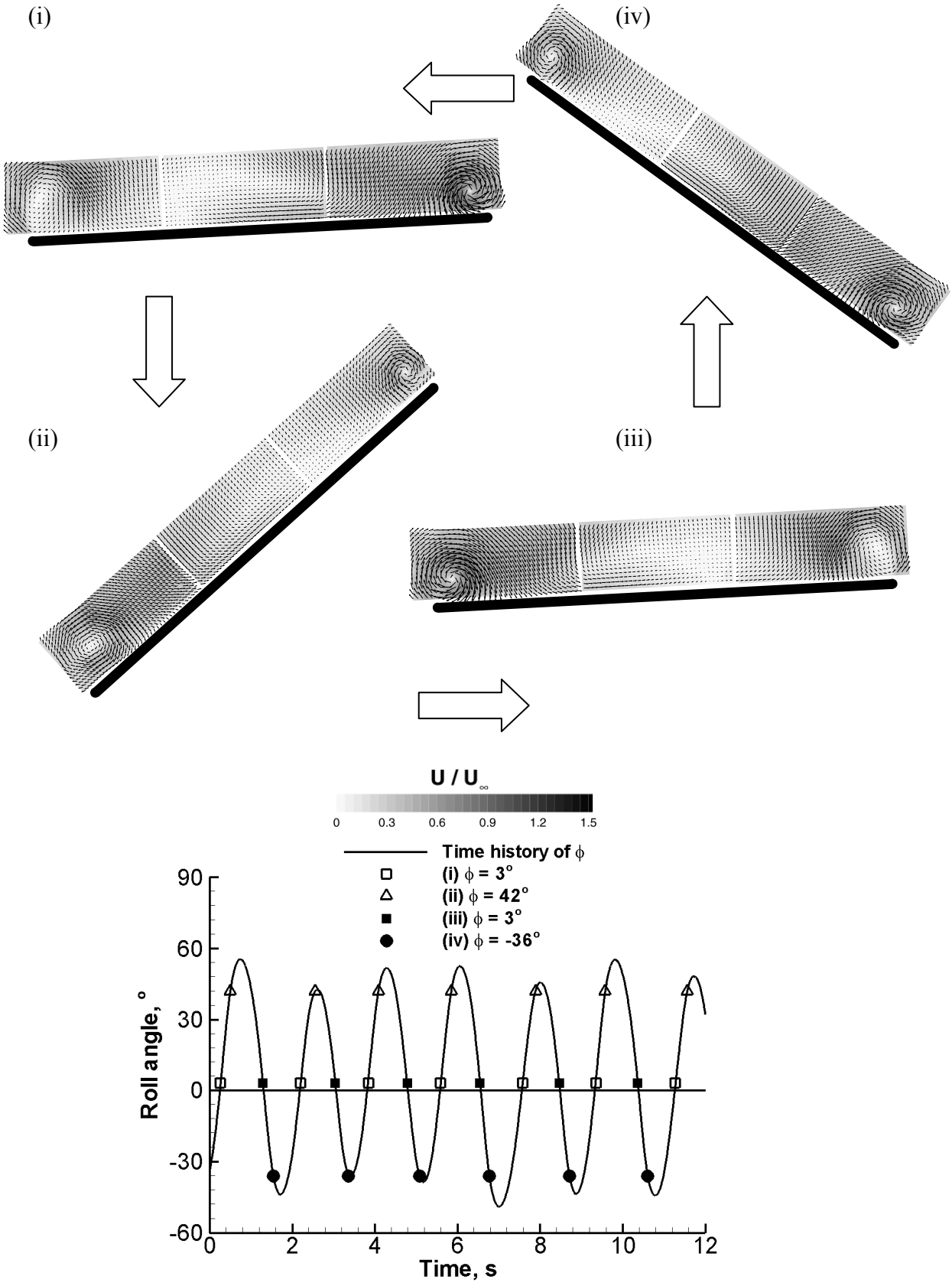

Figure 7.16 Cross-flow phase-averaged velocity fields at Re = 1.14 x 10^5 for (i) at Φ = 3^o; (ii) at Φ = 42^o; (iii) at Φ = 3^o and (iv) at Φ = -36^o for rectangular wing with AR = 2 and round edges at x/c = 1.0 and α = 15^o. The inset shows the roll angle at which measurements are taken for the rolling wing.

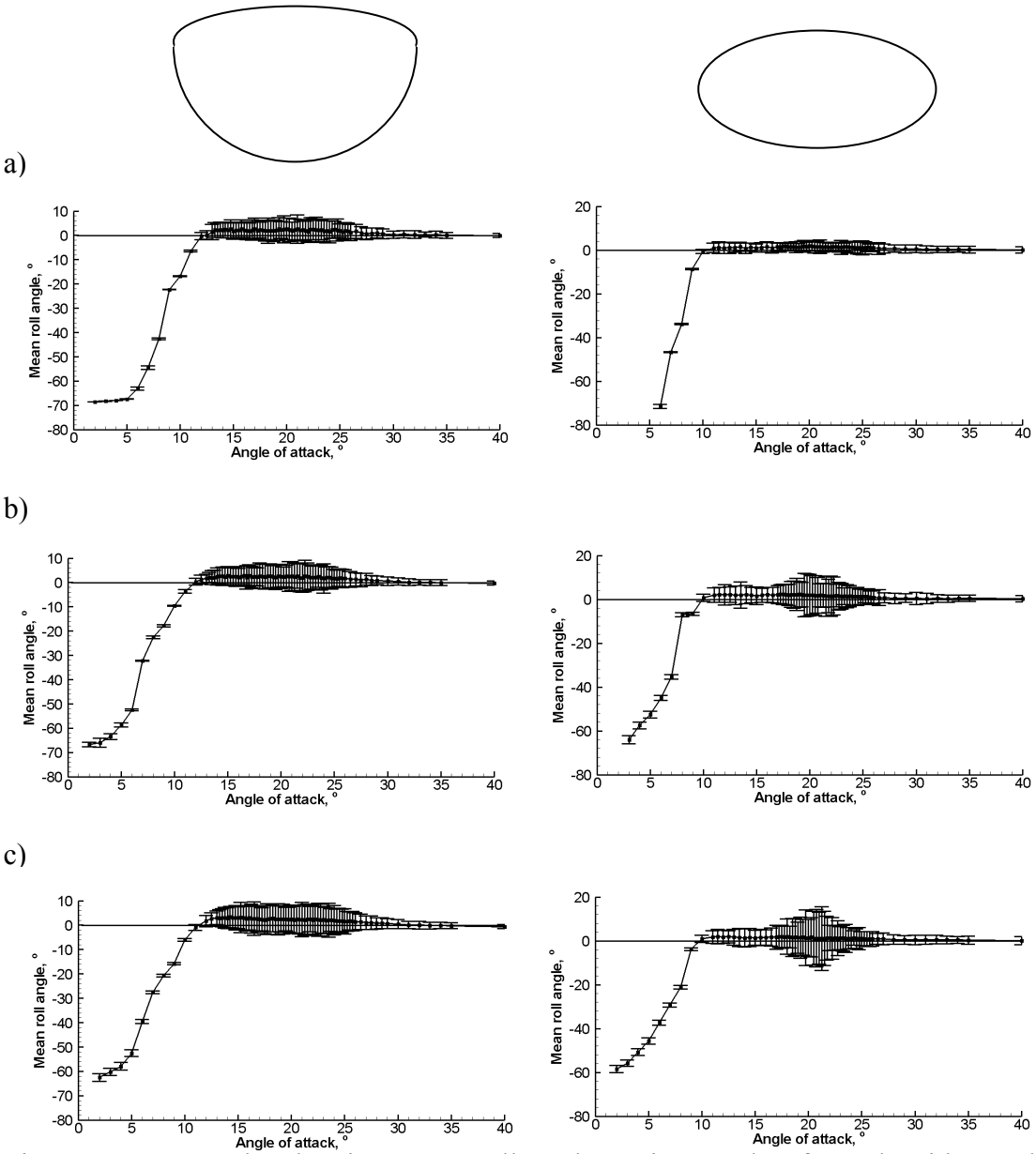

Figure 7.17 Graphs showing mean roll angle against angle of attack with standard deviation as error bars at a) $U_\infty = 10ms^{-1}$; b) $U_\infty = 20ms^{-1}$ and c) $U_\infty = 30ms^{-1}$ together with schematic of planform shapes (top) for Zimmerman (left) and Elliptical (right) wings with round leading-edges.

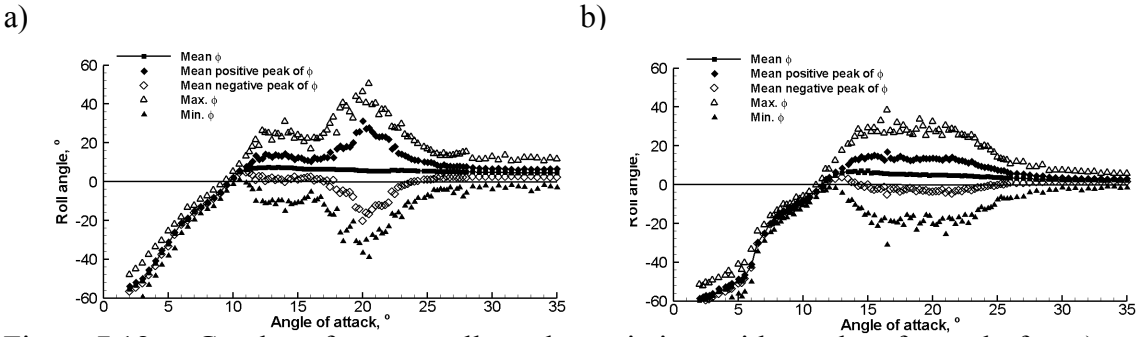

Figure 7.18 Graphs of mean roll angle variation with angle of attack for a) an elliptical wing at Re = 3.42 x 10^5 and b) a Zimmerman wing at Re = 4.35x10^5 both with round edges.

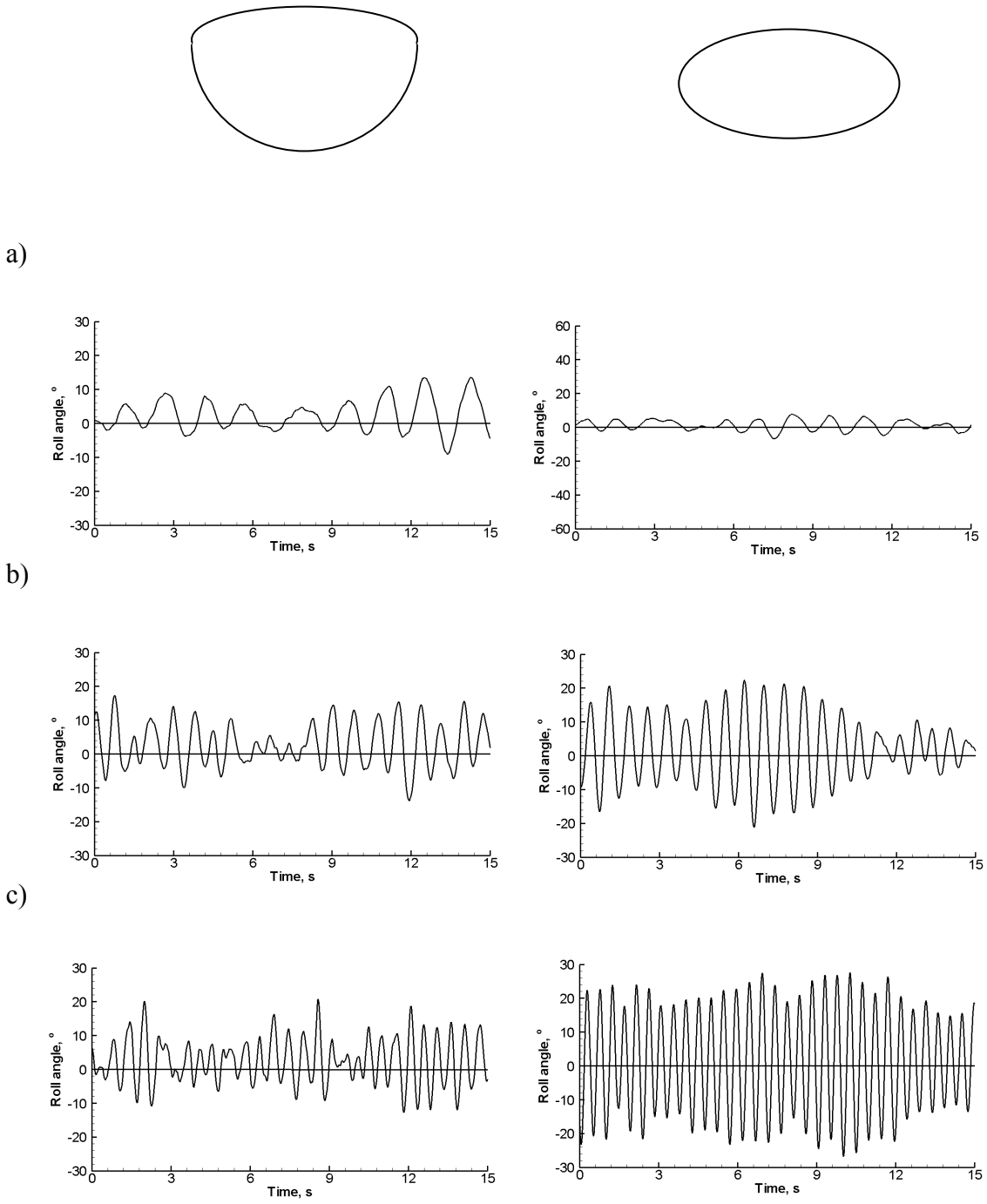

Figure 7.19 Graphs showing time histories of roll angle corresponding to maximum standard deviation at a) $U_\infty = 10$ ms^{-1}; b) $U_\infty = 20$ ms^{-1} and c) $U_\infty = 30$ ms^{-1} together with schematic of planform shapes (top) for Zimmerman (left, α = 21^o, 22.25^o and 21^o respectively) and Elliptical (right, α = 23^o, 19.5^o and 21.25^o respectively) wings with round edges.

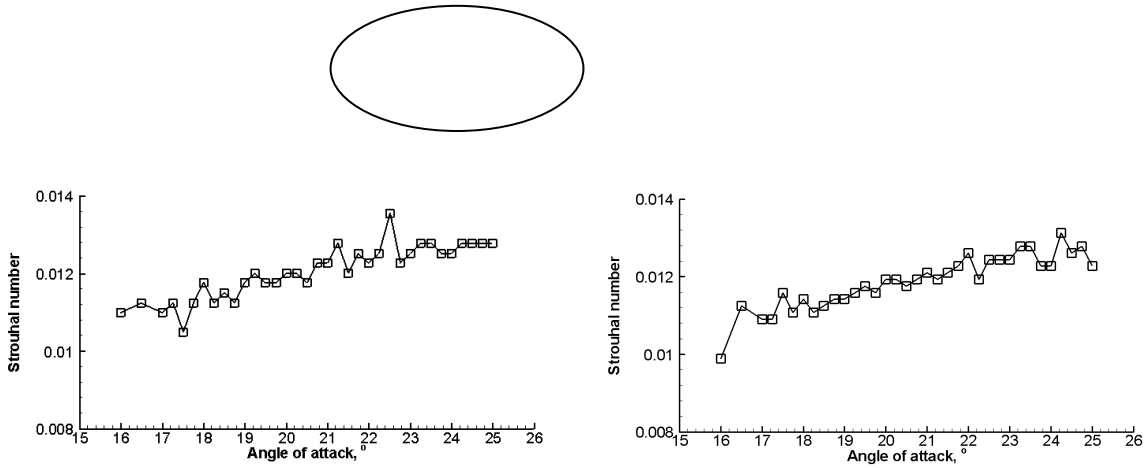

Figure 7.20 Graphs showing Strouhal number against angle of attack for which large oscillations occur for a) $U_\infty = 20ms^{-1}$ and b) $U_\infty = 30ms^{-1}$ together with schematic of planform shape (top) for Elliptical wing with round edges.

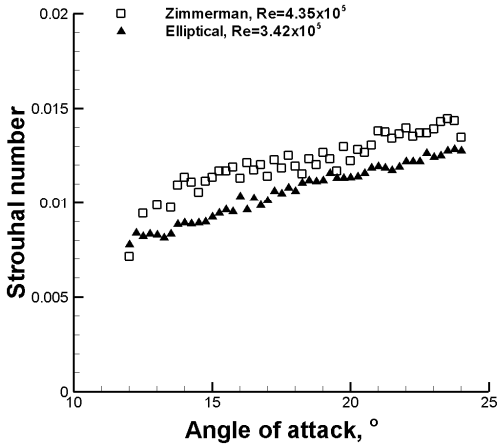

Figure 7.21 Strouhal number of oscillations as a function of angle of attack for Zimmerman and elliptical wings.

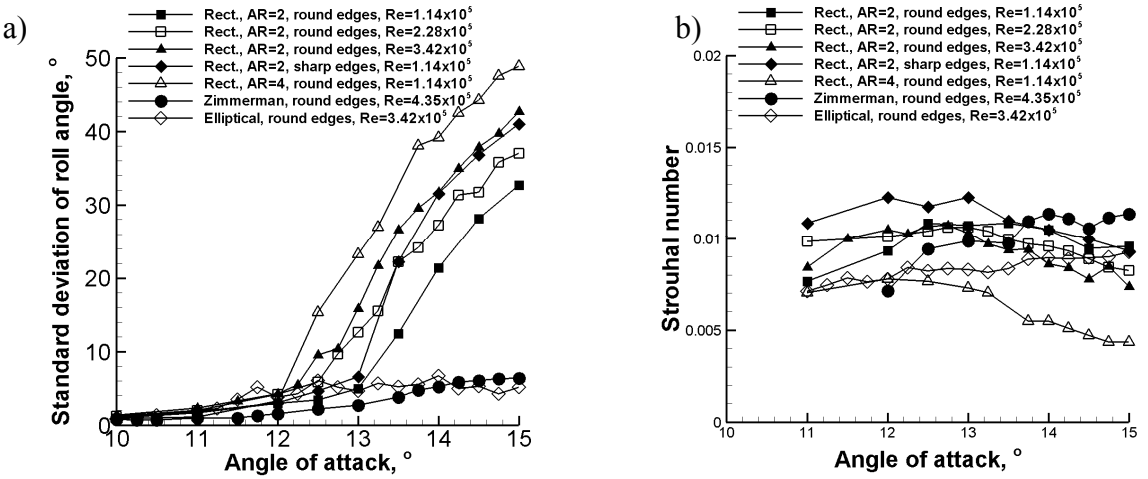

Figure 7.22 Variation of a) standard deviation and b) Strouhal number with angle of attack.

Chapter 8 Conclusions

Work was initially performed on the free-to-roll behaviour of non-slender delta wings with sweep angles of 50^o and different leading-edges. It was found for the first time that a wing with this sweep angle and sharp leading-edges exhibited non-zero roll trim angles and free-to-roll oscillations contrary to previous belief. These oscillations were small in magnitude, but continuous and could affect aircraft with this planform during manoeuvres and gust response of an MAV because of the non-zero mean roll angle and low Strouhal number of the rolling motion.

Delta wing planforms with sweep angles between 50^o and 60^o exhibited the same mechanism of free-to-roll oscillations. This was proved by cross-flow and near-surface PIV measurements as well as tuft visualisation once the free-to-roll behaviour had been recorded with varying angles of attack. These oscillations were caused by the unsteady reattachment of the shear layers on the wing surface rather than the leading-edge separation (which is not fixed on rounded ellipse) as was previously thought. The windward vortex was the same size in each case and is not thought to play a significant role. Hysteresis and time-lag effects are similar to those of slender delta wing rock. Due to lack of free-to-roll experiments, these oscillations have never previously been seen.

The region of oscillation is limited at the upper bound at high sweep angle due to lack of reattachment and at the lower bound at low sweep angle due to the larger portion of stabilising attached flow. The largest oscillations for a non-slender delta wing were found for a 55^o sweep delta wing and this was found to be the upper limiting sweep angle with sudden stall. With larger sweep angle the wing settles to zero mean roll angle much more gradually upon stalling. Normally, a sweep angle of 55^o is taken as the limit between slender and non-slender delta wings and the results here follow that logic. As the roll angle increases, the windward vortex increases in strength, caused by the increase in effective angle of attack. In all cases, as the roll angle increases through the mean, there appears to be interaction between the windward and leeward shear layers. The windward vortex then becomes more compact, caused by decreasing effective angle of attack and increasing effective sweep angle. At the mean roll angle, due to the time

lag in the strength of the vortices a net rolling moment in the direction of the rolling motion is generated.

A second region of angles of attack with continuous free-to-roll oscillations was found for the more slender (sweep 57.5^o and 60^o) delta wings, but not for the higher or lower sweep angles. Within this region, at higher angles of attack, the leeward shear layer is stalled at the maximum roll angle, but reattached flow is present at the minimum. Hence these oscillations appear to be out of phase with the first region. In this case, it is suggested that asymmetry in vortex strength caused by a time lag provides the driving force for these roll oscillations. Stalling seems to play a part in the motion and this can be attributed to the reattachment lines moving to the centreline with increasing sweep angle.

Effect of pitching manoeuvres on the free-to-roll delta wings was investigated and a delay was always present, especially for the 50^o sweep round leading-edge non-slender delta wing, which did not come out of stall. Sharp leading-edges were more responsive than round leading-edges.

Non-zero roll trim angles were found and PIV tests were performed on cropped delta wings with 55^o leading-edge sweep angle and the same span. It was found that the greater the cropped portion, the smaller the roll oscillations. Circulation calculations showed similar values on both wing halves. Experiments were also performed on rectangular wings with varying aspect ratio and it was found that previously unseen free-to-roll oscillations of large amplitude were in existence for wings of aspect ratio $AR \geq 2$. Due to the relatively high aspect ratios, no interaction between the vortices from each side-edge occurs. Non-zero roll trim angles were found for round edges but not sharp edges due to the fixed separation point. These oscillations were large enough to cause autorotation upon increased angle of attack. Once the reattachment of the leading-edge separated bubble failed, the onset of large amplitude roll oscillations was observed, though this angle of attack was smaller than the definition of the stall angle. Low aspect-ratio rectangular wings were found to have very three-dimensional flow characteristics. With increasing angle of attack or sharp leading-edges, the separation bubble becomes more symmetric and this results in near zero roll trim roll angles for the free-to-roll wing. For the wings with round leading-edge, the trim angle can be much

larger than zero at low angles of attack. The separation bubble on a similar (AR = 2) wing with sharp leading-edges is more symmetric, resulting in nearly zero roll trim angles.

The mechanism for the self-induced roll oscillations is again caused by a time lag in the flow response and relies heavily on the side-edge vortices being present and of sufficient strength. Oscillations were smaller for the aspect ratio AR = 4 wing tested. The roll oscillations depend on the proximity of the side-edge vortices to the wing surface, as the low-pressure core generates sufficient lift to drive the wing during roll oscillations. The amplitude of the oscillations strongly depends on the planform shape, with rectangular wings exhibiting large oscillations. Cross-flow PIV velocity measurements and circulation calculations revealed that variations in the strength of the vortices drive the rolling motion. Tests were also carried out on an elliptical and a Zimmerman planform, and oscillations were again seen though of much less significance.

Possible Future Work

Tests of the same Reynolds numbers could be performed for all wings by varying the chord length or wind tunnel velocity appropriately to give exact comparative results. The fixed free-to-roll device bearing friction, however, means an air bearing or suchlike should be used.

Larger sweep-angled delta wing or indeed other types (such as ogee) could be tried on the free-to-roll apparatus (with the same span) to further investigate slender wing rock due to the low friction. Further force and pressure measurements, numerical simulations[78] and reduced-order models[79] could be useful for further understanding of the roll oscillations about a non-zero mean roll angle and simulating them for MAV design.

Work could be performed on different aspect ratios of rectangular wings, as these oscillations have not been seen before. A different facility with a greater working section would be needed to keep the chord length equivalent, which is considered important as we have a fixed bearing friction regardless of the model size for oscillatory purposes. Smaller aspect ratios could be tried to see how they behave just before stalling with the low friction apparatus. Tests on actual (cambered) wing planforms could be interesting, to see how they behave while manoeuvring.

Finally, different manoeuvres could be tried. Pitching was investigated here, but more realistic flight situations could be explored and the wings' reaction recorded.

References

[1] Mueller, T. J., and DeLaurier, J. D., "Aerodynamics of Small Vehicles", *Annual Review of Fluid Mechanics*, Vol. 35, Jan. 2003, pp. 89–111.

[2] Mueller, T.J., "Aerodynamic Measurements at Low Reynolds Numbers for Fixed Wing Micro-Air Vehicles", *RTO AVT/VKI Special Course on Development and Operation of UAVs for Military and Civil Applications*, September 13th-17th, 1999, VKI Belgium, Hessert Centre for Aerospace Research, University of Notre Dame.

[3] Pelletier, A. and Mueller, T.J., "Low Reynolds Number Aerodynamics of Low-Aspect-Ratio Thin/Flat/Cambered-Plate Wings," *Journal of Aircraft,* Vol. 37, No. 5, 2000, pp. 825-832.

[4] Torres, G.E. and Mueller, T.J., "Low-Aspect-Ratio Wing Aerodynamics at Low Reynolds Numbers," *AIAA Journal,* Vol. 42, No. 5, 2004, pp. 865-873.

[5] Gad-el-Hak, M., "Micro-Air-Vehicles: Can They be Controlled Better?", *Journal of Aircraft*, Vol. 38, No. 3, May-June 2001, pp. 419-429.

[6] Matsuno, T. and Nakamura, Y., "Self-Induced Roll Oscillation of 45-degree Delta Wings", AIAA 2000-0655, *38th AIAA Aerospace Sciences Meeting and Exhibit*, 10th-13th January 2000, Reno, NV.

[7] Gursul, I. *Aerodynamics course notes*, University of Bath.

[8] Yaniktepe, B. and Rockwell, D., "Flow Structure on a Delta Wing of Low Sweep Angle", *AIAA Journal*, Vol. 42, No. 3, March 2004.

[9] Earnshaw, P.B. and Lawford, J.A., "Low-Speed Wind Tunnel Experiments on a Series of Sharp-Edged Delta Wings", *ARC Reports and Memoranda*, No. 3424, March 1964.

[10] Gordnier, R.E., "Computation of Vortex Breakdown on a Rolling Delta Wing," *Journal of Aircraft*, vol. 32, no. 3, 1995, pp. 686-688.

[11] Wentz, W.H. and Kohlman, D.L., "Vortex Breakdown on Slender Sharp-Edged Wings", *Journal of Aircraft*, Vol. 8, No. 3, 1971, pp. 156-161.

[12] Payne, F.M., Ng, T.T. and Nelson, R.C., "Visualization and Wake Surveys of Vortical Flow over a Delta Wing", *AIAA Journal*, Vol. 26, No. 2, February 1988.

[13] Boeing website (online picture, available 2007), *http://www.boeing.com/mews/releases/2004/photorelease/q3/pr_040719s.html*, accessed June the 7th, 2008.

[14] Designation Systems website (online picture, available 2007), *http:/www./designation-systems.net/dusrm/app4/wasp.html*, accessed June the 7th, 2008.

[15] McClain, A., "The Aerodynamics of Non-slender Delta Wings", Thesis *(MPhil)*, University of Bath, March 2004.

[16] Taylor, G. and Gursul, I., "Buffeting Flows over a Low Sweep Delta Wing", *AIAA Journal*, 2004; 42 (9), pp. 1737-1745.

[17] Gordnier, R. and Visbal, M., "Higher-Order Compact Difference Scheme Applied to the Simulation of a Low Sweep Delta Wing Flow", AIAA 2003-0620, *41st AIAA Aerospace Sciences Meeting and Exhibit*, 6th-9th January 2003, Reno, NV.

[18] Vardaki, E. and Gursul, I., "Vortex Flows on a Rolling Non-slender Delta Wing", AIAA-2004-4729, *22nd AIAA Applied Aerodynamics Conference*, 16th-19th August 2004, Providence, RI.

[19] Gursul, I.A, Gordnier, R. and Visbal, M., "Unsteady Aerodynamics of Non-Slender Delta Wings," *Progress in Aerospace Sciences*, 41 (2005), pp. 515-557.

[20] Huang, X.Z., Mebarki, Y., Benmeddour, A. and Brown, T., "Experimental and Numerical Studies of Geometry Effects on UAV's Aerodynamics", *AIAA-2004-0403*.

[21] Huang, X. Z., and Hanff, E. S., "Prediction of Normal Force on a Delta Wing Rolling at High Incidence," AIAA Paper 93-3686, *AIAA Atmospheric Flight Mechanics Conference*, 9th-11th August 1993, Monterey, CA.

[22] Ng, T.T., Malcolm, G.N. and Lewis, L.C., "Experimental Study of Vortex Flows over Delta Wings in Wing-Rock Motion", *Journal of Aircraft*, Vol. 29, No. 4, 1991, pp. 598-603.

[23] Arena Jr., A.S. and Nelson, R.C., "Experimental Investigations on Limit Cycle Wing Rock of Slender Wings", *Journal of Aircraft*, Vol. 31, No. 5, September-August 1994.

[24] Jenkins, J. E., Myatt, J. H., and Hanff, E. S., "Body-Axis Rolling Motion Critical States of a 65-Degree Delta Wing," *Journal of Aircraft*, Vol. 33, No. 2, 1996, pp. 268-278.

[25] Hanff, E. S., and Huang, X. Z., "Roll-Induced Cross-Loads on a Delta Wing at High Incidence," AIAA Paper 91-3223, *9th AIAA Applied Aerodynamics Conference*, 23rd-25th September 1991, Baltimore, MD.

[26] Gursul, I., "Review of Unsteady Vortex Flows over Slender Delta Wings", *Journal of Aircraft*, Vol. 2, March-April 2005, pp. 299-319.

[27] Katz, J., "Wing/Vortex Interactions and Wing Rock," *Progress in Aerospace Sciences*, Vol. 35, 1999, pp. 727-750.

[28] Ericsson, L.E., "Slender Wing Rock Revisited", *Journal of Aircraft*, Vol. 30, No. 3, 1993, pp 352-356.

[29] Breitsamter, C., "Unsteady Flow Phenomena Associated with Leading-Edge Vortices", *Progress in Aerospace Sciences*, Vol. 44 (2008), pp. 48-65

[30] Pamadi, B.N., Rao M.D. and Niranjana T., "Wing Rock and Roll Attractor of Delta Wings at High Angles of Attack*," International Council of the Aeronautical Sciences*, ICAS 94-7.1.2, September 1994.

[31] Ericsson, L.E., "Effect of Fuselage Geometry on Delta-Wing Vortex Breakdown", J*ournal of Aircraft*, Vol. 35, No. 6, 1998, pp. 898-904.

[32] Ericsson, L.E., "Flow Physics of Critical States for Rolling Delta Wings", *Journal of Aircraft*, Vol. 32, No. 3, 1995, pp. 603-610.

[33] Ericsson, L.E., "Wing Rock of Nonslender Delta Wings," *Journal of Aircraft*, vol. 38, no. 1, 2001, pp. 36-41.

[34] Levin, D. and Katz J., "Dynamic Load Measurements with Delta Wings Undergoing Self-Induced Roll Oscillations", *Journal of Aircraft*, Vol. 21, No.1, 1984, pp 30-36.

[35] Verhaagen, N.G. and Jobe., C.E., "Wind Tunnel Study on a 65-deg Delta Wing at Sideslip", *Journal of Aircraft*, Vol. 40, No. 2, March-April 2003, pp. 290-296.

[36] Ericsson, L.E., "Analysis of the Effect of Sideslip on Delta Wing Roll-Trim Characteristics," *Journal of Aircraft*, Vol. 34, No. 5, September-October 1997, pp. 585-591.

[37] LeMay, L.E., Batill, S.M. and Nelson, R.C., "Leading-edge Vortex Dynamics on a Pitching Delta Wing", *AIAA 88-2559-CP*, 1988, pp 312-320.

[38] Srinivas, S., Gursul, I. and Batta, G., "Active Control of Vortex Breakdown over Delta Wings", *AIAA paper 94-2215*, June 1994.

[39] Guglieri, G. and Quagliotti, F., "Experimental Observation and Discussion of the Wing Rock Phenomenon", *Aerospace Sciences and Technology*, 1997, No.2, pp. 111-123.

[40] Gordnier, R. and Visbal, M., "Numerical Simulation of Delta Wing Roll", *Aerospace Science and Technology*, No. 6, 1998, pp. 347-357.

[41] Roos, F.W. and Kegelman, J.T., "Control of Coherent Structures in Reattaching Laminar and Turbulent Shear Layers", *AIAA Journal*, Vol. 24, No. 12, pp. 1956-1965.

[42] Margalit, S., Greenblatt, D., Seifert, A. and Wygnanski, I., "Delta Wing Stall and Roll Control using Segmented Piezoelectric Fluidic Actuators", *Journal of Aircraft*, Vol. 42, No. 3, May-June 2005, pp. 698-709.

[43] Elzebda, J.M., Nayfeh, A.H. and Mook, D.T., "Development of an Analytical Model of Wing Rock for Slender Delta Wings", *Journal of Aircraft*, Vol. 26, No. 8, August 1989, pp. 737-743.

[44] Nayfeh, A.H., Elzebda, J.M. and Mook, D.T., "Analytical Study of the Subsonic Wing Rock Phenomenon for Slender Delta Wings", *Journal of Aircraft*, Vol. 26, No. 9, September 1989, pp. 805-809.

[45] McClain, A., Wang, Z-J, Vardaki, E. and Gursul, I., "Unsteady Aerodynamics of Free-to-Roll Non-Slender Delta Wings," AIAA-2007-1074, *45th AIAA Aerospace Sciences Meeting and Exhibit*, 8th-11th January 2007, Reno, NV.

[46] Hüschler, S., "Wing Rock of Non-slender Delta Wings", Thesis *(MEng)*, University of Bath, May 2003.

[47] Ericsson, L.E. and Beyers, M.E, "An Analysis of Self-Induced Roll Oscillations of a 45-degree Delta Wing", AIAA-2000-0655, *41st Aerospace Sciences Meeting and Exhibit*, January 6th-9th, 2003, Reno, NV.

[48] Matsuno, T, Yokouchi, S. and Nakamura, Y., "The Effect of Leading-Edge Profile on Self-Induced Oscillations of 45-degree Delta Wings", AIAA-2000-4004, *18th Applied Aerodynamics Conference*, 14th-17th August 2000, Denver, CO.

[49] Matsuno, T. and Nakamura, Y., "Self-Induced Roll Oscillation of 45-degree Delta Wings", AIAA 2000-0655, *38th AIAA Aerospace Sciences Meeting and Exhibit*, 10th-13th January 2000, Reno, NV.

[50] Ueno, M., Matsuno, T. and Nakamura, Y., "Unsteady Aerodynamics of Rolling Thick Delta Wing with High Aspect Ratio," AIAA 98-2520, *16th AIAA Applied Aerodynamics Conference*, 15th-18th June 1998, Albuquerque, NM.

[51] Ericsson, L.E., "Effect of Leading Edge Cross-Sectional Shape on Nonslender Wing Rock", *Journal of Aircraft*, Vol. 40 No. 2 pp 407-410.

[52] Vardaki, E., Wang, Z. and Gursul, I., "Flow Reattachment and Vortex Re-formation on Oscillating Low-Aspect-Ratio Wings", Vol. 46, No. 6, June 2008, pp. 1453-1462.

[53] Taylor, G.S. and Gursul, I., "Lift Enhancement over a Flexible Delta Wing", AIAA-2004-2618, *2nd AIAA Flow Control Conference*, 28th June-1st July 2004, Portland, OR.

[54] Taylor, G.S., Kroker, A. and Gursul, I., "Passive Flow Control over Flexible Non-slender Delta Wings", AIAA-2005-0865, *43rd Aerospace Sciences Meeting and Exhibit*, 10th-13th January 2005, Reno, NV.

[55] Vardaki, E., Gursul, I. and Taylor, G., "Physical Mechanisms of Lift Enhancement for Flexible Delta Wings", AIAA-2005-0867, *43rd Aerospace Sciences Meeting and Exhibit*, 10th-13th January 2005, Reno, NV.

[56] Williams, N., Wang, Z. and Gursul, I., "Active Flow Control on Non-slender Delta Wings", *Journal of Aircraft*, Vol. 45, No. 6, 2008, pp. 2100-2110.

[57] Richards, P.J., Williams, N.W, and Laing, B., "3-Dimensional Aerodynamics of Plate Type Wind Borne Debris", *Journal of Wind Engineering and Industrial Aerodynamics*, Vol. 96, Issues 10-11, October-November 2008, pp. 2188-2202 .

[58] Wong, G.S., Rock, S.M., Wood, N.J. and Roberts, L., "Active Control of Wing Rock Using Tangential Leading-Edge Blowing", *Journal of Aircraft*, Vol. 31, No. 3, May-June 1994.

[59] Siegel, S., Mclaughlin, T.E. and Albertson, J.A, "PIV Measurements on a Delta Wings with Periodic Blowing and Suction", *Department of Aeronautics*, US Air Force Academy, CO 80840-5222.

[60] Taylor, G.S., Wang, Z., Vardaki, E. and Gursul I., "Lift Enhancement over a Flexible Nonslender Delta Wings", *AIAA Journal*, Vol. 45, No. 12, December 2007, pp. 2979 – 2993.

[61] Shyy, W., Berg, M. and Lyungqvist, D., "Flapping and Flexible Wings for Biological and Micro Air Vehicles", *Progress in Aerospace Sciences 35*, 1999, pp. 455-505.

[62] Gursul, I., Wang, Z. and Vardaki, E., "Review of Flow Control Mechanisms of Leading-Edge Vortices", *Progress in Aerospace Sciences*, 43 (2007), pp. 246-270.

[63] Levin, D. and Katz, J., "Self-Induced Roll Oscillations of Low-Aspect-Ratio Rectangular Wings," *Journal of Aircraft,* Vol. 29, No. 4, 1992, pp. 698-702.

[64] Bastedo, W.G. and Mueller, T.J., "Spanwise Variation of Laminar Separation Bubbles on Wings at Low Reynolds Numbers," *Journal of Aircraft,* Vol. 23, No. 9, 1986, pp. 687-694.

[65] Winkelmann, A.E. and Barlow, J.B., "Flowfield Model for a Rectangular Wing Planform Beyond Stall," *AIAA Journal,* Vol. 18, No. 8, 1980, pp. 1006-1008.

[66] Jian, T. and Ke-Qin, Z., "Numerical and Experimental Study of Flow Structure of Low-Aspect-Ratio Wing", *Journal of Aircraft*, Vol. 41, No. 5, September-October 2004, pp. 1196-1201.

[67] Williams, D.L. and Nelson, R.C., "Fluid-Dynamic Mechanisms Leading to the Self-Induced Oscillations of LARR Wings," AIAA 97-0830, *35th Aerospace Sciences Meeting & Exhibit*, January, 1997, Reno, NV.

[68] Gordnier, R.E. and Melville, R.B., "Physical Mechanisms for Limit-Cycle Oscillations of a Cropped Delta Wing", *Journal of Aircraft,* AIAA-99-3796, 1999.

[69] Zimmerman, C.H., "Aerodynamic Characteristics of Several Airfoils of Low Aspect Ratio," *NACA-TN-539*, August 1935.

[70] Tobak, M. and Peake D.J., "Topology of Three-Dimensional Separated Flows", *Annual Review of Fluid Mechanics,* 1982, Vol. 14, pp. 61-85.

[71] Delery, J.M, Legendre, R. and Werlé, H, "Toward the Elucidation of Three-Dimensional Separation", *Annual Review of Fluid Mechanic,* 2001, No. 33, pp. 129-154.

[72] Rouse, G., "Wing Rock of Micro Air Vehicles", Thesis *(MEng)*, University of Bath, May 2008.

[73] Nelson, R.C., Corke T.C., He C.,Othman H. and Matsuno, T., "Modification of the flow structure over a UAV wing for Roll Control", AIAA 2007-884, *45th Aerospace Sciences Meeting and Exhibit, 8th-11th January 2007*, Reno, NV.

[74] Ganapathisubramani, B. and Clemens N.T, "Effect of Laser Pulse Duration on Particle Image Velocimetry", *AIAA Journal Technical Notes*, Vol. 44, No. 6, June 2006, pp. 1368-1370.

[75] Yavuz, M.M., Elkhoury, M., Rockwell, D., 2004, "Near-surface topology and flow structure on a delta wing", *AIAA Journal*, vol. 42, no. 2, pp. 332–340.

[76] Taylor, G.S, Schnorbus, T. and Gursul, I., "An Investigation of Vortex Flows over Low Sweep Delta Wings", AIAA-2003-4021, *AIAA Fluid Dynamics Conference*, 23rd-26th June, Orlando, Fl.

[77] Lowson, M.V., "Some Experiments with Vortex Breakdown", *Journal of the Royal Aeronautical Society*, Vol. 68, 1964, p. 343.

[78] Arthur, M.T., Allan, M.R., Ceresola, N., Kompenhans, J., Fritz, W., Boelens, O.J. and Pranata, B.B., "Exploration of the Free Rolling Motion of a Delta Wing Configuration in a Vortical Flow", in proceedings of RTO-MP-AVT-123, *Flow Induced Unsteady Loads and the Impact on Military Applications*, Budapest, Hungary, April, 2005.

[79] Badcock, K.J., Woodgate, M.A., Allan, M.R. and Beran, P.S., "Wing-Rock Limit Cycle Oscillation Prediction Based on Computational Fluid Dynamics", *Journal of Aircraft*, vol. 45, no. 3, May-June 2008, pp. 954-961.

Appendix A – Publications

The publications produced from this Thesis are listed:

Journal articles

1) Gresham, N.T., Wang, Z. and Gursul, I.A., "Self-Induced Roll Oscillations of Non-slender Wings," *AIAA Journal*, Vol. 47 (2009), pp. 481-483.

2) Gresham, N.T., Wang, Z. and Gursul, I., "Vortex Dynamics of Free-to-Roll Slender and Non-slender Delta Wings", *Journal of Aircraft*, Vol. 47 (2010), No. 1, pp. 292-302.

3) Gresham, N.T., Wang, Z. and Gursul, I., "Low Reynolds number aerodynamics of free-to-roll low aspect ratio wings", *Experiments in Fluids*, Vol. 49, Issue 1, 2010, pp. 11–25.

4) Gresham, N.T., Wang, Z. and Gursul, I., "Free-to-Roll Oscillations of Cropped Delta Wings" (in preparation).

Conference papers

1) Gresham, N.T., Wang, Z. and Gursul, I., "Vortex Dynamics of Delta Wings Undergoing Self-Excited Roll Oscillations," *38th AIAA Fluid Dynamics Conference and Exhibit,* AIAA-2008-4176, 23rd - 26th June 2008, Seattle, Wa.

2) Gresham, N.T., Wang, Z. and Gursul, I., "Aerodynamics of Free-to-Roll Low Aspect Ratio Wings," *47th AIAA Aerospace Sciences Meeting Including The New Horizons Forum and Aerospace Exposition,* AIAA-2009-543, 5th - 8th January 2009, Orlando, Fl..